Manipulation, readout and analysis of the decoherence ofa superconducting quantum bit

Grégoire Ithier

Thèse de Doctorat de l'Université Paris VI

Spécialité :

PHYSIQUE QUANTIQUE

présentée par **Grégoire Ithier**
pour obtenir le grade de docteur de l'Université Paris VI

Sujet de la thèse :

Manipulation, lecture et analyse de la décohérence d'un bit quantique supraconducteur

Soutenue le 15 décembre 2005 devant le jury composé de:

R. Combescot (président)
P. Delsing, rapporteur
O. Buisson, rapporteur
A. Shnirman (examinateur)
Y. Nakamura (examinateur)
D. Esteve (directeur de thèse)

Thèse préparée au Service de Physique de l'Etat Condensé,
CEA-Saclay

A Christelle
A Béatrice, Philippe et Rodolphe

REMERCIEMENTS

Je tiens à remercier chaleureusement Daniel Estève, mon directeur de thèse, pour son attention constante tout au long de ces trois années passées dans le groupe Quantronique. Sans la qualité de son encadrement, et son recul par rapport à l'expérience, ce travail de thèse n'aurait pas été possible.

Je remercie Denis Vion pour son dynamisme et sa ténacité face à des situations qui semblaient inextricables, ainsi que pour sa disponibilité et ses conseils avisés qui ont toujours été d'un grand secours.

Merci à Abdel Aassime, avec qui j'ai travaillé au début de ma thèse, et qui m'a initié aux techniques de nano-fabrication ainsi qu'aux micro-ondes. Je remercie Eddy Collin, avec qui j'ai travaillé durant près d'un an et demi, toujours dans la bonne humeur, et avec qui j'ai obtenu les résultats principaux de ma thèse. Merci à Nicolas Boulant, avec qui ce fut un grand plaisir de maniper à la fin de ma thèse.

Thanks very much to Philip Meeson with whom I built the experiment of the QND measurement of a quantronium, and with whom it was and it is still a great pleasure to work. Merci à Patrice Bertet pour les discussions et conseils qui m'ont été très utiles à la fin de ma thèse.

Merci à François Nguyen et Pedro Ribero, dont les calculs théoriques et les simulations nous ont permis d'améliorer notre compréhension du phénomène de bifurcation.

Merci aux autres membres du groupe quantronique: Hugues Pothier, Cristiàn Urbina, et Philippe Joyez qui ont toujours été disponibles pour discuter et répondre à mes questions.

Merci à tous les thésards du groupe quantronique que j'ai côtoyé: Anne Anthore, Martin Chauvin, Benjamin Huard, et Hélène Lesueur, avec qui j'ai apprécié de discuter.

Thanks very much to Joachim Ankerhold and Hermann Grabert, for their efficiency, their availability and their proximity with experimental concerns.

Un grand merci à Pierre François Orfila et Pascal Sénat, pour leur compétence précieuse et leur disponibilité, sans qui il serait impossible de construire et de faire fonctionner ces expériences. Merci à Michel Juignet qui m'a initié au maniement du tour et de la fraiseuse. Merci à Jean-Michel Richomme, qui m'a toujours trouvé l'outil adapté à ce que je voulais faire.

Je remercie Frédéric Pierre, qui a fabriqué l'échantillon utilisé à la fin de ma thèse pour l'expérience de mesure non destructrice d'un bit quantique.

Merci aussi à Michel Devoret, Irfan Sidiqqi et Rajamani Vijay pour leurs précieux conseils qui ont permis la mise en place de cette expérience à Saclay.

Je tiens à remercier Olivier Buisson et Per Delsing d'avoir accepté d'être mes rapporteurs, ainsi que Yasunobu Nakamura, Alexander Shnirman et Roland Combescot d'avoir accepté de faire partie de mon jury de thèse.

Merci enfin à mes parents qui m'ont toujours soutenu, encouragé et aidé durant mes études et durant ma thèse. Et un grand merci à Christelle pour son soutien sans failles, sa patience durant ces trois années, et sans qui tout serait si différent.

Contents

Chapter 1

Introduction and summary

1.1 Microelectronic industry scaling down to mesoscopic physics

Since the 60's, the density of transistors integrated on a microprocessor doubles every 18 months, driven by Moore's law. The last generation of MOS transistors, used for instance in the Pentium 4 (2005), has typical dimensions below 100nm.

At a length scale of a few nm, purely quantum effects like energy quantization in the channel of the transistor or tunneling from the gate to the channel, will strongly degrade the performances of this device. CMOS technology scaling to smaller and smaller dimensions is therefore likely to be compromised by these quantum effects and fundamental limits of miniaturization are expected to be reached in the near future, even if progress in materials can still significantly improve transistor performance.

Nevertheless, quantum effects in general are not necessarily only a nuisance and we'll see in the next section, dedicated to quantum computing, that quantum physics provides new principles for information processing. A computer taking advantage of these principles would be able to perform some tasks which are intractable for classical computers.

Although, no quantum computer has yet been operated, many physical systems have been investigated to explore their potential for making quantum processors. Among these, superconducting circuits made of Josephson junctions have attracted a wide interest because present fabrication techniques provide useful design flexibility. In addition, their quantumness is now demonstrated.

The aim of this Ph.D thesis is to further investigate the quantronium circuit developed in the Quantronics group since 2001. This circuit implements a quantum bit, which is the building block of a quantum computer. During this Ph.D, full manipulation and control of the quantum state of this device has been achieved experimentally. The decoherence phenomenon which prevents ordinary circuits from behaving quantum mechanically has also been characterized, and a new setup invented at Yale University by M.Devoret, for reading out the state of our qubit in a non-destructive way, has been implemented.

1.2 Quantum computing

As pointed out in the early 1980's by D. Deutsch [1], a processor that exploit the laws of quantum mechanics could indeed perform some computational tasks more efficiently than can be achieved by classical processors. This striking discovery started a new field called quantum computing.

The simplest description for a quantum processor is an ensemble of coupled two level systems, called quantum bits or qubits. A quantum algorithm consists in the controlled evolution of the quantum state of the whole processor. Measurements of the quantum state are performed during the computation to provide the answer of the problem. It was shown soon after the proposition of quantum computing that a

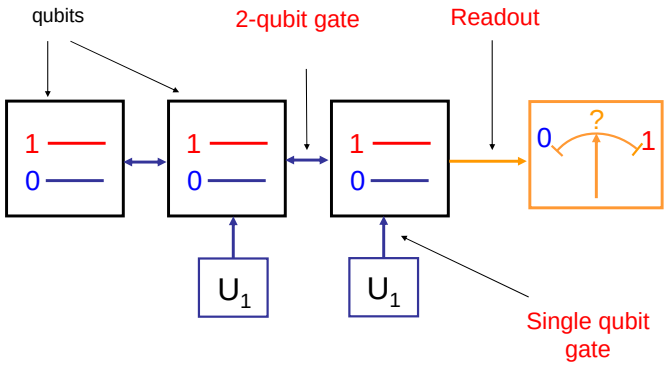

Figure 1.1: A quantum processor is made of coupled qubits, each qubit having a separate manipulation and measurement setup.

small number of single-qubit and two-qubit operations is sufficient for implementing any unitary evolution of a quantum processor. But, could quantum computers provide a large enough advantage over classical ones to compensate for their greater complexity?

In order to answer this question, one first needs to evaluate the difficulty of a given problem for classical computers, using complexity theory.

1.2.1 Evaluating the complexity of a problem

Complexity theory evaluates how the resources needed to solve a given problem, like time or memory, scale with the size of the problem. For instance the addition of two integers takes a time proportional to the number of digits of the integers. One says it has $O(N)$ complexity, where N is the number of digits.

In the ensemble of computable problems, there is a hierarchy, which defines two subensembles:

- 'P': the ensemble of problems having a polynomial complexity. For instance, the multiplication of two integers takes a time proportional to the square of the number of digits: it has a $O(N^2)$ complexity. These problems are said to be easy, since a polynomial cost is almost always supportable.
- 'NP' problems, whose solutions are easy to check. For instance, the factorization of integers. Given an integer n, it is easy to check whether or not an other given integer a is a prime factor of n : the euclidian division of n by a, takes a polynomial time and gives the answer. The P ensemble belongs to NP since if you can find the solution of a problem in a polynomial time, you can also verify a solution in a polynomial time. But it seems that NP is larger than P, and so contains problems that cannot be solved in polynomial time. For example, if you want to find a, a prime factor of n, until now, you have to try almost every integer up to $\sqrt{n}$, a process that takes an exponential time in the length of n. As a consequence, this factorization problem seems for the moment not to be in P. An important problem in computer science is to prove that NP is indeed larger than P.

This classification in different complexity classes relies on the modern Church-Turing thesis which asserts that all classical computers are equivalent. This means that the complexity class of a given problem does not depend on the hardware, i.e. the classification in P or NP problems is universal: a P problem on a Pentium is also a P problem on the last Cray. This universality does not extend however to quantum processors since quantum physics provides new principles for building a computer which is not subject to the Church-Turing thesis. Indeed, in 1994, P. Shor invented a quantum algorithm for the factorization of

integers having a polynomial complexity [2]. The impact of this discovery was extremely important since most of cryptographic protocols used nowadays (such as RSA encoding protocols) rely on the difficulty of factorizing large integers .

1.2.2 Quantum resources

Quantum computing uses several resources relying on the fundamental principles of quantum physics.

The main quantum resource is linearity. Due to the superposition principle, a quantum computer could operate at the same time on a linear combination of several input data and give the output as a superposition of all the results (see figure 1.2).

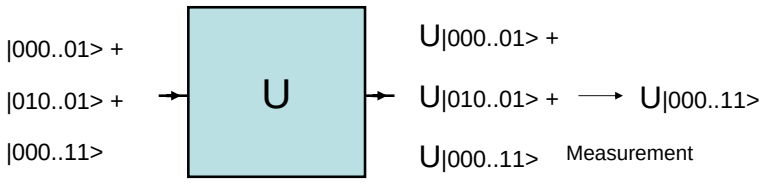

Figure 1.2: The linearity of quantum physics provides a massive parallelism. For instance, an operator U can be calculated for every value of the input register. Nevertheless, the final measurement projects the state of the quantum processor on a unique state and all the other results are lost.

This massive parallelism is not directly useful because the measurement process needed at the end of the calculation projects the quantum processor on a unique state, with a certain probability. As a consequence, quantum algorithms are not deterministic. Furthermore the no-cloning theorem [3] forbids the copy of an unknown quantum state, this probability distribution is not measurable in a single shot.

The art of quantum algorithmics is precisely to restore the power of quantum parallelism by circumventing the drawback of this unavoidable projection at readout. The idea is that, for particular types of problems different from the simple evaluation of a function, the final readout step can provide the searched answer with a high probability. This "quantum distillation" is exemplified by L. K. Grover's search algorithm [4]. This algorithm can find indeed a particular state in a Hilbert space of dimension N, in a time $O(\sqrt{N})$, whereas the best classical search algorithm in a data base of N elements has a $O(N)$ complexity. Starting from a quantum state given by the superposition of all Hilbert space elements, the evolution drives it towards the state that fulfills the particular condition required.

Underlying to this concept of a clever unitary evolution that can be compared with a sort of "distillation" of the quantum states, is the entanglement phenomenon. This is a general property of almost all states in a Hilbert space and it can be seen as a resource by itself, even if, for the moment, no satisfactory measure exists for quantifying this property in a many qubit systems. Entanglement gives rise to non classical correlations between parts of a composite system. Information can be encoded in these correlations, leading to astonishing results. For instance, sharing an entangled pair of qubits permits to communicate two classical bits by sending only one qubit (superdense coding [5]), or to teleport an unknown qubit state by sending two classical bits [6].

The resources of quantum physics can thus be exploited to solve particular tasks, such as: quantum Fourier transform [7], search problems in an unstructured ensemble, and more important, simulation of a quantum system [8, 9]. Today, it is still unknown how many problems can be solved efficiently with a quantum computer. The real potential of a quantum computer compared to a classical one is so far unknown. As a consequence, an important motivation for building such a quantum processor is to deepen our understanding of quantum physics, and in particular of the quantum-classical boundary.

1.2.3 The problem of decoherence

From the experimental point of view the implementation of a quantum processor is obviously a formidable task because quantum states are extremely fragile. Indeed, quantum superpositions of states are very sensitive to errors introduced by the coupling to the environment which is unavoidable if manipulation and measurement have to be performed. This decoherence phenomenon (see chap 4), was considered to be a fundamental limit for quantum computation, until P. Shor [10], A. M. Steane [11] and D. Gottesman [12] proposed schemes for quantum error correction. The idea is to use redundancy, as with classical error correction, by entangling the main qubits with auxiliary ones, called ancillas. The correction of errors is possible by measuring these ancilla qubits and getting enough information on the errors to correct properly the main qubits without losing quantum coherence. For instance, four auxiliary qubits are required to implement this scheme in the frame of the model of single qubit errors. To work, these quantum error correcting codes need a minimal accuracy for every typical qubit operation. If the probability of errors per gate is below a critical value of about 1 over 10^4 operations, which is presently beyond the reach of all proposed implementations, then an arbitrarily long quantum computation could be performed.

1.3 Physical implementations of qubits

The requirements for implementing a quantum computer are given by the DiVincenzo criteria [13]. There are needs for:

- Scalability: a large number of reliable qubits is needed;
- Efficient initialization of the qubit state (reset);
- Quantum coherence: long coherence times compared to gate operation time;
- High fidelity readout of individual qubits;
- Availability of a universal set of quantum gates

As the physical systems currently used for building qubits do not simultaneously satisfy all these criteria, one can roughly classify qubits in two types:

- Microscopic systems like nuclear spins, ions or atoms. They are intrinsically quantum and have long coherence times, but they are not easily scalable mainly because of their typical size.
- Macroscopic systems, like quantum dots or superconducting circuits, are easily scalable with lithography techniques, but not easily quantum, since they are well coupled to their environment.

Having the DiVincenzo criteria in mind, we shall see more precisely what the advantages and the drawbacks are of the main physical systems used as qubits.

1.3.1 Microscopic qubits

Nuclear spins

In NMR quantum computing, qubits are encoded in the nuclear spins of a molecule in a magnetic field [14]. As it is impossible to measure a single nuclear spin about 10^{20} identical molecules are used to get a reasonable signal with a weak ensemble measurement. The state of the system is controlled by applying resonant radiofrequency pulses and logic gates are obtained from scalar coupling, which is an interaction between neighbor spins mediated by the electrons of the chemical bounding. Since k_BT is much higher than the Zeeman splitting it is not possible to initialize the spins in a pure state, hence, the

state of the spin ensemble is highly mixed. It is a major issue, since, a well known input state has to be prepared before performing any quantum algorithm. Fortunately, this problem can be circumvented by preparing a particular state, called a pseudo pure state, which behaves dynamically like a pure state [15].

Despite important breakthroughs in 1998 with the implementation of the Deutsch-Josza algorithm [16] and in 2001 with the implementation of the Shor's factorizing algorithm [17], NMR quantum computing is limited by the preparation of this initial pseudo pure state. This preparation either costs an exponential time in the number of qubits or reduces exponentially the signal to noise ratio, which makes NMR quantum computing not scalable.

Trapped ions

In 1995, I. Cirac and P. Zoller proposed the implementation of a quantum computer with trapped ions [18].

The qubits are stored either in a long-lived optical transition of an ion [19], or in the ground state hyperfine levels [20]. These systems are well known in metrology for their use as frequency standards, since coherence times of several minutes are available.

The ions are confined in a harmonic potential created by a Paul trap and because they repel each other by Coulomb interaction, the mean distance between ions is a few microns allowing individual optical addressing for manipulation and measurement (see figure 1.3).

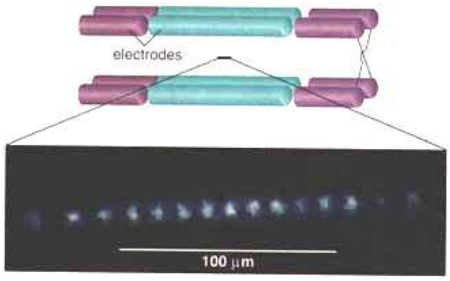

Figure 1.3: A set of electrodes creates a combination of DC and AC electric fields (called a Paul trap) suitable for confining ions. The ions repeal each other by Coulomb interaction allowing individual optical addressing. The modes of vibration of the string are used for coupling the ions.

The idea for implementing quantum gates between ions is to couple the electronic degrees of freedom of the ions to the vibrational modes of the string with Raman transition, and use these phonons as a quantum bus.

With such a scheme a CNOT-gate [21], four ion entangled states [22] and quantum error correction have been achieved [23]. However, the single trap quantum computer is limited to a small number of ions. New "on-chip" architectures based on registers of interconnected traps should permit scaling to a much higher number of ions without inducing significant decoherence [24]. This new type of architecture is presently the most promising for implementing a quantum computer.

Atoms in cavity

Atoms in cavity have been extensively used since the mid 90's mostly for studying quantum measurement and entanglement. Such systems consist of a high Q cavity, which quantizes the spectrum of the vacuum and enhances dramatically the interaction between an atom and the electromagnetic field.

Quantum logic operations based on Rabi oscillations between the atom and the cavity have been achieved [25] and the progressive decoherence process of an atom entangled with a mesoscopic coherent

field has been observed [26], enlightening the quantum-classical boundary. A three particle GHZ (Greenberger, Horne, and Zeilinger) entangled state has been prepared [27], using the field of the cavity like a quantum memory for storing the information of an atom. In the context of quantum computing, these experiments enlighten the roles of entanglement and decoherence, which are two major phenomenon of this field. Nevertheless, the scalability of such a system is limited by the preparation of single atomic samples and by the cavity itself. New schemes for creating Bose Einstein condensates on a chip are now being studied [28], the idea is to use microfabricated circuits similar to those used for ions to trap and manipulate Rydberg atoms.

1.3.2 Macroscopic qubits based on electronic circuits

Electronic quantum bits divide into two classes. In the first class, qubits are encoded in the degrees of freedom of individual electrons trapped or propagating in a semiconductor circuit. Either the orbital state or the spin state of the electron can be used to make a qubit. In the second class, qubits are encoded in the quantum state of an entire electrical circuit. This strategy has only been used for superconducting circuits, which are the only ones with sufficiently weak decoherence for that purpose.

Semiconductor structures

In a semiconductor, transport properties rely on microscopic quantum effects, like for instance the modulation of the carrier density with an electric field. On a macroscopic scale, these properties are subject to a statistical averaging which suppresses any quantum behavior. In order to recover such a behavior, one possibility is to confine a small number of electrons in a quantum dot. If the length of the dot is comparable to the Fermi wavelength, then, energy quantization and Coulomb repulsion permit one to isolate a single electron on a unique quantum state of the dot [29]. The most advanced experiments consists in using a 2D electron gas properly biased with gate electrodes (see figure 1.6). The spin state of an electron trapped in such a dot and subject to a magnetic field (parallel to the electron gas) has a long relaxation time, up to about 1ms. Spin manipulation can be performed using ac magnetic fields and the exchange interaction between neighboring dots provides a controllable coupling of the qubits. A single shot readout is achieved by transferring the spin information into the charge of a dot, which can be measured using a quantum point contact transistor [30]. However, the coherence time is of the order of 10 ns, much shorter than the relaxation time, due to random magnetic fields produced by the nuclear spins of the GaAs substrate [31]. Although decoupling pulse methods inspired from NMR could in principle be used to suppress decoherence due to these random fields, a more reliable solution would be to use materials having a zero nuclear spin.

Alternative approaches have been proposed [32, 33], using ballistic electron propagating in quantum wires. This is the so-called "flying qubit" which consists in encoding the information in the presence or not of an electron propagating on an electronic mode of the circuit. Most promising systems are probably edge channels of a 2D electron gas in the Quantum Hall Effect regime, which provide waveguides for electrons where the phase coherence length can exceed several tens of μm. In addition, single deterministic electron sources using quantum dot in the Coulomb blockade regime have been demonstrated [34].

A fundamental difference here with others types of qubits is that the two states are degenerate but well decoupled due to spatial separation. However, they can be coupled at will in quantum points contacts, which are the equivalent of beam splitters in quantum optics. Coulomb interaction between electrons was first proposed for implementing logical operations between flying qubits, but new ideas exploiting single electron sources, the Fermi statistics and the linear superposition of electronic waves with beam splitters, can lead to entangled 2 electron states [35]. The detection of a single electron in a short time (a few ns), which is an important issue remains to be solved and the mecanisms of dephasing and energy relaxation of an electron in an edge channel, which affects the coherence of the flying qubit, will have to be characterized.

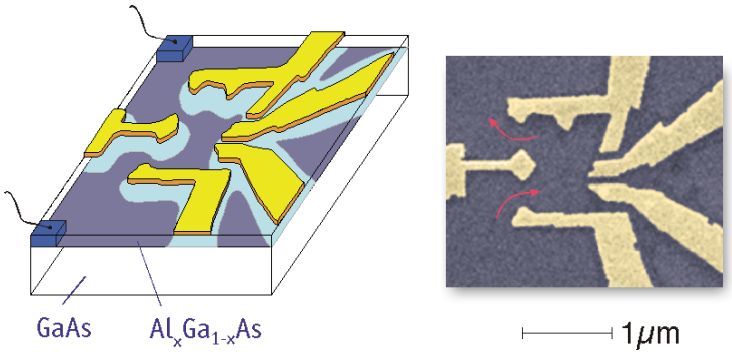

Figure 1.4: Spin qubit in a quantum dot. A 2D electron gas is created at the interface of two semiconductors having different dopant concentrations. This 2D electron gas is depleted by a set of negatively biased electrodes and form a quantum dot. Dark: conducting regions. Bright: isolating regions. Individual electrons can be added to the dot and in a magnetic field parallel to the electron gas, the spin state form a reliable two level system suitable to implement a qubit.

Superconducting qubits

Due to the absence of dissipation, superconductivity gives the opportunity to use a collective quantum degree of freedom, namely, the superconducting phase.

When crossing the critical temperature of a superconductor, the electrons bind to form Cooper pairs. The superconducting ground state can be seen as resulting from the Bose Einstein condensation of these Cooper pairs into a single macroscopic quantum state called the superconducting condensate. This condensate is fully characterized by the order parameter Δ of the transition given by:

$$\Delta = |\Delta| e^{i\theta},$$

where $|\Delta|$ is the superconducting energy gap, isolating the ground state from the first excitations, and θ the superconducting phase. At sufficiently low $k_B T$ compared to the gap, the main microscopic excitations are frozen out and the superconducting phase becomes a robust macroscopic quantum degree of freedom. The energy spectrum of an isolated superconducting electrode thus consists of a non degenerate ground state well separated from excited quasiparticle states.

When two superconducting electrodes are weakly coupled by tunnel effect across a thin isolating barrier, a Josephson junction is formed, which is the simplest possible circuit and the building block of superconducting qubits. This circuit is characterized by two energy scales: E_j, the Josephson energy, characterizing the strength of the tunnel coupling, and $E_c = (2e)^2/2C$, the charging energy of one Cooper pair on the capacitance of the junction (see figure 1.5). These two energies are involved in the Hamiltonian of the junction:

$$H = E_c \widehat{N}^2 - E_j \cos\widehat{\theta},$$

where $\widehat{\theta}$ is the difference between the phases of each electrode and N is the number of Cooper pairs having crossed the junction. These two variables are quantum mechanically conjugated: $[N, \widehat{\theta}] = i$. When $E_c \gg E_j$, i.e. for small junctions (below $0.1\mu m^2$ for aluminium junctions), the eigenstates of the circuit are close to charge number states, whereas, in the opposite limit, they are close to phase states.

Due to the non-linearity of the Josephson Hamiltonian, Josephson junctions can be used to build systems having anharmonic atomic-like spectrum, the two lowest energy levels of which form the qubit. Although superconducting qubits are so far implemented with circuits made of several junctions their

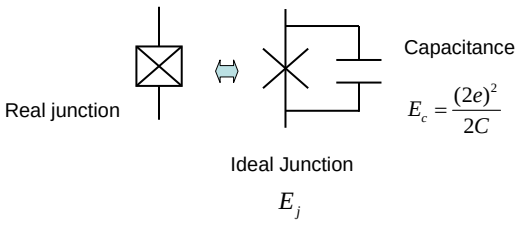

Figure 1.5: Real Josephson junctions are made by the overlap of two metallic electrodes separated by a thin oxide layer. This overlap defines a geometrical capacitance which adds in parallel to the pure Josephson coupling, and defines the charging energy E_c, which is the energy cost for adding an extra Cooper pair on this capacitor.

behavior is always ruled by the comparison between a principal charging energy and a principal Josephson energy defined by the size of the junctions and the topology of the circuit. Depending on the ratio of these two energies E_j and E_c, several types of superconducting qubits have been realized:

- charge qubit $(E_j/E_c \ll 1)$ [36] [37] [38].
- flux qubit $(E_j/E_c \approx 10)$ [39].
- phase qubit $(E_j/E_c \gg 1)$ [40].

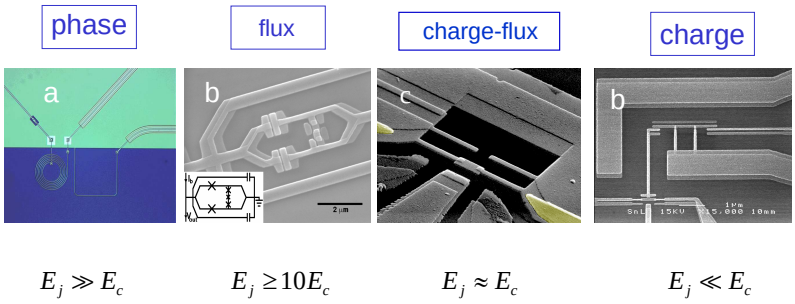

Figure 1.6: Different types of superconducting qubits depending on the ratio E_j/E_c, from left to right: NIST, Delft, Saclay, Chalmers qubits. For large E_j compared to E_c, the eigenstates of the system are almost phase states except near degeneracy points, whereas for large E_c, the eigenstates are almost charge states.

1.4 The Quantronium

In this thesis, we have investigated the Quantronium, a charge-flux qubit $(E_j/E_c \approx 1)$ described in details in chapter 2.

The first successful manipulation of the quantum state of a circuit was performed in 1999 by Nakamura *et.al.* [36] using a circuit derived from the Cooper pair box [41], which is the simplest tunable Josephson circuit.

Since a very short coherence time was also obtained in 2000 for the flux qubit [42], it became clear that getting rid of decoherence was mandatory for making qubits. Although decoherence sources were not analyzed in detail at that time, the dephasing induced by the variations of the qubit transition frequency due to the fluctuations of the control parameters appeared as an important source of decoherence [43]. The quantronium, developed since 2001 in the Quantronics group [44], is the first qubit circuit with a design that protects it from the dephasing resulting from random fluctuations of the control parameters.

1.4.1 Description of the circuit

The quantronium is also derived from the Cooper pair box. It is made of a superconducting loop interrupted by two small Josephson junctions to form an island (see figure 1.7). This island can be biased by a gate voltage V_g and the flux ϕ in the loop can be tuned by an external magnetic field. These two knobs can be recast in terms of the reduced parameters $N_g = C_g V_g / 2e$, which is the reduced charge induced on the island by the gate, and $\delta = \phi/\varphi_0$, where $\varphi_0 = \hbar/2e$ is the reduced flux quantum, the superconducting phase difference across the two junctions in series. These two parameters permit to tune the properties

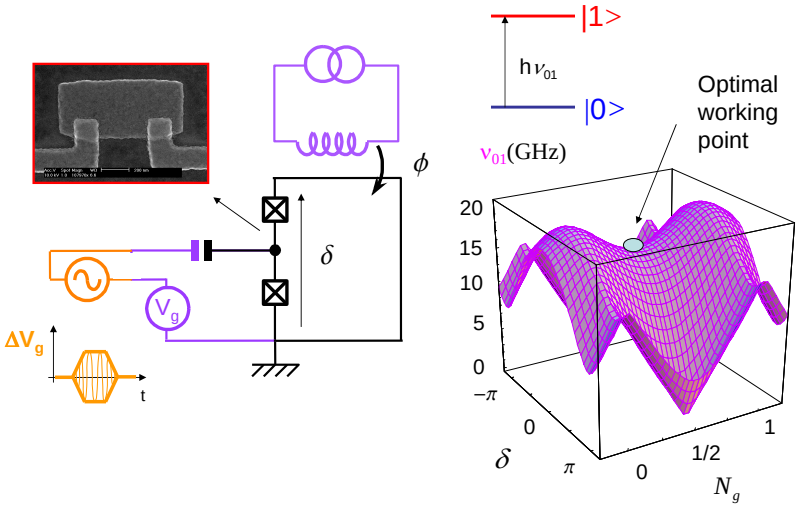

Figure 1.7: Schematics of the split Cooper pair box circuit and dependence of the transition frequency with the reduced parameters: $N_g = C_g V_g / 2e$ and $\delta = \phi/\varphi_0$ the reduced magnetic flux in the superconducting loop.

of the qubit and in particular, its transition frequency (see figure 1.7). One can notice the presence of particular points in the parameter space where the transition frequency is stationary with respect to δ and N_g. Consequently, fluctuations in the control parameters will induce little dephasing at such optimal working points, since the qubit frequency ν_{01} varies only at second order with the control parameters. It is now believed that the existence of an optimal working point is crucial for implementing qubits having long coherence times. In our experiments we have used the saddle point $P_0(N_g = 1/2, \delta = 0)$.

1.4.2 Readout of the quantum state

To read out the qubit state, we use the fact that the persistent current I_k in the superconducting loop depends on the state k. This current is given by:

$$I_k = \frac{1}{\varphi_0}\frac{\partial E_k}{\partial \delta}$$

for $k = 0$ or 1. One can notice that $I_1 - I_0$ is zero at the optimal working point since the transition frequency is stationary with respect to the phase δ, thus one has to move away from this working point in order to get two different currents for the states $|0\rangle$ and $|1\rangle$. We discriminate between these two currents, by inserting in the loop a third Josephson junction, which is used as a current threshold detector (see figure 1.8). When biasing this junction with an appropriate current pulse, it switches to a detectable voltage state with a high probability if the qubit is in state 1, and it switches with a low probability if the qubit is in state 0.

Using this method, the experimental readout fidelity happens to be imperfect: the maximum difference between the switching probabilities in state 1 and state 0 that we have obtained is only 40%, whereas a simple adiabatic theory, which consists in decoupling the dynamics of the qubit from the one of the junction, predicts 95%. We attribute this discrepancy to spurious relaxation effects during the readout, and to a possible non validity of the adiabatic hypothesis. Furthermore, this readout is destructive for the qubit. In chapter 5 of this thesis, we describe a new microwave readout method that may provide a non destructive (i.e. Quantum Non Demolition) readout for the quantronium.

1.5 NMR-like manipulation of the qubit

The aim of the chapter 3 of this thesis is to demonstrate that full control of the quantum state of the quantronium can be achieved. First, an arbitrary unitary transformation of the qubit can be achieved by combining simple rotations using microwave pulses. Second, qubit transformations can be made more robust against experimental imperfections by applying NMR methods. Let us see first how the qubit state is manipulated with the use of microwave pulses applied to the gate electrode of the quantronium, analogous to the way atomic states are manipulated with laser pulses.

1.5.1 Rabi oscillations

The qubit is a two level system for which an equivalent representation is a spin 1/2 in a magnetic field. One can represent quantum states by a vector on the Bloch sphere (see figure 1.9). State $|1\rangle$ is at the South pole, state $|0\rangle$ at the North pole, and the equatorial plane represents superpositions of $|0\rangle$ and $|1\rangle$ with equal weights but different phases. To control coherently the qubit state, the most direct way is to use Rabi precession. It consists of applying a resonant microwave pulse to the gate. In the rotating frame, which rotates at the microwave frequency around the Z axis, such a pulse is equivalent to a static magnetic field lying in the equatorial plane (see figure 1.9) with an angle χ with respect to the X axis defined by the microwave carrier. The pseudo spin of the qubit precesses around this magnetic field at the Rabi frequency, which is proportional to the microwave amplitude. The probability of being in state $|1\rangle$ oscillates with the pulse duration: these are the celebrated Rabi oscillations (figure 1.10). The qubit continuously evolves from $|0\rangle$ to $|1\rangle$, and the phase coherence between the two states is preserved during this oscillation. Two particular values of the pulse duration, for which the spin has rotated by $\pi/2$ and π, are notable. These two specific rotations form the basis of the manipulation of the quantum state, and they will be often used in our experiments.

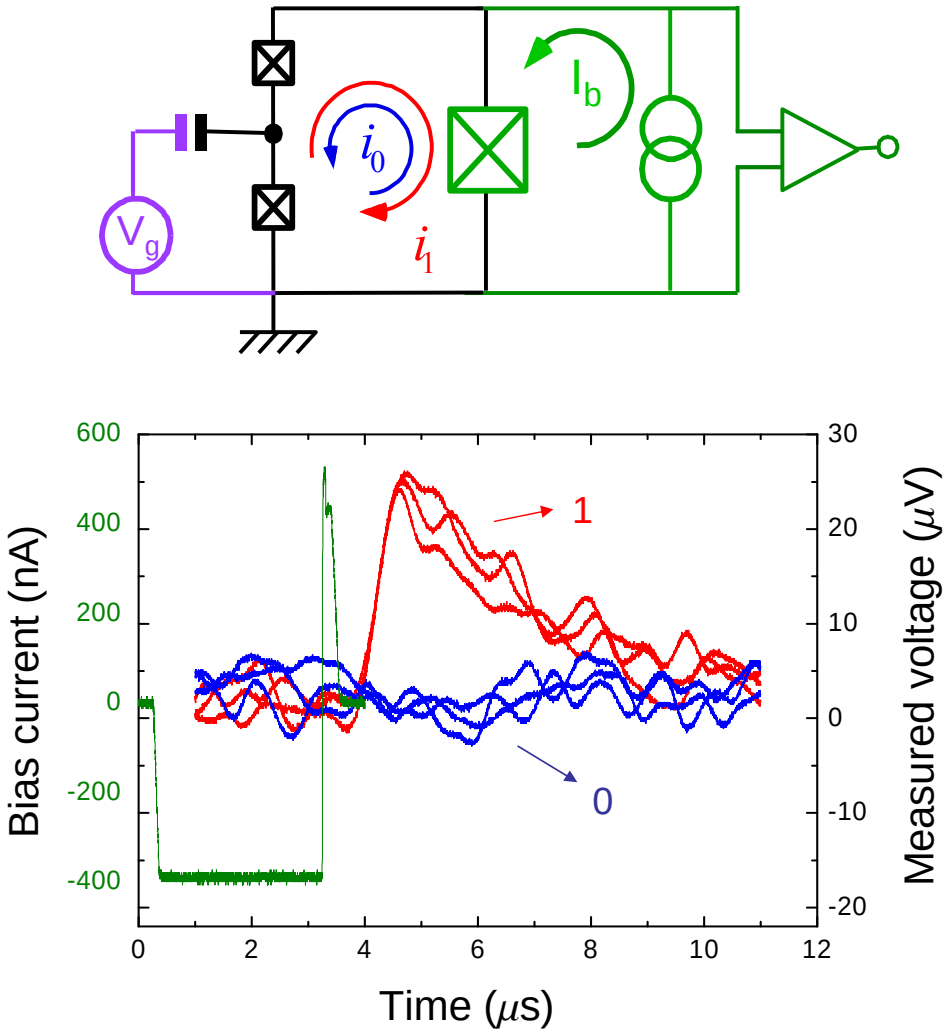

Figure 1.8: Top: schematics of the readout setup. A third Josephson junction is inserted in the loop of the split Cooper pair box. This junction plays the role of a current threshold detector: when biased with an appropriate current pulse, it switches to a detectable voltage state with a high probability if the qubit is in state 1, and with a low probability if the qubit is in state 0. Bottom: current bias pulse and measured voltage when the junction switches and when it keeps superconducting.

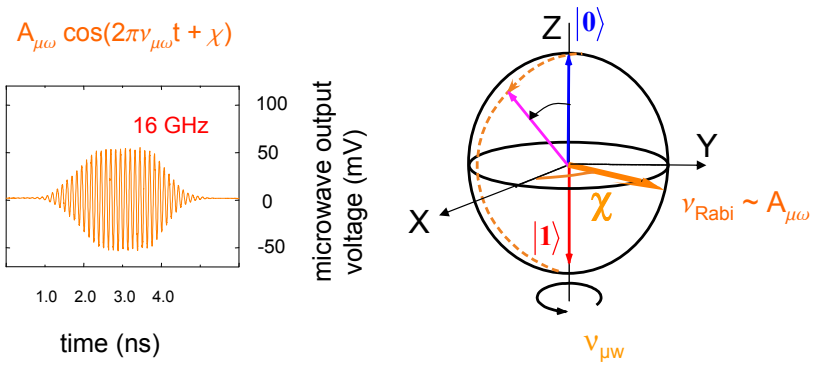

Figure 1.9: Representation of the qubit state using the Bloch sphere. The effective spin of the qubit precesses around the effective microwave field at the Rabi frequency, and the probability of being in state $|1\rangle$ oscillates with the microwave pulse duration.

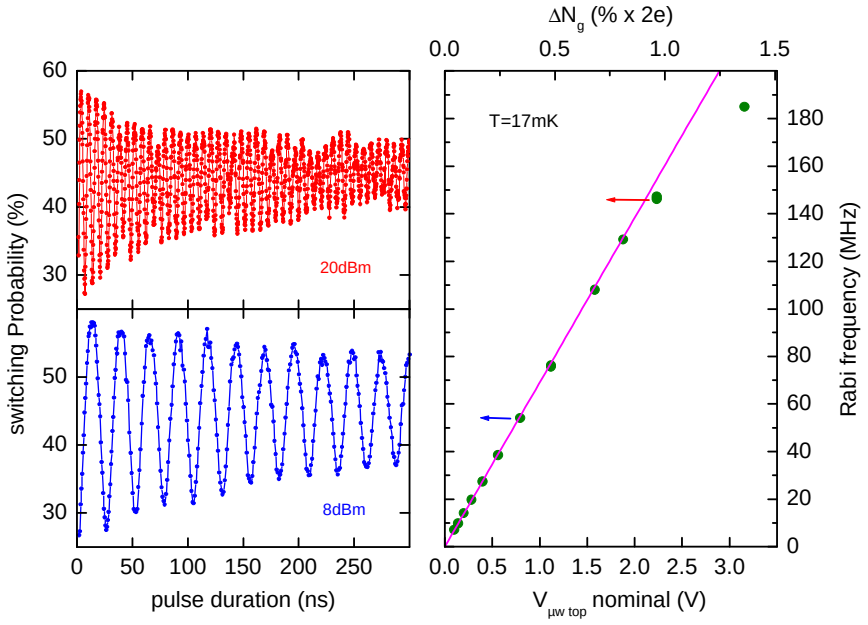

Figure 1.10: Left: Rabi oscillations for 2 different microwave powers. The probability of being in state $|1\rangle$ oscillates with the microwave pulse duration. Right: as expected the Rabi frequency is proportionnal to the microwave amplitude.

1.5.2 Combined rotations

It is well known that any unitary operation on a spin 1/2 can be performed by combining three rotations around two orthogonal axes, such as the X and Y axes of the Bloch sphere [45]. In order to probe if rotations do combine as predicted, we have performed a series of two $\pi/2$ pulse experiments, following the famous Ramsey sequence (see figure 1.11). Between the two $\pi/2$ pulses the spin undergoes a free evolution of duration Δt that corresponds to a rotation at the detuning frequency $\Delta\nu = \nu_{\mu w} - \nu_{01}$ around the Z axis. The switching probability after the second pulse as a function of Δt produces an interfering pattern, oscillating at $\Delta\nu$ which renders the free evolution of the qubit between the two pulses. In further

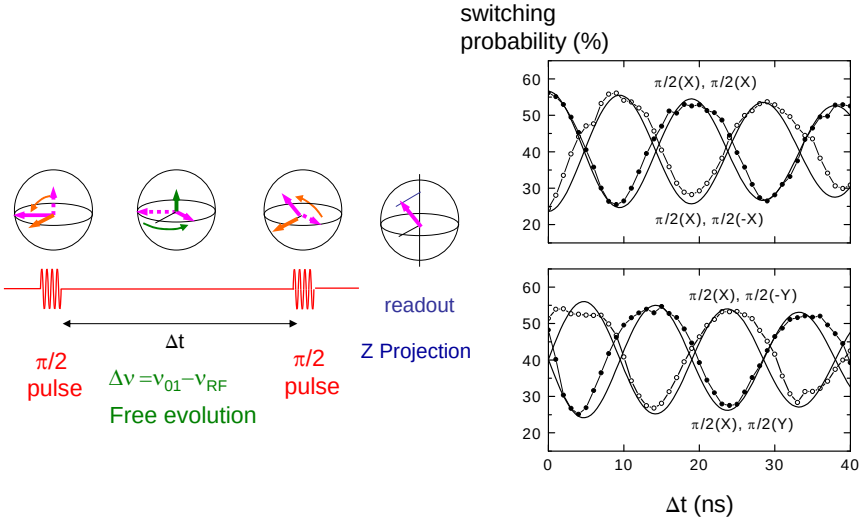

Figure 1.11: Left side: Ramsey sequence. A first $\frac{\pi}{2}$ pulse brings the state vector in the equatorial plane where it precesses at the detuning frequency. Then the probability of being in state 1 is measured after a second $\pi/2$ pulse. Right side: Ramsey fringes resulting from combinations of $\pi/2$ rotations around the (X,X), (X,-X), (X,Y) and (X,-Y) axes. By rotating the axis of rotation by an angle χ, the fringes are dephased by the same angle.

experiments, the second $\pi/2$ pulse is dephased by an angle χ with respect to the microwave carrier, which corresponds to performing the second rotation around an axis in the equatorial plane of the Bloch sphere at an angle χ with respect to the X axis. The observed Ramsey pattern is shifted precisely by the same angle χ, as expected. The results of a series of Ramsey experiments corresponding to phase shifts $\pi/2$ and π are shown in figure 1.11. The overall good agreement with the predictions proves that qubit rotations do combine as predicted, which indicates that arbitrary qubit operations can be performed. The accuracy of these qubit operations is less than that required for quantum computation. However, we will see in the next section that the sensitivity of an operation to unavoidable noise can be improved using control methods borrowed from NMR.

1.5.3 Implementation of robust operations

When performing a rotation of the qubit state many sources of errors are possible: for example the duration and the amplitude of the RF pulse may be wrong, or the frequency may be out of resonance. In NMR several techniques were developed to reduce the sensitivity to pulse imperfections by using combinations of several pulses called composite rotations. For instance, the CORPSE sequence (Compensation for Off Resonance with a Pulse SEquence) aims at reducing strongly the sensitivity to frequency detuning of the qubit. In the case of the implementation of a NOT operation, this sequence was compared with a standard π rotation. As shown in figure 1.12, it is less sensitive to frequency detuning than the π pulse since the efficiency stays close to its maximum over a larger frequency range. By performing the CORPSE sequence after an arbitrary rotation of angle θ around the X axis, we have shown that this sequence works for every initial state and not only for state $|0\rangle$.

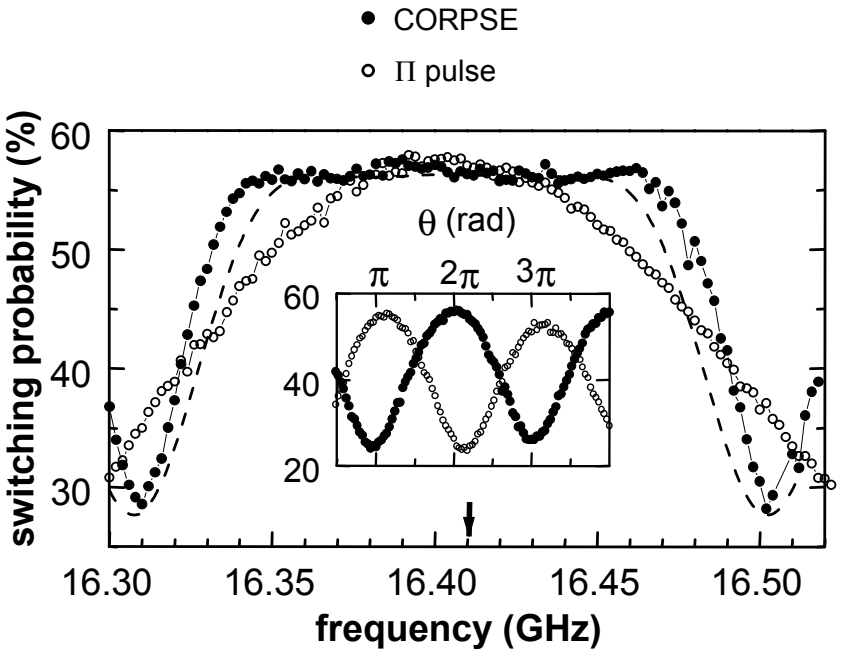

Figure 1.12: Demonstration of the robustness of the CORPSE sequence with respect to frequency detuning. A NOT operation is implemented with a π pulse and with a CORPSE sequence. The efficiency of the CORPSE sequence applied to state $|0\rangle$ is preserved over a larger frequency range than for the π pulse. The dashed line is the prediction for the CORPSE, and the arrow indicates the qubit transition frequency. Inset: to demonstrate that the CORPSE sequence works for any initial state, a rotation of angle θ is performed followed by the CORPSE sequence. The switching probability oscillates with θ in phase opposition compared to a single θ rotation, as predicted for a NOT operation.

To summarize, any one-qubit operation can be performed and the robustness of this operation can be improved by using composite pulse sequences. These fundamental tasks will have to be perfectly mastered before a quantum processor can be built. In this respect, note that these experiments have not reached the accuracy achieved in NMR or ion-trap experiments.

Presently, no system has achieved the accuracy required for error correction of single qubit operations. Although somewhat technical, this difficulty will pose a serious problem for making a quantum processor.

1.6 Analysis of decoherence during free evolution

Single qubit operations permit to prepare coherent superpositions of the qubit states: $\alpha|0> + \beta|1>$. An essential issue is to understand how the quantum coherence of this superposition of states disappears when the system evolves freely or when it is driven with a microwave field. In other words, how does decoherence destroy the quantum behavior of the qubit? The chapter 4 of this thesis addresses this question.

The quantum coherence of the system is limited by its interaction with the degrees of freedom of the environment. In the weak coupling regime, the effect of this interaction can be described in simple terms: it induces depolarization and dephasing. Depolarization processes involve an irreversible energy transfer between the qubit and the environment. At low temperatures, only relaxation of the qubit from

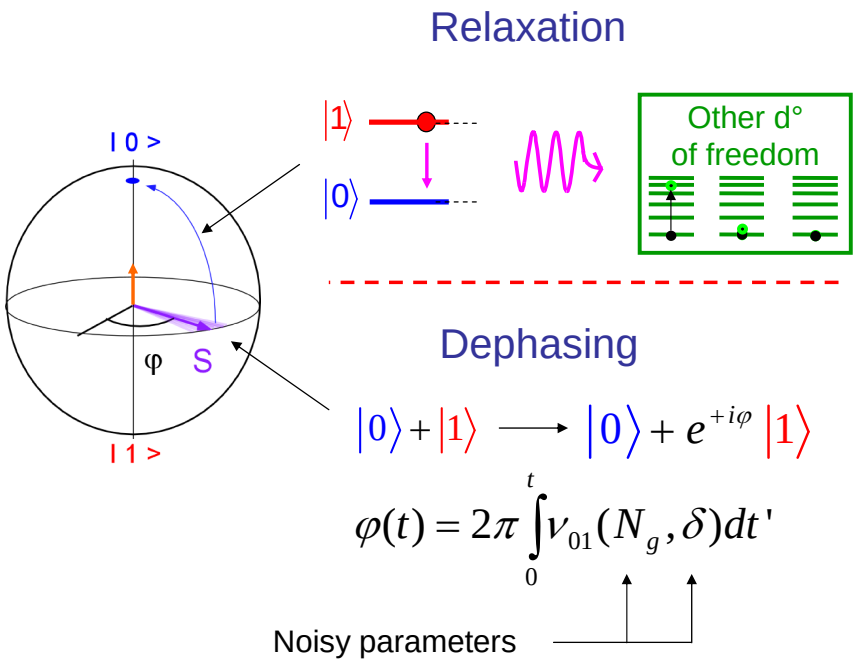

Figure 1.13: Decoherence processes can be divided in two parts: relaxation and pure dephasing. The relaxation process involves the emission of one photon by the qubit which is irreversibly absorbed by the environment. The dephasing process is caracterized by a diffusive behavior of the phase φ accumulated between state $|1\rangle$ and state $|0\rangle$ and coming from the fluctuations of δ and N_g.

its excited state to its ground state has to be considered, since thermal excitation can be neglected. This phenomenon is characterized by a time T_1 which involves the spectral density of the environment at the frequency ν_{01}: $\Gamma_1 = 1/T_1 \propto S(\omega_{01})$.

For dephasing processes, the degrees of freedom of the environment are sources of noise for the control parameters of the qubit, namely, δ and N_g. As the transition frequency of the qubit depends on these two

parameters, a random contribution is added to the phase φ accumulated between states 1 and 0 during free evolution: $|0> + e^{i\varphi}|1>$ where

$$\varphi(t) = 2\pi \int_0^t \nu_{01}(\delta, N_g)dt'.$$

At the optimal working point $P_0 = (\delta = 0, N_g = 1/2)$, $\partial\nu_{01}/\partial\delta = 0$ and $\partial\nu_{01}/\partial N_g = 0$. Fluctuations of the parameters only couple at second order to the phase φ, thus, there is no dephasing at first order. This dephasing process is characterized to first approximation by a rate Γ_φ related to the environmental noise at low frequency: $\Gamma_\varphi \propto S(\omega \approx 0)$.

The aim of these experiments is to relate quantitatively the measured decoherence in the quantronium to the properties of the noise sources coming from its environment.

1.6.1 Noise sources in the quantronium

Through the variables δ and N_g, the quantronium is coupled both to microscopic and macroscopic degrees of freedom of the environment. These degrees of freedom are pictured in fig 1.14. Previous experiments on Cooper pair boxes have shown that the background charge noise contribution to N_g is an important source of dephasing, and the first experiments on flux qubits have shown that the flux noise is also important in small superconducting devices with a loop geometry. The interest of the optimal working point is precisely to minimize the effect of these noise sources.

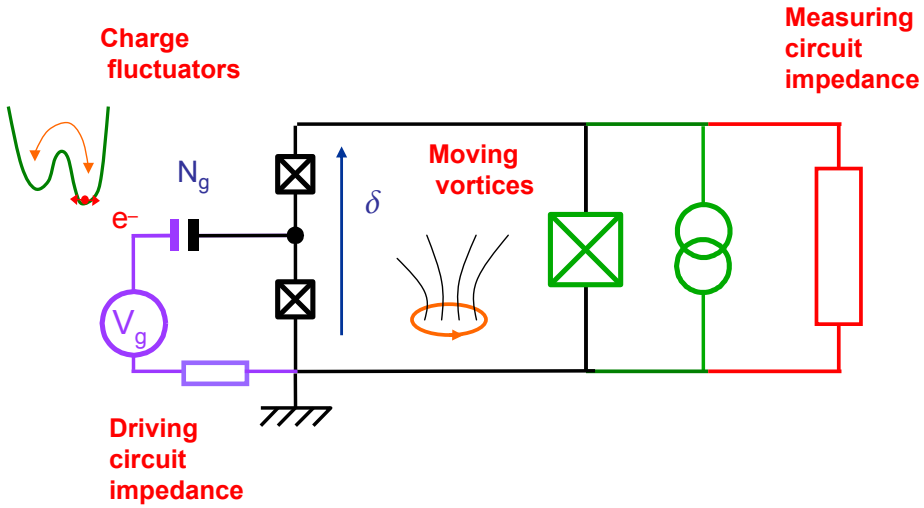

Figure 1.14: Examples of noise sources in the quantronium's environment: microscopic sources, like charge fluctuators or moving vortices and macroscopic sources, such as the impedance of the measuring and driving circuits. These noise sources contribute to relaxation and/or to dephasing.

1.6.2 Relaxation measurement

The relaxation time of the qubit has been measured at the optimal working point $P_0(N_g = 1/2, \delta = 0)$ and also along the lines $\delta = 0$ and $N_g = 1/2$ (see figure 1.15). A dependence of T_1 with the working point

is observed, implying that the density of modes available in the environment for absorbing one photon from the qubit depends on the frequency.

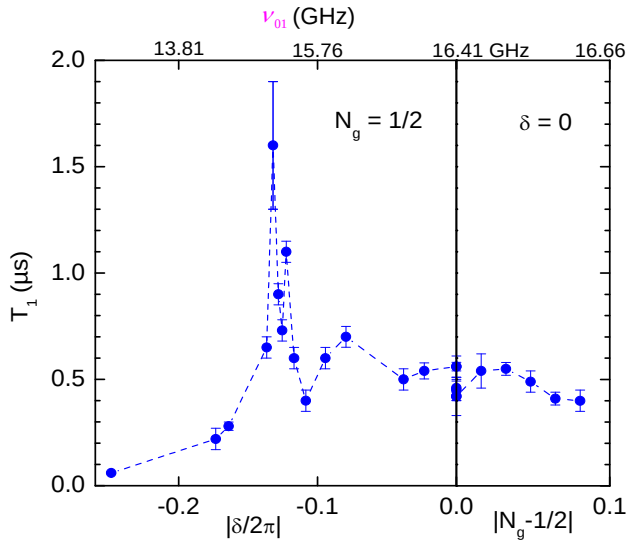

Figure 1.15: T_1 measurements as a function of the working point. The variation of T_1 is a direct signature of the dependance of the density of electromagnetic modes of the environment with the frequency.

1.6.3 Dephasing measurement

For characterizing dephasing, we have used several methods:

- Resonance linewidth measurement

  The resonance line of the qubit is recorded at low microwave power as a function of frequency. The width of the line is equal to $\Gamma_2 = \Gamma_1/2 + \Gamma_\phi$, which includes contributions from dephasing and relaxation. The results of these measurements are summarized on figure 1.18.

- Ramsey Fringe experiments

  The two-pulse Ramsey experiment provides a direct probe of coherence in the time domain. The damping of the Ramsey signal measures the progressive loss of coherence.

- Detuning pulse method

  The detuning pulse sequence is a Ramsey experiment having the two $\pi/2$ pulses performed at the optimal working point. In addition, during the free evolution the qubit is detuned with an N_g pulse or a phase pulse in order to probe T_2 at a specific point in the parameter space. This technique has the advantage that the two $\pi/2$ pulses are always performed at the same working point, which makes the experiment more efficient.

These three methods probes T_2 in different ways but yield consistent results. The next method measures another time scale: T_{echo} and gives information on the characteristic frequency of the noise sources involved in the decoherence phenomenon.

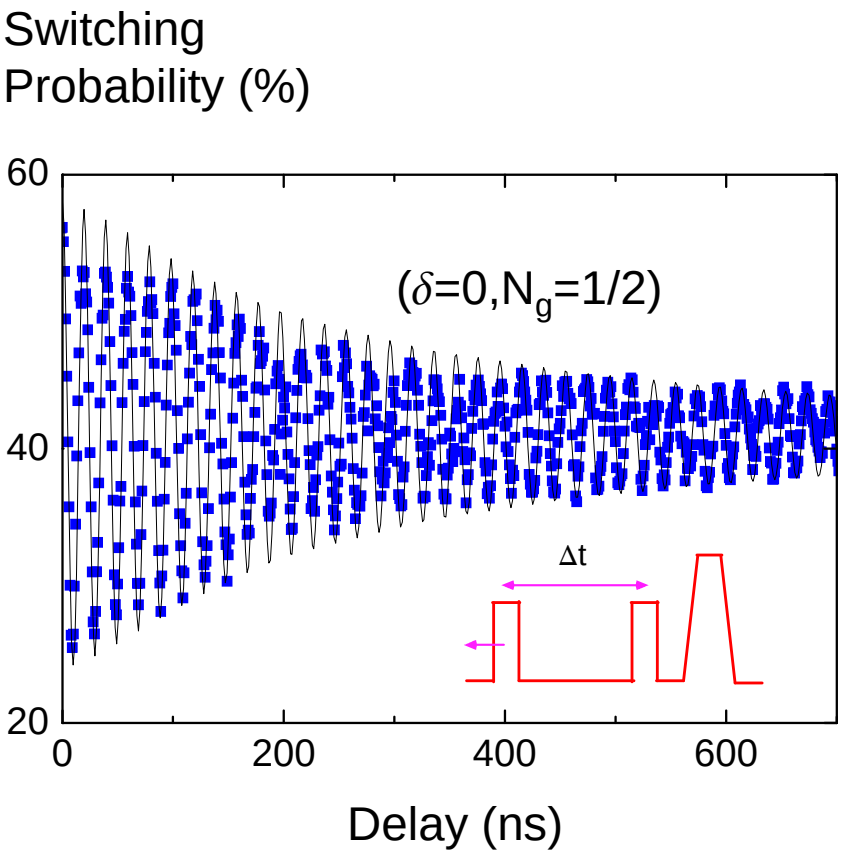

Figure 1.16: The damping of the Ramsey fringes renders the progressive decoherence of the quantum state during its free evolution. The qubit evolves from a pure state to a statistical mixture on a time scale $T_2 = 300$ ns ± 50ns at the optimal working point.

- Echo experiments

  An echo sequence is similar to the Ramsey sequence one but with an additional π pulse (see figure 4.15) precisely in the middle of the free evolution period. It is used in NMR for suppressing, in particular, the broadening of NMR lines due to an inhomogeneous magnetic field around the ensemble of spins. In the case of the Quantronium, there is only a single spin but the experiment is repeated 10^4 times for each data point. The echo sequence thus compensates for inhomogeneous broadening coming from slow fluctuations of the transition frequency from one sequence to an other. The decay of the echo signal with the sequence duration then probes the stability of the qubit frequency on the time scale of the pulse sequence. We obtain experimentally a time T_{echo} of

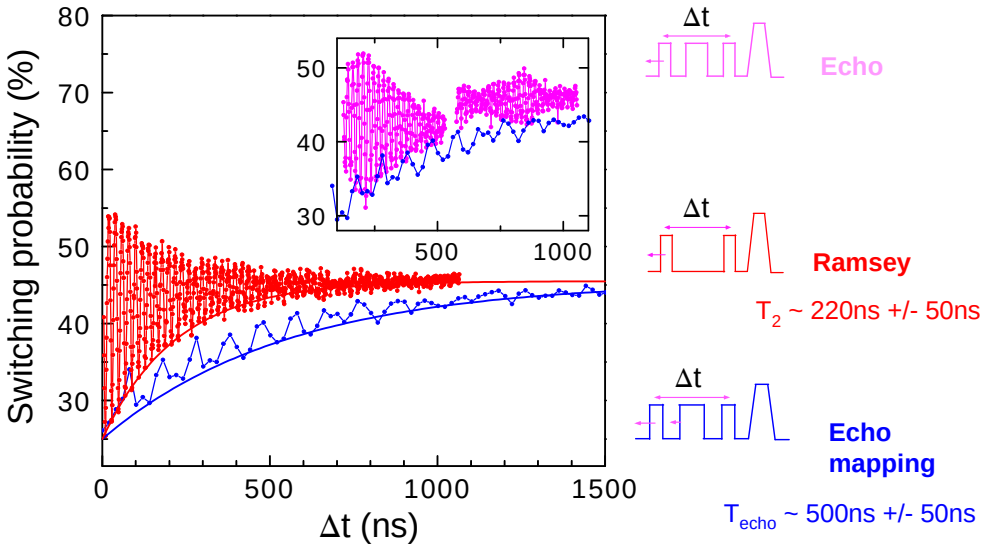

Figure 1.17: An echo sequence is made of a Ramsey one with an additional π pulse. Inset: we observe a revival of the Ramsey signal when this π pulse is just in the middle of the sequence. We have mapped the envelope of this echo revival, and we get a characteristic time scale $T_{echo} = 500ns \pm 50ns$ at the optimal working point.

about 500ns at the optimal working point which is larger than T_2. This result already demonstrates that most of the qubit frequency fluctuations responsible for dephasing occur at low frequency, which was expected from previous measurements of the charge noise in Coulomb blockade devices and of the flux noise in SQUIDs.

1.6.4 Summary and analysis of decoherence during free evolution

We have measured T_{echo} and T_2 at the optimal working point and along the lines $\delta = 0$ and $N_g = \frac{1}{2}$ (see figure 1.18). We find that a detuning of 5% of a Cooper pair in charge or a detuning of 10% of a flux quantum in phase is sufficient for dividing T_2 by a factor 10. This result validates the concept of the optimal working point whose existence is crucial for achieving long coherence times. We notice also that the echo sequence is much more efficient for suppressing the effect of charge fluctuations than that of phase fluctuations.

An important result of this thesis work is that all these decoherence data can be explained within a simple theoretical framework. This framework is inspired from the standard Bloch-Redfield model of decoherence and incorporates some specific features only recently understood. The model assumes that the noisy variables follow a diffusive behavior and treats rigorously divergences of the noise spectra, if any. Departure from a Gaussian model for the noise mechanism has also been considered. The main input for the model is the spectral densities of the charge and phase noises. First, we take a $1/f$ spectrum, both for charge and phase noises, since from experiment, these two noises are well known to have such a behavior at low frequency. These spectra already explain most of the T_2 data, since T_2 is sensitive only to the low frequency part of the noise, but it is not compatible with the echo data.

We then determine the minimum modification to the $1/f$ spectra which renders the model compatible with the echo data. For the charge noise we found that a high frequency cutoff in the MHz range has to be introduced and for the phase noise we found that a white component has to be added. The overall good agreement of the experimental data with the theoretical model implies that this phenomenological description of noise sources is sufficient to describe dephasing in the quantronium and probably in most other qubit circuits. However, these spectral density models do not provide many clues about the underlying mechanisms for the noise generation.

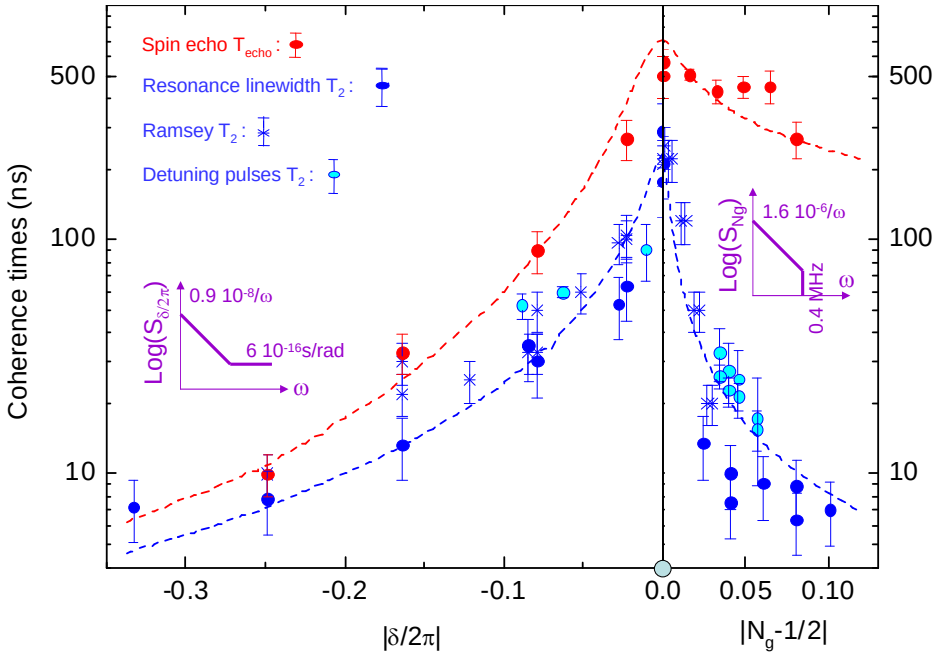

Figure 1.18: Summary of decoherence during free evolution. T_2 and T_{echo} are measured at the optimal working point and on the lines $\delta = 0$ and $N_g = \frac{1}{2}$. Several techniques are used for measuring T_2: Ramsey experiments, resonance line width and detuning pulse methods, (be aware of the logarithmic scale). Dashed line: predicted decay times calculated with a simple model for the spectral densities of the charge and phase noise sources (insets).

All of the measurements so far consider decoherence processes during free evolution. In the second part of chapter 4 we explore decoherence when a microwave field is applied to the qubit.

1.7 Decoherence during driven evolution

The concept of decoherence is usually only considered during the free evolution of a qubit. It is however important to understand and characterize the phenomenon when the qubit is controlled via an external hamiltonian. A particular situation relevant for qubits is when the system undergoes Rabi precession in a resonant microwave field. An interesting question then arises: is quantum coherence of a driven qubit better or worse than during free evolution?

During driven evolution, depolarization and dephasing are defined with respect to the new eigenbasis of the qubit coupled to the field, $\{|0^*>,|1^*>\}$ (see figure 1.19). The effective rates of relaxation and

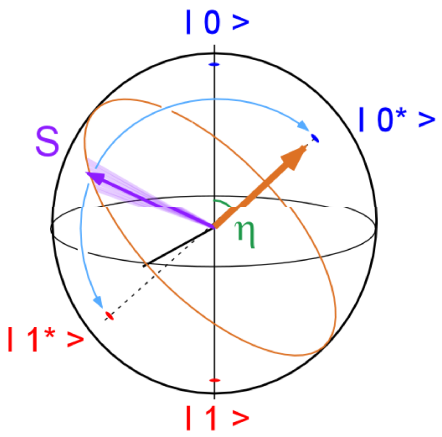

Figure 1.19: Driven evolution of a qubit. The depolarization and dephasing rates are given with respect to the new eigenbasis of the system coupled to the field $\{ |0^*>,|1^*>\}$. η is the angle between the free evolution eigenbasis and the driven evolution one. This angle is related to the Rabi frequency and to the detuning: $\tan\eta = \nu_{Rabi}/\Delta\nu$.

dephasing: $\widetilde{\Gamma_1}$ and $\widetilde{\Gamma_2}$ pertain to the decay of the longitudinal and transverse parts of the density matrix in the rotating frame. The theoretical expressions for these rates involve a new quantity related to the noise of the environment at the Rabi frequency: $\Gamma_{\nu_{Rabi}} \propto S(\omega_{Rabi})$. One has:

$$\widetilde{\Gamma_1} = \tfrac{1}{2}\Gamma_1 + \tfrac{1}{2}\Gamma_{\nu_{Rabi}}, \quad \widetilde{\Gamma_2} = \tfrac{3}{4}\Gamma_1 + \tfrac{1}{2}\Gamma_{\nu_{Rabi}}. \tag{1.1}$$

The measurement of decoherence in the rotating frame thus provides new information on the spectral density of the noise sources. Experimentally, the effective relaxation rate $\widetilde{\Gamma_1}$ is measured by preparing a longitudinal density matrix in the rotating frame using the so-called spin-locking protocol in NMR. The effective dephasing rate is simpler to obtain, since it is given by the decay of the Rabi oscillations. We have measured this time $\widetilde{T_2}$ by exciting on resonance the qubit (see figure 1.20). We find that $\widetilde{T_2}$ is greater than T_2, which means that the phase coherence of the qubit is better preserved when driving the qubit than during free evolution. Secondly, $\widetilde{T_2}$ is almost constant from 1 MHZ to 100 MHz, which means that the noise of the environment is white in this frequency range, in qualitative agreement with our analysis of decoherence during free evolution. In further experiments, the Rabi frequency is fixed to a value of 15MHz, while we detune progressively the microwave from the resonance. We see that $\widetilde{T_2}$ drops down to T_2 and the free evolution case is recovered on a frequency scale which is the Rabi frequency.

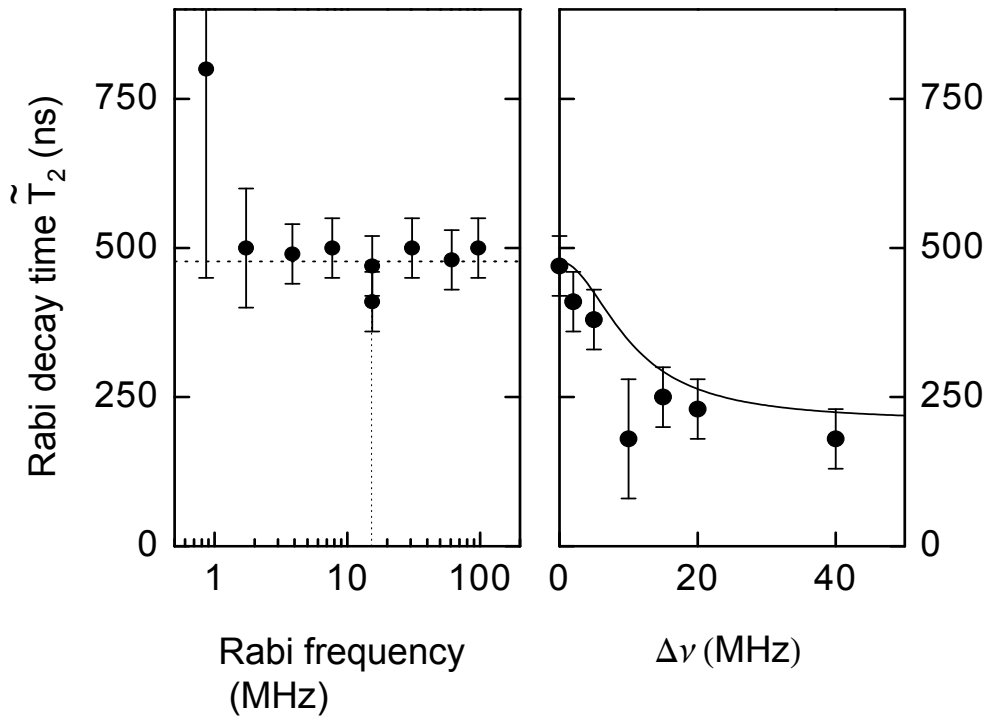

Figure 1.20: Characteristic decay time $\widetilde{T_2}$ of the Rabi oscillations at the optimal working point. Left panel: $\widetilde{T_2}$ measured as a function of the Rabi frequency with zero detuning. $\widetilde{T_2}$ is constant for all Rabi frequencies from 1 MHz to 100MHz, which indicates that the noise of the environment is white in this frequency range. Right panel: $\widetilde{T_2}$ measured as a function of the detuning with a fixed Rabi frequency of 15.4MHz. As $\Delta\nu$ increases, one recovers the free evolution case on a frequency scale which is the Rabi frequency.

To summarize, by encoding the information on the dynamical states of the qubit coupled to the field it is possible to preserve the coherence on a longer time than during free evolution. Studying the decoherence under driven evolution is also a powerful tool for probing the environment within the available range of Rabi frequencies.

1.8 Towards Quantum Non Demolition measurement of a qubit

The successful operation of the quantronium and soon after of the flux-qubit at an optimal point, raised the problem of how to further improve this strategy. In particular, could it be possible to perform the readout without moving away from the optimal working point and in a QND mode, i.e. by projecting and letting the qubit on states $|0\rangle$ and $|1\rangle$ according to their probability amplitudes in the measured state? A QND readout would be useful for probing quantum correlations between coupled qubits and in particular, Bell inequalities for mesoscopic systems. The hope is also that a QND readout could yield a better readout fidelity, which is a key issue. For that purpose, the qubit can be maintained close to the optimal point by applying a small ac drive in the microwave domain and by measuring the ac response of the circuit. Different microwave reflectometry methods have now been developed for the quantronium, for the flux qubit and for the Cooper pair box.

1.8.1 Principle of the ac dispersive readout of the quantronium: the JBA

For the Quantronium, M. Devoret and his team at Yale University have developed a readout scheme based on the dynamics of the readout junction when it is excited by a nearly resonant microwave signal [46, 47]. I have implemented the same readout in Saclay and its study is described in the chapter 5 of this thesis.

The dynamics of the resonator formed by the readout junction depends on the qubit state because its resonance frequency is modified by the state dependent qubit inductance L_{Q_k} connected in parallel (see figure 1.21):

$$\frac{1}{L_{Q_k}} = \frac{1}{{\varphi_0}^2}\frac{\partial^2 E_k}{\partial \delta^2},$$

for $k = 0$ or 1.

At low driving amplitude the behavior of the circuit is simply that of an LC oscillator. Although a direct measurement of the state dependent resonance frequency could be envisioned, the frequency change between state 0 and 1 is too small to achieve single shot readout with current low noise amplifiers and in a reasonable amount of time. The required sensitivity can however be obtained due to the bifurcation phenomenon.

When increasing the driving microwave power, the non-linear regime of the Josephson junction resonance is explored, and at large enough driving amplitude, the readout junction undergoes a dynamical transition to an oscillation state with a larger amplitude and a different phase. This bifurcation phenomenon is identical to the transition of the well known Duffing anharmonic oscillator in classical mechanics [48]. Two oscillation states for the phase of the junction in the Josephson potential can coexist, the first with a small oscillation amplitude and the second with a large one (see figure 1.21). The switching from one dynamical state to the other discriminates between the qubit states because it is extremely sensitive to the different parameters and in particular to the effective inductance of the readout junction. It provides a sensitive amplifier, called the Josephson Bifurcation Amplifier (JBA), which permits single shot readout. In addition, this readout is dispersive since the plasma frequency and consequenctly the probing frequency is chosen far away from the qubit resonance.

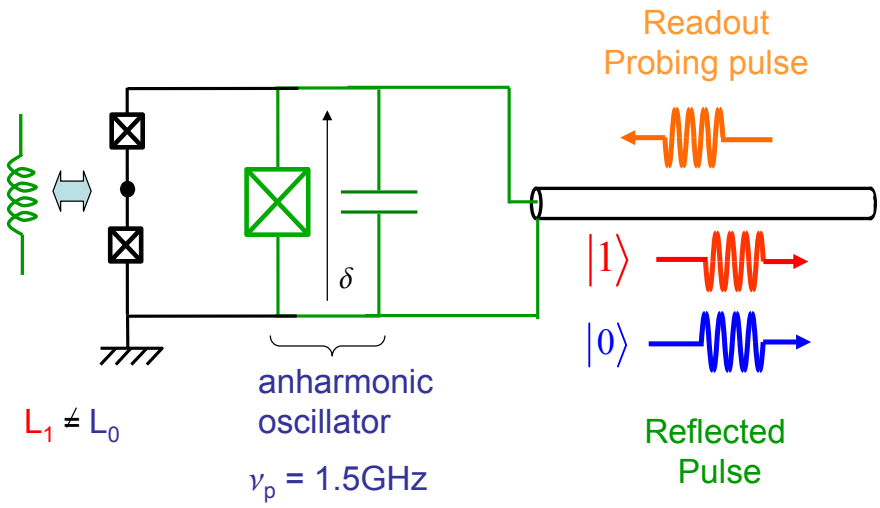

Figure 1.21: Principle of the AC dispersive readout of the quantronium. The qubit has a state dependent inductive behavior which moves the plasma resonance of the anharmonic oscillator formed by the readout junction in parallel with an on-chip capacitor. At large microwave driving, this resonator undergoes a bifurcation between two oscillation states in the Josephson potential, which depends on the qubit state. The signature of this bifurcation, and thus the qubit state, appears in the phase of the reflected microwave probing pulse.

1.8.2 Characterization of the microwave readout circuit

The setup we have built is close to the one at Yale, with the extra possibility of performing both DC switching and dynamical switching measurements.

The plasma frequency of the readout junction in the sample, which were fabricated at Yale, is lowered to the convenient $1-2$GHz range by an on-chip capacitor in parallel with the junction.

The first experiment performed was to characterize the bifurcation phenomenon of the readout junction with the qubit in the ground state. For this purpose, a CW signal is sent to the sample, and the phase of the reflected signal is measured with a network analyser, as a function of frequency. As there is no dissipation in this superconducting circuit all the microwave power is reflected and the phase of the reflected component gives a convenient signature of the dynamics of the junction.

At low driving amplitude we can observe the resonance of the readout circuit and the associated phase shift (see figure 1.22). When increasing the microwave power, the phase shift of the plasma resonance gets steeper and steeper, as the junction starts to explore the nonlinear region of the Josephson potential. The bifurcation occurs above a certain microwave amplitude which depends on the driving frequency.

1.8.3 Measurement of the quantronium qubit with a JBA

In order to readout the state of the qubit in a time shorter than the qubit relaxation time T_1, we have measured the switching probability from one dynamical state to the other during a probing pulse of about 100ns. These measurements were done as a function of the microwave power and for the two qubit states 0 and 1 (see figure 1.23).

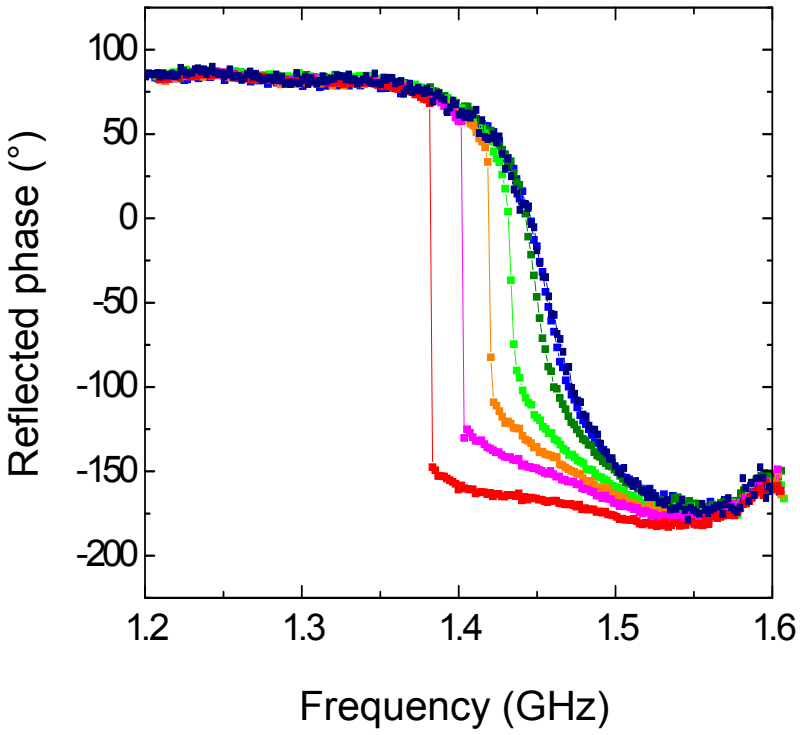

Figure 1.22: Phase of the reflected signal in the JBA operated with continuous microwave. The phase of the reflected microwave is measured as a function of frequency and for different probing powers. At low microwave power (right), one observes the plasma resonance of a linear system. When increasing the power (from right to left), the superconducting phase starts exploring the non linear region of the Josephson potential and a bifurcation happens for a critical power.

One observe a behavior similar to the one observed with DC pulses: there is an optimal amplitude for which the contrast between states 0 and 1 is maximized. The best value achieved is 51%, a value larger than the 40% obtained with dc switching, but still significantly lower than the predicted one. Rabi oscillations measured at maximum readout contrast are also shown in Fig.1.23. We attribute the lack of readout fidelity to spurious relaxation during the ac excitation of the system. This phenomenon is similar to the one observed with the DC switching readout and it might be attributed to a coupling with two level systems recently identified in phase qubits with larger junctions [49, 50].

This unwanted relaxation also affects the QND character of the readout, as we shall discuss now.

1.8.4 Partially non-demolition behavior of the readout

Excitation and relaxation induced by the readout not only corrupt the result of the measurement but also affect the projection of the quantum state. The error on the projection of the state during the readout can be quantified by the probabilities q_0 and q_1 (see figure 1.24). These two probabilities define the QND fraction of each state at readout. In order to measure q_0 and q_1, an experiment with two adjacent identical readout pulses was performed. Preparing the qubit either in state $|1\rangle$ or in state

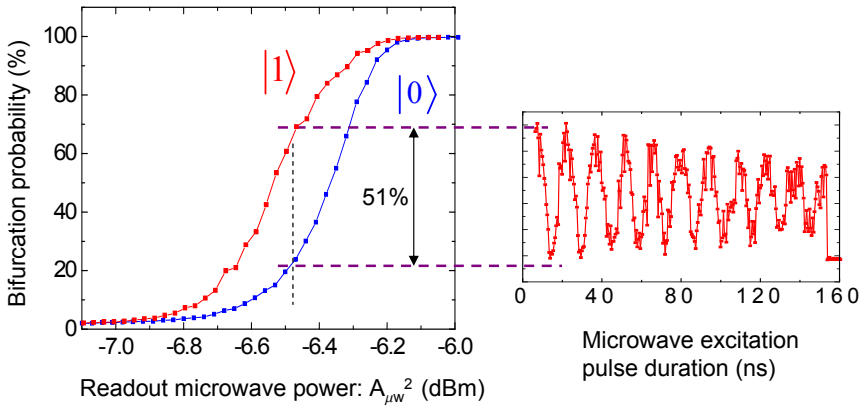

Figure 1.23: Left: bifurcation probability as a function of the microwave power for the two qubit states at the optimal working point. Right: Rabi oscillations at the maximum contrast.

$|0\rangle$, the switching probabilities was measured during the first and second readout pulses and also the conditional probabilities.

From these measurements and using a simple probabilistic model we have determined $q_1 = 0.34$ and $q_0 = 1$. There is, thus, no excitation of the qubit during readout, but significant relaxation.

Starting from state 1, the correct answer and the correct projection occur with a probability of only 0.24. The experiment is thus far from implementing an ideal quantum measurement of the qubit state.

1.9 Conclusion

If one compares our results to the requirements of the DiVincenzo criteria for quantum computing, it is clear that there is still a long way to go. For single qubit gates we estimate the accuracy achieved for the quantronium at about a few per cent, whereas the most optimistic value requires 10^{-4}.

For two qubit gates, the gate accuracy is unknown yet but the complexity of the presently considered designs for the quantronium leaves little hope of achieving an excellent figure. For readout, the achieved contrast of 0.5 is far from being sufficient for operating even a very simple processor.

But one can expect future improvements since there is no known fundamental reasons that limits the quantum performance of electronic circuits. Even if building a quantum computer in the near future is not realistic, this research field is important since it addresses a fundamental question in Physics: Does the quantum framework developed during the first part of the 20th century, and thoroughly tested since then in the microscopic world apply to large objects? for instance, objects having collective variables? And in particular, is there a limit for the size of a system showing quantum coherence and entanglement phenomena?

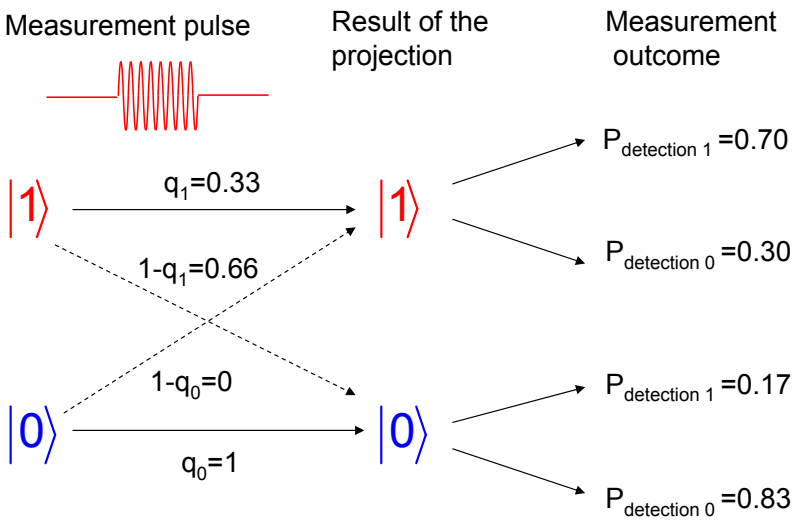

Figure 1.24: With a simple probabilistic model for the readout process, the QND fractions of each state, and the probabilities of the outcomes for the five as a function of the result of the projection, can be determined.

Chapter 2

A superconducting qubit: the Quantronium

The circuit of the quantronium is derived from the Cooper pair box [51] which is the first superconducting qubit whose quantum state was manipulated coherently [36].

2.1 The Cooper pair box

Circuit description

A Cooper pair box is made of a superconducting island, connected to a superconducting reservoir by a small junction (area $\lesssim 0.1\mu m^2$). A gate capacitance C_g permits to bias the island, adjust the number $\widehat{N}$ of excess Cooper pairs on the island by tunneling of the Cooper pair pairs through the junction (see Fig. 2.1).

The Hamiltonian of the system is the one of a single junction (see Fig. 2.1) with a shifted kinetic energy term

$$\widehat{H} = E_c(\widehat{N} - N_g)^2 - E_j \cos(\widehat{\theta}),$$

where $\widehat{N}$ is the charge operator of the island conjugated of the gauge invariant phase difference $\widehat{\theta}$ across the junction: $[\widehat{N}, \widehat{\theta}] = i$.

$E_c = (2e)^2/2C_\Sigma$ is the charging energy of the island, with $C_\Sigma = C_j + C_g$ the total capacitance of the island to ground and $N_g = C_g V_g/2e$ is the reduced gate charge with e the absolute value of the charge of an electron.

Charge regime

In the case of aluminum junctions having an area smaller than $\approx$ 100nm$\times$100nm, one has $E_c > E_j$ and the Cooper pair box is said to be in the charge regime. The eigenstates of the system are then almost charges states $|N\rangle$ of the island, with eigenenergies $E_c(N - N_g)^2$, except near the degeneracy points: $N_g = 1/2 + n$, $n \in \mathbb{Z}$ where the Josephson coupling mixes successive charge states (see Fig. 2.2). The two lowest energy states form the qubit.

Coherent manipulation and measurement of the Cooper pair box

The first time domain measurement of the coherent oscillations of a Cooper pair box was performed in 1999 by Nakamura *et al* [36]. By pulsing the gate voltage, the system was moved back and forth

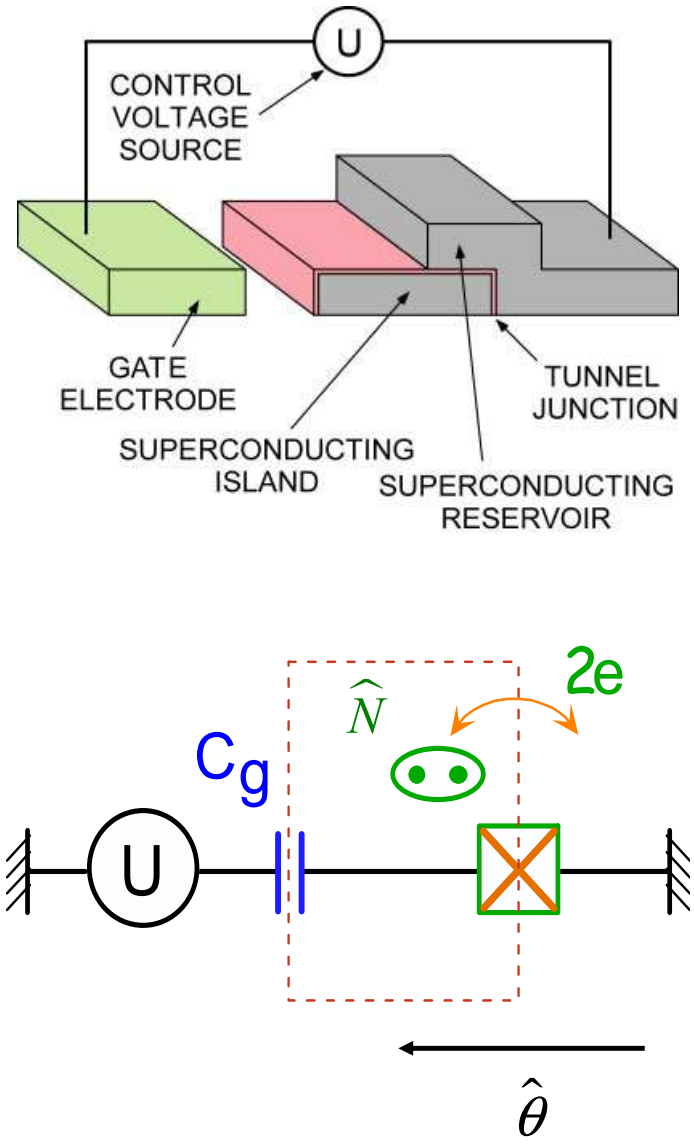

Figure 2.1: A Cooper pair box is made of a superconducting island connected to a superconducting reservoir through a single Josephson junction. By biasing the island with a gate voltage, the number of excess Cooper pairs on the island can be ajusted.

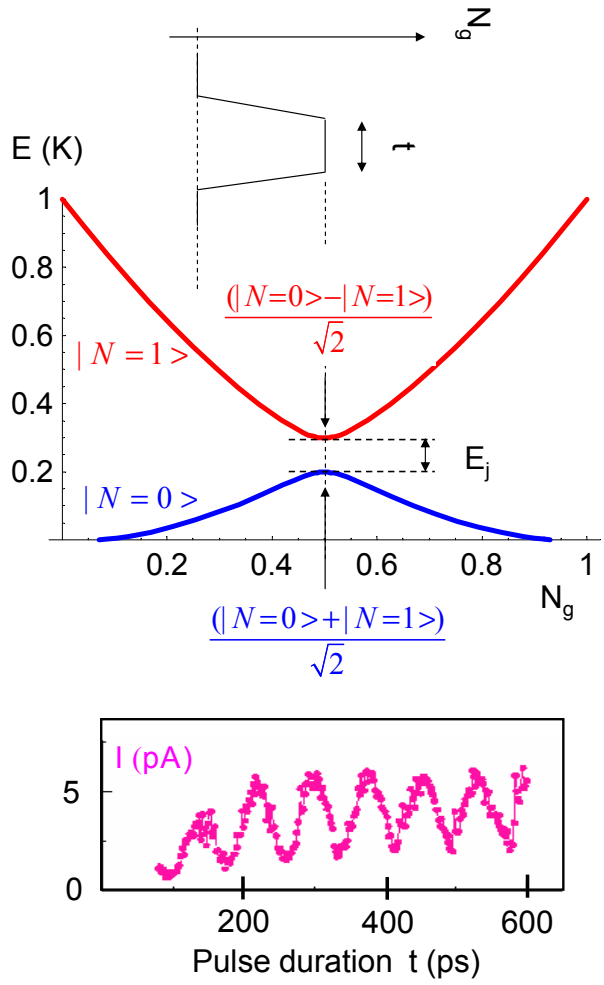

Figure 2.2: Top: principle of the manipulation of the quantum state of the Cooper pair box. A non-adiabatic trapezoidal gate pulse of duration t brings the working point to the degeneracy point $N_g = 1/2$, where the Josephson coupling mixes successives charge states and induces coherent oscillation. Bottom: coherent oscillations of the quantum state of the Cooper pair box (Nakamura & al [36]).

non-adiabatically to its degeneracy point. At this point, two successive charge states are coupled during a time t, which induces coherent oscillations (see Fig. 2.2).

An extra probing junction provides readout in a similar way than the selective ionization in atomic physics: the Cooper pair box is "ionized" only if it is in state $|1\rangle$, which gives rise to a sequential flow of two electrons, measurable by repeating the experiment at a fast enough rate. This measurement setup is destructive but has the advantage to reset the qubit in its ground state. The readout is thus not a single shot readout, since the quasi-particle current needs to be averaged over many experiments to be detectable.

The coherence time obtained ($\lesssim$ 10 ns) could not be fully explained by the relaxation induced by the measuring apparatus. It appeared later that the fluctuations of the control parameter N_g, due to background charge noise, was also an important source of decoherence for this charge qubit [52].

2.2 The Quantronium

The Quantronium, developed in the Quantronics group in 2001, is the first qubit having a design that protects it from decoherence due to random fluctuations of its control parameters, which appear to be the dominant source of decoherence in this type of qubit. It combines a split Cooper pair box implementing the quantum bit and an hysteretic Josephson junction for read out. It can be easily manipulated using microwave techniques analogous to spin manipulation in NMR and the readout setup has the advantage that it can be switched off during the manipulation of the qubit, which minimize the back-action. In addition, the sensitivity of this readout is sufficient for allowing a single shot measurement, that we define by a probability of error on the answer of a measurement $\lesssim 10\%$.

2.2.1 Quantronium circuit

The circuit is made of a superconducting loop interrupted by two small Josephson junctions ($area \approx$ 150nm×150nm) with Josephson energies: $E_{j1} = E_j(1-d)/2$ and $E_{j2} = E_j(1+d)/2$, where d is an asymmetry parameter made as small as possible for minimizing relaxation (see chapter 4), and by the readout junction with Josephson energy: $\mathcal{E}_j \gg E_j$ (see Fig. 2.3 and Fig. **??**).

The two small junctions define an island which has a total capacitance to ground: $C_\Sigma = C_{j1}+C_{j2}+C_g$, where C_{ji} are the capacitance of each junction and C_g is the gate capacitance. The Cooper pair charging energy is $E_c = (2e)^2/2C_\Sigma$.

This island can be biased by a gate voltage V_g and the flux Φ in the loop can be tuned by an external magnetic field. These two parameters V_g and Φ can be recast in terms of the reduced parameters : $N_g = C_g V_g/2e$ the reduced gate charge, and $\delta_m = \Phi/\varphi_0$ (where $\varphi_0 = \hbar/2e$).

N_g controls the electrostatic term of the split box Hamiltonian:

$$E_c(\widehat{N} - N_g)^2,$$

where $\widehat{N}$ is the reduced charge operator of the island.

As the inductance of the loop is negligeable compared to the inductance of the junctions, δ_m and $\widehat{\gamma}$ are related to the phase $\widehat{\delta} = \widehat{\delta_1} + \widehat{\delta_2}$ across the two small junctions in series by the relation: $\widehat{\delta} = \widehat{\gamma} + \delta_m$.

The Josephson Hamiltonian of the split box alone is given by:

$$H_j = -E_j \cos(\widehat{\delta}/2)\cos\widehat{\theta} + dE_j \sin(\widehat{\delta}/2)\sin\widehat{\theta},$$

where $\widehat{\theta} = (\widehat{\delta_1} - \widehat{\delta_2})/2$ is the phase operator of the superconducting island, conjugated of $\widehat{N}$: $[\widehat{\theta}, \widehat{N}] = i$.

The total hamiltonian of the split Cooper pair box is thus:

$$\widehat{H} = E_c(\widehat{N} - N_g)^2 - E_j \cos(\widehat{\delta}/2)\cos\widehat{\theta} + dE_j \sin(\widehat{\delta}/2)\sin\widehat{\theta}. \tag{2.1}$$

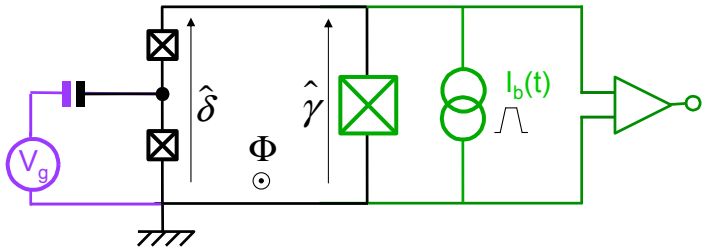

Figure 2.3: The Quantronium is based on a split Cooper pair box made of a superconducting loop interrupted by two small Josephson junctions to form an island, and by a large junction for readout. The superconducting island can be biased by a gate voltage V_g, and the flux in the loop Φ can be tuned by an external magnetic field. The two reduced parameters $N_g = -C_g V_g/2e$ and $\delta = \Phi/\varphi_0 + \gamma$ permits to tune the properties of the qubit. For readout, the large junction is biased by a current source near its critical current, and a room temperature amplifier is used to detect the possible switching of this junction which is correlated to the state of the qubit.

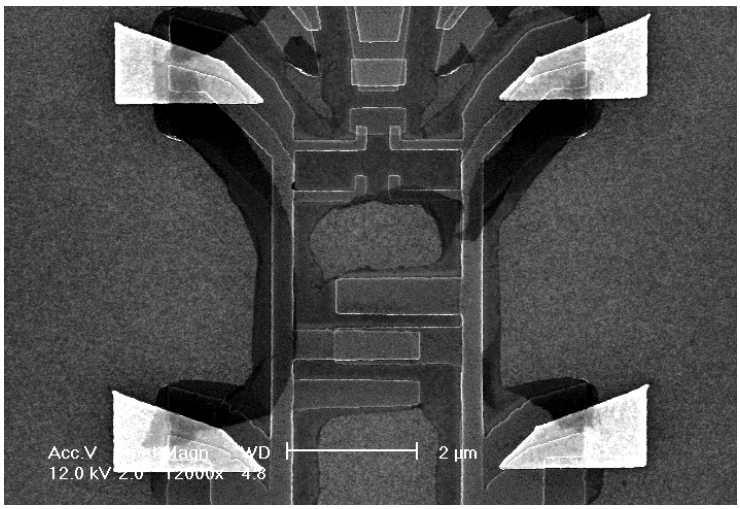

Figure 2.4: SEM image of the Quantronium sample A. Bright: quasi-particle traps made with a 40nm thick gold film deposited with an e-gun evaporator. Grey strips: aluminum electrodes (20nm of thickness for the first deposited layer and 30nm for the second layer) deposited in the same evaporator. Top: gates electrodes for DC biasing and AC excitation. The black regions are probably alumina films coming from aluminum scattered during the evaporation below the undercut of the resist by gas residues.

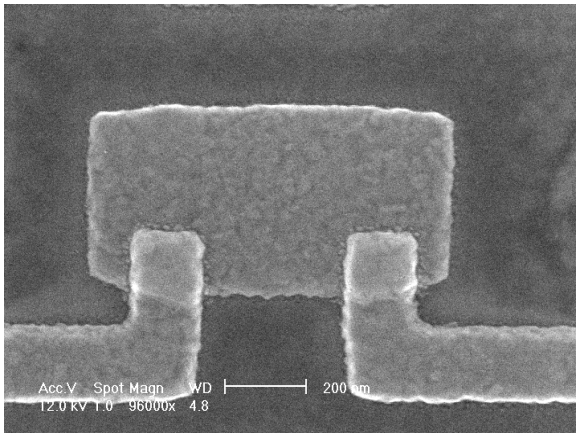

Figure 2.5: SEM image of the island of the Quantronium sample A. The two Josephson junctions ($\approx$ 160 nm x 160 nm for each junction) are made by oxidation under a O_2 20%, A_r 80% mixture during $10'$ and at a pressure of 12 mbar.

The third Josephson junction has a Josephson energy $\mathcal{E}_j$ and a charging energy $\mathcal{E}_c = (2e)^2/2C_j$.

As $\mathcal{E}_j \gg \mathcal{E}_c$, for a small biasing current $I_b < I_c$, the Josephson junction is equivalent to a harmonic oscillator. As this resonator is off-resonance with the qubit, it is always in a quasi-classical coherent state. The behavior of the phase $\widehat{\gamma}$ is thus almost classical. The split Cooper pair box eigenstates are thus only determined by the parameters: N_g and $\widehat{\delta} \approx \delta = \gamma + \delta_m$.

Note that in the ideal case where $d = 0$, the Josephson Hamiltonian is the one of a Cooper pair box with a tunable Josephson energy: $E_j^{'} = E_j \cos(\delta/2)$. In practice, the value of d is a few %, but qualitatively, the split Cooper pair box behaves like a single Cooper pair box with a tunable E_j.

For the two samples investigated in this thesis, one has $E_j \approx E_c$. A numerical diagonalization of the Hamiltonian is required, which gives the eigenstates and the spectrum of the split Cooper pair box, and their dependance with the external parameters N_g and δ (see Fig. 2.6).

2.2.2 Energy spectrum

Contrary to an atom or an ion, where Hamiltonians are set by natural constants, the parameters E_j and E_c, are controlled by the fabrication of the junctions (size and oxide thickness). The typical capacitance of the junctions made at Saclay with a standard low pressure O_2 oxidation at room temperature, is 1fF per 100nm$*$100nm and does not depend on the oxidation parameters with a $\pm$10% accuracy. By tuning the oxidation pressure and time, it is possible to tune E_j from about 2 to 20K/μm^2. The transition frequency of the qubit can thus be chosen by design, in a wide frequency range: from $\approx$ 1GHz to a few tens of GHz for aluminum junctions.

Then, because of the non-linearity of the Josephson junctions, the spectrum is sufficiently anharmonic to isolate the transition between the two lowest energy levels $|0\rangle \rightarrow |1\rangle$. On figure 2.7 is plotted the anharmonicity of the system, for a fixed transition frequency of 16GHz and as a function of the ratio E_j/E_c. The minimum acceptable value of the anharmonicity is given by the transition frequency of the qubit and the speed of manipulation desired: for instance, for operating a resonant qubit at about 20GHz, with a bandwidth of 1GHz (one-qubit operation of $\approx$ 1ns) the anharmonicity must be larger than 5%.

The transition frequency between state $|0\rangle$ and state $|1\rangle$ is tunable with the parameters δ and N_g, like electric and magnetic fields can modify the spectrum of an atom with the Stark and Zeeman effects (see figure 2.6). However, much smaller fields are here required to change the Hamiltonian drastically:

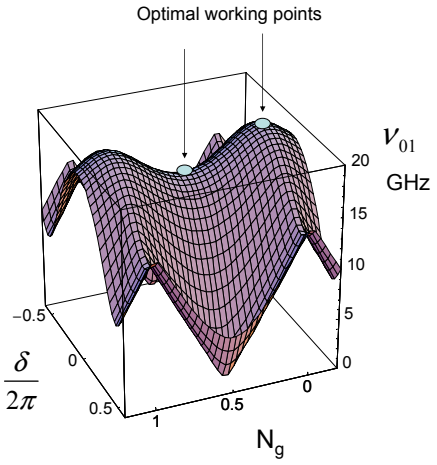

Figure 2.6: Dependance of the transition frequency with the parameters N_g and δ for the sample A ($E_j = 0.87$K and $E_c = 0.655$K). There are several points in the parameter space where the transition frequency is stationary with respect to δ and N_g. At these points, any noise on these two parameters couples only at second order, and thus induces less dephasing. In our experiment, we have used the optimal working point $P_0 = (\delta = 0, N_g = 1/2)$.

an applied magnetic field of a few mT gives rise to one flux quantum in the loop and several mV on the gate, with a reasonable coupling capacitance, gives rise to a Cooper pair induced on the island. This tunability is required to compensate for static offsets in charge and in flux due for instance to background charges or vortices in the vicinity of the sample.

2.2.3 The optimal working point strategy

During the free evolution of the qubit, an initial pure state $\alpha|0\rangle + \beta|1\rangle$ evolves like:

$$\alpha|0\rangle + \beta e^{i\phi_0(t)} e^{i\Delta\phi(t)}|1\rangle,$$

where $\phi_0(t) = 2\pi\overline{\nu}_{01}t$ is the deterministic phase related to the mean value of the transition frequency and

$$\Delta\phi(t) = 2\pi \int_0^t \delta\nu_{01}(t)dt'$$

is an extra random phase related to time fluctuations of ν_{01}. Indeed, as ν_{01} depends on N_g and δ, any noise on these two external parameters induces fluctuations of ν_{01}. The extra random phase $\Delta\phi(t)$ thus destroys the quantum coherence between state $|0\rangle$ and $|1\rangle$, leading to a statistical mixture of these two states.

The quantronium incorporates a strategy for minimizing the dephasing coming from the fluctuation of the control parameters. Indeed, as the dependance of ν_{01} is periodic with N_g and δ, there are stationary points in the parameter space where ν_{01} depends only at second order on the parameters. At these points, the possible fluctuations of δ and N_g are thus coupled to ν_{01} only at second order, which is essential for achieving long coherence times (see chapter 4). During our experiments, we have used the optimal point $P_0 = (N_g = 1/2, \delta = 0)$. The other point $(N_g = 0, \delta = 0)$ could have also be used, but the transition frequency at that point was higher than the maximum frequency achievable by our microwave generator. Note, however that in the charge regime ($E_c > E_j$), at the optimal point $(N_g = 1/2, \delta = 0)$,

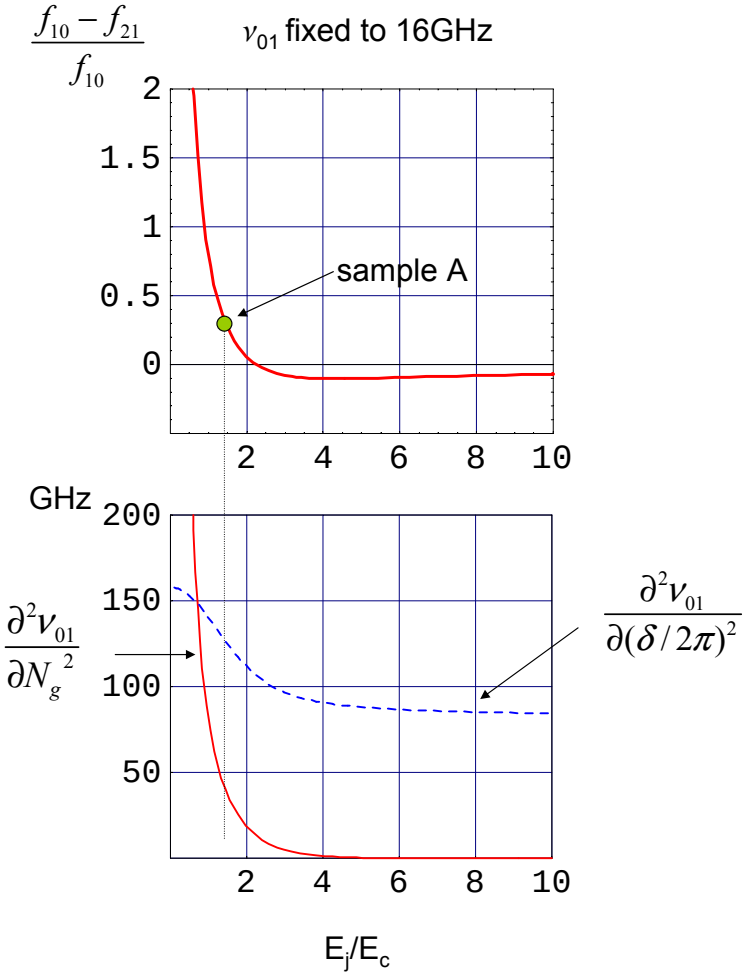

Figure 2.7: Top: anharmonicity of the system at the optimal working point as a function of E_j/E_c and for a fixed transition frequency of 16GHz. For the sample A of this thesis, the anharmonicity is about 40%. Bottom: sensitivity to phase and charge noise at the optimal working point $P_0 = (N_g = 1/2, \delta = 0)$ as a function of E_j/E_c and for a fixed transition frequency $\nu_{01} = 16GHz$.

the transition $0 \rightarrow 1$ can be to close from the $0 \rightarrow 2$ one. This is not the case in the mixed charge-phase regime, and there is no fundamental reason for not using the working point $N_g = 0, \delta = 0$. Concerning the optimal point ($N_g = 1/2, \delta = \pi$), the transition frequency is of order of the temperature, for a reasonable asymmetry of the junctions ($d < 5\%$) and for typical parameters ($E_j \approx 1$K and $E_c \approx 1$K), which prevents from using this working point. At the optimal point ($N_g = 0, \delta = \pi$), the curvature of the energy bands $(E_0(\delta), E_1(\delta))$ with respect to the phase is stronger than at P_0, which could be interesting for the dispersive readout described in chapter 5. Note however that this higher curvature in phase increases the sensitivity to phase noise.

On figure 2.7, the curvature of the transition frequency at the optimal working point P_0 is plotted as a function of the ratio E_j/E_c and for a fixed $\nu_{01} = 16$GHz. As expected, when E_j/E_c increases, the sensitivity to charge noise decreases to zero exponentially.

2.2.4 Loop current

The quantum operator associated with the current circulating in the loop is [44]:

$$\widehat{I}(N_g, \delta) = \frac{1}{\varphi_0} \frac{\partial \widehat{H}}{\partial \delta}.$$

Following this relation, the average currents for states $|0\rangle$ and $|1\rangle$ are:

$$i_k(N_g, \delta) = \langle k|\widehat{I}|k\rangle = \frac{1}{\varphi_0} \frac{\partial E_k(N_g, \delta)}{\partial \delta}.$$

Examples of current dependance with δ are given on Fig. 2.8.

A first strategy for the readout is to measure the state of the qubit by discriminating between the two currents i_0 and i_1.

Indeed, apart from the line $\delta = 0$, the two currents i_0 and i_1 are different and $|i_0 - i_1|$ has a maximal value of $|\Delta I_{max}| \approx 5 - 20$nA (depending on the values of E_j and E_c) which can be measured with the readout Josephson junction used as a current threshold detector.

2.3 Measuring the quantum state of the quantronium

A good readout setup has to fulfil two apparently contradictory requirements: long coherence times, which supposes that the qubit is well decoupled from its environment, and efficient readout, which supposes that the qubit is well coupled to the measuring apparatus. The readout implemented with the quantronium satisfies these two requirements since it is a single shot readout that can be switched off during the manipulation of the qubit, in order to minimize decoherence.

2.3.1 Principle of the switching readout

The large Josephson junction inserted in the loop of the split Cooper pair box is used as a current threshold detector in order to discriminate between i_0 and i_1. Roughly speaking, this third Josephson junction is a very sensitive fuse: if the current flowing inside exceeds its switching current I_s, the junction switches to a detectable voltage state $V \approx 2\Delta/e \approx 400\mu$V.

Let us see in details how the switching of a junction takes place and what is the current resolution of such a threshold detector.

2.3.2 Dynamics of a current biased Josephson junction

Since $\mathcal{E}_j \gg \mathcal{E}_c$, the junction is in the phase regime and its dynamics can be conveniently described by a pseudo particle with position γ moving in a potential.

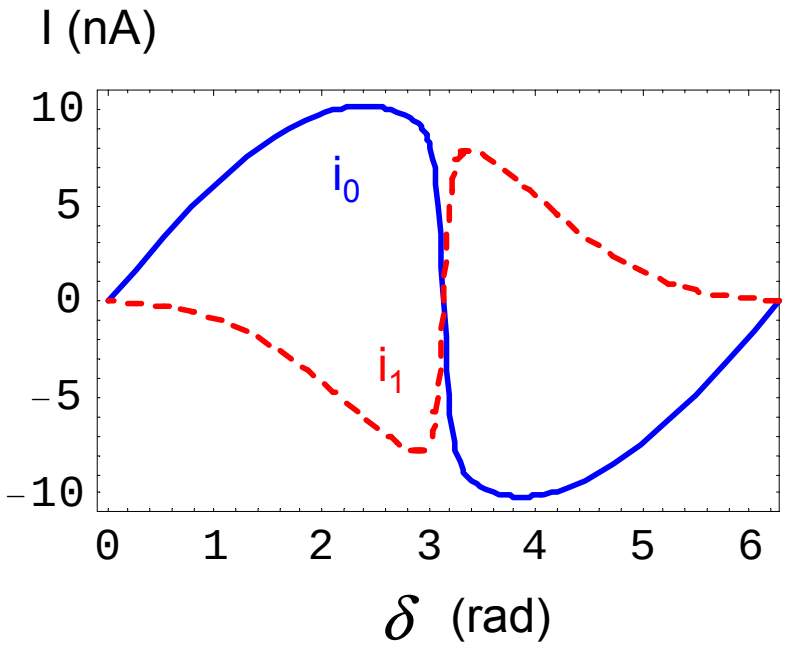

Figure 2.8: Theoretical loop current dependance on δ for $N_g = 1/2$, for the states $|0\rangle$ and $|1\rangle$, in the case of sample A. The maximum expected value of $|i_0 - i_1|$ is ≈ 15nA.

Potential of the pseudo particle

When biasing a Josephson junction with a current I_b, an extra energy term $-\varphi_0 I_b \gamma$ adds to the Josephson energy term $-\mathcal{E}_j \cos\gamma$ and leads to metastable wells in the potential energy U of the pseudo particle:

$$U(\gamma) = -\mathcal{E}_j \cos\gamma - \varphi_0 I_b \gamma = -\mathcal{E}_j(\cos\gamma + s\gamma).$$

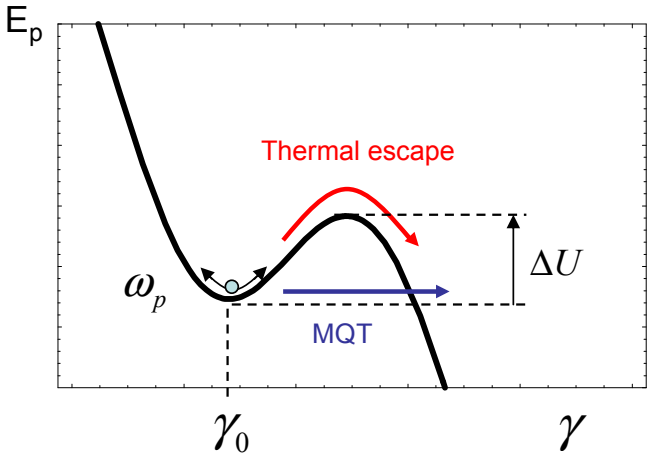

Figure 2.9: Metastable well in the tilted Josephson potential. The phase γ of the junction oscillates in the well around the local minimum $\gamma_0 = \arcsin s$ ($s = I_b/I_c$) at the plasma frequency $\omega_p(s)/2\pi = \omega_p^0/2\pi(1-s^2)^{1/4}$. The pseudo particle can escape out of the well either by thermal activation when $T > T_{co}$ or by tunnel effect when $T < T_{co}$.

When the tilt coefficient $s = I_b/I_c$ is smaller than 1, the phase γ oscillates in a well around its equilibrium position: $\gamma_0 = \arcsin(s)$ (see Fig. 2.9), at the characteristic angular frequency $\omega_p = \omega_0(1-s^2)^{1/4}$, ω_0 being the bare plasma frequency at zero tilt ($\omega_p^2 = I_c/(\varphi_0 C)$ with C the capacitance of the junction).

In the hysteretic regime, characterized by underdamped dynamics ($Q = RC\omega_p > 1$ where R is the parallel resistance of the environment of the junction), the escape of the phase γ out of a well triggers its run away all along the potential, which gives rise to a detectable voltage $V = \varphi_0\dot{\gamma}$ across the junction.

Mechanism of the escape

The escape of the pseudo-particle from the well is a probabilistic process for which two different regimes have to be distinguished:

- The quantum regime called Macroscopic Quantum Tunneling (MQT) at low temperature [53, 54]. The term macroscopic stands for the superconducting phase which is a collective variable of the circuit. In this regime, the escape is dominated by tunnelling out of the well from the ground state at a rate [55](when $Q \gg 1$)

$$\Gamma_s(I_b) \approx 52\sqrt{\frac{\Delta U}{\hbar\omega_p}}e^{-7.2\frac{\Delta U}{\hbar\omega_p}},$$

where $\Delta U(s)$ is the height of the energy barrier

$$\Delta U(s) \approx \frac{4\sqrt{2}}{3}\mathcal{E}_j(1-s)^{3/2}.$$

- The classical regime at high temperature where the escape is dominated by thermal activation up to the top of the barrier, at a rate given by a Kramers law:

$$\Gamma_s(I_b) = a\frac{\omega_p}{2\pi}e^{(-\frac{\Delta U}{k_B T})},$$

where $a \approx 1$ is a prefactor depending on the quality factor Q.

The crossover temperature $T_{co} = \hbar\omega_p/2\pi k_B$ from the quantum regime to the classical one is reached when the thermal fluctuations of the phase in the well are of the same order of magnitude than the quantum fluctuations.

Escape temperature

A useful quantity is the escape temperature T_{esc}, defined by:

$$\Gamma_s = \frac{\omega_p}{2\pi}e^{\frac{-\Delta U}{k_B T_{esc}}}.$$

T_{esc} is equal to the real temperature at high temperature and saturates at a value $T^0_{esc} = \hbar\omega_p/7.2k_B$ when T goes to zero (quantum regime, see figure 2.10).

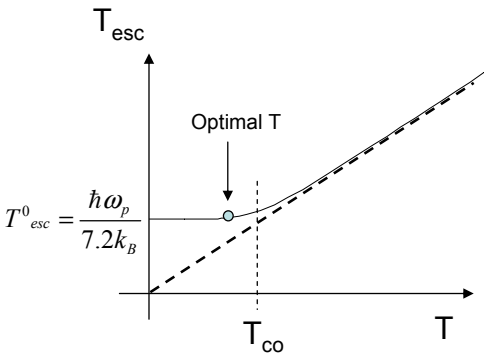

Figure 2.10: The escape temperature T_{esc}, defines the current resolution of the readout junction by quantifying the fluctuations either quantum or classical of the phase across the junction. At high temperatures: $T > T_{co}$, one has $T_{esc} \approx T$, whereas at low temperature: $T < T_{co}$, T_{esc} saturates at $T^0_{esc} = \hbar\omega_p/7.2k_B$. The optimal operating temperature is thus $T \lesssim T_{co}$ where the current resolution is maximum and does not depend on the temperature.

The escape temperature represents the equivalent noise temperature of either the quantum fluctuations or the thermal fluctuations of the phase in the well. It defines the current resolution of the detector. In our experiments, the plasma frequency of the junction is lowered with a shunt capacitor in order to get a smaller T^0_{esc}, slightly higher than the actual temperature of the experiment. The sensitivity os thus maximum and constant on small temperature changes.

We now consider the complete circuit of the quantronium: the split Cooper pair box coupled to the readout junction.

2.3.3 Escape dynamics of the readout junction coupled to the split Cooper pair box

When the superconducting loop is biased by a magnetic flux $\Phi = \varphi_0\delta_m$, the phase δ across the split Cooper pair box is equal to $\delta_m + \gamma$, where γ is the phase across the readout junction (see figure 2.3).

The Hamiltonian of the whole system is given by:

$$H = H_{qubit}(N_g, \delta_m + \gamma) + \mathcal{E}_c q^2 - \mathcal{E}_j \left[\cos(\gamma) + s\gamma\right],$$

where q is the reduced charge on the readout junction capacitance, conjugated variable of γ.

Adiabatic approximation

A first approach for solving the dynamics of H is to use an adiabatic approximation: over a wide range of parameters ($|\delta| < \pi/2$ and any N_g), the transition frequency of the qubit is higher than the plasma frequency of the readout junction ($\nu_{01} \approx 10$GHz to be compared to $\omega_p/2\pi \approx 4$GHz when s is close to 1).

One can then diagonalize the Hamiltonian of the qubit for each value of the phase γ and get a modified adiabatic potential for γ in each state k of the qubit:

$$U_k(\gamma, I_b, N_g, \delta_m) = E_k(N_g, \delta = \delta_m + \gamma) - \mathcal{E}_j(\cos\gamma + s\gamma),$$

Expression of the potential with the loop current

Since $\mathcal{E}_j \gg E_j$, a simple approximation consists in neglecting the dependance of γ_0, the minimum of the potential $U_k(\gamma, I_b, N_g, \delta_m)$ (see figure 2.9), with N_g or δ. γ_0 depends only on $s = I_b/I_c$:

$$\gamma_0 \simeq \arcsin(s).$$

A first order expansion of the energy $E_k(N_g, \delta_m + \gamma)$ with respect to γ around γ_0, yields to the potential [44]:

$$\widetilde{U_k}(s, N_g, \gamma) = -\mathcal{E}_j \cos\gamma - [I_b - i_k(N_g, \delta_m + \gamma_0)]\gamma\varphi_0.$$

In the framework of this adiabatic approximation, the effect of the qubit state can thus be described by the addition of the current $-i_k(N_g, \delta_m + \gamma)$ to the biasing current I_b, which modifies the tilt of the potential and consequently the height of the barrier ΔU.

Switching rate of the complete system

As a consequence, the switching rate of the whole system can be approximated by:

$$\Gamma_k(I_b, N_g, \delta_m) \approx \Gamma_s(I_b - i_k(N_g, \delta_m + \gamma_0)).$$

One can notice that the current in the loop of the quantronium is probed at $\delta = \delta_m + \gamma_0$. The phase δ is thus shifted between the manipulation and the readout of the qubit.

The predicted ratio between the escape rates for states $|0\rangle$ and $|1\rangle$ is:

$$\frac{\Gamma_1}{\Gamma_0} = \exp\left(\frac{2\sqrt{2}}{k_B T_{esc}}\sqrt{1 - s_0}\varphi_0(i_0 - i_1)\right),$$

where s_0 is the mean s value at which switching occurs. One can notice that this ratio depends on $\mathcal{E}_j$ only through the tilt s_0 and T_{esc}.

With typical values $s_0 = 0.96$, $T_{esc} = 40$mK, and $i_0 - i_1 \approx 10$nA, we expect $\Gamma_1/\Gamma_0 \approx 100$. For measuring the qubit state, a trapezoidal current bias pulse of duration τ is applied to the junction in such a way that: $\tau\Gamma_1 \gg 1$ and $\tau\Gamma_0 \ll 1$. The junction switches with a high probability if the qubit is in state 1, and with a low probability if the qubit is in state 0.

Pre-bias technique

The qubit being operated at the optimal working point $\delta = \delta_m = 0$, a standard readout pulse probes the loop current at $\delta = \gamma_0 \approx 75°$ and get a value $|i_0 - i_1| \approx 9$nA for sample A, which is not the optimal value (see figure 2.11). Indeed, for larger δ, the current difference $|i_0 - i_1|$ is larger, and has a maximal value of 16nA for $\delta \approx 160°$.

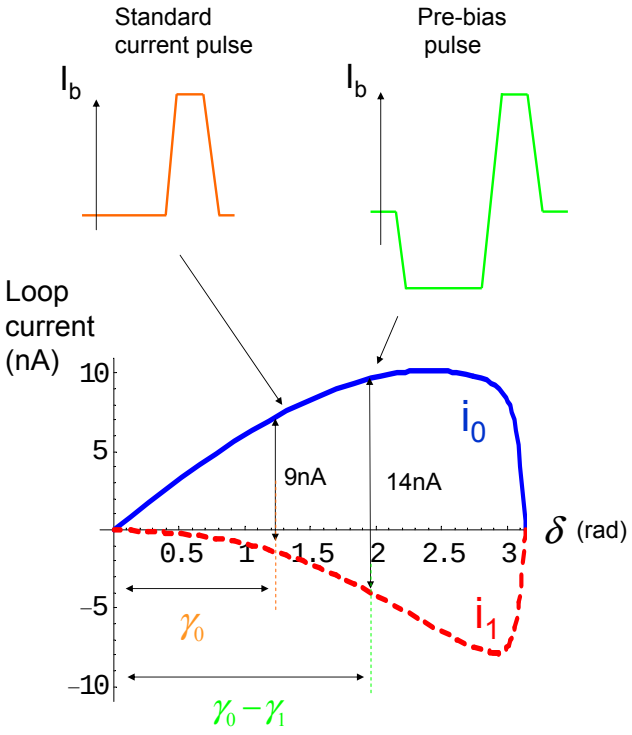

Figure 2.11: In the case where the qubit is manipulated at the optimal working point, a standard readout pulse probes the loop current for a phase $\delta = \gamma_0 \approx 75°$ where the current difference is only 9nA. With a prebias pulse, the flux in the loop is tuned to compensate the pre-biasing of the junction: $\delta = \delta_m + \gamma_1 = 0$, $\gamma_1 \approx -45°$ being the phase across the junction during the prebiasing pulse. The total phase shift experienced by the qubit during the readout is thus $\gamma_0 - \gamma_1 \approx 120°$, which increases the current signal to be measured.

In order to get a larger signal, the readout junction is biased during the manipulation of the qubit. During this pre-bias pulse, the phase across the junction is $\gamma_1 \approx -45°$ which is, according to the pre-pulse duration, the minimum value achievable without switching the junction. The flux in the loop $\delta_m \varphi_0$ is ajusted in such a way that $\delta = \gamma_1 + \delta_m = 0$. The qubit is thus tuned to its optimal working point where it can be efficiently manipulated.

Then, during the ramping of the readout pulse, the phase of the junction experiences a shift of $\gamma_0 - \gamma_1 \approx 120°$, which sets the phase of the qubit to a value $\delta \approx 120°$ where $|i_1 - i_0|$ is expected to be ≈ 14nA (see figure 2.11).

Switching probability during a readout pulse

The probability for the large junction to switch to its voltage state during a pulse of duration τ is given by:

$$P_k(I_b, \tau, N_g, \delta_m) = 1 - e^{-\Gamma_k(I_b, N_g, \delta_m)\tau},$$

for $k = 0$ or $k = 1$.

This expression can be very well approximated by a universal curve:

$$P(s) = 1 - \exp\left(-|\ln 0.4| \exp\left(\frac{\alpha}{0.4|\ln 0.4|}\Delta s\right)\right),$$

where $\Delta s = s - s_0$, s_0 being defined by $P(s_0) = 0.6$, where the slope of the P_s curve is maximum and equal to α with

$$\alpha = 0.4|\ln 0.4| \frac{2\sqrt{2}\mathcal{E}_j}{k_B T_{esc}} \sqrt{1 - s_0}.$$

α defines the sensitivity of the readout setup and $1/\alpha$ gives the typical width of the $P(s)$ curve (see figure 2.12). For the sample A, we expect $1/\alpha \approx 1.9\%$ of I_c leading to a current resolution of ≈ 8nA. The theoretical switching curves for state $|0\rangle$ and $|1\rangle$ are plotted on figure 2.12. The expected contrast between state $|0\rangle$ and $|1\rangle$ is 90% for the set of parameters: $T_{esc} = 40$mK, $|i_0 - i_1| \approx 10$nA, $\mathcal{E}_j/\varphi_0 = 500$nA and $s_0 \approx 0.96$, which should lead to a single shot measurement.

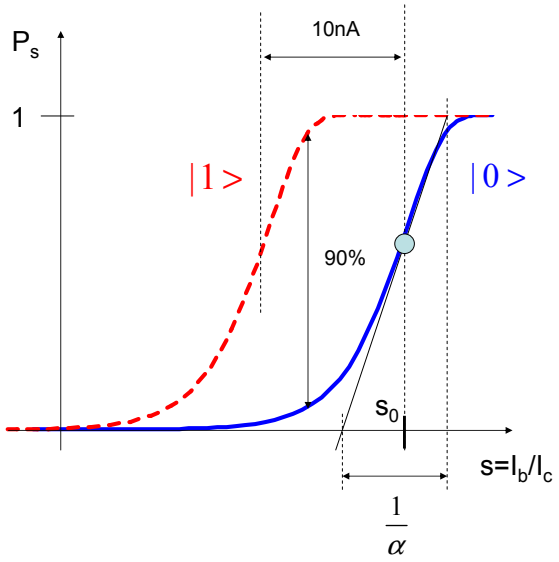

Figure 2.12: Calculated switching curves $P(s)$ for the ground state (in plain) and for the excited state (in dash). The quantity $1/\alpha$ defines the current sensitivity of the readout junction. For $i_1 - i_0 \approx 10$nA, $I_c \approx 500$nA and $T_{esc} \approx 40$mK, the theoretical resolution is 90%.

Switching probability for any state of the qubit

Now, we consider the case where the qubit is in a coherent superposition $\alpha|0\rangle + \beta|1\rangle$ before the readout. The ramping of the bias current moves the qubit out of the optimal point; as a consequence, the dephasing rate increases transforming the qubit state into a statistical mixture with a probability $|\alpha|^2$ for state $|0\rangle$

and a probability $|\beta|^2$ for state $|1\rangle$ (see chapter 4). The switching probability of the readout junction is then the weighted sum of the probabilities of switching for state $|1\rangle$ and state $|0\rangle$:

$$P(I_b, \tau, N_g, \delta_m) = |\alpha|^2 P_0(I_b, \tau, N_g, \delta_m) + |\beta|^2 P_1(I_b, \tau, N_g, \delta_m).$$

2.4 Experimental setup and characterization of the readout

The full experimental setup for reading out the state of the qubit is described on figure 2.13.

2.4.1 Current biasing line

For biasing the readout junction, we use an arbitrary waveform generator Agilent 33250, with a minimum rise time of 5ns. The voltage pulses generated are strongly filtered along a lossy line going from room temperature to 20mK, and attenuated with -30dB and -20dB discrete attenuators at 4K and 600mK respectively. The aim of this strong attenuation is to increase the signal to noise ratio by using the full dynamic range of the generator. Any spurious RF or microwave noise received on top of the cryostat is thus strongly attenuated. The aim of the filtering is to reduce the bandwidth to the minimum required in order to strongly suppress microwave noise, and particularly noise around the frequencies ν_{01} and $\omega_p/2\pi$. This filtering is achieved of course at the expense of the speed: here, the rise time of the line is 50ns which could probably be reduced to 5ns, while keeping an adiabatic ramping of the current readout pulse.

The voltage pulse biases a 4kΩ resistor at 20mK in order to inject in the readout junction a current of about 1μA for a few Volts at the top of the cryostat. This 4kΩ resistor is made of several resistors in series included into a copper box filled with black Stycast, in order to properly thermalize the electrons at the base temperature of the dilution refrigerator ($T_{base} \approx 15$mK for the Kelvinox300 fridge from Oxford Instruments used for this experiment).

In order to decrease the escape temperature, the plasma frequency of the large junction is lowered with an interdigitated capacitor of 0.6pF, to a value of about 8GHz at $s = 0$, and ≈ 4GHz at $s \approx 0.97$, giving expected value for the escape temperature $T^0_{esc} = \hbar\omega_p/7.2k_b \approx 35$mK and the crossover temperature ≈ 40mK.

2.4.2 Measuring line

The switching of the junction gives rise to a voltage pulse of $2\Delta/e \approx 400\mu$V across it. This voltage pulse is measured with a room temperature low noise amplifier NF LI75A ($1.2nV/\sqrt{\text{Hz}}$ with 1MHz bandwidth). This amplifier is connected to the sample with a lossy twisted pair, which gives a differential voltage measurement and a continuous filtering from room temperature down to 20mK. An extra filtering is needed at 20mK to suppress any noise at the frequency of the qubit ν_{01} or at the plasma frequency of the readout junction. This extra filtering is provided by microfabricated RC distributed filters placed at 20mK and avoids either spurious excitation of the qubit or an artificial increase of the escape temperature of the readout junction, leading to a diminution of the discrimination power.

Due to this strong filtering, the capacitance of the measuring line needs several μs to be loaded, which creates a delay between the switching of the junction and the measurement of the voltage pulse at the top of the cryostat. After amplification, the signal is sent to a threshold detector and then to a counter in order to obtain the statistics of the switching of the readout junction over 10^4 events.

2.4.3 Experimental characterization of the readout junction

The switching probability of the readout junction is measured by repeating the experiment 10^4 times, at a rate $10 - 50$kHz, in order to lower the statistical noise to a value $\leq 1\%$. The experimental results are shown on figure 2.15: the qubit being in its ground state, P_0 is measured as a function of I_b and

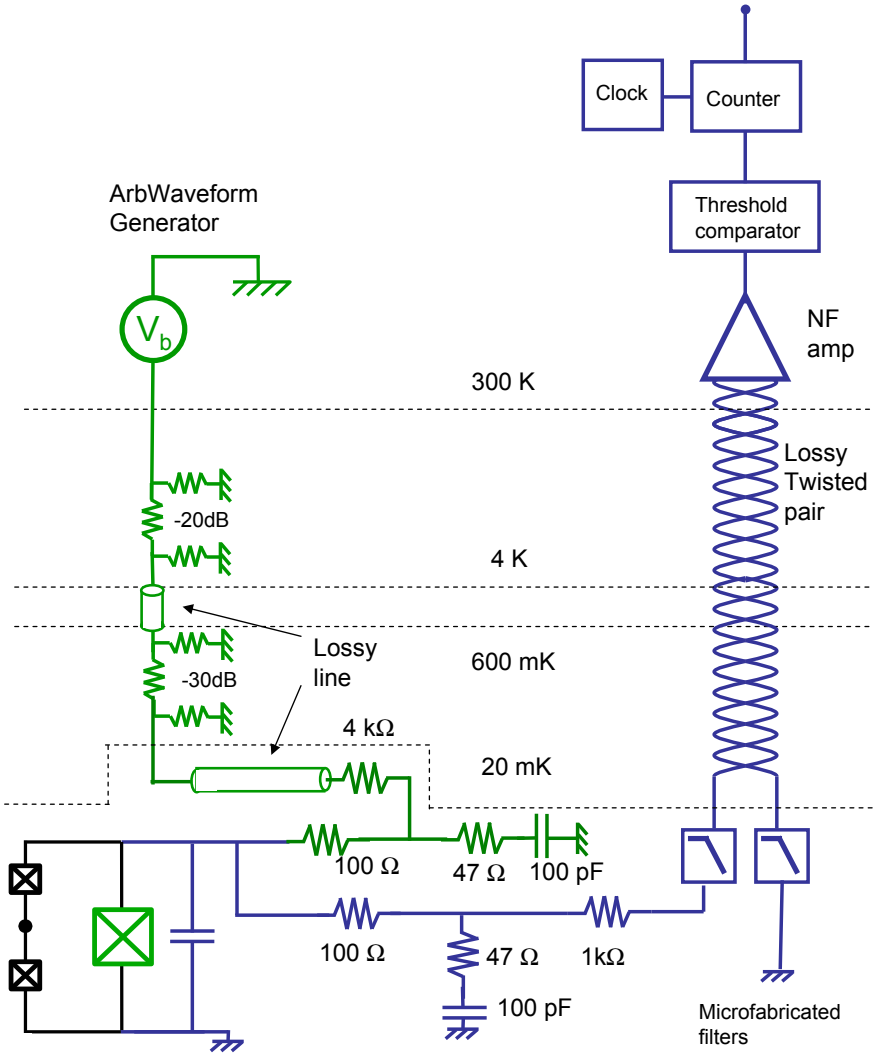

Figure 2.13: Experimental setup of the readout. Left: current biasing line. Right: measuring line. The two $RC = 47\Omega/100\text{pF}$ shunts the measuring and biasing lines above 100MHz, which protects the qubit from any spurious resonance in these lines and sets the quality factor of the readout junction to $Q \approx 3$. Since the measuring line is not attenuated contrary to the biasing one, this line needs an extremely strong filtering in the microwave frequency range, in order to avoid any thermal photons exciting the qubit or the readout junction. This filtering is provided by microfabricated distributed RC filters, having more than 110dB attenuation above 100 MHz.

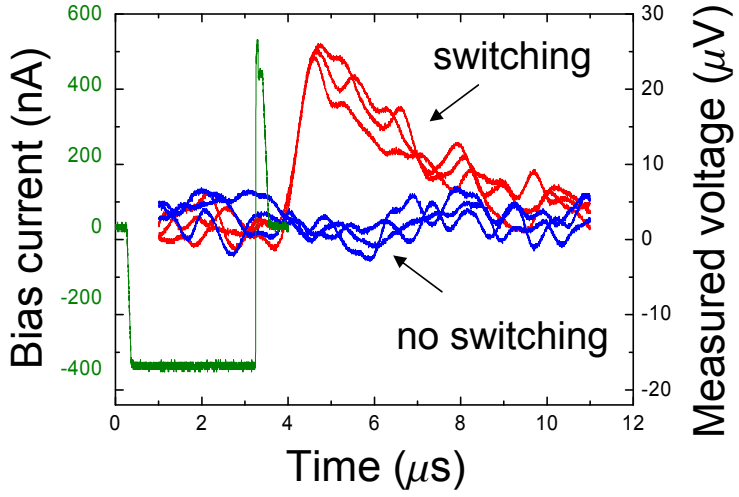

Figure 2.14: Typical current pulse used for biasing the readout junction. A prebias plateau is used for increasing the signal to be measured (see section 2.3.3), then the junction is tilted near its critical current for a duration of 50ns. In case the readout junction switches, a sustain prevents any retrapping, the voltage can thus develop across the junction.

for $\delta = 0$ and $N_g = 0$. The quantity $[-\ln(2\pi\Gamma/\omega_p)]^{(2/3)}$ is plotted as a function of $s = I_b/I_c$ and for several temperatures. The slope of these curves gives the escape temperature of the readout setup: $T_{esc} = 35\text{mK}\pm5\text{mK}$ at $T \approx 15\text{mK}$.

2.4.4 Experimental characterization of the quantronium sample A

Apart from reading out the qubit state, it is also important to probe the dependance of the ground state current i_0 with the parameters δ and N_g. This permits to find the optimal working points in the parameter space, and also to check the behavior of the readout setup.

Modulation of the ground state current

The measurement of the ground state current of the quantronium is a preliminary experiment needed for finding the optimal working point in the parameter space. i_0 is measured by using the readout setup in a feed-back mode: as the parameter δ_m or N_g is ramped, the amplitude of the bias current pulse is adjusted in order to keep a constant switching probability of 60%, where the sensitivity is maximum. One thus gets an effective switching current: $I_b^{60\%}(N_g, \delta_m)$ for the whole system, which depends on the pulse duration (here 50ns). Assuming the adiabatic approximation is valid, $I_b^{60\%}$ should be equal to the switching current of the readout junction alone modulated by the ground state current i_0:

$$I_b^{60\%}(N_g, \delta) = I_s + i_0(N_g, \delta). \tag{2.2}$$

Charge modulation of i_0

The effective switching current of the system $I_b^{60\%}$ is measured as a function of N_g (see figure 2.16). This experimental curve is periodic as expected permits to locate the half integer N_g points, where the

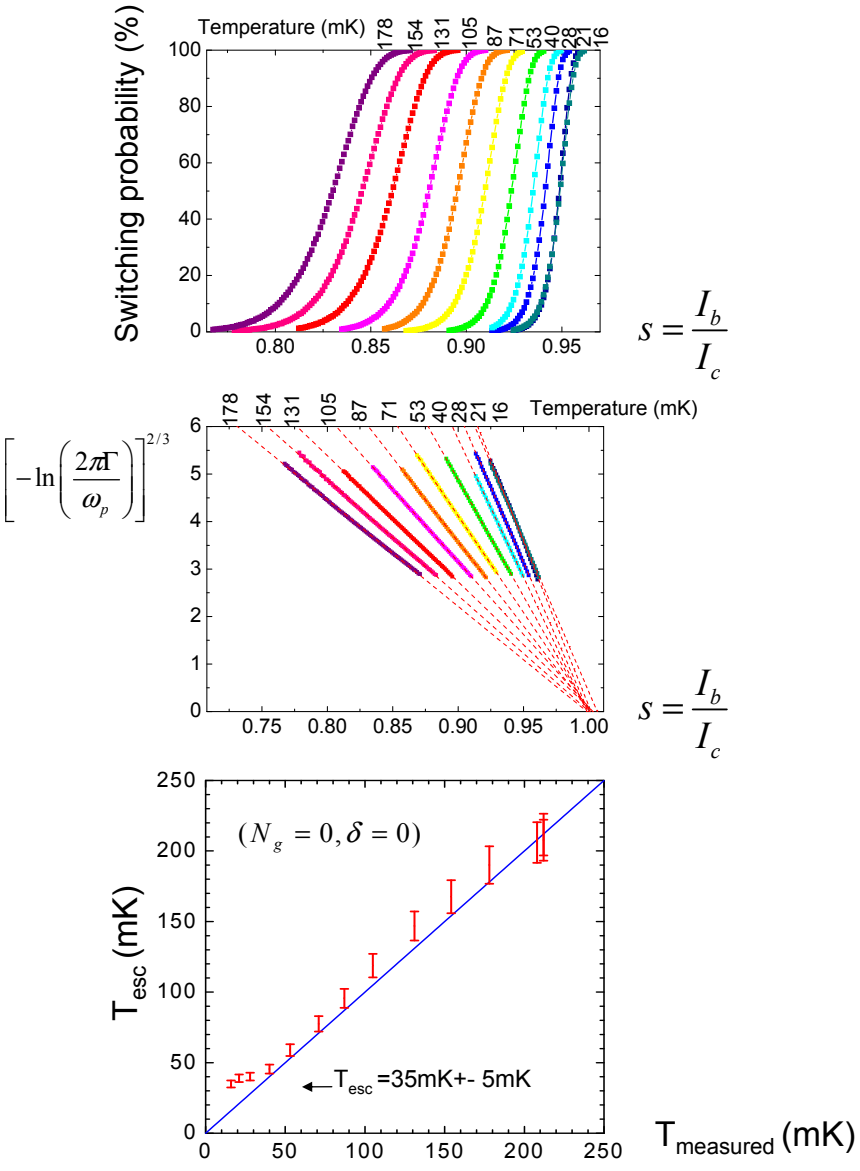

Figure 2.15: Top: switching probability of the readout junction as a function of the bias current, for different temperatures. Middle: $[-\ln(2\pi\Gamma/\omega_p)]^{(2/3)}$ is plotted as a function of the bias current. The slope of these curves is directly related to the escape temperature. Bottom: escape temperature as a function of the real temperature. The minimum escape temperature obtained is 35mK ±5mK at the base temperature 15mK. For this sample A, $I_c = 445$nA ±20nA, and $C \approx 0.7$pF.

sensitivity of the qubit to charge noise is minimum.

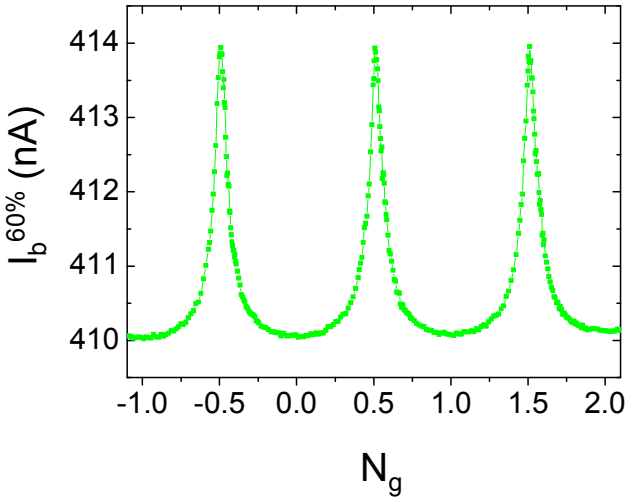

Figure 2.16: Dependance of the effective switching current of the quantronium $I_b^{60\%}$ on N_g. The modulation is recorded at $\delta \approx 165°$ where its amplitude is maximum. This modulation is one Cooper pair periodic and permits to locate the half integer N_g points.

Flux modulation of i_0

The current $I_b^{60\%}(N_g, \delta_m)$ has been measured at $N_g = 1/2$ and $N_g = 0$ as a function of δ (see figure 2.16).

For $N_g = 0$, the sensitivity to charge noise of the ground state current is minimum, which makes the flux modulation a robust tool for characterizing the ground state current. We observe experimentally that the amplitude of the current modulation $\approx$ 10nA for the sample A, is much smaller than the one calculated with the Hamiltonian 2.1 in the adiabatic approximation ($16nA$). We attribute this mismatch to the non validity of the adiabatic approximation. Indeed, during the readout the qubit frequency is only twice the plasma frequency of the readout junction (8GHz to be compared to 4GHz).

In ref [56, 57], a framework going beyond the adiabatic approximation is developed in order to explain quantitatively the flux modulation of the ground state current, and succeeds at fitting the experimental data.

2.4.5 Spectroscopy of the qubit

After having characterized the ground state of the qubit, we look now for the resonance line of the transition $|0\rangle \rightarrow |1\rangle$.

Spectroscopy

For this purpose, the switching probability is measured as a function of the microwave frequency after a long microwave pulse ($\approx 1\mu$s) is applied on the gate. The microwave power is sufficiently low for getting

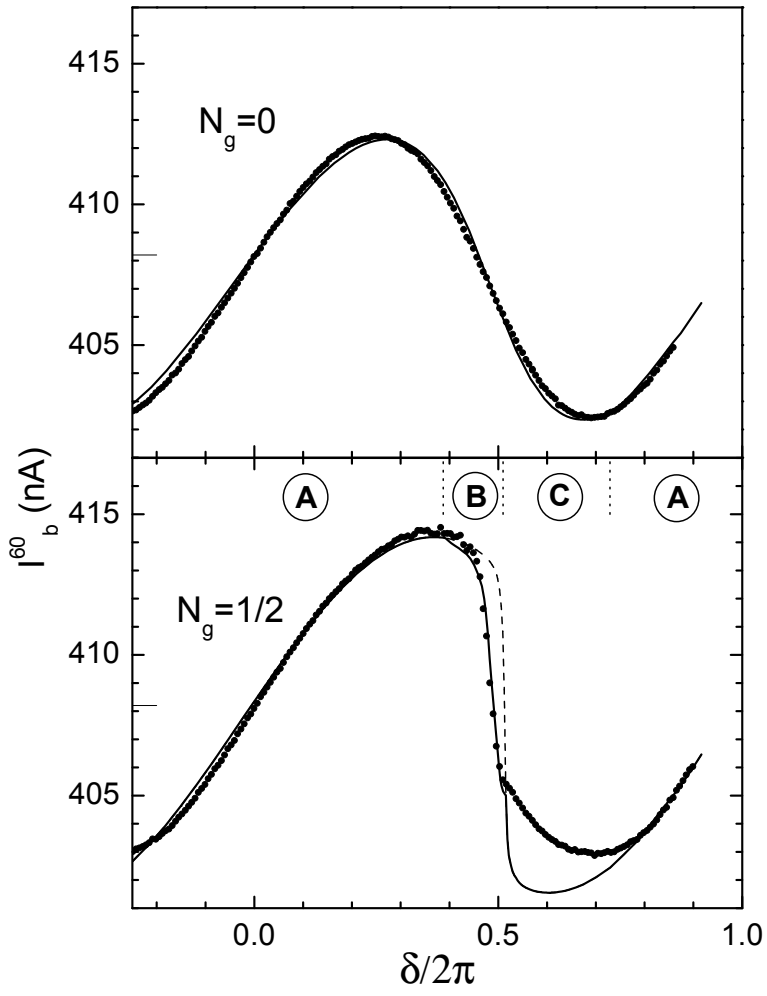

Figure 2.17: Experimental (dots) and theoretical (lines) amplitudes $I^{60\%}$ of 100 ns long current pulses giving a switching probability $p = 60\%$, as a function of the reduced phase $\delta/2\pi$ at $N_g = 0$ (top) and $N_g = 1/2$ (bottom). The solid lines are best fits using the formalism of ref [56, 57] based on the calculation of *diabatic* potentials for the readout junction, and considering the possibility of Landau-Zener transitions between the two states of the qubit during the tunneling. These fits lead to $\mathcal{E}_C = 0.0051\ k_B$K, $\mathcal{E}_J = 10.2\ k_B$K for the readout junction, and to the CPB asymmetry $d = 3.0\ \%$. The dashed curve of the bottom panel is a fit calculated without Zener flips. For $N_g = 0$, the shape of the current modulation has a similar shape than the one obtained with the simple adiabatic approximation but the current amplitude modulation is smaller by a 0.6 factor. For $N_g = 1/2$, in the B region, the $I_b^{60\%}$ curve is modified by Landau-Zener transitions during macroscopic quantum tunneling, which enhance the tunneling rate. In the region C, the transition frequency of the qubit is comparable to K_BT, thermal population of state 1 is thus possible. In region A, there is no Zener flips of the qubit state during the tunneling.

a desaturated line (see figure 2.18). The dependance of the transition frequency with the working point is plotted on the same figure. Notice that the dependance of ν_{01} along the lines $\delta = 0$ and $N_g = 1/2$ leads to the parameters $E_j = 0.870 k_B\text{K}$ $\pm 0.5\%$ and $E_c = 0.65 k_B\text{K}$ $\pm 0.5\%$, for the sample A of this thesis.

Note also that the derivative of ν_{01} with δ gives the difference between the two currents i_0 and i_1:

$$i_1 - i_0 = \frac{e}{\pi}\frac{\partial \omega_{01}}{\partial \delta / 2\pi} \approx 43 \frac{\delta}{2\pi}\text{nA},$$

for $|\delta| < 2$rad (sample A).

Via spectroscopy, we thus have a direct access to the loop current difference $i_1 - i_0$ which should be around 14nA during readout with a prebias pulse ($\delta = 120°$). One can thus check if the expected $i_1 - i_0$ is coherent with the discrimination power obtained. We'll see that this is not the case.

As predicted, the resonance line is the sharpest at the optimal working point. At this point, the resonance linewidth is $\approx$ 1.3MHz leading to a quality factor of $Q = \nu_{01}/\Delta\nu \approx 12.10^3$ suitable for performing time resolved experiments (see next chapter).

Discrimination power

The qubit being tuned to its optimal working point, one can prepare state $|1\rangle$ by applying a π pulse (see for more details Sect. 3.1.2), and compare the switching curve of the readout junction for the two states $|0\rangle$ and $|1\rangle$ (see figure 2.19).

We observe experimentally that, even with the prebias technique, the maximum sensitivity is only 40% instead of the 90% expected in the adiabatic hypothesis. Taking into account this loss of contrast, the readout process can be phenomenologically modelized by the schematic diagram on figure 2.20.

The expected switching curves for state $|1\rangle$ are also plotted on Fig. 2.19 for 2 values of $i_1 - i_0$. One can notice that the shift between the experimental curves (from state $|0\rangle$ to state $|1\rangle$) differs from the current difference $i_1 - i_0$ expected from the adiabatic approximation by a factor 2. In addition, an extra relaxation phenomenon, increasing when the switching probability increases, is also present.

As explained in Sect. 2.4.4, the amplitude of the flux modulation of the ground state current is different from the expected value by an important factor: 10nA measured instead of the 16nA expected. The discrepancy between the expected sensitivity and the experimental one also suggest that the adiabatic approximation is not valid. Further investigations using the theoretical framework developed in [56, 57] are now in progress, in order to go beyond the adiabatic approximation.

2.4.6 Back-action of the readout on the qubit

During manipulation of the qubit

For $I_b < I_c$, the readout junction behaves as a small inductor $L \approx 1nH$. With the interdigitated shunting capacitor $C \approx 0.5$pF, this readout junction forms an LC filter which rejects any noise coming down the measuring lines outside of a bandwidth centered at the plasma frequency and whose broadness is defined by the quality factor of the plasma oscillations. The phase fluctuations across the readout junction are those of an harmonic oscillator with resonant frequency $\omega_p/2\pi = 8$GHz thermalized at the temperature $T_{esc} \approx 35$mK, and are thus dominated by quantum fluctuations. We'll see in detail in chapter 4 that the phase noise is not the dominant noise source for the dephasing process at the optimal working point.

Back-action during the readout

One can estimate the strength of the coupling Δ between the readout junction and the qubit, during the measurement.

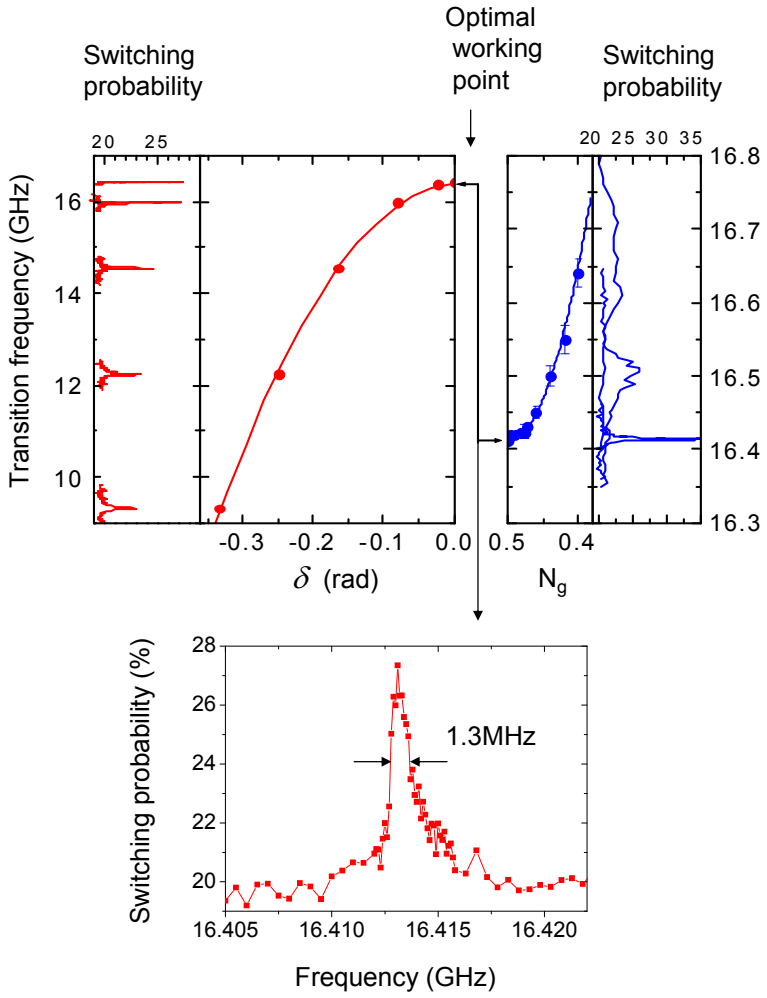

Figure 2.18: Spectroscopic data of sample A. Top: the transition frequency is plotted as a function of δ(left) and N_g(right). The resonance line broadens as the working point is moved away from $P_0 = (\delta = 0, N_g = 1/2)$, as expected. Note that the curvature of the transition frequency (in the charge direction: $25\text{GHz}/(2e)^2$ and in the phase direction: $1.66\text{GHz}/(\text{rad})^2$ for sample 1) leads to a precise determination of the parameters E_j and E_c. Bottom: resonance line at P_0. The linewidth is 1.3MHz, which corresponds to a quality factor of 12.10^3.

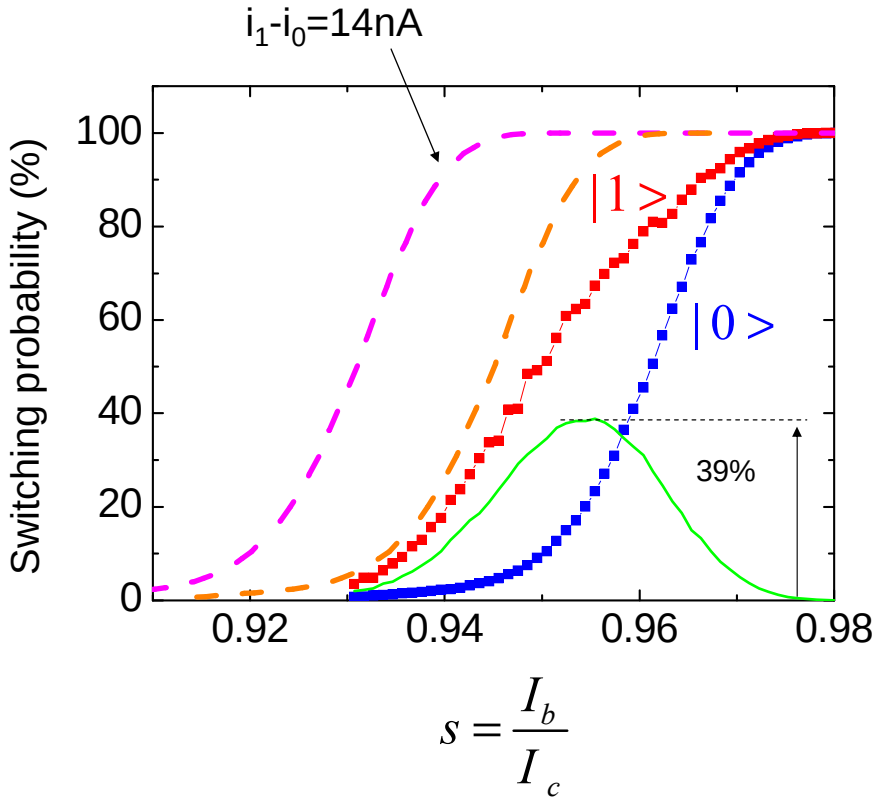

Figure 2.19: Square: switching probability of the readout junction measured for the two states of the qubit (50ns readout pulse). Solid line: difference between the two switching curves. The maximum contrast obtained is only $\approx 40\%$. Two expected switching curves for state $|1\rangle$ are plotted: one calculated in the adiabatic approximation framework, in the case where $i_1 - i_0 = 14$nA (left dashed line) and one in the case of the diabatic model (right dashed line).

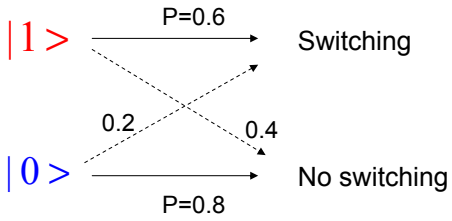

Figure 2.20: Phenomenological model for the readout process. The readout junction has a probability 0.6 to switch if the qubit is in state 1 and a probability 0.2 to switch if the qubit is in state 0.

As explained in section 2.3.3, the interaction term is $\widehat{I}\gamma\varphi_0$. Since at $s \approx 0.96$ and $T = 20$mK, one has $\omega_p(s)/2\pi = 4\text{GHz} \gg k_B T/\hbar$, the fluctuations of γ are thus determined by quantum effects. One can estimate $\langle(\gamma - \gamma_0)^2\rangle$ in the harmonic oscillator limit:

$$\langle(\gamma - \gamma_0)^2\rangle = L\hbar\omega_p/\varphi_0^2,$$

assuming that the junction is in its ground state during the measurement.

This leads to a mean value for the phase fluctuations of $\sqrt{\langle(\gamma - \gamma_0)^2\rangle} = 0.1$rad. With a typical current term of $\langle\widehat{I}\rangle = 10$nA, the interaction strength is thus $\Delta = 5\%$ of $h\nu_{01}$. The qubit is weakly coupled to the measuring apparatus.

As a consequence, the projection during the readout happens in the eigenbasis of the hamiltonian of the qubit and not in the eigenbasis of the coupling operator, $\widehat{I}$ [58, 59].

Relaxation during the ramping of the readout pulse

Assuming that the qubit is operated at the optimal working point P_0 with the prebias technique (see section 2.3.3), the phase across the qubit experiences a total shift of 120° during the ramping of a readout pulse. As a consequence, the transition frequency decreases from ≈ 16GHz to $\approx 8GHz$: the qubit can thus cross spurious resonances in the environment which induce relaxation. Such a phenomenon has already been observed on other qubits [50, 49]. In order to quantify the loss of population of state $|1\rangle$ during the ramping of the readout pulse, we have added to the biasing pulse a plateau with tunable height I_p and duration (see figure 2.21). On such a plateau the transition frequency is constant and depends on the current flowing in the readout junction. When ramping the amplitude of the plateau, one can observe dips in the signal for particular values of I_p. This dips correspond to a resonance of the qubit with some spurious mode of the environment, which induces a faster relaxation of the qubit state.

With this method, it is possible to probe this relaxation phenomenon for I_p up to 95% of the amplitude of the readout pulse, but not above because the junction starts switching on the plateau. Due to the relative high speed of the ramping of the readout pulse, we estimate that this spurious relaxation during 95% of the ramping explains only 5% of the signal loss.

Back-action during the switching of the readout junction

When the readout junction switches to the finite voltage state, the phase accross this junction aquires a dynamical behavior which modulates the qubit transition frequency over about an order of magnitude. As a consequence, relaxation of the qubit can occur by crossing any spurious resonance of the environment.

Then, the finite average speed of the phase running down the tilted potential generates about 10^5 quasi-particles ($\approx 1\mu$A during ≈ 50ns). These quasi-particles are extra sources of relaxation for the qubit, which explains why this readout can not be QND.

We'll see in chapter 5 that it is possible to use the same measurement circuit, i.e. a large Josephson junction, to implement a possibly QND readout with an AC dispersive method.

In addition, these quasi-particles take a certain time to recombine together, which limits the repetition rate of the experiment.

By using small pads of a normal metal (here gold) connected to the superconducting circuit and close to the junctions, it is possible to trap spurious quasi-particles and thus increase the repetition rate up to 50kHz which makes the acquisition process more convenient.

2.4.7 Conclusion

In the framework of the adiabatic approximation, the readout setup should have an error rate $\lesssim 5\%$, which is not what we observe experimentally. In addition, the ground state current modulation shows that the adiabatic picture of the qubit current adding to the biasing current in the readout junction does

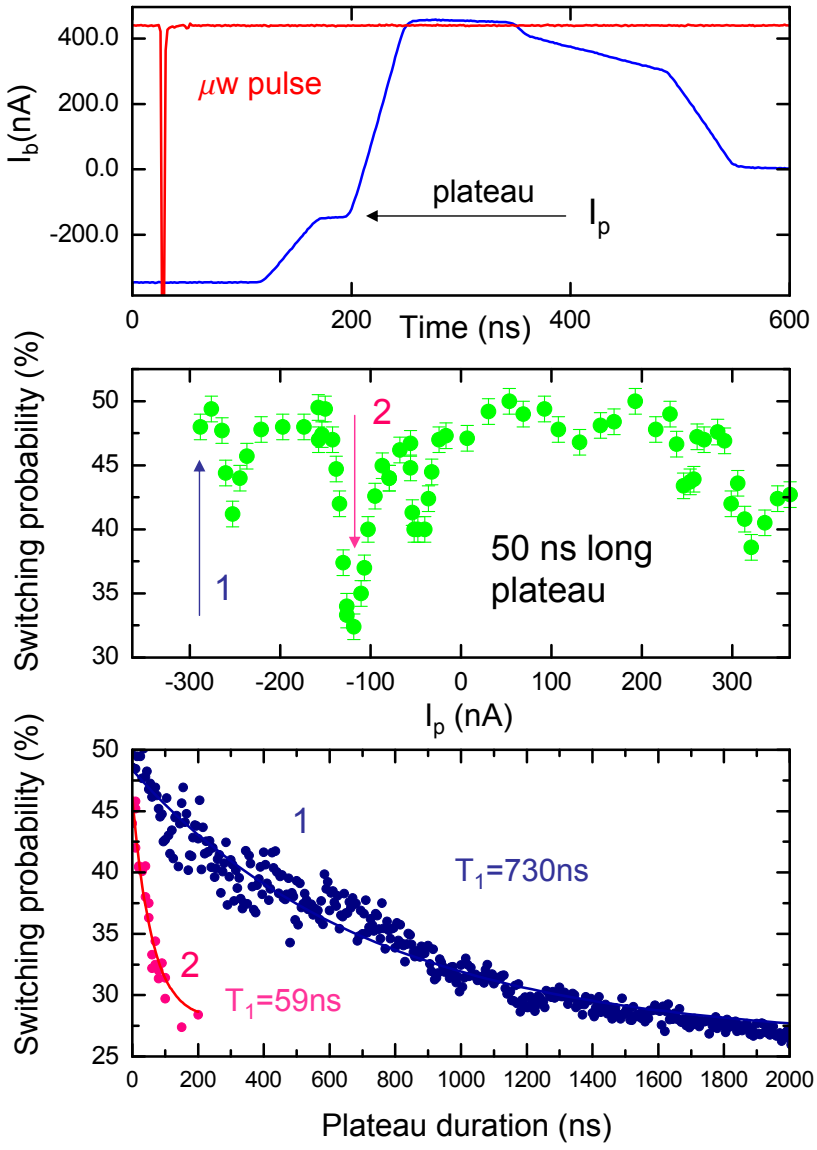

Figure 2.21: Top: for probing the relaxation during the ramping of the readout pulse, and extra plateau is added to the current biasing pulse. Middle: for a fixed duration (100ns), the amplitude of the plateau is ramped from −300nA to +380nA. One can observe dips in the signal for particular values of the plateau height. On these dips, the transition frequency of the qubit is on resonance with some spurious mode of the environment. Down: the amplitude of the plateau is fixed to two particular values 1 and 2, and the duration of the plateau is ramped. For the plateau value n°1, the relaxation time is of the same order than the relaxation time of the qubit at the optimal working point, whereas for the plateau value n°2, which corresponds to a transition frequency for the qubit of about $\approx$ 15.6GHz, the relaxation time is shorter meaning that the qubit can relax its energy faster in the environment at this frequency.

not hold. This simple picture, which separate the dynamics of the two subsystems: qubit and readout junction, does not yield the correct switching rates for the global system. This is not so surprising when considering the typical frequencies of these two systems during the readout: 8GHz and 4GHz for the qubit and the readout junction respectively. The framework developed in [56, 57], which goes beyond the adiabatic approximation, explains well this ground state modulation. Using this framework, further investigations are now in progress to determine the escape rate of the excited state of the qubit, and test quantitatively the adiabatic hyphothesis.

Whatever, the fidelity of the readout was sufficient to perform time resolved experiments using the high quality factor of the resonance line of the qubit (see chapter 3).

Zener Enhancement of Quantum Tunneling in a Two-Level Superconducting Circuit

G. Ithier,[1] E. Collin,[1] P. Joyez,[1] D. Vion,[1] D. Esteve,[1] J. Ankerhold,[1,2] and H. Grabert[2]

[1]*Quantronics group, Service de Physique de l'Etat Condensé, DSM/DRECAM, CEA Saclay, 91191 Gif-sur-Yvette, France*

[2]*Physikalisches Institut, Albert-Ludwigs-Universität Freiburg, Hermann Herder Straße 3, 79104 Freiburg, Germany*

(Received 5 November 2004; published 10 February 2005)

We have investigated the macroscopic quantum tunneling (MQT) of the phase across a Josephson junction embedded in a superconducting circuit. This system is equivalent to a spin 1/2 particle in a potential energy well. The MQT escape rate of such a particle was recently predicted to be strongly modified when a crossing of its inner Zeeman levels occurs while tunneling. In this regime, we observe a significant enhancement of the MQT rate and compare it to theory.

DOI: 10.1103/PhysRevLett.94.057004 PACS numbers: 74.50.+r, 74.78.–w, 85.25.Cp

The escape out of a potential well by quantum tunneling is ubiquitous in many areas of physics and chemistry [1]. The simplest model is that of a particle moving in a one-dimensional potential presenting a metastable minimum such that the escape rate is dominated by tunneling at sufficiently low temperature. The theoretical predictions of this model, including the effect of damping, were thoroughly tested for macroscopic quantum tunneling (MQT) of the phase in current-biased Josephson junctions [2]. Recently, the MQT problem was extended to the case when the particle has an additional spin 1/2-like degree of freedom [3], with a position dependent Zeeman splitting. A significant effect on tunneling has been predicted when this splitting happens to be suppressed at a certain point under the barrier, referred to below as the "crossing point," as sketched in Fig. 1. The calculated escape rate is strongly increased due to Zener flips between the spin states during tunneling. This theoretical work was motivated by experiments on the quantronium [4], a superconducting circuit implementing a two-level quantum system used as a qubit. The readout of this qubit is based on the MQT of a Josephson junction whose escape rate differs for the two qubit states. In this Letter, we present MQT rate measurements for a quantronium circuit initialized in its ground state prior to readout.

The quantronium circuit shown in Fig. 2 is based on a superconducting loop including a Cooper pair box (CPB) whose Josephson junction is split in two small junctions with Josephson energies $E_J(1 \pm d)/2$, delimiting an island with total capacitance C_Σ and charging energy $E_C = (2e)^2/2C_\Sigma$. When a phase difference γ across the series combination of the two junctions is imposed by an external magnetic field, the degree of freedom is only the number operator N of extra Cooper pairs on the island whose conjugate is the island phase δ. The Hamiltonian of this first subsystem is

$$h_{\mathrm{CPB}} = E_C(N - N_g)^2 - E_J\left[\cos\frac{\gamma}{2}\cos\delta + d\sin\frac{\gamma}{2}\sin\delta\right], \tag{1}$$

where the reduced gate charge $N_g = C_g V_g/2e$ is an external parameter. The energy spectrum of h_{CPB} is discrete, and the ground state with energy E_0 and the first excited state with energy E_1 define a quantum bit equivalent to a spin 1/2. For $N_g = 1/2$, the energy separation $E_{01} = E_1 - E_0$ between these states has a minimum at $\gamma = \pi$, which vanishes with d, as shown in Fig. 2. In parallel with the two small junctions is a larger readout junction (RJ) with Josephson energy $\mathcal{E}_J \gg E_J$, effective capacitance $C_J \gg C_\Sigma$, and Cooper pair Coulomb energy $\mathcal{E}_C \ll \mathcal{E}_J$, biased with a current source I_b. The Hamiltonian of this second subsystem,

$$h_{\mathrm{RJ}} = \mathcal{E}_C q^2 - \mathcal{E}_J(\cos\theta + s\theta), \tag{2}$$

is that of a fictitious particle with mass $m = C_J/4e^2$, position θ, and conjugate momentum $q = Q/2e$, moving in a tilted cosine potential with tilt slope $s = I_b/\mathcal{I}_0$, where $\mathcal{I}_0 = \mathcal{E}_J/\varphi_0$ is the critical current of the junction, and $\varphi_0 = \Phi_0/2\pi$ with $\Phi_0 = h/2e$ the flux quantum. Notice that the magnetic field used to control γ can also slightly penetrate the readout junction and lower $\mathcal{I}_0$. The plasma frequency is then $\omega_P = \omega_{P0}(1 - s^2)^{1/4}$ with $\omega_{P0} = (\varphi_0 C_J/\mathcal{I}_0)^{-1/2}$, and the escape out of the well corresponds to the switching to a finite voltage state $V = \varphi_0\langle d\theta/dt\rangle$.

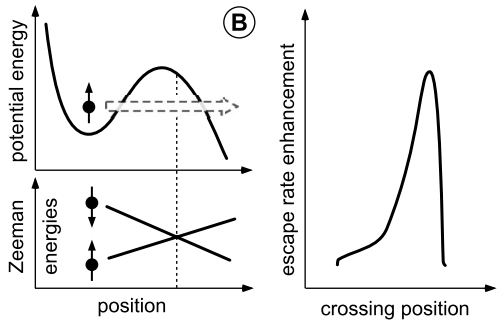

FIG. 1. The rate at which a particle escapes by quantum tunneling out of a metastable potential well has been predicted to strongly increase [3] when the particle carries a spin 1/2 degree of freedom whose Zeeman energies are position dependent and cross in the barrier, so that the spin can flip while tunneling.

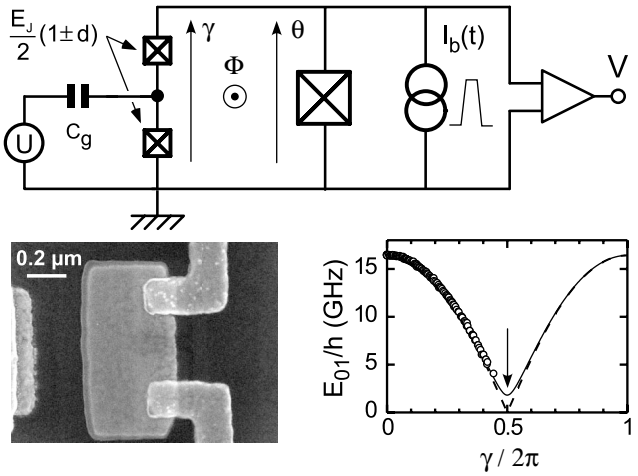

FIG. 2. Top: the quantronium circuit [4] is based on a split Cooper pair box (CPB) with charging energy E_C, Josephson energy E_J, and asymmetry d (see the text), controlled by a gate voltage U and a magnetic flux Φ. For readout, a larger Josephson junction with phase difference θ is biased by a current pulse I_b able to induce the switching to the voltage state. Bottom left: scanning electron micrograph of the island with the two small junctions. Bottom right: measured energy splitting E_{01} of the two lowest energy eigenstates of the CPB (dots), at $N_g = C_g U/2e = 1/2$, as a function of $\gamma = \theta + 2e\Phi/\hbar$. The dashed and solid lines are fits using $E_J = 0.655\ k_B$K and $E_C = 0.870\ k_B$K, with $d = 0$ and $d = 0.1$, respectively. At $\gamma = \pi$ (see the arrow), a level crossing or a small gap occurs depending on d.

The superconducting loop formed by the three junctions imposes the phase relation $\gamma = \theta + 2\pi\phi \pmod{2\pi}$, where $\phi = \Phi/\Phi_0$ is the reduced external magnetic flux applied to the loop. This relation couples the two subsystems and the Hamiltonian of the complete circuit, $H = h_{\mathrm{CPB}} + h_{\mathrm{RJ}}$, describes a spin 1/2 particle moving in a potential well.

At small bias $s \ll 1$, the phase θ, and consequently γ, can be seen as classical variables with negligible kinetic energies due to the large capacitance C_J. The fictitious particle can thus, depending on its spin state, be regarded as evolving in one of the two θ-dependent *adiabatic* potentials $E_k - \mathcal{E}_J(\cos\theta + s\theta)$, $k = 0, 1$. On the contrary, when s is close to 1, the switching occurs by MQT. When the reduced magnetic flux ϕ locates the crossing point $\theta_c = \pi(1 - 2\phi)$ within the barrier range, the Hamiltonian H is most conveniently represented [3] in the spin eigenstate basis at the minimum $\theta_{\min}$ of the lower adiabatic potential, i.e.,

$$H = \begin{pmatrix} \frac{q^2}{2m} + V_+(\theta) & \Delta(\theta) \\ \Delta(\theta)^* & \frac{q^2}{2m} + V_-(\theta) \end{pmatrix}. \qquad (3)$$

Here $V_\pm(\theta)$ denote two *diabatic* potentials, which are coupled by the off-diagonal element $\Delta(\theta)$. By construction, at $\theta_{\min}$, H is diagonal in spin space and the diabatic potential energies $V_\pm(\theta_{\min})$ coincide with the adiabatic ones. As long as $V_\pm$ are sufficiently separated so that $|V_- - V_+| \gg \Delta$, the spin is frozen and the particle tunnels through V_- by standard MQT at a rate $\Gamma_B = f_B \exp(-S_B/\hbar)$, with S_B the action of the bounce trajectory in the inverted potential [5]. When the crossing point θ_c lies within the barrier range, the MQT rate is $\Gamma_{\mathrm{tot}} = \Gamma_B + f_{\mathrm{flip}} \exp(-S_{\mathrm{flip}}/\hbar)$, where the Zener flip contribution involves the action S_{flip} along the flip bounce trajectory [3]. Since the ordinary and the flip contributions to the rate are exponentially sensitive to the shape of the barrier, a changeover from the V_- to the V_+ surface during tunneling may lead to a much smaller action $S_{\mathrm{flip}} < S_B$, and thus to a substantial rate enhancement.

Experimentally, the switching rate Γ is measured by repetitively initializing the quantronium in its ground state and applying then a trapezoidal current pulse with a rise sufficiently slow that the circuit follows adiabatically. The dimensionless peak value $s_{\max} = I_{\max}/I_0$ and the duration τ of this pulse are such that the switching to the voltage state occurs with a probability $p(s_{\max}) = 1 - \exp[-\Gamma(s_{\max})\tau]$. Practically, for each flux ϕ, p can be measured as a function of $s_{\max}$ (direct mode), or $s_{\max}$ can be adjusted to maintain p, and consequently Γ, at a constant value (feedback mode).

The actual sample on which measurements have been performed has been fabricated using Al evaporation and oxidation through a resist shadow mask patterned by e-beam lithography. The scanning electron micrograph of Fig. 2 shows the central part of this quantronium with the two small Josephson junctions formed by two fingers overlapping the island. The 0.67 μm^2 readout junction has an effective capacitance $C_J = 0.6 \pm 0.2$ pF dominated by a parallel on-chip interdigitated capacitor whose goal is to lower ω_P. An RC filter also in parallel with the junction limits its quality factor $2.5 < Q < 10$. The sample is placed in a shielding box thermally anchored to the mixing chamber of a dilution refrigerator with a 15 mK base temperature and is wired using carefully filtered lines. The rise time of the trapezoidal readout pulse is 50 ns and the plateau duration is either 100 or 200 ns. A switching event is detected by measuring the voltage V across the junction with a room temperature amplifier, and the switching probability p is determined by repeating the sequence a few 10^4 times at a rate between 10 and 50 kHz.

We have first inferred the parameters entering h_{CPB} from the increase of p when a resonant microwave pulse is applied to the gate at $I_b = 0$, just before the readout pulse. By fitting $E_{01}(N_g, \gamma)$, we deduce $E_C = 0.870\ k_B$K and $E_J = 0.655\ k_B$K (see Fig. 2). The gap E_{01} cannot be measured at its minimum $\gamma = \pi$ where the two quantronium states have vanishing loop currents. From the fit in the vicinity $\gamma \simeq \pi$, we deduce the upper bound $d \leq 0.13$, which implies $E_{01}(N_g = 1/2, \gamma = \pi) \leq 0.1\ k_B$K. Then, we follow a standard procedure [2,6] to determine $I_0(\phi)$ and to check that the MQT regime is reached at low temperature. For that purpose, p is measured as a function of I_b at a reference point R ($\phi_R = -0.22$) where the

quantronium loop current is close to zero at the switching of the readout junction, and at $N_g = 0$ and $\gamma \simeq 0$ between $T = 15$ mK and $T = 200$ mK. The values of Γ obtained from p are fitted to the expression for thermal activation, which leads to an equivalent escape temperature $T_{\rm esc}(T)$ and to $\mathcal{I}_0(\phi \simeq 0) = 445 \pm 20$ nA. As shown in the inset of Fig. 3, $T_{\rm esc}$ follows T at high temperature and saturates at a value $T_{\rm esc} = 35 \pm 2$ mK. Finally the switching current is measured in the feedback mode while sweeping the external flux over about $20\Phi_0$. These data lead to $\mathcal{I}_0(\phi) = \mathcal{I}_0(0) \times (1 - 0.005\phi^2)$.

To probe Zener flips, we also operate in the feedback mode by finding the value I_{60} of $I_{\rm max}$ that corresponds to $p = 60\%$. There, the slope $\partial p/\partial I_{\rm max}$ is the steepest and provides a maximal sensitivity to rate variations. For a readout pulse duration $\tau \simeq 100$ ns, the rate is $\Gamma_{60} \simeq$ 14.5 MHz. Figure 3 shows I_{60} as a function of ϕ, for $N_g = 0$ and $N_g = 1/2$. At $N_g = 0$ (top panel), the dependence $I_{60}(\phi)$ is fitted from the standard MQT rate $\Gamma_B(I_{60}, \phi) = \Gamma_{60}$, taking into account the $\mathcal{I}_0(\phi)$ dependence. The best fits are completely insensitive to d and give $\mathcal{E}_C = 0.0051\ k_B$K and $\mathcal{E}_J = 10.2\ k_B$K, thus fixing the junction parameters ($\mathcal{I}_0 = 427$ nA, $\omega_{P0}/2\pi \simeq 7.5$ GHz).

At $N_g = 1/2$ (bottom panel), three ϕ regions have to be distinguished. The first region noted by A, where $\gamma \neq \pi$ anywhere in the barrier range, is also well described by the standard MQT expression. In a second region noted by B, where Zener flips are predicted to occur since $\gamma = \pi$ somewhere in the barrier, $I_{60}(\phi)$ deviates from the standard MQT prediction but is well fitted by the full theory, i.e., from $\Gamma_{\rm tot}(I_{60}, \phi) = \Gamma_{60}$. The optimal fit gives the remaining parameter $d = 3.0 \pm 0.1\%$, which corresponds to a minimum gap $E_{01} = 26\ k_B$mK. We have also plotted in

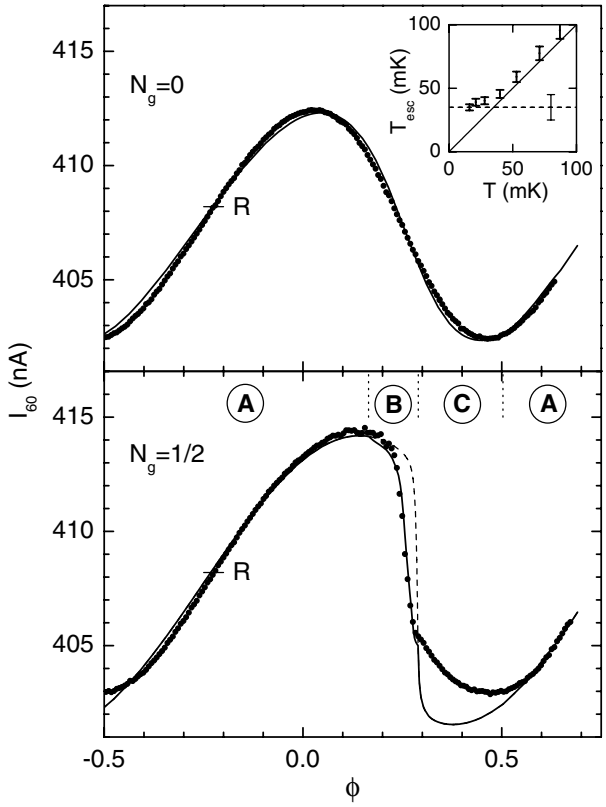

FIG. 3. Experimental (dots) and theoretical (lines) amplitudes I_{60} of 100 ns long current pulses giving a switching probability $p = 60\%$, as a function of the reduced flux ϕ at $N_g = 0$ (top) and $N_g = 1/2$ (bottom). The lines are best fits leading to $\mathcal{E}_C = 0.0051\ k_B$K, $\mathcal{E}_J = 10.2\ k_B$K for the readout junction, and to the CPB asymmetry $d = 3.0\%$. The solid (dashed) curve of the bottom panel is a fit calculated with (without) Zener flips. Three regions A, B, and C have to be distinguished (see the text), and R denotes a reference point. Inset: escape temperature $T_{\rm esc}$ calculated from escape rate measurements performed at R and at $N_g = 0$ with 200 ns long current pulses, as a function of the measured temperature T. The solid line corresponds to $T_{\rm esc} = T$, and the dashed line to the theoretical zero temperature limit.

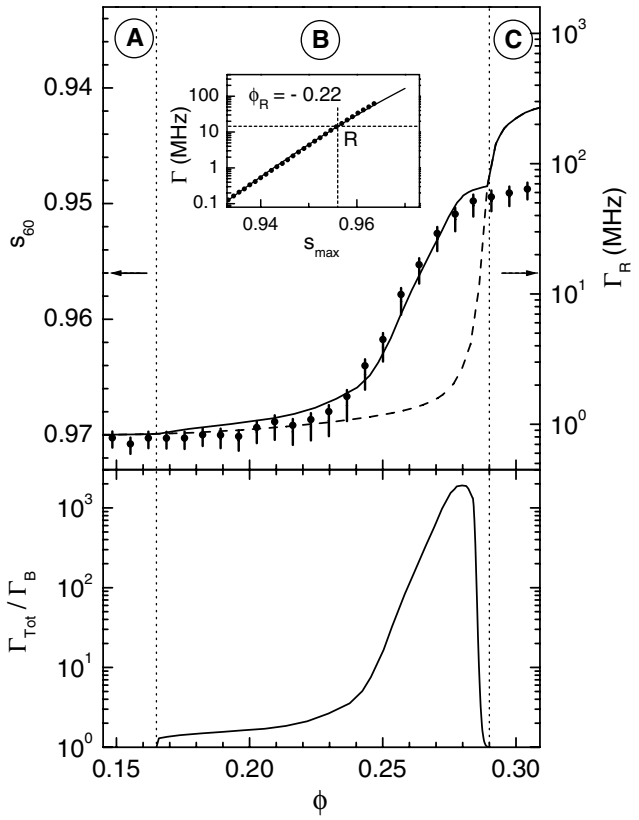

FIG. 4. Top panel: experimental (dots) and calculated (lines) values of $s_{60} = I_{60}/\mathcal{I}_0$, as a function of the reduced flux ϕ, in region B. Error bars are mainly due to gate-charge noise. The curves are calculated with (solid line) and without (dashed line) Zener flips. The right vertical scale results from the conversion of s_{60} into a rate Γ_R according to the inset (see the text). Arrows indicate the reference point R. Inset: escape rate $\Gamma(s_{\rm max})$ measured (dots) and calculated (line) at $N_g = 1/2$ at the reference point R. Bottom panel: escape rate enhancement calculated at constant rate $\Gamma_{\rm tot}(\phi, s_{60}) = \Gamma_{60}$ by dividing Γ_{60} by the rate Γ_B that would be observed at the same s_{60} in the absence of Zener flips.

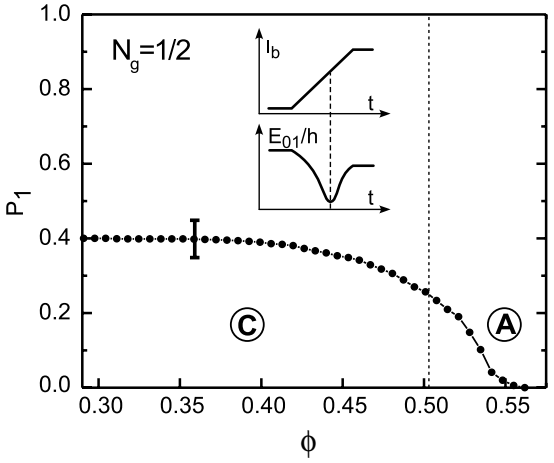

FIG. 5. Average population P_1 of the first excited state of the quantronium as a function of the reduced flux ϕ, calculated from the difference between the theoretical and experimental I_{60} in and close to region C, where the minimum of E_{01} is crossed during the current ramp, as depicted in the inset. The error bar indicates the systematic error on the plateau.

the top panel of Fig. 4 $s_{60}(\phi)$ together with both predictions. With the 0.4% experimental error bars on s_{60} that result principally from N_g noise, the experimental data agree well only with the prediction taking into account Zener flips. Although our experimental procedure has the advantage of maximizing the sensitivity to rate variations, it is more useful for the sake of clarity to convert the data into rates Γ_R that would have been measured at a constant reference value $s = s_R$. For that purpose, we use again the reference point R of region A where $s_R = 0.956$. The rate $\Gamma(\phi_R, s_{\max})$ is directly measured as a function of $s_{\max}$ and compared to the theoretical prediction, as shown in the inset of Fig. 4. With the value $Q \simeq 3.6$, both theoretical and experimental rates follow the same exponential variation with a precision on the rate better than 10%. Using the slope $K = \partial \log\Gamma/\partial s_{\max}$, s_{60} is converted into Γ_R according to $\log(\Gamma_R) = K \times (s_R - s_{60}) + \log(\Gamma_{60})$. Note that this conversion procedure is reliable because rate measurements performed at different ϕ show very similar behaviors. The top-right scale of Fig. 4 now shows that the tunneling rate Γ_R is increased by up to a factor of about 20 by Zener flips and that our error bars correspond to less than a factor of 2 in rates. This Zener flip effect can also be modeled by a tunneling rate enhancement ratio calculated at constant total rate Γ_{tot} rather than at constant s: The bottom panel of Fig. 4 shows that this theoretical ratio $\Gamma_{\text{tot}}(\phi, s_{60})/\Gamma_B(\phi, s_{60})$ with s_{60} chosen so that $\Gamma_{\text{tot}}(\phi, s_{60}) = \Gamma_{60}$, increases by up to 3 orders of magnitude.

A corollary effect of the Zener flip tunneling in region B is the large deviation between the theoretical prediction for MQT from the ground state and the experimental data in a third region C. In this region, the intersection of $V_{\pm}$ does occur in the well region *during* the rise of the bias current prior to the set-in of MQT. As a consequence, for the minimal E_{01} being of the order of the mean thermal energy per degree of freedom, at the crossing point all collective and microscopic degrees of freedom can excite the spin. In addition, conventional Zener transitions may also take place. Accordingly, the switching occurs by standard MQT from a statistical mixture of the spin states, the deeper excited potential well leading to a higher s_{60} as we indeed observe. Predicting quantitatively this effect would require an exact knowledge of all the environmental degrees of freedom and of their coupling to the quantronium, which is not available. So we have fitted the experimental s_{60} to a weighted average of the standard MQT rates in the two adiabatic potentials, which gives the population P_1 of the excited spin state inside and in the vicinity of region C. As shown in Fig. 5, P_1 is close to its thermal equilibrium saturation value $1/2$ on the left side of C, where the crossing point is traversed just before MQT sets in. On the contrary, P_1 decreases on the right side of the region, where the intersection appears at the foot of the current ramp so that the spin can relax again before the top of the pulse is reached.

To summarize, we have reported on the first observation of "Zener flip quantum tunneling," a general effect recently predicted, which consists of a large increase of the escape rate of a particle that tunnels out of a well when this particle has an inner spin degree of freedom undergoing a level crossing somewhere in the barrier. This phenomenon may be also of relevance for other physical systems, such as other superconducting qubit circuits [7] or recent realizations of atomic transport in optical lattices [8].

We acknowledge essential interactions in the Quantronics group, the technical help of P. F. Orfila, P. Sénat, and J. C. Tack, the support of the European project SQUBIT, of Yale University (DAAD 19-02-1-0044), and of DFG.

[1] *Quantum Tunneling in Condensed Media*, edited by Yu. Kagan and A. J. Leggett (Elsevier, Amsterdam, 1992).
[2] M. H. Devoret *et al.*, in Ref. [1], p. 313.
[3] J. Ankerhold and H. Grabert, Phys. Rev. Lett. **91**, 016803 (2003).
[4] D. Vion *et al.*, Science **296**, 886 (2002).
[5] A. O. Caldeira and A. J. Leggett, Ann. Phys. (N.Y.) **149**, 374 (1983).
[6] A. Cottet *et al.*, Physica (Amsterdam) **367C**, 197 (2002).
[7] I. Chiorescu *et al.*, Science **299**, 1869 (2003).
[8] O. Mandel *et al.*, Phys. Rev. Lett. **91**, 010407 (2003).

Chapter 3

Manipulation of the quantum state of the Quantronium

The quantum state of the quantronium can be efficiently manipulated by techniques inspired from NMR. A significant difference with NMR is that the quantronium is a unique two level system operated at a temperature $T = 20$mK much smaller than the splitting energy $h\nu_{01} \approx 1 k_B K$. At thermal equilibrium, the qubit is thus in its ground state, and relaxation provides a natural reset of the qubit.

3.0.8 Bloch sphere representation

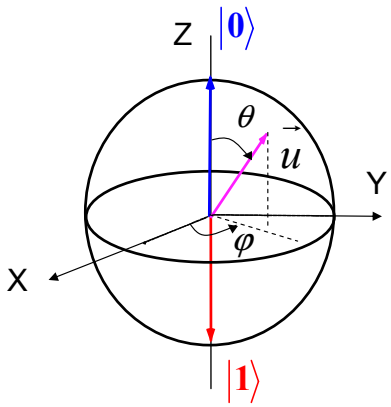

Figure 3.1: A qubit is a two level system, equivalent to a spin 1/2 in a magnetic field, which can be conveniently represented by a vector on the Bloch sphere.

The qubit is a two-level system which is equivalent to a spin 1/2 in a magnetic field. Any state $|\overrightarrow{u}\rangle$ of the qubit can thus be conveniently represented by a unit vector $\overrightarrow{u}$ on the Bloch sphere. The angles characterizing $|\overrightarrow{u}\rangle$ are given by the decomposition of $|\overrightarrow{u}\rangle$ on the basis $\{|0\rangle, |1\rangle\}$:

$$|\overrightarrow{u}\rangle = \cos(\theta_u/2)e^{-i\varphi_u/2}|0\rangle + \sin(\theta_u/2)e^{i\varphi_u/2}|1\rangle.$$

In this thesis, states $|0\rangle$ and $|1\rangle$ correspond to the North and South pole respectively. The equatorial plane represents the superpositions of states $|0\rangle$ and $|1\rangle$ with equal weight.

A single qubit unitary gate $\widehat{U}$ is equivalent to a rotation of the vector state on the Bloch sphere, and as a consequence can be decomposed on the Pauli matrices basis:

$$\widehat{U} = e^{i\zeta} R_{\overrightarrow{u}}(\theta) = e^{i\zeta} \exp\left(-i\overrightarrow{u}.\overrightarrow{\widehat{\sigma}}\,\theta/2\right),$$

where $\overrightarrow{u}$ and θ are the axis and the angle of the rotation respectively, ζ is a phase factor, and $\overrightarrow{\sigma} = (\widehat{\sigma_x}, \widehat{\sigma_y}, \widehat{\sigma_z})$, with $\widehat{\sigma_i}$ the Pauli matrices.

In order to implement a qubit operation, an external parameter of the Hamiltonian has to be modulated either in a non-adiabatic way with DC pulses (rise time much shorter than the characteristic evolution time) or AC resonant pulses, or in an adiabatic way by using slowly varying trapezoidal pulses.

3.1 Manipulation of the qubit state with non-adiabatic pulses

The Rabi precession is the simplest coherent manipulation of the qubit state in the time domain. It can be either implemented with DC or AC non-adiabatic pulses.

3.1.1 Non-adiabatic DC pulses

This technique was developed by Nakamura *et awl* for manipulating the quantum state of a Cooper pair box [36, 60]. A non adiabatic gate pulse brings the system to its degeneracy point where the Josephson coupling mixes successive charge states and induces Rabi precession (see section 2.1). To be non-adiabatic, the rise time of the gate pulse has to be much smaller than the characteristic time of the Josephson coupling: $\tau \approx 1/E_j \approx 200$ps. As a consequence, the required bandwidth for properly controlling the shape of such pulses is several tens of GHz. The excitation technique using AC resonant pulses is more versatile and easier to implement experimentally.

3.1.2 Non-adiabatic AC resonant pulses

This technique has already been used for several superconducting qubits [61, 60, 40]. An important advantage of AC resonant pulses is that the qubit can stay at the optimal working point, which preserves the quantum coherence of the qubit.

In the case of the quantronium, a nearly resonant microwave pulse is applied to the gate, $\Delta N_g(t) = \Delta N_g^0 \cos(2\pi\nu_{\mu w}t + \chi)$ (see figure 3.2), which adds the time dependant term

$$H_{\mu w} = -2E_c \Delta N_g \cos(2\pi\nu_{\mu w}t + \chi)\widehat{N},$$

to the Hamiltonian.

$\widehat{H_{\mu w}}$ couples states $|0\rangle$ and $|1\rangle$ through the operator $\widehat{N}$ with $\widehat{N} = N_x\widehat{\sigma_x + 1}/2$ at the optimal working point P_0 and $N_x = Re[\langle 1|\widehat{N}|0\rangle]$ ($Im[\langle 1|\widehat{N}|0\rangle] = 0$ at P_0. However any σ_y component appearing at $P \neq P_0$ can be converted into a phase shift of χ). Note that the operator $\widehat{N}$ aquires a small $\widehat{\sigma_z}$ component N_z, when the working point is detuned from the optimal one. However, $N_z \leqslant 0.2N_x$ if $N_g \in [0.45, 0.55]$, which is the typical range of N_g explored experimentally in this thesis. Neglecting the $\widehat{\sigma_z}$ component, $\widehat{H_{\mu w}}$ can be decomposed in two counter rotating terms:

$$\widehat{H_{\mu w}^{\pm}} = -\frac{h\nu_{R0}}{2}(\cos(2\pi\nu_{\mu w}t + \chi)\widehat{\sigma_x} \pm \sin(2\pi\nu_{\mu w}t + \chi)\widehat{\sigma_y}),$$

where $\nu_{R0} = 2E_c\Delta N_g|\langle 1|\widehat{N}|0\rangle|/h$ is called the Rabi frequency on resonance.

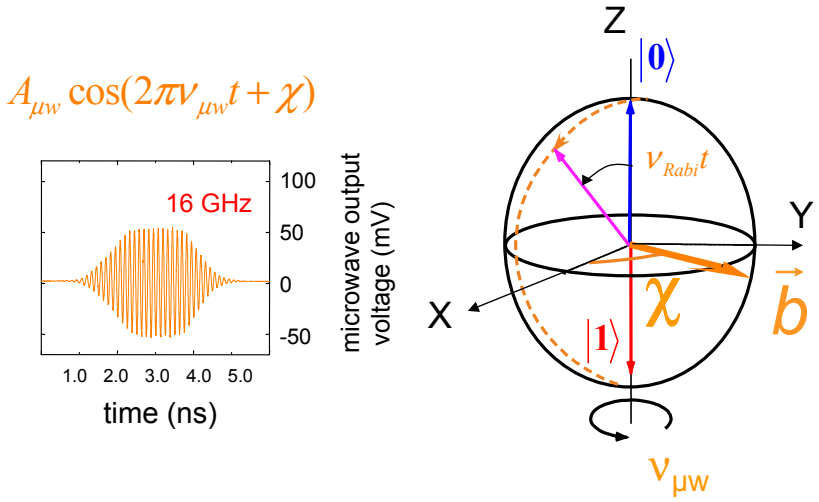

Figure 3.2: Left: oscilloscope trace of a typical microwave pulse applied to the qubit. Right: in the rotating frame, the precession of the vector state happens around the effective dc field, at the Rabi frequency ν_R.

In the frame rotating at the microwave frequency $\nu_{\mu w} \approx \nu_{01}$, the effect of the component $H^{-}_{\mu w}$ can be neglected within the scope of the rotating wave approximation (RWA) [62, 63]. The only efficient term in the rotating frame is $H^{+'}_{\mu w}$:

$$\widehat{H^{+'}_{\mu w}} = -\frac{h\nu_{R0}}{2}(\widehat{\sigma_x}\cos\chi + \widehat{\sigma_y}\sin\chi).$$

When the microwave excitation field is out of resonance, an extra detuning term appears in the rotating frame:

$$\widehat{\Delta H} = -\frac{h\Delta\nu}{2}\widehat{\sigma_z},$$

where $\Delta\nu = \nu_{01} - \nu_{\mu w}$ is called the Ramsey frequency. The total effective Hamiltonian in the rotating frame is thus:

$$\widehat{H'_{\mu w}} = -\frac{h\Delta\nu}{2}\widehat{\sigma_z} - \frac{h\nu_{R0}}{2}(\widehat{\sigma_x}\cos\chi + \widehat{\sigma_y}\sin\chi)$$

The dynamics of the vector state in the rotating frame is then equivalent to that of a spin 1/2 in a static magnetic field

$$\overrightarrow{b} = \Delta\nu\,\overrightarrow{u}_z + \nu_{R0}(\overrightarrow{u}_x\cos\chi + \overrightarrow{u}_y\sin\chi),$$

where $\overrightarrow{b}$ is expressed in units of frequency.

During the driven evolution, the dynamics of the vector state on the Bloch sphere is given by the equation:

$$\frac{d\overrightarrow{u}}{dt} = \overrightarrow{b} \wedge \overrightarrow{u}.$$

The fictitious spin 1/2 thus precesses around $\overrightarrow{b}$ at the Rabi frequency:

$$\nu_R = \sqrt{\nu_{R0}^2 + \Delta\nu^2}.$$

When the qubit evolves freely, the precession takes place around the detuning field $\overrightarrow{\Delta b} = \Delta\nu\,\overrightarrow{u}_z$ at the Ramsey frequency $\Delta\nu$.

Experimental setup

For generating the excitation pulses, we use a continuous microwave generator (Rhode&Schwartz SMR20), whose output is split into two channels. One of the channels, used as a carrier reference, feeds two Marki mixers (M80420LS) in series controlled by trapezoidal pulses (see figure 3.3). These trapezoidal pulses used for shaping the envelopes of the microwave pulses are generated by a BitErrorRate analyser (Agilent 81200). This generator has 6 programmable outputs (which permits to combine several pulses) and has an accuracy time base better than 50ps providing a precise control of the pulse duration and of the delays between pulses. In addition, the minimum rise time of the generator is 0.5 ns which permits to generate short pulses of duration < 2ns.

The other channel is dephased by a tunable dephasor (DC-16GHz Arra) before being mixed which permits to excite the qubit with sequences of pulses having very well defined dephasings. Note that each DC line drives two mixers in series in order to increase the On/Off ratio of the microwave signal ($P_{on}/P_{off} \gtrsim 40$dB).

The two channels are then recombined together and sent to a 50Ω strongly attenuated line (-20dB at 4K, -20dB at 600mK and -3dB at 20mK), the idea here being also to work with the highest signal to noise ratio, and to attenuate gradually the thermal noise generated by each stage. At 20mK, the signal is coupled to the island of the qubit by a gate capacitance of 80aF. The amplitude of the N_g oscillation is about 0.6% of a Cooper pair for a typical Rabi frequency of 100MHz, which corresponds to a gate voltage of several μV.

Experimental results

For an applied microwave excitation pulse of fixed duration t and amplitude, the switching probability P_s of the readout junction is measured by repeating 10^5 times the same sequence of excitation and measurement pulses. The observed Rabi oscillations of P_s (see fig. 3.4) when t is ramped are a consequence of the coherent oscillation of the qubit between states $|0\rangle$ and $|1\rangle$, during the precession around the microwave field. Note that the maximum amplitude of the Rabi oscillations is only 40%.

The π and $\pi/2$ rotations are noticeable since they are at the basis of the manipulation of the quantum state of the qubit. A π pulse implements the NOT operation (with an extra phase term), and prepares state $|1\rangle$ starting from state $|0\rangle$. A $\pi/2$ pulse prepares the coherent superposition $(|0\rangle + |1\rangle)/\sqrt{2}$ starting from state $|0\rangle$.

The dependance of the Rabi frequency with the microwave amplitude is plotted in figure 3.4, and has a linear behavior until the mixers get saturated, which demonstrates that the microwave excites a transition between two discrete energy levels and not a spurious resonance of the environment of the circuit. The maximum Rabi frequency available is 140MHz, without saturating the mixers, which provides a minimum bit flip time smaller than ≈ 4ns.

Fidelity of a qubit manipulation

One can notice a loss of contrast of the Rabi oscillations (see fig. 3.5) as the driving time increases. This phenomenon is related to the decoherence during driven evolution (see chapter 4) and leads to errors when implementing a rotation. These random errors affect the unitary character of the implemented rotation. Indeed, we'll see in the next chapter that starting from a pure state, the ground state for instance, the result of the operation is a statistical mixture. By fitting the decay of the Rabi oscillations, and taking into account the simplest model for the readout (see section 2.20), one can evaluate the coefficients of the density matrix resulting from the rotation (see section 4.4). For instance, the state after a π rotation

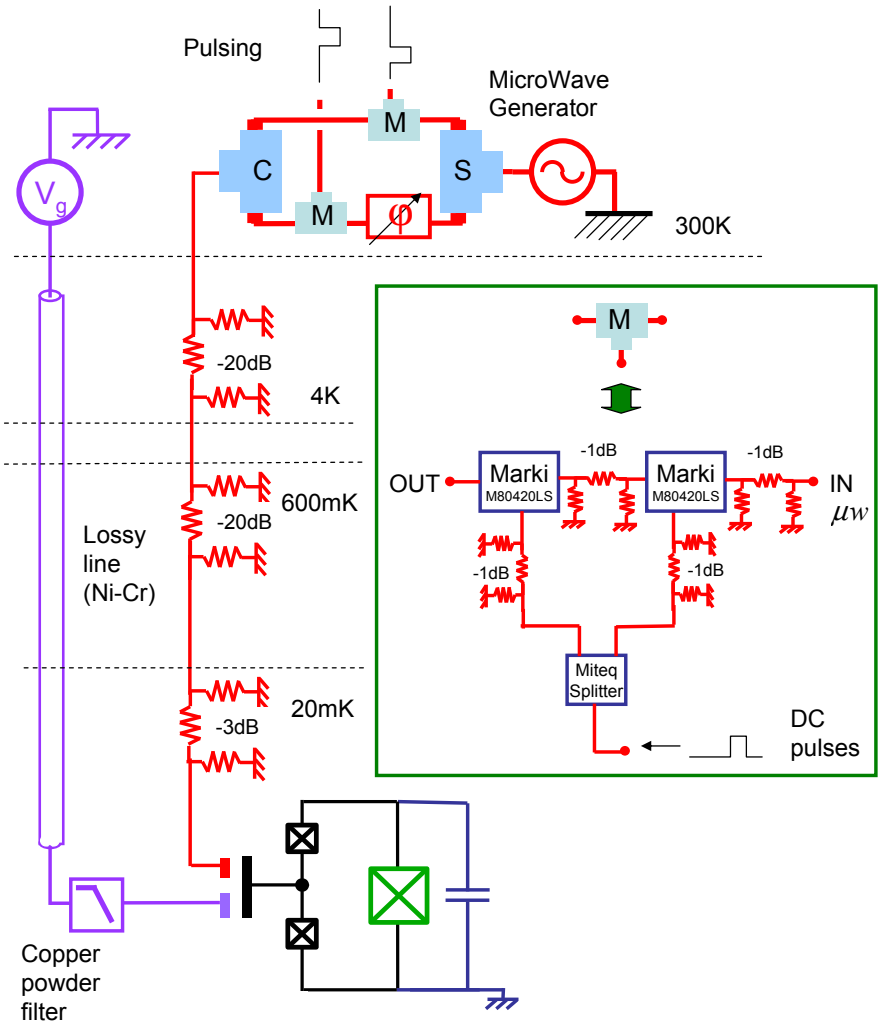

Figure 3.3: Experimental setup for the manipulation of the qubit state. A microwave source is split in two channels, one of them being dephased by a tunable dephasor. Then the two channels are mixed with trapezoidal pulses coming form a pulse pattern generator before being recombined together. The microwave pulses are applyied on a strongly attenuated line in order to use the full dynamic range of the microwave generator and increase the signal to noise ratio. The microwave line is then coupled to the superconducting island through a gate capacitance. Inset: each mixing line is made of 2 Marki mixers in series in order to increase the ON/OFF ratio ($>$ 40dB). Attenuators of 1dB are added in order to minimize the effects of possible standing waves in the setup, coming from impedance mismatches.

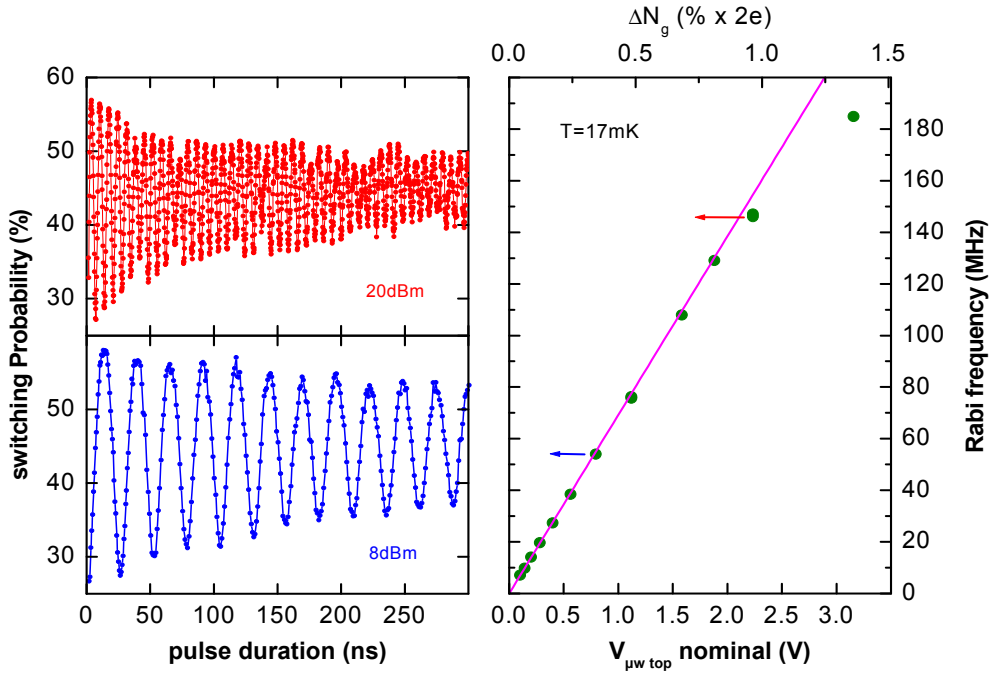

Figure 3.4: Left: Rabi oscillations for two different microwave powers. Right: the Rabi frequency depends linearly on the microwave amplitude as expected for the excitation of a transition between two discrete energy levels. The discrepancy at Rabi frequencies higher than 150MHz comes from the saturation of the microwave mixers.

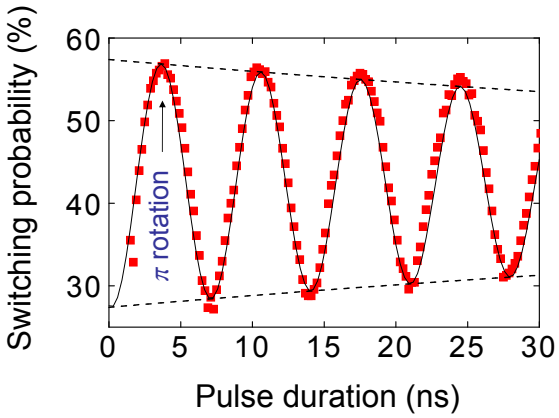

Figure 3.5: A typical π rotation takes a time $\lesssim$ 4ns. The decay of the Rabi oscillations is related to the decoherence during driven evolution. This phenomenon introduces errors into any rotation which can be estimated by fitting the decay and using the simple model of the readout described in section 2.20. The error is $\approx 0.3\%$/ns of rotation. After a π rotation of typical duration 4ns, the qubit state is thus represented by a density matrix ρ with $\rho_{11} \approx 0.99$ and $\rho_{00} \approx 0.01$.

of duration $\approx$ 4ns, is described by a density matrix ρ with $\rho_{11} \approx 0.99$, $\rho_{00} \approx 0.01$, $\rho_{10} = 0$, and $\rho_{01} = 0$. The fidelity is thus $\approx 99\%$.

3.2 Combination of rotations: Ramsey experiments

Any one qubit operation $\widehat{U}$ can be decomposed into the product of 3 rotations around two perpendicular axes such as the X and Y axes [64]. As a consequence, there exist real numbers: $\alpha, \beta, \gamma, \delta$ such that:

$$\widehat{U} = e^{i\alpha} R_x(\beta) \circ R_y(\gamma) \circ R_x(\delta).$$

The ability to properly combine several rotations is thus an important issue for implementing an arbitrary single qubit gate. The aim of this section is to demonstrate that rotations around either the X and the Y axes are achievable and that they can be combined together. For this purpose, a Ramsey experiment based on a well known manipulation sequence in atomic physics and NMR is performed.

The Ramsey experiment combines two excitation pulses separated by a tunable delay and gives the most precise way to compare the frequency of an excitation source with the transition frequency of a two-level system. For instance, this sequence is used in atomic clocks for defining the time reference.

In our case, a Ramsey sequence constitutes the simplest experiment for probing the free evolution of the qubit in the time domain.

3.2.1 Principle

A first $\pi/2$ pulse around the axis $\overrightarrow{u}_1$ defined by the microwave phase χ_1 is applied to the qubit and bring the vector state in the equatorial plane where it precesses around the detuning field at the Ramsey frequency $\delta\nu$ (see Fig. 3.6). During this free evolution, a phase $\phi(t) = \int \Delta\nu dt'$ is accumulated between state $|1\rangle$ and state $|0\rangle$.

After a time t of free evolution, a second $\pi/2$ pulse around the axis $\overrightarrow{u}_2$ defined by χ_2 is applied. This pulse converts the information about the phase $\phi(t)$ into a change of the population of state $|1\rangle$ which is then measured. At the end of the sequence, the probability for the qubit to be in state $|1\rangle$ is thus

$$P_1(t) = \cos^2\left(\frac{\phi(t) + (\chi_1 - \chi_2)}{2}\right).$$

P_1 oscillates with time t, at the Ramsey frequency, as a consequence of the free precession of the qubit between the two pulses. The phase of the Ramsey oscillations is given by the difference between the microwave phases of the two $\pi/2$ pulses.

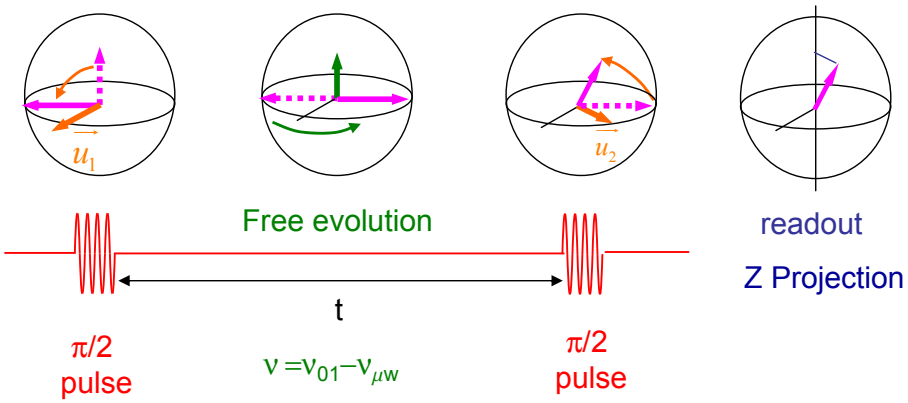

Figure 3.6: The Ramsey sequence is the simplest sequence revealing the free evolution of the qubit in the time domain. It consists of two $\pi/2$ pulses separated by a free evolution period of duration t. During the free precession, state $|1\rangle$ accumulates a phase $\phi(t) = \int \Delta\nu dt$ with respect to state $|0\rangle$. The second $\pi/2$ pulse converts the information about ϕ into the population of state $|1\rangle$, which is then measured.

3.2.2 Experimental results

The switching probability of the readout junction is plotted on fig. 3.7 for different combinations of two $\pi/2$ rotations around two of the four axes: X,-X,Y and -Y.

The switching probability of the readout junction oscillates at the Ramsey frequency as predicted and the Ramsey pattern is phase shifted by the difference of microwave phase between the two $\pi/2$ pulses, as expected, which proves that the two rotations combine properly. However, one can notice sudden phase shifts that we assume to be due sudden jumps of the transition frequency of the qubit due to charge two level fluctuators (see chapter 4). We'll see in section 3.4, how it is possible to decrease the sensitivity of an operation to such errors.

One can also notice a slight decay of the contrast of the Ramsey fringes, which is related to the decoherence during free evolution (see chapter 4).

Nevertheless, the fact that combinations of rotations combine as expected at least qualitatively shows that any single qubit operation can be achieved.

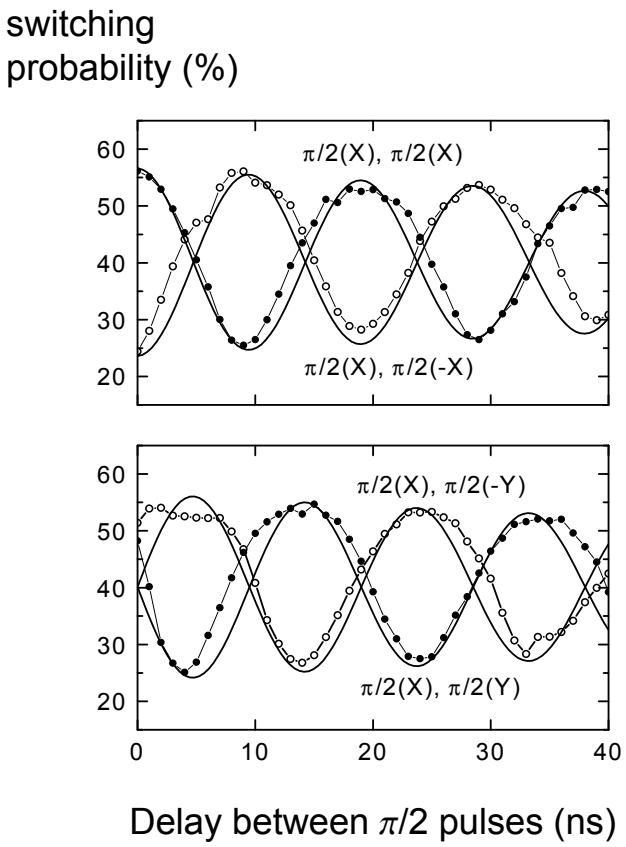

Figure 3.7: Combination of rotations around the X,-X,Y, and -Y axes. The Ramsey patterns are shifted by the expected dephasing proving that the rotations combine together properly. The sudden phase shifts are assumed to be due to small frequency drifts of the transition frequency of the qubit.

3.3 Manipulation of the quantum state with adiabatic pulses: Z rotations

Any rotation around the Z axis can be implemented by applying three microwave induced rotations around the X and Y axes (see section 3.4.1):

$$R_Z(\theta) = R_X(\frac{\pi}{2}) \circ R_Y(\theta) \circ R_{\overline{X}}(\frac{\pi}{2}).$$

But it can be implemented in a simpler way by a period of free evolution in the rotating frame with a finite fixed frequency detuning. By controlling the detuning $\Delta\nu(N_g, \delta)$ of the transition frequency with adiabatic pulses on the parameters N_g or δ, one can control the speed of precession around the Z axis. The qubit is therefore moved away from the optimal working P_0 to a working point $P = (N_g, \delta)$ for a certain time t so that an extra rotation of angle

$$\theta = 2\pi \int \Delta\nu(N_g, \delta) dt'^{t}_{0},$$

is achieved around Z.

3.3.1 Principle

As described in chapter 4, the sensitivity of the qubit to charge noise is higher than to phase noise. As a result, only Z rotations coming from a detuning of the working point in the phase direction are considered. For changing the phase $\delta = \delta_m + \gamma$ at a fast enough speed, one cannot use the coil which controls δ_m since the bandwidth is not sufficient ($\approx$ 100Hz). As a consequence, a biasing current I_b into the readout junction is used and sets the phase across the readout junction to $\gamma = \arcsin(I_b/I_c)$. Due to a limited bandwidth of 100MHz, we use triangular pulses. During this pulse, an extra phase builds up between state $|0\rangle$ and $|1\rangle$, whose total value is at the end of the current biasing pulse:

$$\zeta = 2\pi \int \delta\nu_{01}(N_g, \delta(t)) dt.$$

Near the optimal working point, the dependance of $\delta\nu_{01}$ with δ can be approximated with a 1% accuracy by a parabolic function: $\delta\nu_{01} \approx -\alpha\delta^2$ with $\alpha = 1.66\text{GHz/rad}^2$ (sample A), over the range $[-\pi/2, \pi/2]$. Using the prebias technique, the value of δ for a biasing current I_b is expected to be:

$$\delta = \arcsin(\frac{I_b}{I_c}) - \arcsin(\frac{I_{pb}}{I_c}) \approx \frac{\Delta I}{\sqrt{I_c^2 - I_{pb}^2}},$$

where I_{pb} is the current during the prebias plateau, I_b is the biasing current during the detuning pulse, and $\Delta I = I_b - I_{pb}$.

The predicted extra phase for a triangular detuning pulse of maximum amplitude ΔI and total duration τ is thus:

$$\zeta = \frac{2\pi}{3}\alpha\frac{\Delta I^2}{I_c^2 - I_{pb}^2}\tau.$$

This current detuning pulse is inserted into a Ramsey sequence (see fig. 3.8) for probing the extra phase factor ζ.

Note that the current pulse has to fullfil the adiabaticity criterion:

$$|d\lambda/dt\langle 1|\partial\widehat{H}_{qb}/\partial\lambda|0\rangle|/(\hbar\omega_{01}) \ll \omega_{01},$$

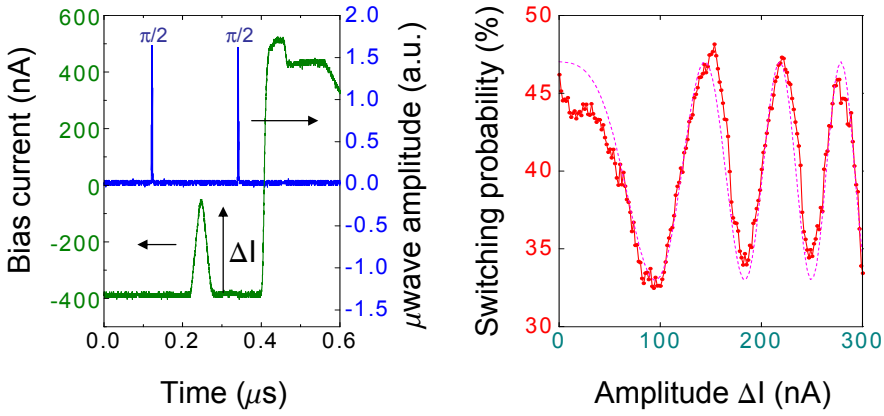

Figure 3.8: Rotation around the Z axis with a detuning pulse. Left: a current pulse changes adiabatically the transition frequency during a Ramsey sequence. Top: during triangular adiabatic current pulse, the working point is moved away from ($\delta = 0, N_g = 1/2$) in the phase direction and put back. Right: The switching probability oscillates with the amplitude of the current detuning pulse which renders the rotation of the qubit around the Z axis. The experimental curve is fitted (dashed line) by taking into account the parabolic dependance of ν_{01} with δ. The maximum contrast of the signal has been optimized and is lower than during a Rabi. We attribute this discrepancy to errors on the microwave pulses durations.

with $\lambda = \delta$. This is indeed the case for the typical set of parameters: $\langle 1|\partial \widehat{H}_{qb}/\partial\delta|0\rangle/\varphi_0 = \langle 1|\widehat{I}|0\rangle < 10nA$ and $d\delta/dt < 40$Mrad/s, which give

$$|d\lambda/dt\langle 1|\partial \widehat{H}_{qb}/\partial\lambda|0\rangle|/(\hbar\omega_{01}) \approx 10^8 \ll \omega_{01} \approx 10^{11}.$$

3.3.2 Experimental setup and results

The adiabatic detuning pulse is generated by an Agilent 33250 arbitrary waveform generator and is added to the readout pulse, with a combiner.

The experimental results are plotted on figure 3.8. The switching probability of the readout junction oscillates as the amplitude of the current bias ΔI is increased, as a consequence of the rotation of the vector state around the z axis. The experimental curve is fitted by the function

$$\cos\zeta = \cos\left(\frac{2\pi}{3}\alpha\frac{\Delta I^2}{I_c^2 - I_{pb}^2}\tau\right),$$

where the parameters $\alpha = 1.66$GHz/rad^2, $I_c = 445$nA$\pm$20nA, have been measured by previous experiments, and where $I_{pb} = 330$nA and $\tau = 50$ns are set experimentally.

We now discuss how to improve the robustness of a rotation with respect to experimental imperfections.

3.4 Implementation of more robust operations

The manipulation and the evolution of the qubit state is very sensitive to random errors arising from decoherence processes (see chapter 4). But, systematic errors coming from reproducible imperfections of the microwave pulses can affect also the manipulation of the qubit state. The accuracy of a single-qubit operation is indeed very sensitive to imperfections of the driving field used. For instance, a Rabi pulse implementing a rotation of the vector state on the Bloch sphere is characterized by the Rabi frequency ν_R given by the microwave amplitude, its duration τ, and by the detuning $\Delta\nu$ and the phase χ. Errors

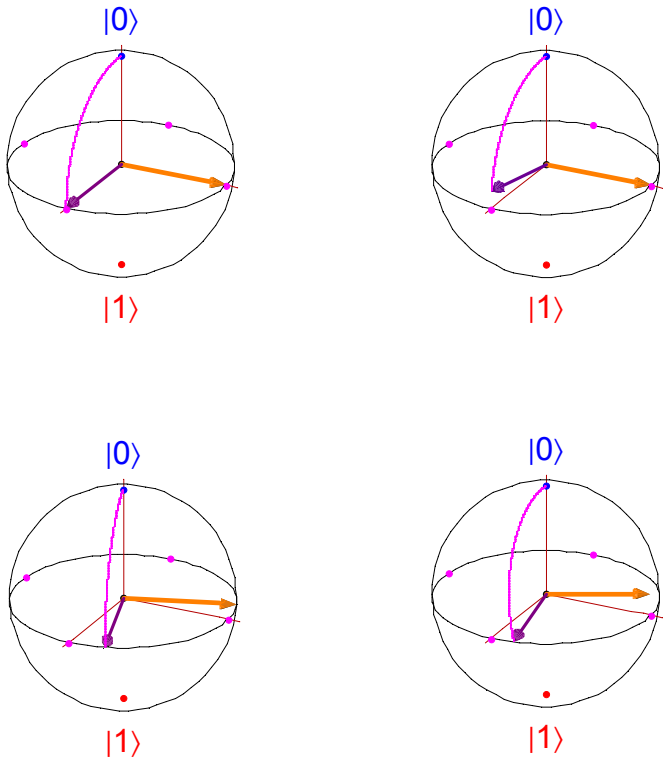

Figure 3.9: Errors during the implementation of a $\pi/2$ rotation around the Y axis starting from the initial state $|0\rangle$. Top left: ideal rotation. Top right: 10% error on the pulse duration. Bottom left: 20° error on the microwave phase. Bottom right: error on the excitation frequency ($\Delta\nu = 0.2\nu_{R0}$ error).

on these quantities are directly translated into errors on the axis and on the angle of the rotation. A frequency offset, coming from fluctuations of the transition frequency of the qubit (see Fig. 3.7) affects both the axis and the angle of the rotation, whereas an error on the microwave phase will affect only the axis of the rotation. Fig. 3.9 illustrates these different errors in the case of a $\pi/2$ rotation around the Y axis.

3.4.1 Composite rotations

As previously mentionned, any rotation can be decomposed into the product of three rotations around two perpendicular axes. As a consequence, there are many equivalent ways to implement the same operation on the Bloch sphere. These different ways can however have different sensitivities to pulses imperfections. Indeed, in NMR, sequences made of several rotations, called composite sequences, have demonstrated being less sensitive than single pulse operation to systematic errors. The idea is that the systematic error affecting a single pulse can cancel during the concatenation of several pulses adequately chosen [45, 65]. At first sight, one could think that a composite sequence just redistributes the errors on the Bloch sphere so that the sensitivity to imperfections is decreased compared to a single rotation only for some particular initial states. This is indeed the case for most of the composite rotations used in NMR, where a compensation of imperfections is only needed for particular initial states.

But surprisingly, there exist also composite sequences of pulses whose sensitivity to imperfections is lower compared to a single rotation for every initial state on the Bloch sphere, which is a crucial requirement of quantum computing.

First, we will quantify the difference between an ideal unitary operation and its practical implementation.

3.4.2 Fidelity of unitary operations

For quantifying the effect of systematic errors, we will define the fidelity between an ideal operation and its practical implementation. First, one can notice that, contrary to random errors caused by the decoherence for instance, systematic errors does not affect the unitary character of an ideal rotation.

Having a particular initial state $|a\rangle$, and two unitary operations $\widehat{U_1} = R_{\overrightarrow{u_1}}(\alpha_1) = \exp(i\overrightarrow{u_1}.\overrightarrow{\widehat{\sigma}}\,\alpha_1/2)$ and $\widehat{U_2} = R_{\overrightarrow{u_2}}(\alpha_2) = \exp(i\overrightarrow{u_2}.\overrightarrow{\widehat{\sigma}}\,\alpha_2/2)$, one can quantify the difference between the final states $|b\rangle = \widehat{U_1}|a\rangle$ and $|c\rangle = \widehat{U_2}|a\rangle$ with the hermitian product:

$$hp(|a\rangle) = \langle b|c\rangle = |\langle a|\widehat{U}_2^\dagger \widehat{U}_1|a\rangle|.$$

If hp is equal to one, then $|b\rangle$ and $|c\rangle$ are equal up to a phase factor. If $hp < 1$, the difference of hp with 1 quantifies the discrepancy between the final states of $\widehat{U}_1$ and $\widehat{U}_2$ applied to the same particular state $|a\rangle$.

By using the general formula:

$$(\overrightarrow{\widehat{\sigma}}.\overrightarrow{u_1})(\overrightarrow{\widehat{\sigma}}.\overrightarrow{u_2}) = \overrightarrow{u_1}.\overrightarrow{u_2} + i\overrightarrow{\widehat{\sigma}}.(\overrightarrow{u_1}\wedge\overrightarrow{u_2}),$$

the hermitian product hp can be expressed for any initial state as a function of the angles and of the vectors $\overrightarrow{u_1}$ and $\overrightarrow{u_2}$ of the rotations $\widehat{U}_1$ and $\widehat{U}_2$:

$$hp(|a\rangle) = i\left[\cos(\tfrac{\alpha_1}{2})\sin(\tfrac{\alpha_2}{2})\overrightarrow{u_2} - \sin(\tfrac{\alpha_1}{2})\cos(\tfrac{\alpha_2}{2})\overrightarrow{u_1} + \sin(\tfrac{\alpha_2}{2})\sin(\tfrac{\alpha_1}{2})\overrightarrow{u_1}\wedge\overrightarrow{u_2}\right].\overrightarrow{a}$$

$$+\tfrac{1}{2}Tr(\widehat{U}_2^\dagger\widehat{U}_1).$$

with

$$Tr(\widehat{U}_2^\dagger\widehat{U}_1) = 2\left[\cos(\frac{\alpha_1}{2})\cos(\frac{\alpha_2}{2}) + \sin(\frac{\alpha_1}{2})\sin(\frac{\alpha_2}{2})\overrightarrow{u_1}.\overrightarrow{u_2}\right].$$

We can now define the averaged fidelity between two rotations, which does not depend on the initial state:

$$F(U_1,U_2) = \overline{|\langle a|U_2^\dagger U_2|a\rangle|} = \frac{|Tr(U_2^\dagger U_1)|}{2},$$

where the average is taken over all initial states $|a\rangle$.

Since quantum error correcting codes need for working a single qubit gate accuracy of $1 - F < 10^{-4}$ in the best case, the issue of implementing robust gates is thus crucial.

In the following, we use the algebra of quaternions to calculate F in the case of composite rotations.

Quaternions and rotations of the qubit state

The quaternion corps give another representation of rotations which is more convenient than the Pauli matrices for calculating composition of rotations.

A rotation of angle θ around a unitary axis $\overrightarrow{u}$ is represented by a 4−component vector $q = \{s, \overrightarrow{v}\}$, where $s = \cos\theta/2$ and $\overrightarrow{v} = \overrightarrow{u}\sin\theta/2$.

For instance, a $\pi/2$ rotation around the X axis is given by the quaternion: $q = (1/\sqrt{2}, 1/\sqrt{2}, 0, 0)$, whereas a π rotation around X has the quaternion: $q = (0, 1, 0, 0)$.

The composition of two rotations can then be easily calculated by multiplying quaternions according to the product rule:

$$q_1 * q_2 = \{s_1.s_2 - \overrightarrow{v_1}.\overrightarrow{v_2}, s_1\overrightarrow{v_2} + s_2\overrightarrow{v_1} + \overrightarrow{v_1} \wedge \overrightarrow{v_2}\}.$$

As an example, the combination of the three rotations: $R_{-x}(\pi/2) \circ R_y(\theta) \circ R_x(\pi/2)$ can be easily calculated and gives $R_z(\theta)$.

Then, to quantify the difference between an ideal rotation and its practical implementation, one uses the quaternion fidelity, which is defined by:

$$F(\overrightarrow{q_1}, \overrightarrow{q_2}) = |\overrightarrow{q_1}.\overrightarrow{q_2}| = |s_1.s_2 + \overrightarrow{v_1}.\overrightarrow{v_2}|,$$

and is equal to the average fidelity defined for two operators $F(\widehat{U_1}, \widehat{U_2})$.

A fidelity of 1 means that the two quaternions q_1 and q_2 correspond to the same rotation, up to a phase factor.

As an example, one can compare an ideal π rotation around X with the same rotation having an error on the excitation frequency: $\epsilon = \Delta\nu/\nu_{R0}$, where ν_{R0} is the Rabi frequency on resonance. The corresponding quaternions are given by:

$$q_1 = (0, 1, 0, 0)$$

and

$$q_2 = \left[\cos(\pi/2\sqrt{1+\epsilon^2}), \sin(\pi/2\sqrt{1+\epsilon^2})/\sqrt{1+\epsilon^2}, 0, \epsilon\sin(\pi/2\sqrt{1+\epsilon^2})/\sqrt{1+\epsilon^2}\right].$$

The fidelity between q_1 and q_2 is:

$$F(\epsilon) = \frac{\sin(\pi/2\sqrt{1+\epsilon^2})}{\sqrt{1+\epsilon^2}} \approx 1 - \frac{\epsilon^2}{2},$$

which is plotted on fig. 3.10. Around $\epsilon = 0$, the fidelity thus scales at second order with ϵ.

In the following, we will focus on off-resonance errors and we'll see that the fidelity of a composite pulse sequence coming from NMR, the CORPSE sequence, scales like ϵ^4.

3.4.3 The CORPSE sequence

The CORPSE sequence, which means Compensation for Off Resonance with a Pulse Sequence, was developed in the context of NMR [65]. It is used for applying the same rotation $R_x(\theta)$ to different spins even if they have different transition frequencies.

In the quantronium case, the CORPSE sequence can reduce strongly the sensitivity of an operation to frequency detuning of the qubit, caused by low frequency fluctuations of ν_{01}.

The CORPSE sequence is composed of the three subsequent rotations: $R_x(\theta_1)$, then $R_{-x}(\theta_2)$ and finally $R_x(\theta_3)$. For any rotation $R_x(\theta)$, there exist several sets of angles $\{\theta_1, \theta_2, \theta_3\}$ for which the CORPSE sequence implements the rotation $R_x(\theta)$. The angles can be calculated with the quaternion product and are given by the formulas [65]:

$$\theta_1 = 2n_1\pi + \frac{\theta}{2} - \arcsin\left(\frac{\sin\theta/2}{2}\right)$$

$$\theta_2 = 2n_2\pi - 2\arcsin\left(\frac{\sin\theta/2}{2}\right)$$

$$\theta_3 = 2n_3\pi + \frac{\theta}{2} - \arcsin\left(\frac{\sin\theta/2}{2}\right)$$

where n_1, n_2, n_3 are integers. It can be shown [65] that the fidelity of the CORPSE sequence compared with the ideal rotation $R_x(\theta)$ does depend on ϵ only at fourth order, and that the behavior of the ϵ^4 term is only determined by $n_1 - n_2 + n_3$ which is the number of turns additional to the desired rotation around the X axis. The ϵ^4 term is then minimum for $n_1 - n_2 + n_3 = 0$.

We have experimentally tested the CORPSE sequence in the particular case of the implementation of a NOT operation.

3.4.4 Implementation of a robust NOT operation

The CORPSE sequence has been tested and compared to a single π rotation.

The integers n_i were chosen such that $n_1 = n_2 = 1$ and $n_3 = 0$, which gives the angles $7\pi/3_X, 5\pi/3_{-X}, \pi/3_X$ for the different rotations. The fidelities of the CORPSE sequence and of a real π rotation with respect to an ideal π rotation are plotted as a function of the frequency detuning on figure 3.10.

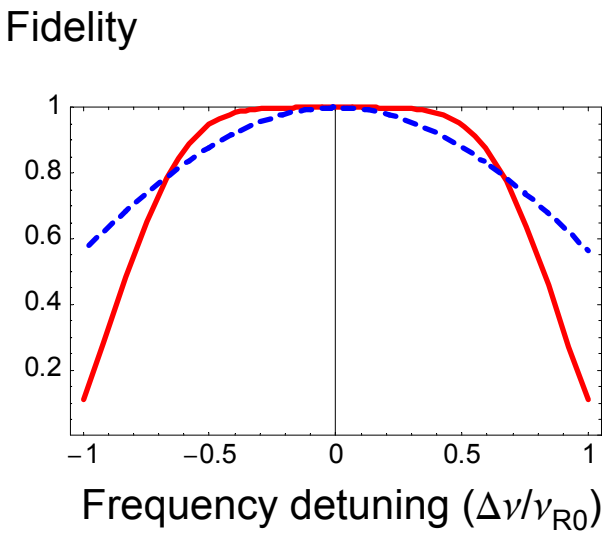

Figure 3.10: The fidelity of π rotation with a single pulse as a function of the frequency error $\epsilon = \Delta\nu/\nu_{R0}$ is plotted in dashed. The fidelity scales like ϵ^2 around $\epsilon = 0$. In plain is plotted the theoretical fidelity for the CORPSE sequence, which scales like ϵ^4.

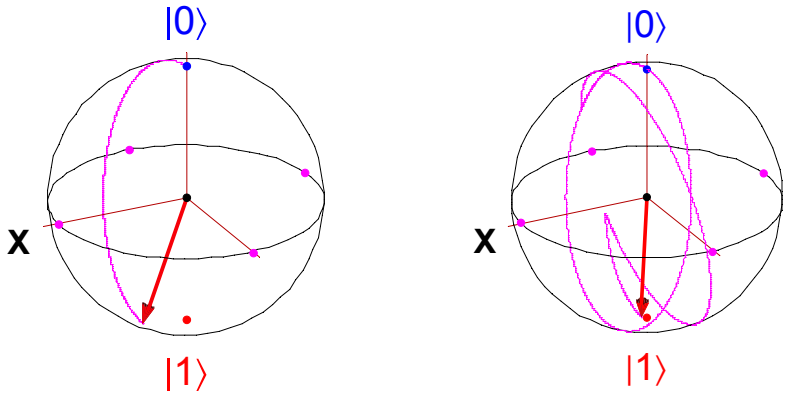

Figure 3.11: Comparison between the trajectory of the vector state during a simple π rotation (left) for a detuning of 20MHz and a Rabi frequency of 100MHz, and the corresponding case of the CORPSE sequence (right).

The fidelity of the standard π pulse has a ϵ^2 behavior as previously described, whereas the CORPSE fidelity scales like:

$$1 - \alpha\epsilon^4 - \beta\epsilon^6,$$

with $\alpha = 0.003$, and $\beta = 4.9$, for the considered sequence $(7\pi/3_x, 5\pi/3_{-x}, \pi/3_x)$. As a consequence, for an error of 10^{-4}, the maximum acceptable detuning for the CORPSE sequence is 16% of ν_{R0} whereas for a single Rabi pulse, it is only 1.5% of ν_{R0}.

For the typical parameters: $\nu_{R0} \approx 100$MHz and a maximum frequency fluctuation $\Delta\nu \lesssim 10MHz$, one can estimate the different errors expected. For the CORPSE: $1 - F \lesssim 5.10^{-6}$ whereas for the standard π rotation $1 - F \lesssim 5.10^{-3}$.

The error due to a frequency detuning is thus greatly reduced by the CORPSE sequence. To illustrate this, on fig. 3.11 is plotted the trajectory of the vector state on the Bloch sphere in the case of a π rotation and of a CORPSE sequence both applied to the ground state.

Experimental results

We have first compared the CORPSE sequence and a standard π pulse for the same initial state: $|0\rangle$.

It happens that in this particular case, the probability P_1 for the qubit to be in state $|1\rangle$ after each operation is rigorously equal to the square of the fidelity, F^2, of the considered operation. By measuring P_1, one gets the fidelity of the CORPSE sequence compared to an ideal π rotation.

The switching probability of the readout junction is then measured after each sequence and as a function of the frequency detuning (see fig. 3.12). As expected, the efficiency of the CORPSE sequence is better than those of a standard π pulse since the switching probability stays close to its maximum over a wider frequency range.

Then, we have checked that the CORPSE sequence was implementing a NOT operation for every initial state, by performing the sequence after an arbitrary rotation $R_{\overline{x}}(\theta)$. The experimental results are plotted on figure 3.12, the switching probability for the combination of the rotation $R_{\overline{x}}(\theta)$ and of the

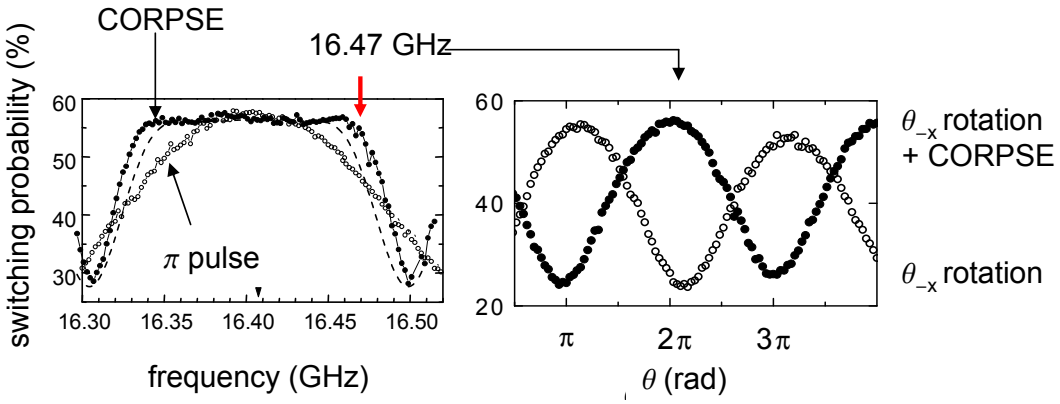

Figure 3.12: NOT operation is implemented with a standard π pulse and with a CORPSE sequence, on the quantronium whose transition frequency is 16.402GHz. Left: switching probabilities after a CORPSE sequence and a π pulses. The sensitivity of the CORPSE sequence to frequency detuning is smaller since the switching probability stays close to its maximum over a larger frequency range than for the π pulse. The theoretical prediction for the CORPSE sequence is represented in dash. Right: for a 70MHz detuning, a sequence of a CORPSE with an additionnal rotation of tunable angle θ around the $-X$ axis (full points), is applied and compared with the θ rotation alone (open points). The two switching probabilities oscillates in phase opposition as expected for a NOT operation. One can notice however a slight phase shift possibly due to pulse length errors.

CORPSE sequence oscillates qualitatively in phase opposition with the rotation $R_{\overline{x}}(\theta)$ alone, as predicted for a NOT operation. However, one can notice a slight phase shift that is assumed to be due to pulse length errors.

The CORPSE sequence thus implement a NOT operation for every initial state on the Bloch state, and not only for state $|0\rangle$.

3.5 Conclusion

The quantum state of the qubit can be efficiently manipulated with non-adiabatic AC resonant pulses and adiabatic pulses. The evolution of the qubit is equivalent to the one of a spin 1/2 precessing in a static magnetic field. Any rotation of the state vector on the Bloch sphere can be achieved, and as a consequence any one-qubit operation. The error rate of single qubit operations has been estimated: $\approx 1\%$ for a fast single π rotation. It is far from the fidelity achieved with trapped ions.It will be shown in the next chapter that this error rate is dominated by random errors coming from the decoherence during the driven evolution of the qubit. Another source of errors coming from the imperfections of the manipulation pulses has been characterized. These systematic errors are not the dominant one for the moment for our qubit. However, it has been shown that the sensitivity to these systematic errors could be decreased by using composite sequences coming from NMR. In addition, these composite sequences are also efficient for compensating the effects of slow fluctuations of the transition frequency the qubit, slower than the duration of the composite sequence.

The fidelity of an operation remain to be probed with a better precision, and for this purpose, a high fidelity readout would be of great interest.

NMR-like Control of a Quantum Bit Superconducting Circuit

E. Collin, G. Ithier, A. Aassime, P. Joyez, D. Vion, and D. Esteve

Quantronics group, Service de Physique de l'Etat Condensé, DSM/DRECAM, CEA Saclay, 91191 Gif-sur-Yvette, France

(Received 17 March 2004; published 6 October 2004)

Coherent superpositions of quantum states have already been demonstrated in different superconducting circuits based on Josephson junctions. These circuits are now considered for implementing quantum bits. We report on experiments in which the state of a qubit circuit, the quantronium, is efficiently manipulated using methods inspired from nuclear magnetic resonance (NMR): multipulse sequences are used to perform arbitrary operations, to improve their accuracy, and to fight decoherence.

DOI: 10.1103/PhysRevLett.93.157005 PACS numbers: 85.25.Cp, 03.67.Lx, 74.50.+r, 74.78.Na

Despite progress in the development of quantum bit (qubit) electronic circuits, the complexity and robustness of the operations that have been performed on them are presently still too primitive for demonstrating quantum computing (QC) [1]. Presently, the most advanced qubit circuits are superconducting ones based on Josephson junctions. The preparation of coherent superpositions of the two states of a qubit has already been demonstrated for several circuits [2–9], and a two qubit gate was operated [10]. However, qubit operations are far less developed for qubit circuits than for atoms or spins. In this Letter, we report on experiments that successfully manipulate a Josephson qubit based on the quantronium circuit [11], using NMR methods. We demonstrate that any transformation of the qubit can be implemented, that they can be made robust, and that decoherence can be fought. Note that using NMR methods for qubit manipulation does not bring in the intrinsic limitations of QC with nuclear spins, such as the lack of scalability, because in this approach the NMR sequence is applied to a single distinguishable qubit, not to an ensemble.

The quantronium circuit, described in Fig. 1, is derived from the Cooper pair box [12,13]. It consists of a superconducting loop interrupted by two adjacent small Josephson tunnel junctions with Josephson energy $E_J/2$ each, and by a larger Josephson junction ($E_{J0} \approx 15E_J$) for readout. The island between the small junctions, with total capacitance C_Σ and charging energy $E_C = (2e)^2/2C_\Sigma$, is biased by a voltage source U through a gate capacitance C_g. The characteristic energies measured in the present sample are $E_J = 0.87k_B$ K and $E_C = 0.66k_B$ K. Experiments are performed at 20 mK using filtered lines. The eigenstates of this system are determined by the dimensionless gate charge $N_g = C_gU/2e$, and by the superconducting phase $\delta = \gamma + \phi$ across the two small junctions, where γ is the phase across the large junction and $\phi = \Phi/\varphi_0$, with Φ the external flux through the loop and $\varphi_0 = \hbar/2e$. The two lowest energy states $|0\rangle$ and $|1\rangle$ form a two-level system suitable for a qubit. At the optimal working point ($\delta = 0, N_g = 1/2$), the transition frequency ν_{01} is stationary with respect to changes in the control parameters, which makes the quantronium insensitive to noise at first order [3,11]. For the sample investigated, $\nu_{01} \simeq 16.40$ GHz at the optimal working point. For readout, $|0\rangle$ and $|1\rangle$ are discriminated through the difference in their supercurrents in the loop [3]. A trapezoidal readout pulse $I_b(t)$ with a peak value slightly below

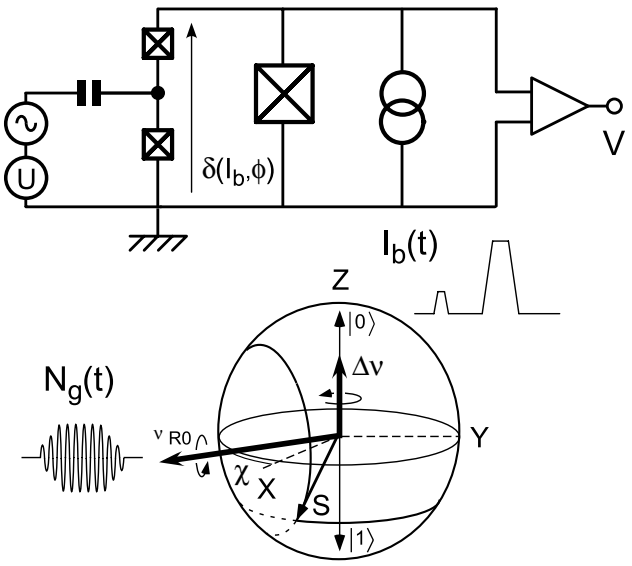

FIG. 1. Top: quantronium circuit. The Hamiltonian is controlled by the gate charge N_g applied to the island between the two small junctions, and by the phase δ across their series combination. This phase is determined by the flux ϕ through the loop, and by the bias current I_b. The two lowest energy states form a two-level system suitable for a qubit. The readout is performed by inducing the switching of the larger readout junction to a finite voltage V with a bias-current pulse $I_b(t)$ approaching the critical current of this junction. Bottom: The quantum state is manipulated by applying resonant microwave pulses (phase χ) on the gate, or adiabatic pulses on the bias current. These pulses induce a rotation of the effective spin $\vec{S}$ representing the qubit state on the Bloch sphere in the rotating frame. The Rabi precession of $\vec{S}$ during a microwave pulse results in oscillations of the switching probability p with the pulse length τ.

the critical current $I_0 = E_{J0}/\varphi_0 \simeq 450$ nA is applied so that the switching of the large junction to a finite voltage state is induced with a large probability p_1 for state $|1\rangle$ and with a small probability p_0 for state $|0\rangle$. The switching is detected by measuring the voltage across the readout junction, and p is determined by repeating the experiment a few 10^4 times. The fidelity η of the measurement is the largest achieved value of $p_1 - p_0$.

The manipulation of the qubit state is achieved by applying time dependent control parameters $N_g(t)$ and $I_b(t)$. When a nearly resonant microwave modulation $\Delta N_g \cos(2\pi\nu_{\mu w}t + \chi)$ is applied to the gate, the Hamiltonian described in a frame rotating at the microwave frequency $h = -\vec{H}\cdot\vec{\sigma}/2$ is that of a spin 1/2 in an effective magnetic field $\vec{H} = h\Delta\nu\vec{z} + h\nu_{R0}[\vec{x}\cos\chi + \vec{y}\sin\chi]$, where $\Delta\nu = \nu_{\mu w} - \nu_{01}$ is the detuning, and $\nu_{R0} = 2E_C\Delta N_g\langle 1|\hat{N}|0\rangle/h$ the Rabi frequency. At $\Delta\nu = 0$, Rabi precession takes place around an axis lying in the equatorial plane, at an angle χ with respect to the X axis. Rabi precession induces oscillations of the switching probability p with the pulse duration [3]. The range of Rabi frequencies ν_{R0} that could be explored extends above 250 MHz, and the shortest π pulse duration for preparing $|1\rangle$ starting from $|0\rangle$ was less than 2 ns. The fidelity was $\eta \simeq 0.3$–0.4 for readout pulses with 100 ns duration at the optimal value of δ at readout. This fidelity might be improved using rf methods that avoid switching to the voltage state [14].

In order to perform arbitrary operations on the qubit, one has to combine rotations around different axes [1], i.e., pulses with different phases. For that purpose, a continuous microwave signal is divided on two lines, one being phase shifted as desired. Both lines are fed to mixers controlled by dc pulses, and then recombined and applied to the gate. In Fig. 2, measurements of the switching probability p following two-pulse sequences combining $\pi/2$ rotations around the axes $X, Y, -X$, or $-Y$, are shown. Theory predicts that p oscillates at frequency $\Delta\nu$ with the delay Δt between pulses. This experiment is analogous to the Ramsey experiment in atomic physics, and to the free induction decay in NMR. When the two pulses have different phases χ_1 and χ_2, the Ramsey pattern is phase- shifted by $\chi_2 - \chi_1$. Despite the presence of spurious frequency jumps due to individual charge fluctuators near the island, the overall agreement for the phase shift of the Ramsey pattern demonstrates that rotations around axes X and Y combine as predicted. Arbitrary unitary transformations can thus be performed. Rotations around the Z axis can, however, be more readily performed by changing the qubit frequency for a short time. A triangular bias-current pulse with maximum amplitude ΔI is applied in a Ramsey experiment. During this detuning pulse, a phase difference $\zeta = 2\pi\int\delta\nu_{01}(t)dt$ builds up between the qubit states, which is equivalent to a rotation around the Z axis with an angle ζ. The Ramsey pattern is phase shifted

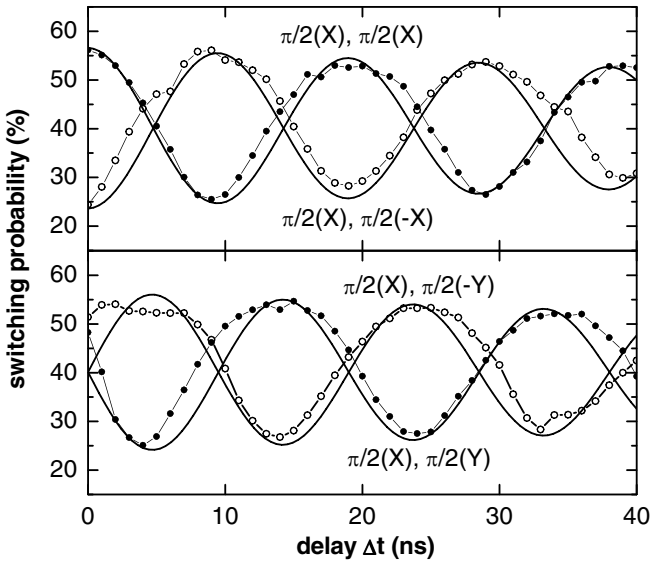

FIG. 2. Switching probability after two $\pi/2$ pulses with detuning $\Delta\nu = +52$ MHz, and with different phases corresponding to rotation axes X, Y, $-X$, or $-Y$, as a function of the delay between the pulses. The solid lines are fits including a finite decay time of 250 ns. The Ramsey patterns are phase shifted as predicted for the different combinations of rotation axes.

by ζ as shown by the oscillations of p with ΔI (right panel of Fig. 3).

The accuracy and robustness of these qubit operations are also important issues. In NMR, composite pulse methods have been developed to make such manipulations less sensitive to rf pulse imperfections [15,16]. In the case of the CORPSE sequence (compensation for off-resonance with a pulse sequence), the sensitivity to de-

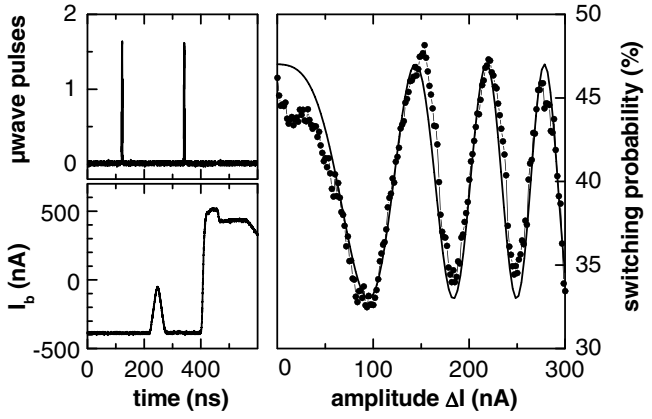

FIG. 3. Demonstration of rotations around the Z axis. Left: a triangular bias-current pulse applied between the two pulses of a Ramsey sequence induces a frequency change, and thus a phase shift between the two qubit states. Right: this phase shift, equivalent to a rotation around the Z axis, results in oscillations of the switching probability p (symbols) with the pulse amplitude ΔI. The fit (thick line) uses the measured dependence of the transition frequency with the phase δ.

tuning is strongly reduced, the error starting at fourth order. We have tested this sequence in the case of a π rotation around the X axis, which performs a NOT operation on the qubit. The corresponding CORPSE $\pi(X)$ pulse sequence is $\{7\pi/3(X), 5\pi/3(-X), \pi/3(X)\}$ [15]. As shown in Fig. 4, it is significantly more robust against detuning than a single pulse $\pi(X)$ since the switching probability stays close to its maximum value over a larger frequency range, comparable to the Rabi frequency. By performing the CORPSE sequence after an arbitrary rotation $\theta(-X)$, we have also checked that the sequence works for a general initial state.

Another major concern of qubit circuits is to improve quantum coherence, which is limited by relaxation and dephasing. The relaxation time T_1 was 500 ± 50 ns at the optimal working point. The lifetime of coherent superpositions is given by the decay of the Ramsey oscillations. This decay was close to exponential with $T_2 = 300 \pm 50$ ns for the present sample at the optimal working point (see top panel of Fig. 5), showing that dephasing dominates decoherence. T_2 becomes progressively shorter when the working point is moved away [3]. NMR concepts are again useful for fighting decoherence. First, the well known spin-echo technique [17] suppresses the effect of slow variations of the qubit frequency [5]. By inserting a π pulse in the middle of a Ramsey sequence, the random phases accumulated during the two free evolution periods before and after the π pulse cancel provided that the perturbation is almost static on the time scale of the sequence. The echo method thus provides a simplified form of error correction between an initial time and a final one. As shown in Fig. 5 (middle panel), we have recorded echoes, and the echo minimum at the nominal echo position as a function of the total sequence duration. The small residual oscillations on the echo mimimum result from the finite duration of the pulses and from a slight residual detuning, and simulations taking these effects into account, show that the echo decay time T_E is the decay time of the envelope of these oscillations. At the optimal point, we find $T_E = 550 \pm 50$ ns $\sim 2T_2$, which agrees with the prediction for the second order contribution of the charge noise, propor-

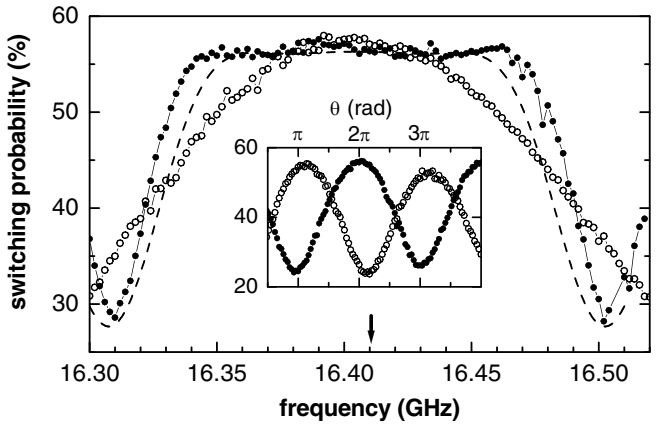

FIG. 4. Demonstration of the robustness of a composite pulse with respect to frequency detuning: switching probability after a CORPSE $\pi(X)$ sequence (disks), and after a single $\pi(X)$ pulse (circles). The dashed line is the prediction for the CORPSE, and the arrow indicates the qubit transition frequency. The CORPSE sequence works over a larger frequency range. The Rabi frequency was 92 MHz. Inset: oscillations of the switching probability after a single pulse $\theta(-X)$ followed (disks) or not (circles) by a CORPSE $\pi(X)$ pulse. The patterns are phase shifted by π as predicted.

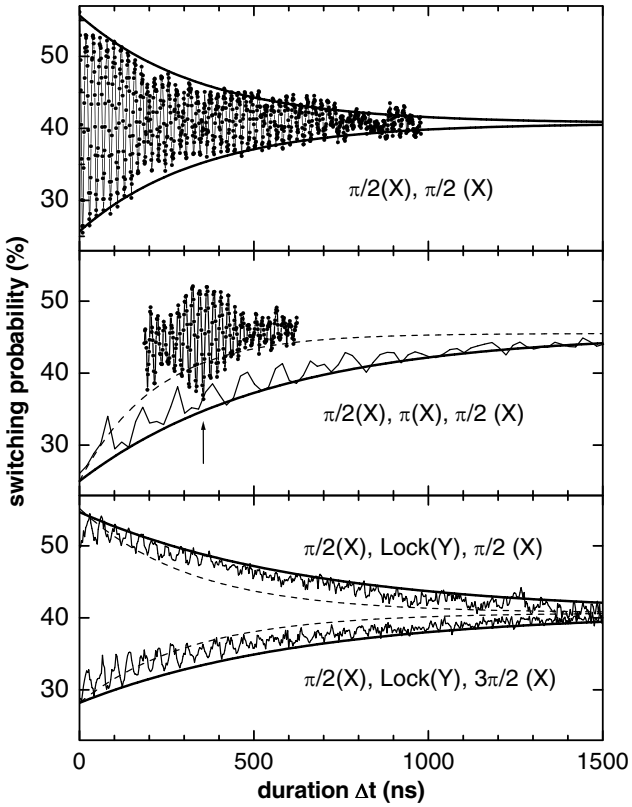

FIG. 5. Top panel: switching probability (dots) after a Ramsey $\{\pi/2(X), \pi/2(X)\}$ sequence at $\Delta\nu = +50$ MHz, as a function of the time delay between pulses. The lines are exponential fits of the envelope with a time constant $T_2 = 350$ ns. Middle panel: example of echo measured with a $\{\pi/2(X), \pi(X), \pi/2(X)\}$ sequence by increasing only the delay between the first $\pi/2$ and the π pulses (dots). The arrow indicates the nominal position of the echo minimum. Thin line: echo signal at the nominal minimum position, obtained by increasing the total sequence duration, while keeping the π pulse precisely in the middle. The bold line is an exponential fit of the envelope with a 550 ns time constant. The dashed line shows a fit of the lower envelope of the Ramsey pattern measured in the same conditions (220 ns time constant). Bottom panel: switching probability (thin lines) after two spin-locking sequences with a Rabi locking frequency of 24 MHz, at the optimal working point, versus sequence duration. Thick lines: exponential fits of the envelopes, with time constant 650 ns (see text). The dashed lines show a fit of the envelope of the Ramsey pattern measured in the same conditions (time constant: 320 ns).

tional to the second derivative $\partial^2\nu_{01}/\partial N_g^2$. Although T_2 and T_E are 2 orders of magnitude longer than found in Ref. [2] using dc gate-charge pulses and a continuous measurement, the echo efficiencies T_E/T_2 in the two experiments are comparable. Theoretically, the effect of charge noise could be further reduced by using larger values of E_J/E_C, at the expense of reduced anharmonicity.

Another way to increase the effective coherence time is to continuously drive the qubit with a microwave signal. The dynamics of the qubit then takes place in the rotating frame, with times T_1 and T_2 being replaced by $\tilde{T}_1$ and $\tilde{T}_2$. The time $\tilde{T}_1$ is measured in a spin-locking sequence, which consists of a Ramsey sequence with a driving locking field along the direction Y or $-Y$ continuously applied between the two $\pi/2(X)$ pulses. The state $|-Y\rangle$ prepared by the first pulse is thus an eigenstate of the Hamiltonian in the rotating frame, and only its phase evolves in time. Depolarization of the states $|-Y\rangle$ and $|Y\rangle$ occur under the effect of fluctuations at the Rabi locking frequency. The bottom panel of Fig. 5 shows the decay of the signals after the two spin-locking sequences $\{\pi/2(X), \mathrm{Lock}(Y), \pm\pi/2(X)\}$. Again, small oscillations are present and due to finite pulse length and detuning. The envelope yields $\tilde{T}_1 = 650 \pm 50$ ns. Notice that $\tilde{T}_1 > T_1$ and does not depend on the orientation of the locking field along Y or $-Y$ because the energy difference between the states $|Y\rangle$ and $|-Y\rangle$ in the rotating frame is $h\nu_{R0} \ll kT$. Similarly, the decay time of the transverse part of the density matrix in the rotating frame is $\tilde{T}_2 = 480 \pm 60$ ns, deduced from the decay of Rabi oscillations for Rabi frequencies in the range (2–100 MHz) (data not shown). By encoding in the rotating frame a coherent superposition of the eigenstates, decoherence is fought, but the superposition is recovered only once per Rabi period, with an effective coherence time $\tilde{T}_2 > T_2$.

In conclusion, we have demonstrated that the state of a quantronium qubit can be efficiently manipulated using methods inspired from NMR. Rotations on the Bloch sphere around X and Y axes have been performed with microwave pulses and combined, rotations around Z have been done with adiabatic pulses, and robust rotations have been implemented using composite pulses. Finally, the spin-echo and spin-locking methods have yielded a significant reduction of decoherence. The quantitative investigation of qubit decoherence in the case of free and driven evolutions will be reported elsewhere.

We acknowledge numerous discussions in the Quantronics group, the technical help of P. F. Orfila, P. Sénat, and J. C. Tack, the support of the European project SQUBIT, of the "Action Concertée Nanosciences," and of Yale University (Grant No. DAAD 19-02-1-0044).

[1] M. A. Nielsen and I. L. Chuang, *Quantum Computation and Quantum Information* (Cambridge University Press, Cambridge, 2000).
[2] Y. Nakamura, Yu. A. Pashkin, and J. S. Tsai, Nature (London) **398**, 786 (1999); Y. Nakamura *et al.*, Phys. Rev. Lett. **88**, 047901 (2002).
[3] D. Vion *et al.*, Science **296**, 886 (2002).
[4] A. Cottet, Ph.D. thesis, Université Paris VI, 2002; www-drecam.cea.fr/drecam/spec/Pres/Quantro/.
[5] D. Vion *et al.*, Fortschr. Phys. **51**, 462 (2003).
[6] J. M. Martinis *et al.*, Phys. Rev. Lett. **89**, 117901 (2002).
[7] I. Chiorescu *et al.*, Science **299**, 1869 (2003).
[8] T. Duty *et al.*, Phys. Rev. B **69**, 140503 (2004).
[9] O. Buisson *et al.* (to be published).
[10] Yu. Pashkin *et al.*, Nature (London) **421**, 823 (2003).
[11] A. Cottet *et al.*, Physica (Amsterdam) **367C**, 197 (2002).
[12] V. Bouchiat *et al.*, Phys. Scr. **T76**, 165 (1998).
[13] Y. Nakamura, C. D. Chen, and J. S. Tsai, Phys. Rev. Lett. **79**, 2328 (1997).
[14] I. Siddiqi *et al.*, cond-mat/0312623.
[15] H. K. Cummins, G. Llewellyn, and J. A. Jones, Phys. Rev. A **67**, 042308 (2003).
[16] L. M. K. Vandersypen and I. L. Chuang, quant-ph/0404064.
[17] C. P. Slichter, *Principles of Magnetic Resonance* (Springer-Verlag, Berlin, 1990), 3rd ed.

Chapter 4

Analysis of decoherence in the quantronium

4.1 Introduction

4.1.1 Decoherence

The decoherence phenomenon controls the transition from the quantum world to the classical one. The interaction between a quantum system and its environment induces a complex entanglement between both parties that selects so-called classical states for the system after a certain interaction time T_2 called the coherence time [58, 59]. During this time T_2, quantum properties such as interferences can still be demonstrated after the preparation of a coherent superposition of states, whereas for longer times, the state of the system gets projected on one of the classical states, which correspond to a small fraction of the Hilbert space states robust with respect to the system-environment interaction.

Coherence times range from ns in mesoscopic solid state devices, up to seconds for trapped ions, atoms or nuclear spins.

From a quantum computing point of view, this decoherence phenomenon is equivalent to random errors affecting qubit state during an operation and thus severely hinders the implementation of a quantum computer. The discovery of algorithms for quantum error correction proved nevertheless that decoherence can be fought and does not completely rules out quantum computing. The idea behind quantum error correction is to encode a qubit using several ones, and to perform partial measurements on the group of qubits in order to retrieve the error performed, if any, and to correct for it. These codes nevertheless require an error rate of less than 1 error for 10^4 operations, or equivalently long coherence times.

4.1.2 Decoherence in superconducting quantum bits

Despite significant advances in coherence times during recent years, with coherence times of order 0.5 μs reached, decoherence due to the coupling between the quantum electrical circuit and the degrees of freedom of the environment is still a major issue to solve before using these circuits for developing a quantum processor [64], even with a small number of qubits. The quantitative characterization and understanding of decoherence processes in superconducting circuits is thus presently a major concern for the development of superconducting qubits.

In this chapter, largely inspired from [66], we present experiments that characterize the sources of decoherence in the quantronium circuit. First, the principal noise sources responsible for decoherence are described. In Sect. 4.2, a general framework, elaborated in collaboration with A.Shnirman, Y. Makhlin,

J.Schriefl, and G.Schön, is introduced for the description of decoherence processes during the free evolution of the qubit and during its driven evolution when coupled to a small AC excitation. This theoretical framework, which can be adapted to other circuits, takes into account both linear and quadratic coupling of the qubit to variations in the control parameters. The decoherence rates are related to the spectral densities of the noise sources coupled to the qubit.

In Sects. 4.3 and 4.4, experimental results on the measurement of decoherence in all these situations are reported, and analyzed within the theoretical framework of Sect. 4.2. Methods inspired from nuclear magnetic resonance (NMR) are then introduced, such as spin echoes and spin locking, which probe the spectral density of the noise sources responsible for decoherence at different frequencies. From the experimental results, we infer constraints on the spectral density of the noise sources. Improvement of the quantum coherence time of a qubit is also discussed. Then, Sect. 4.5 summarizes what has been learnt with the quantronium on decoherence processes in Josephson qubits, and how to fight decoherence.

4.1.3 Decoherence sources in the Quantronium circuit

Like any other quantum object, the quantronium qubit is subject to decoherence due to its interaction with uncontrolled degrees of freedom in its environment, including those in the device itself. This interaction leads in the general case to a complex entanglement between the qubit and the environment. However, at low temperature, the main microscopic dissipation channel due to quasiparticles is suppressed in a superconductor, the qubit is thus only weakly coupled to the remaining sources of decoherence present in the environment. In this weak coupling regime, the effect of the interaction with the environment is to turn the parameters E_j, δ and N_g (see Fig. 4.1) into dynamical variables. The full dynamics of the control parameters being unknown, the degrees of freedom of the environment appear as a noisy modulation of the qubit Hamiltonian (4.1):

$$\widehat{H}_{CPB}(N_g,\delta) = E_C(\widehat{N}-N_g)^2 - E_J\cos(\widehat{\delta}/2)\cos\widehat{\theta} + d\,E_J\sin(\widehat{\delta}/2)\sin\widehat{\theta}. \tag{4.1}$$

The external control parameters are thus open channels for a coupling to the environment.

Using dimensionless parameters $\lambda = E_J/E_{J0}$ (E_{J0} being the nominal E_J), $\lambda = N_g$, or $\lambda = \delta/(2\pi)$, each noise source is conveniently described by its quantum spectral density $S_\lambda(\omega) \equiv 1/(2\pi)\int dt\langle\widehat{\delta\lambda}(0)\widehat{\delta\lambda}(t)\rangle e^{-i\omega t}$, where $\widehat{\delta\lambda}$ is regarded here as an operator acting on environmental variables. This function quantifies the ability of the source to absorb and to emit an energy quantum $\hbar|\omega|$, at positive and negative ω, respectively. The symmetrized spectral density $Ss_\lambda(\omega) = 1/2[S_\lambda(-\omega) + S_\lambda(\omega)]$ and its classical limit $Sc_\lambda(\omega)$ at $k_BT \gg \hbar\omega$ will also be used. Decoherence of the qubit will be described here in terms of energy exchange with a noise source on one hand, and in terms of random dephasing between states $|0\rangle$ and $|1\rangle$ due to adiabatic variations of the transition frequency on the other hand. We distinguish between, on one hand, relaxation involving $S_\lambda(+\omega_{01})$ and excitation involving $S_\lambda(-\omega_{01})$, i.e. the quantum noise and, on the other hand, dephasing processes involving the classical noise $Sc_\lambda(|\omega| \ll \omega_{01})$. As $k_BT \ll h\nu_{01}$ in our experiment, the excitation process is negligeable compared to the relaxation one. In addition, since "pure" dephasing (see Sect. 4.2) dominates decoherence, special attention is paid to the low-frequency part of the noise $Sc_\lambda(\omega \ll 1/T_2)$, where T_2 is the coherence time.

The main noise sources acting in the quantronium are schematically depicted in Fig. 4.1, and their spectral densities are discussed below. They can be roughly separated into macroscopic sources including the excitation and measurement circuits and microscopic sources, like charge fluctuators or moving vortices for instance.

Critical current noise: Two-level fluctuators in the tunnel barriers

A first source of decoherence arises from the fluctuations of the Josephson energy E_J of the two small junctions. The associated critical current noise, which has not been measured in our samples, has been

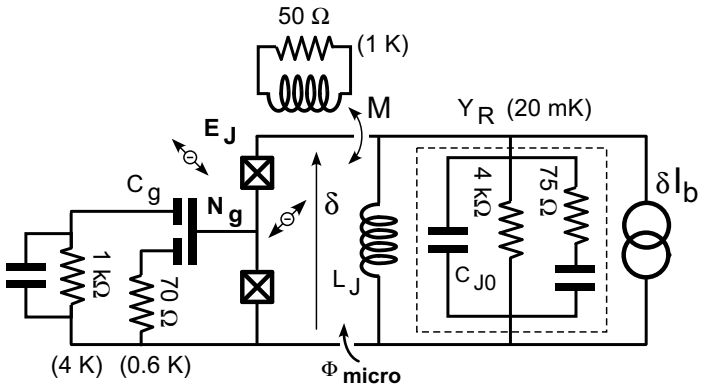

Figure 4.1: Equivalent schematic drawing of the noise sources responsible for decoherence in the quantronium. These sources are coupled to E_J, N_g, or δ. In part, they are of microscopic nature like the two-level fluctuators (TLFs) inside the junction that induce E_J variations, like a charged TLFs (represented as a minus sign in a small double arrow) coupled to N_g, or like moving vortices (Φ_{micro}) in the vicinity of the loop. The macroscopic part of the decoherence sources is the circuitry, which is represented here as an equivalent circuit as seen from the qubit. The relevant resistances and temperatures of the dissipative elements are indicated. Capacitance with no label represent a shunt at the qubit frequency and an open circuit at frequencies below 200 MHz.

characterized, at frequencies f up to 10 kHz and at temperatures T between 100 mK and 4 K, in various Josephson devices [67, 68] made of different materials, and different processes, including the Al-AlOx-Al junction process used in this work. The Josephson energy noise is empirically described, for a single junction with critical current $\mathcal{I}_0$ and area A, by a $1/f$ spectral density that scales as

$$S_{I_0}(f) = C\frac{\mathcal{I}_0^2 T^2}{Af},$$

where $C \approx 10^{-23}\mathrm{m}^2/\mathrm{K}^2$ was found to be remarkably constant (up to a factor 3) for several oxydation parameters and junction technologies. The T^2 dependance has been experimentally verified from 90mK to $T = 4.2$K [69].

By extrapolating the above expression down to the measured temperature T_e of the quantronium during its operation, 40 mK, one obtains an estimate for the spectral density of relative E_J fluctuations:

$$Sc_{\delta E_J/E_J}(|\omega| < 2\pi \times 10 \text{ kHz}) \sim (0.5 \times 10^{-6})^2/|\omega|/\text{rad.s}.$$

The critical current noise is presently attributed to charge trapping at atomic defects located in the oxide of the tunnel junctions. A simple model assumes that these defects are independant two-level fluctuators (TLFs) switching between two states that correspond to an open and a closed tunneling channel through the junction.

The distribution of the energy splittings of these TLFs is thought to be very broad and to extend above the transition energies of Josephson qubits. This picture is supported by the observation of a coupling between a phase qubit and uncontrolled TLFs randomly distributed in frequency [49]. By isolating a particular level crossing between the qubit and a unique sufficiently coherent TLF, Martinis *et al* were even able to observe coherent oscillations between the qubit and the TLF [50].

With the quantronium sample A, an avoided level crossing in the spectroscopic data (see fig. 4.2) was also observed in one of the experimental runs, which demonstrated a strong coupling (in this case $\approx$ 400MHz) between the qubit and an unknown degree of freedom that was later eliminated by annealing the sample at room temperature. These observations suggest that this spurious resonance should come from the microscopic environment of the qubit, and probably from TLFs located in the tunnel barriers. These TLF would thus not only generate low-frequency E_J noise, but could also play an important role in the relaxation of Josephson qubits.

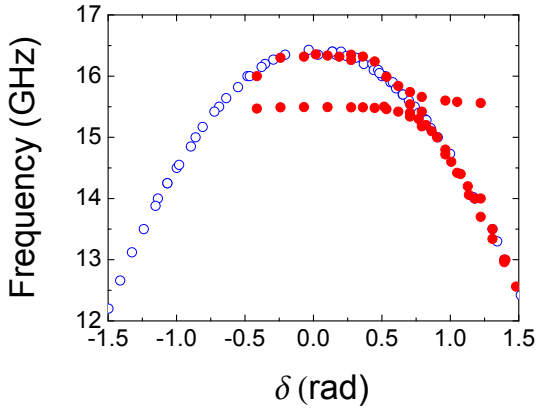

Figure 4.2: Spectroscopy of the qubit as a function of the phase δ. Solid dots: level crossing between the qubit and a spurious resonance, on sample A. The level splitting is $\approx$ 400MHz. Open dots: the level crossing was eliminated by annealing sample A at room temperature.

Charge noise: Background charged two-level fluctuators and gate line impedance

A second source of decoherence is the noise on the gate charge N_g. Like any Coulomb blockade device, the quantronium is subject to background charge noise (BCN) due to microscopic charged TLFs acting as uncontrolled additional N_g sources. These TLF could either be trapped electrons or ions in defects of the material, moving between 2 metastable positions.

Although the whole collection of TLFs produces a noise whose spectral density approximately follows a $1/f$ law [70, 71, 72] telegraph noise due to some well-coupled TLFs can be observed as well [41, 70]. These well-coupled TLFs are, for instance, responsible for the substructure of the quantronium resonance line recorded at $N_g \neq 1/2$ (see Fig. 4.12 further below). Complementary works [73] have shown that the charged TLFs are partly located in the substrate, partly in the oxide layer covering all the electrodes, and partly in the oxide barriers of the tunnel junctions themselves. It has been suggested that some TLFs contribute both to the critical current noise and to the charge noise[74]. Indeed, fluctuating charges in the oxide layer of the junctions and generating the charge noise could also open or close tunneling channels due to Coulomb repulsion, which would induce a correlation between N_g and E_j noises.

The typical amplitude A of the spectral density $Sc_{Ng}^{BCN}(|\omega| < 2\pi \times 100 \text{ kHz}) = A/|\omega|$ depends on temperature, on junction size and on the screening of the island by the other electrodes. Its value is commonly found in the range $\left[10^{-6}, 10^{-7}\right]$ for the parameters of our experiment. The amount and the energy splitting distribution of charged TLFs in Josephson devices is still unknown at frequencies of the order of ω_{01}, and their role in the relaxation of a Josephson qubit has not been clearly established. Note

that a recent work on a CPB qubit [52] suggests that they might contribute significantly to relaxation.

Another cause of charge noise is the finite impedance Z_g (see Fig. 4.1) of the gate line (GL), which can be treated as a set of harmonic oscillators coupled to $\widehat{N}$. As seen from the pure Josephson element of the CPB (junction capacitance not included), the gate circuit is equivalent [44] to an effective impedance Z_{eq} of about 70Ω in series with a voltage source $\kappa_g V_g$, with $\kappa_g = C_g/C_\Sigma$. Here $\kappa_g \approx 2\%$, the weak-coupling limit $\kappa_g \ll 1$ is achieved and for all relevant frequencies, one has $\mathrm{Re}(Z_{eq}) \simeq \kappa_g^2 \mathrm{Re}(Z_g)$. At thermal equilibrium, the contribution of the gate line to N_g fluctuations is characterized by the spectral density

$$S_{Ng}^{GL}(\omega) \simeq \kappa_g^2 \frac{\hbar^2 \omega}{E_C^2} \frac{\mathrm{Re}[Z_g(\omega)]}{R_k} \left[1 + \coth\left(\frac{\hbar\omega}{2k_B T}\right)\right], \tag{4.2}$$

where $R_k = h/e^2 \simeq 26$ kΩ. At low frequencies ($\omega \ll kT/\hbar \approx 400$MHz at 20mK), the noise spectral density simplifies to

$$Sc_{Ng}^{GL}(\omega) \simeq 2{\kappa_g}^2 \frac{\hbar k_B T}{E_C^2} \frac{\mathrm{Re}[Z_g(\omega)]}{R_k}$$

and gives with the parameters previously mentionned:

$Sc_{Ng}^{GL}(|\omega| < 2\pi \times 10 \text{ MHz}) \simeq (20 \times 10^{-9})^2/(\text{rad/s})$, which is negligeable compared to the background charge noise at all frequencies smaller than 1GHz . At large positive frequencies ($\omega \gg 400$MHz), the spectral density due to the gate impedance simplifies to:

$$S_{Ng}^{GL}(\omega) \simeq 2\kappa_g^2 \frac{\hbar^2 \omega}{E_C^2} \frac{\mathrm{Re}[Z_g(\omega)]}{R_k},$$

which leads to $S_{Ng}^{GL}(\omega) \simeq (1 - 4 \times 10^{-9})^2/(\text{rad/s})$ in the $6 - 17$ GHz frequency range. Finally, the out-of-equilibrium noise generated by the dc gate voltage source is fully filtered by the line and does not contribute to decoherence. The conclusion of this analysis is that the background charge noise dominates $S_{Ng}^{GL}(\omega)$ at low frequency.

Phase noise: Magnetic flux noise and readout circuit

The last source of decoherence encountered is the noise on the superconducting phase δ. A first contribution is the noise in the macroscopic flux externally applied to the quantronium loop. This contribution is however negligible because the external flux is shielded by a superconducting aluminum cylinder surrounding the sample holder, and because the coupling to the flux coil is weak: $\kappa_L = M E_J/\varphi_0^2 \ll 1$, where M is the mutual inductance between the qubit loop and the coil.

A second phase noise source arises from the magnetic vortices moving in the superconducting electrodes of the device. Taking the width ℓ of the aluminum lines used in this work ($\ell \approx 200$nm), the depinning field of these vortices [74, 75] $B_m \backsimeq \Phi_0/\ell^2$ is of order 50 mT, a value two orders of magnitude larger than the maximum field we apply, which suggests that vortices should be pinned. Nevertheless, many experiments on superconducting quantum interference devices (SQUIDs) have shown that an extra flux noise whose origin is unknown, and which does not depend on the temperature below a few 100 mK[69, 76], is always present with a spectral density

$$Sc_{\delta/2\pi}^{micro}(|\omega| < 2\pi \times 1 \text{ kHz}) \sim (10 \times 10^{-6})^2/\left|\omega\right|/\text{rad.s}.$$

Finally, the readout circuitry also induces phase fluctuations, due to the thermal noise of the admittance Y_R (see Fig. 4.1) in parallel with the pure Josephson element of the readout junction, and due to the output noise of the arbitrary waveform generator (AWG) used. More precisely, when a bias current $I_b < \mathcal{I}_0$ is applied to the quantronium, the effective inductance $\mathcal{L}_J \simeq (\varphi_0/\mathcal{I}_0)/\sqrt{1 - (I_b/\mathcal{I}_0)^2}$ of the

readout junction converts the current noise produced by Y_R into phase fluctuations characterized by the spectral density

$$S^{YR}_{\delta/2\pi}(\omega) = \frac{1}{\pi^2}\frac{\mathrm{Re[Z}(\omega)]}{R_k}\frac{1}{\omega}\left[1+\coth\left(\frac{\hbar\omega}{2k_BT}\right)\right]. \tag{4.3}$$

where $Z(\omega)$ is the total impedance seen by the qubit:

$$Z(\omega) = \frac{1}{1/\mathcal{L}_J\omega j + Y_R(\omega)}.$$

This spectral density is the result of the filtering of the white noise generated by the resistive components of the biasing and measuring line by the LC resonator formed by the readout junction and its shunting capacitor. The transfert function from the current Johnson noise in $Y_R(\omega)$ to the δ noise is

$$H(\omega) = \frac{\delta(\omega)}{i(\omega)} = \frac{Z(\omega)}{2\pi\phi_0\omega j} = \frac{R(\omega)}{\phi_0\omega j\left[1+jQ(\frac{\omega}{\omega_0}-\frac{\omega_0}{\omega})\right]},$$

where Q is the quality factor of the plasma oscillations of the readout junction. Q is given by the resistive part $R(\omega)$ of $Y_R(\omega)$, which incorporates the biasing resistor and the RC shunt.

At low frequency $\omega \ll \omega_p$, $Z(\omega) \approx \mathcal{L}_J\omega j$ and

$$H(\omega) \approx \frac{\mathcal{L}_J}{(2\pi\phi_0)} = \frac{2\pi}{I_c}. \tag{4.4}$$

The filtering of the low frequency noise source increases as the critical current increases. At high frequency ($\omega \gg \omega_p$), $Z(\omega) \approx 1/C\omega j$ and $H(\omega) \approx -1/(2\pi\phi_0 C\omega^2)$, the high frequency noise is filtered by the capacitor. Only the current noise at the plasma frequency can enhance the fluctuations of the phase. This is why the biasing and measuring lines are extremely well filtered in this frequency range (see section 2.4). Using the parameters mentioned in the previous section, we find $Sc^{YR}_{\delta/2\pi}(|\omega| < 2\pi\times 10\ \mathrm{MHz}) \simeq (2\times10^{-9})^2/(\mathrm{rad/s})$ and $S^{YR}_{\delta/2\pi}(\omega) \simeq [(20-80)\times10^{-9}]^2/(\mathrm{rad/s})$ in the $6-17$ GHz frequency range.

Apart from the thermal equilibrium noise generated by the resistive parts of the measuring lines, the noise coming from the arbitrary waveform generator used for generating the readout current pulses is also filtered by the readout junction. This noise is flat up to 200MHz and has a typical standard deviation of 0.15% of the total dynamic range of the generator (5V). Considering the attenuation of the line and the final $4k\Omega$ biasing resistor, this voltage noise gives rise to a current noise in the readout junction of $\sqrt{< i^2 >} \approx 0.6$nA which is converted in a phase noise $\Delta\delta$ by the relation 4.4. The spectral density of this phase noise is equal to $Sc^{AWG}_{\delta/2\pi}(|\omega|) \simeq (15\times10^{-9}/\cos\gamma)^2/(\mathrm{rad/s})$ and γ is the average phase across the readout junction.

A last possible source of phase noise is due to the parasitic junction due to the double shadow evaporation process (see ref [77]). As the number of junctions in the quantronium loop is odd, the connection between the top and the bottom aluminum layers is provided by a fourth unintended junction distributed all over the overlapping electrodes. As the distance required for the loop current to go from the bottom layer to the top one is approximately given by the Josephson length: $\lambda_J \approx 100\mu$m for Al and for typical electrodes dimensions (width $\approx 200nm$ and thickness ≈ 40nm), trapped vortices inside this long parasitic junction might be coupled to the qubit, and contribute to dephasing and to relaxation. The observation of a sub-gap structure in the $I-V$ curves of the readout junction already proves that the readout+parasitic junctions can dissipate energy at Josephson frequencies in the $10-100GHz$ range , and thus possibly the energy of the qubit itself. This dissipation phenomenon, whose origin is unclear, requires further investigation, and fabrication methods avoiding parasitic junctions should be tested.

The conclusion of this analysis is that the phase noise is dominated at low frequency by local sources close to the junction loop.

4.2 Theoretical description of decoherence

We now consider the dynamics of a qubit from a general point of view in two situations: free evolution, and evolution driven by a sinusoidal excitation.

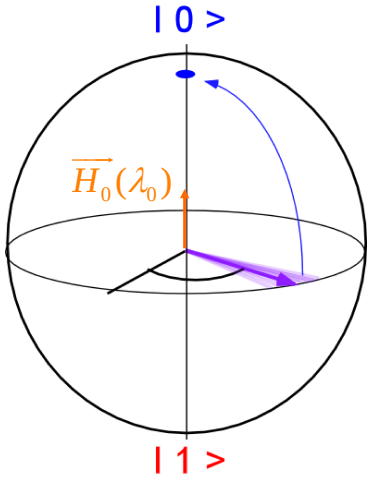

Figure 4.3: During decoherence, the fluctuations of the effective field induces relaxation to the ground state and pure dephasing, which is caracterized by fluctuations of the precession speed around the Z axis.

During the free evolution, after an initial preparation in a coherent superposition of the two qubit states, the effective spin precesses under the influence of the static field $\vec{H}_0$, set by the control parameters λ_0, and of its classical and quantum fluctuations, set by the fluctuations $\delta\lambda$. One distinguishes two time scales, the depolarization time T_1 (dominated at low temperatures by the relaxation to the ground state) for the decay of the diagonal Z component of the spin density matrix, and the decay time T_2 of the off-diagonal part, which is the qubit coherence time (see Fig. 4.3). As described in the experimental Sect. 4.3, the time T_2 is inferred from the decay of Ramsey oscillations in a two-$\pi/2$-pulse experiment. These Ramsey oscillations are the equivalent of the free induction decay in NMR [62]. Note that the decay law can be non-exponential, the time T_2 being then defined by a decay factor $\exp(-1)$. In a modified version of the Ramsey experiment, an extra π pulse is applied in the middle of the sequence in order to perform a Hahn echo experiment[78, 62]. The decay time T_E of this echo is longer than T_2, and the enhancement factor provides important information on the spectral density of the noise mechanisms.

In the driven case, the decay of the spin density matrix is investigated in the rotating frame. Experimentally, this decay is obtained from spin-locking signals [62] and from Rabi oscillations. It is shown that time scales $\tilde{T}_1$ and $\tilde{T}_2$, similar to T_1 and T_2, describe the dynamics in the rotating frame[62, 79].

4.2.1 Expansion of the Hamiltonian

We first start by expanding the Hamiltonian of the qubit

$$\widehat{H}_{qb} = -\frac{1}{2}\vec{H}_0(\lambda_0).\vec{\widehat{\sigma}}$$

to second order in the perturbation $\delta\lambda$:

$$\widehat{H}_{qb} = -\frac{1}{2}\left[\vec{H}_0(\lambda_0) + \frac{\partial \vec{H}_0}{\partial \lambda}\,\delta\lambda + \frac{\partial^2 \vec{H}_0}{\partial \lambda^2}\,\frac{\delta\lambda^2}{2} + ...\right]\vec{\widehat{\sigma}}\,. \tag{4.5}$$

Introducing the notations $\vec{D}_\lambda \equiv (1/\hbar)\,\partial\vec{H}_0/\partial\lambda$ and $\vec{D}_{\lambda 2} \equiv (1/\hbar)\,\partial^2\vec{H}_0/\partial\lambda^2$, one finds in the eigenbasis of $\vec{H}_0(\lambda_0).\vec{\widehat{\sigma}}$:

$$\widehat{H}_{qb} = -\frac{1}{2}\hbar\,(\omega_{01}\widehat{\sigma}_z + \delta\omega_z\widehat{\sigma}_z + \delta\omega_\perp\widehat{\sigma}_\perp) \tag{4.6}$$

where $\hbar\omega_{01} \equiv |\vec{H}_0(\lambda_0)|$, $\delta\omega_z \equiv D_{\lambda,z}\delta\lambda + D_{\lambda 2,z}\,\delta\lambda^2/2 + ...$, and $\delta\omega_\perp \equiv D_{\lambda,\perp}\delta\lambda + ...$ Here $\sigma_\perp$ denotes the transverse spin components [i.e., the last term in Eq. (4.6) may include both σ_x and σ_y]. We write explicitly only the terms in the expansion that dominate decoherence (as will become clear below).

These longitudinal coefficients $\vec{D}_{\lambda,z}$ and $\vec{D}_{\lambda 2,z}$ are related to the derivatives of $\omega_{01}(\lambda)$:

$$\frac{\partial\omega_{01}}{\partial\lambda} = D_{\lambda,z}\ , \tag{4.7}$$

and

$$D_{\lambda 2,z} = \frac{\partial^2\omega_{01}}{\partial\lambda^2} - \frac{D_{\lambda,\perp}^2}{\omega_{01}} \tag{4.8}$$

As discussed below, the quantities $\partial\omega_{01}/\partial\lambda$ and $\partial^2\omega_{01}/\partial\lambda^2$ are sufficient to treat pure dephasing whereas the calculation of the depolarization rates involves $D_{\lambda,\perp}$.

Application to the quantronium sample used in this work

As already mentioned in chapter 2, the parameters of the qubit for sample A are $E_J = 0.87k_B$ K, $E_C = 0.66k_B$ K and were measured by fitting the spectroscopic data $\omega_{01}(N_g, \delta)$ (see Fig. 4.12 below) with a numerical diagonalization of the Hamiltonian $\widehat{H}_{CPB}$. This fit gives an upper limit for the asymmetry of the qubit junctions, $d < 13\%$. By measuring the enhancement of MQT coming from Landau Zener transitions [57, 56], this value was estimated as $d \sim 3\%$. From E_J, E_C, and d, the numerical values of the D_λ's introduced above were calculated as a function of the working point (δ, N_g). Since we have characterized decoherence only along the two segments $\delta/(2\pi) \in [-0.3, +0.3]$, $N_g = 1/2$ and $\delta = 0$, $N_g - 1/2 \in [-0.1, +0.1]$ in the (δ, N_g) plane, we only give below simple expressions that approximate ω_{01}, D_λ and $\partial^2\omega_{01}/\partial\lambda^2$ with a ± 3 % accuracy in the range of parameters explored experimentally. We found for the transition frequency

$$\omega_{01}(\delta, N_g = 1/2) \simeq \left[103 - 425\,(\delta/2\pi)^2\right]\ \times 10^9 \text{ rad/s}, \tag{4.9}$$

$$\omega_{01}(\delta = 0, N_g) \simeq \left[103 + 145\,(N_g - 1/2)^2\right]\ \times 10^9 \text{ rad/s}, \tag{4.10}$$

which lead for the longitudinal coefficients to

$$D_{\delta/2\pi,z}(\delta = 0 \text{ or } N_g = 1/2) = \frac{\pi}{e}(i_1 - i_0) \simeq -850\ \frac{\delta}{2\pi}\ \times 10^9 \text{ rad/s}, \tag{4.11}$$

$$\frac{\partial^2\omega_{01}}{\partial(\delta/2\pi)^2} \simeq -850\ \times 10^9 \text{ rad/s}, \tag{4.12}$$

$$D_{Ng,z}(\delta = 0 \text{ or } N_g = 1/2) = -\frac{2E_C}{\hbar}(\langle 1|\,\widehat{N}\,|1\rangle - \langle 0|\,\widehat{N}\,|0\rangle) \simeq +290\ \left(N_g - \frac{1}{2}\right) \times 10^9 \text{ rad/s}, \tag{4.13}$$

$$\frac{\partial^2\omega_{01}}{\partial N_g^2} \simeq +290\ \times 10^9 \text{ rad/s}, \tag{4.14}$$

where i_0 and i_1 are the average currents $\left\langle \widehat{i} \right\rangle$ in the two states. Note that $D_{N_g,z}$ vanishes at $N_g = 1/2$ for all δ, so that a gate microwave pulse corresponds to a purely transverse perturbation of the Hamiltonian. Consequently, the perturbed Hamiltonian of Eq. (4.53) does apply exactly to the quantronium at $N_g = 1/2$. At other values of N_g, Eq. (4.53) would nevertheless be a good approximation. For critical current noise, the coupling coefficient

$$D_{\delta E_J/E_J,z}(\delta = 0) = \cot(\frac{\delta}{2})\frac{i_1 - i_0}{e} \simeq +85 \ \times 10^9 \text{ rad/s} \tag{4.15}$$

$$D_{\delta E_J/E_J,z}(N_g = 1/2) \simeq \left[+85 - 240 \ \left(\frac{\delta}{2\pi}\right)^2\right] \ \times 10^9 \text{ rad/s} \tag{4.16}$$

is maximal at the optimal working point P_0. One can notice that the coupling to the critical current noise is much smaller than for flux qubit [67], where the tunnel coupling between flux states is exponentially dependant on I_c leading to value of $D_{\delta E_J/E_J,z}$ in the range 5.10^{12} rad/s.

Expressed in the same way, the transverse coefficients $D_{\lambda,\perp}$, which are involved in the manipulation and in the relaxation of the qubit, are given by

$$D_{\delta/2\pi,\perp}(\delta = 0 \text{ or } N_g = 1/2) = \frac{2\pi}{e}\left|\langle 0|\,\widehat{i}\,|1\rangle\right| \simeq 380 \ d \ \left[1 + 6.0 \ \left(\frac{\delta}{2\pi}\right)^2\right] \ \times 10^9 \text{ rad/s}, \tag{4.17}$$

$$D_{Ng,\perp}(\delta = 0 \text{ or } N_g = 1/2) = \frac{4E_C}{\hbar}\left|\langle 0|\,\widehat{N}\,|1\rangle\right| = 193 \ \times 10^9 \text{ rad/s}. \tag{4.18}$$

The relaxation through the phase channel being proportional to the asymmetry of the junctions, in the ideal case $d = 0$, the current operator $\widehat{i}$ is diagonal in the qubit eigenbasis and the $1 \longrightarrow 0$ transition is forbidden. The coupling coefficient to the critical current noise is

$$D_{\delta E_J/E_J,\perp}(\delta = 0 \text{ or } N_g = 1/2) = \frac{2E_J\cos(\delta/2)}{\hbar}\left|\langle 0|\cos\widehat{\theta}\ |1\rangle\right| = 108\left|N_g - \frac{1}{2}\right| \ \times 10^9 \text{ rad/s}. \tag{4.19}$$

Since it vanishes at $N_g = 1/2$, there is no relaxation through the channel of critical current fluctuations at the optimal working point (at first order). Finally, note that since the lines $\delta = 0$ and $N_g = 1/2$ are symmetry lines in the parameter space, the cross derivative $\partial^2\omega_{01}/\partial\delta\partial N_g$ is equal to zero along these two lines.

Bloch-Redfield approach

In the regime of weak coupling between the qubit and its environment, the Bloch-Redfield [63, 79, 80] theory gives a simple description of the decoherence process. The dynamics of two-level systems (spins) involves two rates (times): the longitudinal relaxation (depolarization) rate $\Gamma_1 = T_1^{-1}$ and the transverse relaxation (dephasing) rate $\Gamma_2 = T_2^{-1}$. The dephasing process is a combination of effects of the depolarization (Γ_1) and of the so-called pure dephasing. The pure dephasing is usually associated with the inhomogeneous broadening in ensembles of spins, but occurs also for a single spin due to the longitudinal low-frequency noise. Indeed, due to our experimental protocol, we will suffer from an equivalent temporal inhomogeneous broadening (see Sect. 4.3). The pure dephasing is characterized by the rate Γ_φ. The two processes of relaxation and pure dephasing combine to a rate

$$\Gamma_2 = \frac{1}{2}\Gamma_1 + \Gamma_\varphi \ . \tag{4.20}$$

The Bloch-Redfield approach applies only if the noise is short-correlated and weak[62] (i.e. $\tau_c, h/k_BT \ll T_1, T_2$, where τ_c is the correlation time of the environment), regardless of the noise statistics. The decay is exponential since weak dissipative elements from many uncorrelated time intervals add up. In more general situations the decay of the off-diagonal part of the density matrix is non-exponential. In particular, when the pure dephasing is dominated by a noise singular near $\omega \approx 0$, the decay law $\exp(-\Gamma_\varphi t)$ is replaced by other decay functions which we denote as $f_{z,\ldots}(t)$ (additional indices ... describe the particular experiment). It can be shown [81] that the transversal decays due to the depolarization and to the pure dephasing processes factorize, provided the high-frequency noise responsible for the depolarization is regular. That is, instead of the exponential decay $e^{-\Gamma_2 t}$, one obtains the transverse decay law $f_{z,\ldots}(t)\exp(-\Gamma_1 t/2)$. In this general case, one can write the density matrix of the system at any time t during the free evolution, and for an initial pure state $\alpha|0\rangle + \beta|1\rangle$ at $t = 0$:

$$\begin{pmatrix} 1+(|\alpha|^2-1)e^{-\frac{t}{T_1}} & \alpha^*\beta e^{-\frac{t}{2T_1}} f_{z,R}(t) e^{-i\Delta\nu t} \\ \alpha\beta^* e^{-\frac{t}{2T_1}} f_{z,R}(t) e^{i\Delta\nu t} & |\beta|^2 e^{-\frac{t}{T_1}} \end{pmatrix}$$

4.2.2 Depolarization (T_1)

For the relaxation process, we assume a short correlated noise of the environment and we thus keep the framework of the Bloch-Redfield approximation. The depolarization rate $\Gamma_1 = T_1^{-1}$ is given by the sum

$$\Gamma_1 = \Gamma_{rel} + \Gamma_{ex}, \tag{4.21}$$

of the relaxation rate Γ_{rel} and the excitation rate Γ_{ex}. The Fermi golden rule gives

$$\Gamma_{rel} = \frac{\pi}{2} S_{\delta\omega_\perp}(\omega_{01}) = \frac{\pi}{2} D^2_{\lambda,\perp} S_\lambda(\omega_{01}), \tag{4.22}$$

$$\Gamma_{ex} = \frac{\pi}{2} S_{\delta\omega_\perp}(-\omega_{01}) = \frac{\pi}{2} D^2_{\lambda,\perp} S_\lambda(-\omega_{01}). \tag{4.23}$$

Thus

$$\Gamma_1 = \pi S s_{\delta\omega_\perp}(\omega_{01}) = \pi D^2_{\lambda,\perp} S s_\lambda(\omega_{01}). \tag{4.24}$$

This result holds irrespective of the statistics of the fluctuations. At lowest order of the perturbation theory in $D_{\lambda,\perp}$, the expression of the rates only require the second moments of the noise expressed through the correlator S_λ. This approximation is sufficient when the noise is weak enough with a smooth spectrum at the transition frequency ω_{01} on the scale of the relaxation rate Γ_1. At low temperatures $k_B T \ll \hbar\omega_{01}$, making the assumption that the high frequency environment is at thermal equilibrium, the available modes at the transition frequency of the qubit are empty, the excitation rate Γ_E is exponentially suppressed, and $\Gamma_1 \approx \Gamma_R$.

4.2.3 Pure dephasing

During pure dephasing, the transition frequency of the qubit is fluctuating due to the coupling to the environment. The phase difference $\phi_{01} = \int_0^t \omega_{01} dt'$ between state $|0\rangle$ and $|1\rangle$ thus diffuses around an average value $\langle\phi\rangle(t) = \langle\omega_{01}\rangle t$. Disregarding relaxation, an initial pure state $\alpha|0\rangle + \beta|1\rangle$ turns into a statistical mixture of states $\alpha|0\rangle + \beta e^{i(\Delta\phi(t)+\omega_{01}t}|1\rangle$, with a probability distribution of $\Delta\phi(t)$. The density matrix of such a statistical mixture is given by:

$$\begin{pmatrix} |\alpha|^2 & \alpha\beta^* e^{i\Delta\nu t} f_{z,R}(t) \\ \alpha^*\beta e^{-i\Delta\nu t} f_{z,R}(t)^* & |\beta|^2 \end{pmatrix},$$

where $f_{z,R}(t) = \langle e^{i\Delta\phi(t)}\rangle$, this average being considered over all possible realization of the random process $\delta\lambda(t')$ from $t' = 0$ to $t' = t$. Assuming the ergodic character of the process, this ensemble average

is equivalent to the temporal sampling average that we perform during the data acquisition process. The next paragraph is dedicated to the calculation of the Ramsey and Echo functions in different practical cases.

Linear coupling

First, we analyze a noise source coupled linearly (and longitudinally) to the qubit, i.e., $\partial\omega_{01}/\partial\lambda = D_{\lambda,z} \neq 0$. As a starting point, we make the assumption that the noisy parameter λ follows Gaussian statistics, which is a reasonable hypothesis. Indeed, due to the central limit theorem, Gaussian statistic is a general property of any noise generated by many independant fluctuators, regardless of their individual noise statistics, and provided they are weakly coupled to the considered parameter λ.

The weak coupling hypothesis will be questionned in Sect. 4.2.4, where the possibility of non-Gaussian effects is considered.

Considering $\delta\lambda$ as Gaussian, the random phase accumulated at time t,

$$\Delta\phi = D_{\lambda,z} \int_0^t dt' \delta\lambda(t'),$$

is then also Gaussian distributed, and one can calculate the decay law of the free induction signal as $f_{z,R}(t) = \langle \exp(i\Delta\phi) \rangle = \exp(-(1/2)\langle \Delta\phi^2 \rangle)$. The average is performed here over all possible realizations of the stochastic process $\Delta\phi(t)$.

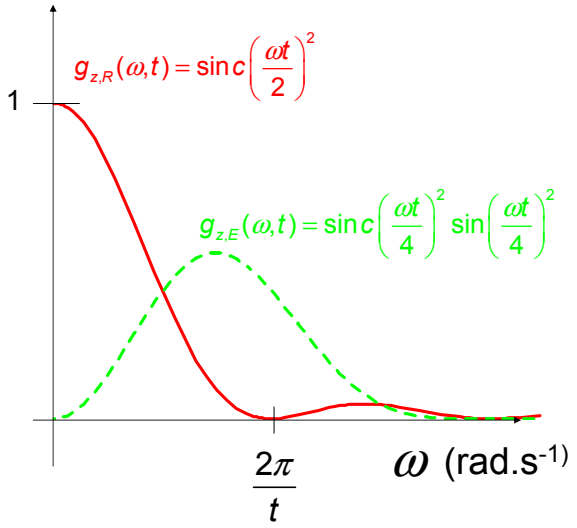

Figure 4.4: Weighting functions of the noise spectral density entering equations **??**. The Ramsey decay is thus sensitive to the low frequency part of the spectrum ($\omega < 2\pi/t$), whereas the Echo one is sensitive to frequencies around $\omega \approx 2\pi/t$. Note that the area under these two weighting functions is the same which explains that, in the case of a white noise, the echo technique is unefficient.

This gives

$$f_{z,R}(t) = \exp\left[-\frac{t^2}{2} D_{\lambda,z}^2 \int_{-\infty}^{+\infty} d\omega S_\lambda(\omega) \mathrm{sinc}^2 \frac{\omega t}{2}\right], \tag{4.25}$$

where $\mathrm{sinc}x \equiv \sin x/x$. In an echo experiment, the acquired phase is the difference between the two phases accumulated during the two free evolution periods,

$$\Delta\phi_E(t_1,t_2) = -\Delta\phi_1 + \Delta\phi_2 = -D_{\lambda,z}\int_0^{t_1} dt'\delta\lambda(t') + D_{\lambda,z}\int_{t_1}^{t_1+t_2} dt'\delta\lambda(t')\,, \tag{4.26}$$

so that when $t_1 = t_2 = t/2$ (echo revival)

$$f_{z,E}(t) = \exp\left[-\frac{t^2}{2}\,D_{\lambda,z}^2\int_{-\infty}^{+\infty} d\omega S_\lambda(\omega)\sin^2\frac{\omega t}{4}\mathrm{sinc}^2\frac{\omega t}{4}\right]. \tag{4.27}$$

For the echo, the spectral density is weighted by the function $g_{z,E}(\omega,t) = \mathrm{sinc}^2(\omega t/4)\sin^2(\omega t/4)$. Note that, since the noise is supposed Gaussian, only the second moment of the fluctuations, related to the spectral density $S_\lambda(\omega)$, enters the dephasing function. In addition, the spectral density of the noise is weighted by the functions $g_{z,R}$ and $g_{z,E}$ (see fig. 4.4), which involves only the very low frequency part of the spectrum for the Ramsey and the echo ($0 < \omega < 1/t$ with $t \lesssim T_2$s).

White spectrum

In the case of a white spectrum, the decay functions simplify to :

$$f_{z,R}(t) = f_{z,E}(t) = \exp\left[-\pi D_{\lambda,z}^2 t S_\lambda(\omega=0)\right] \tag{4.28}$$

Both Ramsey and echo decays are thus exponential and identical. The echo technique does not improve the coherence time.

These results can be generalized for the case of a regular spectrum at $\omega = 0$ on a frequency scale $|\omega| < 1/t \lesssim 1/T_2$. In this case one has

$$\int_{-\infty}^{+\infty} d\omega S_\lambda(\omega)\mathrm{sinc}^2\frac{\omega t}{2} \approx \frac{2\pi}{t}S_\lambda(0).$$

One recovers the result of the Bloch-Redfield theory for the dephasing time:

$$\Gamma_\varphi = \pi S_{\delta\omega_z}(\omega=0) = \pi D_{\lambda,z}^2\, S_\lambda(\omega=0) = \ \pi D_{\lambda,z}^2\, Sc_\lambda(\omega=0). \tag{4.29}$$

which is also valid for the echo time. This result is of the golden rule type [similar to Eq. (4.24)] and is meaningful if the noise power Sc_λ is regular near $\omega \approx 0$ up to frequencies of order Γ_φ.

The Bloch-Redfield approach fails when the noise has very long correlation time (compared to T_1 and T_2), and thus a singular spectral density at $\omega = 0$, like $1/f$ noise.

$1/f$ spectrum:

Here and below we assume a $1/f$ Gaussian noise with a $1/f$ law extending in a wide range of frequencies limited by an infrared cutoff ω_{ir} and an ultraviolet cutoff ω_{c}:

$$S_\lambda(\omega) = A/|\omega|,\ \omega_{\mathrm{ir}} < |\omega| < \omega_{\mathrm{c}}\,. \tag{4.30}$$

The infrared cutoff ω_{ir} is usually determined by the measurement protocol, as discussed further below. The decay rates typically depend only logarithmically on ω_{ir}, and the details of the behavior of the noise power below ω_{ir} are irrelevant to logarithmic accuracy. For most of our analysis, the same remark applies to the ultraviolet cutoff ω_c. However, for some specific questions considered below, frequency integrals may be dominated by $\omega \gtrsim \omega_{\mathrm{c}}$, and thus the detailed behavior near and above ω_{c} (cutoff "shape") is relevant. We will refer to an abrupt suppression above ω_{c} ($S(\omega) \propto \theta(\omega_{\mathrm{c}} - |\omega|)$, with $\theta(\omega)$ the Heaviside function) as a "sharp cutoff", and to a crossover at ω_{c} to a faster $1/\omega^2$ decay (motivated by modelling of the noise via a set of bistable fluctuators, see below), as a "soft cutoff".

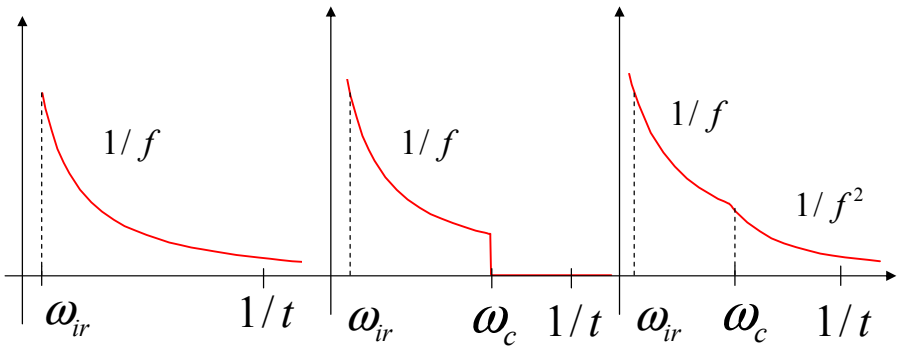

Figure 4.5: $1/f$ possible spectrums. Left: wide band $1/f$ noise. Middle: static $1/f$ noise having a hard cutoff at ω_c. Right: quasi-static $1/f$ with a soft cutoff at ω_c, the noise crossovers to a $1/f^2$ behavior. The frequency ω_{ir} is a low frequency cutoff introduced for taking into account the finite time of data acquisition.

For wideband Gaussian $1/f$ noise (see fig. 4.5), at times t such that $\omega_{ir} \ll 1/t < \omega_c$, the free induction (Ramsey) decay is dominated by the frequencies $\omega < 1/t$, i.e., by the quasistatic contribution[44], and Eq. (4.25) reduces to:

$$f_{z,R}(t) = \exp\left[-t^2\, D_{\lambda,z}^2\, A\, \left(\ln\frac{1}{\omega_{ir}t} + O(1)\right)\right]. \tag{4.31}$$

where $A\ln(1/\omega_{ir}t) = \sigma_\lambda^2$ is the variance of the $1/f$ noise and is logarithmically time dependant. The expected decay for a wide band $1/f$ noise is thus almost Gaussian.

The infrared cutoff $\omega_{\rm ir}$ ensures the convergence of the integral 4.25.

For the echo decay, using the fact that $\int_{-\infty}^{+\infty} \sin(x)^4/x^3 dx = 2\ln 2$ we obtain

$$f_{z,E}(t) = \exp\left[-t^2\, D_{\lambda,z}^2\, A\cdot \ln 2\right]. \tag{4.32}$$

The echo method thus only increases the decay time by a logarithmic factor:

$$T_E/T_R \approx \sqrt{\frac{|\ln\omega_{ir}t|}{\ln 2}},$$

of order 4.5 when calculated with $\omega_{ir} = 1$Hz and $t = 1\mu$s. This limited echo efficiency is due to the high frequency tail of the $1/f$ noise [82, 83].

Static case:

As the experiment is performed by repeating each sequence of excitation pulses and readout about 10^4 times in order to decrease the statistical noise, the measured quantities are subject to low frequency fluctuations form one sequence to the other. By "static noise", we thus consider noise having frequencies slow compared to the typical duration of a single sequence, such that the transition frequency is constant over a sequence ($\approx 1\mu$s), but its fluctuations are fast compared to the total acquisition time (~ 1s).

In many cases, the contribution of low frequencies $\omega \ll 1/t$ dominates the pure dephasing. This happens when the noise spectrum is strongly peaked at low frequencies [cf. Eq. (4.31)], in particular when it has a sufficiently low ultraviolet cutoff frequency $\omega_{\rm c}$. This simple regime pertains to the quantronium.

We distinguish two approximations used to perform the calculation of the f_z functions: In the static approximation, the noisy control parameter λ is considered as constant during each pulse sequence and its value is given by an effective distribution probability $P(\delta\lambda)$. This approach gives a direct evaluation of the Ramsey decay function $f_{z,R}(t)$. In the relevant cases of linear or quadratic coupling to the fluctuations, the decay function $f_{z,R}(t)$ is the Fourier- or Fresnel-type transform of the distribution $P(\delta\lambda)$, respectively. Since the static approximation would yield no decay for the echoes, the calculation of the echo decay function $f_{z,E}(t)$ requires a "quasistatic approximation" that takes into account variations within each pulse sequence. A noise with an ultraviolet cutoff frequency ω_c can be considered as quasistatic on time scales shorter than ω_c^{-1}. The relevant results obtained in Refs. [84, 85, 86] are given below.

In the static approximation, the contribution of low frequencies $\omega \ll 1/t$ to the integral in Eq. (4.25) is evaluated using the approximation $\mathrm{sinc}(\omega t/2) \approx 1$:

$$f_{z,R}^{\mathrm{stat}}(t) = \exp\left[-\frac{t^2}{2} D_{\lambda,z}^2 \sigma_\lambda^2\right], \tag{4.33}$$

where $\sigma_\lambda^2 = \int_{-\infty}^{+\infty} d\omega\, S_\lambda(\omega)$ is the variance of $\delta\lambda$. The decay is thus Gaussian for any Gaussian static noise.

This formula can be generalized to the case of an arbitrary static noise, regardless of its statictics, by using the Fourier tranform of the probability distribution of $\delta\lambda$:

$$f_{z,R}^{\mathrm{stat}}(t) = \int d(\delta\lambda) P(\delta\lambda)\, e^{i D_{\lambda,z}\, \delta\lambda\, t}. \tag{4.34}$$

For $1/f$ Gaussian noise, characterized by $S_\lambda = (A/|\omega|)$ in the bandwidth $[\omega_{ir}, \omega_c]$, we obtain $\sigma_\lambda^2 = 2A \ln(\omega_c/\omega_{ir})$. The result is only logarithmically sensitive to the value of the ultraviolet cutoff ω_c and to the specific functional form of the suppression of noise at high $\omega \gtrsim \omega_c$. The static approximation is sufficient for the evaluation of the dephasing rate if, e.g., $1/T_\phi > \omega_c$, i.e., $D_{\lambda,z}^2\, A\, \ln(\omega_c/\omega_{ir}) \gg \omega_c^2$.

Let us now analyze the echo decay. For $1/f$ noise with a low ω_c, the integral in Eq. (4.27) over the interval $\omega \lesssim \omega_c$ is dominated by the upper limit. This indicates that the specific behavior at $\omega \gtrsim \omega_c$ is crucial. For instance, in the case of a sharp cutoff, by using $\sin(\omega t/4)^2 \mathrm{sinc}^2 \omega t/4 \approx (\omega t/4)^2$ we obtain

$$f_{z,E}(t) = \exp\left(-\frac{1}{32} D_{\lambda,z}^2\, A\, \omega_c^2\, t^4\right). \tag{4.35}$$

However, if the $1/f$ behavior for $\omega < \omega_c$ crosses over to a faster decay $\propto 1/\omega^2$ at $\omega > \omega_c$ (as one would expect when the noise is produced by a collection of bistable fluctuators with Lorentzian spectra, cf. Refs. [87, 88, 89]) then the integral in Eq. (4.27) is dominated by frequencies $\omega_c < \omega < 1/t$, and we find

$$f_{z,E}(t) = \exp\left(-\frac{1}{12} D_{\lambda,z}^2 A \omega_c t^3\right).$$

In either case, one finds that the decay is slower than for a wide band $1/f$ noise (i.e., with a high cutoff $\omega_c > 1/T_\phi \approx D_{\lambda,z} A^{1/2}$): the exponent involved in the decay function is indeed reduced by a factor $\sim (\omega_c t)^2$ for the sharp cutoff, or $\omega_c t$ for the soft one.

To summarize, in the case of a linear coupling, the decay of the Ramsey and echo signals are expected to be exponential in the case of a regular noise spectrum around $\omega = 0$ on a frequency scale $1/T_2$. For a $1/f$ noise having Gaussian statistics the Ramsey decay is expected to be gaussian, whereas the echo signal follows a $\exp(-\alpha_n t^n)$ law, the exponent n depending on the precise high frequency cuttoff of the noise spectrum.

Quadratic coupling

At the optimal working point, the first-order longitudinal coupling $D_{\lambda,z}$ vanishes and eq. 4.20 predicts that the decay of the coherent oscillations is determined only by the relaxation processes: $\Gamma_2 = \Gamma_1/2$. However, it appears that the second-order contribution of the longitudinal noise can be comparable, or even dominate over $\Gamma_1/2$. Due to the quadratic coupling, the qubit is subject to an a priori non-Gaussian λ^2 noise, which modifies the type of the decay of the Ramsey function that is no longer exponential as in the Bloch-Redfield approximation.

To evaluate this second order contribution, one has to calculate

$$f_z(t) = \left\langle \exp\left(i\,\frac{1}{2}\,\frac{\partial^2\omega_{01}}{\partial\lambda^2}\int_0^t \chi(\tau)\,\delta\lambda^2(\tau)d\tau \right) \right\rangle . \tag{4.36}$$

Equation (4.36) can be used for the analysis of the free induction decay (Ramsey signal) if one sets $\chi(\tau) = 1$, and for the investigation of the echo-signal decay using $\chi(\tau < t/2) = -1$ and $\chi(\tau > t/2) = 1$.

Gaussian hypothesis for the λ^2 noise

A first way to estimate the Ramsey decay is to assume λ^2 as a Gaussian variable, and apply the framework for linear coupling to the new noisy variable $\lambda' = \lambda^2$.

The spectral density of λ^2 can be evaluated by the approximated formula:

$$S_{\lambda^2}(\omega) = \frac{1}{\pi}\int_{-\infty}^{+\infty} S_\lambda(\omega')S_\lambda(\omega-\omega')d\omega', \tag{4.37}$$

which is an exact formula when λ is itself a Gaussian variable.

For a $1/f$ noise, $S_\lambda(\omega) = A/\omega$, the spectral density of λ^2 is [84]

$$S_{\lambda^2}(\omega) = \frac{4}{\pi}A\frac{\ln|\frac{\omega}{\omega_{ir}}|}{|\omega|},$$

and the decay is gaussian and given by:

$$f_{z,R}(t) = \exp\left[-\left(\frac{1}{2}\frac{\partial^2\omega_{01}}{\partial\lambda^2}\frac{A}{\pi}t\ln\omega_{ir}t \right)^2 \right] \tag{4.38}$$

One can also calculate the pseudo-dephasing rate in the case of a regular noise at low frequency:

$$\Gamma_\phi \approx \frac{\partial^2\omega_{01}}{\partial\lambda^2}^2 \int_{-\infty}^{+\infty} d\omega S_\lambda(\omega)^2.$$

These formulas will be useful for estimating the dephasing rate at the optimal working point due to the white noise generated by the gate and measuring lines.

Gaussian hypothesis for λ

A more elaborate approach which assumes λ to be Gaussian has been implemented for revaluating the free induction decay in the case of a $1/f$ noise with a high cutoff ω_c [84] (the highest energy scale in the problem). The decay law can be approximated by the product of the low-frequency ($\omega < 1/t$, quasistatic) and of the high-frequency ($\omega > 1/t$) contributions:

$$f_{z,R}(t) = f^{\rm lf}_{z,R}(t)f^{\rm hf}_{z,R}(t).$$

This approximation permits one to determine the decay law qualitatively; moreover, in the short- and long-time limits one of the terms dominates, and one obtains accurate estimates. The contribution of low frequencies is given by (cf. Refs. [84, 85, 86]):

$$f^{\rm lf}_{z,R}(t) = \frac{1}{\sqrt{1 - i\,(\,\partial^2\omega_{01}/\partial\lambda^2)\;\sigma_\lambda t}}\,. \tag{4.39}$$

At short times:

$$|f^{\rm lf}_{z,R}(t)| \approx 1 - \left(\frac{\partial^2\omega_{01}}{\partial\lambda^2} \frac{A}{\pi} t \ln \omega_{ir} t \right)^2 \tag{4.40}$$

matches with the result obtained when assuming the noisy variable λ^2 as being Gaussian (see eq. 4.38). The dephasing time being defined by $|f^{\rm lf}_{z,R}(t)|/|f^{\rm lf}_{z,R}(0)| = 1/e$ is:

$$\frac{1}{T_\phi} = \frac{1}{7.3} \frac{\partial^2\omega_{01}}{\partial\lambda^2} \sigma^2_\lambda,$$

which corresponds to the value obtained using the Gaussian approximation for λ^2, the 7.3 factor being replaced by a 2π factor. The crude approximation of considering the noisy variable λ^2 as Gaussian thus give the correct value of the dephasing time, and the correct decay shape at short times, but a wrong decay law at long times: gaussian instead of algebric, the latter being experimentally distinguishable from the first (see Sec. 4.3.4).

For $1/f$ noise with variance $\sigma^2_\lambda = 2A\ln(1/\omega_{\rm ir}t)$, the low frequency contribution is

$$f^{\rm lf}_{z,R}(t) = \frac{1}{\sqrt{1 - 2i\,(\,\partial^2\omega_{01}/\partial\lambda^2)\; t\,A\;\ln(1/\omega_{ir}t)}}\,. \tag{4.41}$$

At longer times: $t \gg t_c = \left[(\partial^2\omega_{01}/\partial\lambda^2)\,A/2\right]^{-1}$, the high-frequency contribution dominates the decay and one finds

$$\ln f^{\rm hf}_{z,R}(t) \approx -t \int\limits_{\sim 1/t}^{\infty} \frac{d\omega}{2\pi}\, \ln\left(1 - 2\pi i\, \frac{\partial^2\omega_{01}}{\partial\lambda^2}\, S_\lambda(\omega)\right) \tag{4.42}$$

i.e.

$$f^{\rm hf}_{z,R}(t) \approx \exp\left(-(\pi/2)(\partial^2\omega_{01}/\partial\lambda^2)At\right).$$

The decay at long time should thus be exponential in this case.

The crossover between the algebraic decay and the exponential one happens at a time t_c, and is observed only if $t_c < T_2$.

Note that the experimentally quantity to monitor is a spin component, say $\langle\sigma_x\rangle$, in the rotating frame which evolves according to $\langle\sigma_x\rangle = {\rm Re}[f_{z,R}(t)\; e^{i\Delta\omega t}]$, where $\Delta\omega$ is the detuning frequency. In a typical situation of interest $f_{z,R}(t)$ changes more slowly than the period of oscillations, and thus the envelope of the decaying oscillations is given by $|f_{z,R}(t)|$, the phase of $f_{z,R}(t)$ shifting the phase of the oscillations. In the opposite limit $\Delta\omega = 0$, the measured decay curve reproduces the real part of $f_{z,R}(t)$ (the imaginary part corresponds to σ_y and could also be measured).

Static case: In the quasistatic case, that is, when $\omega_c \ll \Gamma_\phi$, i.e. when ω_c is lower than $1/t$ for all relevant times, the Ramsey decay is simply given by the static contribution (4.39). At all relevant times the decay is algebraic and the crossover to the exponential law is not observed. More generally, in the static approximation with a distribution $P(\delta\lambda)$, the dephasing law is given by the Fresnel-type integral transform

$$f^{\rm st}_{z,R}(t) = \int d\,(\delta\lambda)\, P(\delta\lambda)\, e^{i\,(\,\partial^2\omega_{01}/2\partial\lambda^2)\,\delta\lambda^2\,t}\,, \tag{4.43}$$

which reduces to Eq. (4.39) for a Gaussian $P(\delta\lambda) = 1/\sqrt{2\pi\sigma_\lambda}\exp\left(-\delta\lambda^2/2\sigma^2_\lambda\right)$. In general, any distribution $P(\delta\lambda)$, finite at $\delta\lambda = 0$, which can be approximated by a Gaussian, yields a $t^{-1/2}$ decay for $f^{\rm st}_{z,R}$ at long times.

For a Gaussian quasistatic noise in λ, the echo decay is given by [90]

$$f_{z,E}(t) = \frac{1}{\sqrt{1 + (\,\partial^2\omega_{01}/\partial\lambda^2)^2\;\; \sigma^2_\lambda \int_{-\infty}^{+\infty} d\omega\,(\omega t/4)^2\, S_\lambda(\omega)\; t^2}}\,, \tag{4.44}$$

where we assumed that the frequency integral converges at $|\omega| \ll 1/t$. This is the case, for instance, if $S_\lambda(\omega)$ has a sharp cutoff at $\omega_c \ll 1/t$. For $1/f$ noise, $S_\lambda = (A/|\omega|)\theta(\omega_c - |\omega|)$ with $\omega_c \ll 1/t$, Eq. (4.44) yields

$$f_{z,E}(t) = \frac{1}{\sqrt{1 + 1/16\,(\,\partial^2\omega_{01}/\partial\lambda^2)^2\;\;\sigma_\lambda^2\,A\,\omega_c^2\,t^4}}\,. \tag{4.45}$$

Note that this result is sensitive to the precise form of the cutoff. At an optimal working point, the echo decay is thus predicted to be algebraic.

4.2.4 $1/f$ noise: a few strongly coupled fluctuators versus many weakly coupled ones

The background charge fluctuations are induced by random redistributions of charge in the vicinity of the sample, e.g., trapping and release of electrons or by random rearrangements of charged impurities. Many groups have observed this noise with a smooth $1/f$ spectrum in the frequency range from 1 Hz to 1 MHz([89, 87]). Occasionally, single fluctuators were observed, with a significant fraction of the total charge noise [41, 70]. When individual fluctuators play an important role, the noise statistics is non-Gaussian and mesoscopic fluctuations from sample to sample become important. We summarize here some of the results([88, 91]) relevant to this thesis.

The noise $\delta\lambda(t)$ contains contributions from all TLFs:

$$\delta\lambda(t) = \sum_n v_n \sigma_{n,z}(t). \tag{4.46}$$

Every fluctuator switches randomly between two positions, denoted by $\sigma_{n,z} = \pm 1$ with rate γ_n (for simplicity, we assume equal rates in both directions for relevant TLFs) and is coupled to the qubit with a strength v_n. Assuming independant fluctuators to simplify the problem, these random flips create charge telegraphic noise which contributes to the total noise power $S_\lambda = \sum_n S_n$:

$$S_n = \frac{1}{\pi}\,\frac{\gamma_n v_n^2}{\omega^2 + \gamma_n^2}\,. \tag{4.47}$$

For a single fluctuator (longitudinally and linearly coupled to the qubit) the free induction (Ramsey) and the echo decays are given by

$$f_{z,R,n}(t) = e^{-\gamma_n t}\left(\cos\mu_n t + \frac{\gamma_n}{\mu_n}\sin\mu_n t\right), \tag{4.48}$$

and

$$f_{z,E,n}(t) = e^{-\gamma_n t}\left(1 + \frac{\gamma_n}{\mu_n}\sin\mu_n t + \frac{\gamma_n^2}{\mu_n^2}(1 - \cos\mu_n t)\right), \tag{4.49}$$

where $\mu_n \equiv \sqrt{(D_{\lambda,z}v_n)^2 - \gamma_n^2}$. The main effect of a single slow fluctuator $\gamma \ll 1/t$ for every relevant t, is thus to induce a static energy shift of the qubit $\pm\hbar D_{\lambda,z}v_n$ leading to a beating in the Ramsey signal having the envelope: $\cos D_{\lambda,z}v_n t$.

In the case of several independant fluctuators, the decay produced by all the fluctuators is given by the product of the individual contributions, i.e., $f_{z,R}(t) = \Pi_n\, f_{z,R,n}(t)$ and $f_{z,E}(t) = \Pi_n\, f_{z,E,n}(t)$. In the intermediate case of a noise produced or dominated by a few fluctuators, the conditions of the central limit theorem are not satisfied and the distribution of $\delta\lambda(t)$ may be strongly non-Gaussian. Then the simple relation between decoherence and noise power given by $S_\lambda(\omega)$ does not hold and the knowledge of higher orders of the statistics of the noise is needed. In Ref. [91], a continuous distribution of v_n's and γ_n's was considered, with a long tail of the distribution of the coupling strengths v_n such that rare

configurations with very large v_n dominate the ensemble properties. The distribution $P(v,\gamma)$ considered in Ref. [91] is defined in the domain $[v_{min},\infty]\times[\gamma_{min},\gamma_{max}]$ by:

$$P(v,\gamma)=\frac{\xi}{\gamma v^2}\,. \tag{4.50}$$

Assuming the rates γ are exponentially dependant on some barrier height ΔU which is uniformely distributed, then the density of probability of γ follows a $1/\gamma$ law. The broad distribution of coupling constants in $1/v^2$ is similar to the models of spectral diffusion in NMR: two different types of spins A and B interact and the random flip-flop of spin B lead to a random walk of the resonance line of spin A [92, 93].

Let us introduce the parameter $v_{\max}^{\mathrm{typ}}\equiv N v_{\min}$, which gives the typical value of the strongest (closest) fluctuator, with N being the number of fluctuators. Normalization of P to N fluctuators requires that $\xi = v_{\max}^{\mathrm{typ}}/\ln(\gamma_{max}/\gamma_{min})$. For this distribution any quantity whose average value (that is integrals over v's and γ's) is dominated by TLFs with[91] $v\gtrsim v_{\max}^{\mathrm{typ}}$ is not self-averaging, i.e., depends on the particular realization of the environment and has thus considerable sample-to-sample fluctuations. The free induction decay averaged over many sequences repeated on the same sample is described by [91]

$$\ln|f_{z,R}(t)|\propto -D_{\lambda,z}\,\xi\,t\,\ln(\gamma_{max}/\gamma_{min})=-D_{\lambda,z}\,v_{\max}^{\mathrm{typ}}t. \tag{4.51}$$

It is dominated by the fluctuators with strength of order $v\sim v_{\max}^{\mathrm{typ}}$ and is thus not self-averaging. Consequently, the decay is exponential and the decaying rate can have important sample to sample fluctuations.

Similarly, the echo signal on a unique sample but averaged over many repeated experimental sequences is given by [91]

$$\begin{aligned}&\ln|f_{z,E}(t)|\propto -D_{\lambda,z}\,\xi\,\gamma_{max}t^2 \quad \text{for} \quad t<\gamma_{max}^{-1}\\ &\ln|f_{z,E}(t)|\propto -D_{\lambda,z}\,\xi\,t\,[\ln(\gamma_{max}t)+O(1)] \quad \text{for} \quad t>\gamma_{max}^{-1}\,.\end{aligned} \tag{4.52}$$

The situation depends on whether $D_{\lambda,z}\,\xi>\gamma_{max}$ or $D_{\lambda,z}\,\xi<\gamma_{max}$. In the former the dephasing is static (i.e., it happens on a time scale shorter than the flip time of the fastest fluctuators, $1/\gamma_{max}$) and the first line of Eq. (4.52) applies. This gaussian decay is self-averaging because it is dominated by many fluctuators with strength $v\approx\sqrt{\xi\,\gamma_{max}/D_{\lambda,z}}<\xi<v_{\max}^{\mathrm{typ}}$. In the opposite regime $D_{\lambda,z}\,\xi<\gamma_{max}$ the dephasing is due to multiple flips of a few fluctuators and the second line of Eq. (4.52) applies. In this case, the decay is almost exponential and dominated by a small number of fluctuators with strength $v\approx\xi$, which is smaller than $v_{\max}^{\mathrm{typ}}$ only by a logarithmic factor. The decay time thus depends on the particular configuration of the most coupled fluctuators, which can lead to important sample-to-sample fluctuations.

To summarize, in the case of a linear coupling to the noise, if a few strongly coupled fluctuators dominate the dephasing process, we expect a strongly non-Gaussian statistics for the noise generated by such a set of fluctuators. The decays of the free induction and of the echo signals are expected to be exponential and the characteristic decay times should show important sample to sample fluctuations. The decoherence is not self-averaging in the sense that the experimental averaging coming from the data acquisition protocol (10^5 measured events for calculating one switching probability) is not equivalent to the ensemble averaging over all the possible realizations of the qubit environment.

4.2.5 Decoherence during driven evolution

In the presence of a harmonic drive $2\omega_{R0}\cos(\omega t)\widehat{\sigma}_x$, the Hamiltonian is

$$\widehat{H}=-\frac{1}{2}\hbar\left[\omega_{01}\widehat{\sigma}_z+\delta\omega_z\widehat{\sigma}_z+\delta\omega_\perp\widehat{\sigma}_\perp+2\omega_{R0}\cos(\omega t)\widehat{\sigma}_x\right]. \tag{4.53}$$

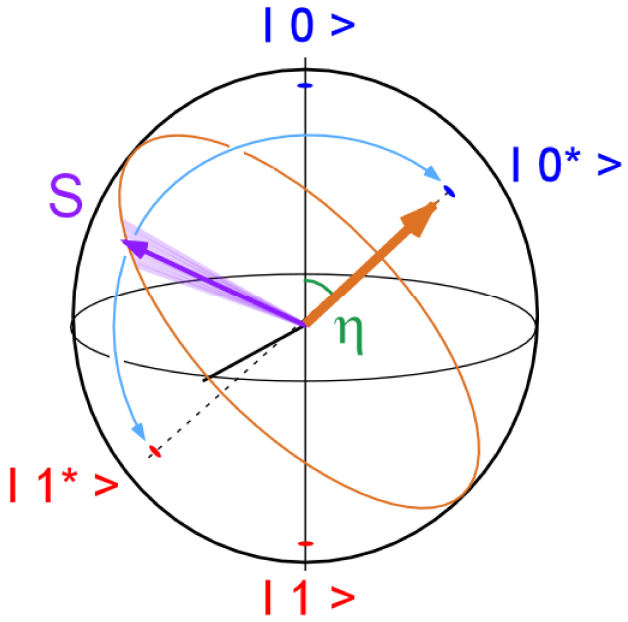

Figure 4.6: Decoherence during driven evolution is conveniently represented in the rotating frame by using the new eigenbasis $\left\{\left|\widetilde{0}\right\rangle, \left|\widetilde{1}\right\rangle\right\}$ of the qubit coupled to the field. Effective rates of relaxation and dephasing $\tilde{\Gamma}_1$ and $\tilde{\Gamma}_\phi$ can be defined with respect to this eigenbasis.

The qubit dynamics is conveniently described in the frame rotating at the driving frequency ω, and a new eigenbasis $\left\{\left|\widetilde{0}\right\rangle, \left|\widetilde{1}\right\rangle\right\}$ is defined by the total static fictitious field composed of a vertical component given by the detuning $\Delta\omega = \omega_{01} - \omega$ and an horizontal (x or y) component ω_{R0}. That is, the static part of the Hamiltonian in the rotating frame reads (see Sec. 3)

$$H_{\rm st} = -\frac{1}{2}\hbar\left[\Delta\omega\widehat{\sigma}_z + \omega_{R0}\widehat{\sigma}_x\right]. \tag{4.54}$$

The length of the total field is $\omega_R = \sqrt{\omega_{R0}^2 + \Delta\omega^2}$ and it makes an angle η with the z-axis: $\Delta\omega = \omega_R\cos\eta$, $\omega_{R0} = \omega_R\sin\eta$. The evolution of the spin is a rotation around the field at the Rabi precession frequency ω_R. As in the case of free evolution, decoherence during driven evolution involves the phenomena of relaxation and dephasing: one defines a relaxation time $\tilde{T}_1$ and a coherence time $\tilde{T}_2$ analogous to T_1 and T_2, which correpond to the decay of the longitudinal and of the transversal part of the density matrix [62] in the new eigenbasis, respectively. First, as a reference point, we present the golden-rule-type results which are valid if all the noises are short correlated and smooth at frequencies $\omega = 0$, ω_R, and ω_{01} on a frequency scale $\widetilde{\Gamma_1}, \widetilde{\Gamma_2}$ (self-consistent condition). Analyzing which parts of the fluctuating fields $\delta\omega_z$ and $\delta\omega_\perp$ are longitudinal and transverse with respect to the total field ω_R in the rotating frame, and taking into account the frequency shifts due to the transformation to the rotating frame one obtain [79]

$$\tilde{\Gamma}_1 = \sin^2\eta\,\Gamma_\nu + \frac{1+\cos^2\eta}{2}\,\Gamma_1\ , \tag{4.55}$$

where $\Gamma_\nu \equiv \pi S_{\delta\omega_z}(\omega_R)$ involves the spectral density at the Rabi frequency ν_R. By studying the decoherence during driven evolution of the qubit, we have thus a way to access the spectral density of the noise of the environment for frequencies extending from $\approx$ 1MHz to $\approx$ 200MHz in our experiment. We have disregarded the difference in the noise power $S_{\delta\omega_\perp}$ at frequencies ω_{01} and $\omega_{01}\pm\omega_R$, which allows us to use the depolarization rate Γ_1 from Eq. (4.24). We do, however, distinguish between Γ_ν and $\Gamma_\varphi = \pi S_{\delta\omega_z}(\omega = 0)$ in order to later analyze a noise spectrum singular at $\omega \approx 0$.

For the dephasing rate we again have the relation

$$\widetilde{\Gamma}_2 = \frac{1}{2}\widetilde{\Gamma}_1 + \widetilde{\Gamma}_\varphi, \tag{4.56}$$

where

$$\tilde{\Gamma}_\varphi = \Gamma_\varphi\cos^2\eta + \frac{1}{2}\Gamma_1\sin^2\eta. \tag{4.57}$$

As a result, we obtain

$$\tilde{\Gamma}_2 = \frac{3-\cos^2\eta}{4}\Gamma_1 + \Gamma_\phi\cos^2\eta + \frac{1}{2}\,\Gamma_\nu\sin^2\eta\ . \tag{4.58}$$

The derivation of these expressions is simplified if one notes that due to the fast rotation at $\omega_{\mu w} \approx \omega_{10}$, the high-frequency transverse noise $S_{\delta\omega_\perp}(\omega \approx \omega_{01})$ is effectively mixed to low frequencies $\lesssim \omega_R$. In the rotating frame it effectively reduces to "independent" white noises in both the x and y directions with amplitudes $\delta\omega_\perp/\sqrt{2}$ and corresponding noise powers $S_{\delta\omega_\perp}(\omega \approx \omega_{01})/2$. Only the noise along the x axis (its longitudinal component with factor $\sin^2\eta$) contributes to $\tilde{\Gamma}_\varphi$ (the noise along the y axis is purely transverse).

Note the limit values of the rates: at zero detuning, $\cos\eta = 0$ and the expression 4.58 yields $\tilde{\Gamma}_2 = \frac{3}{4}\Gamma_1 + \frac{1}{2}\,\Gamma_\nu$, Γ_ϕ is not relevant for the driven evolution in resonance. Actually, the low frequency noise is indeed not irrelevant but at first order only; at second order, it induces fluctuations of the Rabi frequency:

$$\omega_R = \sqrt{\omega_{R0}^2 + \Delta\omega^2} \approx \omega_{R0} + \frac{\Delta\omega^2}{2\omega_{R0}}.$$

Note that if the working point is the optimal one, the noise is thus coupled to the Rabi frequency at fourth order only. One can estimate the amplitude of the fluctuations of the Rabi frequency: for a typical $\Delta\omega = 2\pi 2$MHz corresponding to the minimum resonance line-width, and a Rabi frequency of 100MHz, the fluctuations of the Rabi frequency is $\approx$ 20kHz much smaller than $\widetilde{\Gamma_2}$. These ω_R fluctuations can dominate $\widetilde{\Gamma_2}$ only for very small $\omega_{R0} < \Delta\omega = 2$MHz. Otherwise, in the resonant case, the effect of the very low frequency noise is suppressed and $\tilde{\Gamma}_2$ is given by the Bloch-Redfield theory :$\tilde{\Gamma}_2 = \frac{3}{4}\Gamma_1 + \frac{1}{2}\Gamma_\nu$. At large detuning compared to the Rabi frequency, $\cos\eta = 1$, and $\tilde{\Gamma}_2 = \frac{1}{2}\Gamma_1 + \Gamma_\phi$: one recovers thus the decoherence rate Γ_2 of the free evolution, because the field is unefficient to drive the qubit transition.

For a noise spectrum singular at $\omega = 0$ (i.e. $1/f$ noise), and for $\eta \neq \pi/2$, we no longer find an exponential decay. We consider here only the simple case where the Rabi frequency is high enough to use the rate Γ_ν and the associated exponential decay. Then one should combine the exponential decay associated with the rates Γ_1 and Γ_ν with the nonexponential one substituting the rate Γ_φ. For the decay of the Rabi oscillations we obtain

$$f_{Rabi}(t) = f_{z,\cos\eta}(t) \cdot \exp\left(-\frac{3-\cos^2\eta}{4}\Gamma_1\, t - \frac{1}{2}\sin^2\eta\, t\Gamma_\nu\right) , \tag{4.59}$$

where $f_{z,\cos\eta}(t)$ is given by one of the decay laws derived in the preceding sections (depending on whether the coupling is linear or quadratic, and whether the statistics is Gaussian or not) with the noise $\delta\omega_z$ substituted by $\cos\eta\,\delta\omega_z$. That is, in the linear case, we have to substitute $D_{\lambda,z} \to \cos\eta\, D_{\lambda,z}$, while in the quadratic case $(\partial^2\omega_{01}/\partial\lambda^2) \to \cos\eta\,(\partial^2\omega_{01}/\partial\lambda^2)$.

Application to the fidelity of a single qubit operation

In Sect. 3.4.2, we studied the fidelity of a unitary rotation taking into account the possible systematic errors than can occur during the experimental implementation of the pulse sequence. Here we consider another source of errors coming from the decoherence during driven evolution. This phenomenon induces random errors which alters the unitary character of the implemented operation. For evaluating the fidelity of the practical implementation of this rotation, we will first compare the density matrices of the qubit state after an ideal Rabi precession during a time t, which is equivalent to a rotation of angle $\theta = \omega_R t$, and after its experimental realisation. We consider here only the case $\eta = \pi/2$. Starting form the initial state $\alpha|\widetilde{0}\rangle + \beta|\widetilde{1}\rangle$, the density matrix in the basis $\{|\widetilde{0}\rangle, |\widetilde{1}\rangle\}$ should ideally evolves during the applied microwave field, like:

$$\rho_{theo} = \begin{pmatrix} |\alpha|^2 & \alpha^*\beta\exp(-i\omega_R t) \\ \alpha\beta^*\exp(i\omega_R t) & |\beta|^2 \end{pmatrix}$$

whereas practically the density matrix evolves like

$$\rho_{exp} = \begin{pmatrix} \frac{1}{2}(1+(2|\alpha|^2-1)e^{-(\frac{t}{T_1})}) & \alpha^*\beta e^{-(\frac{t}{T_2})}e^{-i\omega_R t} \\ \alpha\beta^* e^{-\frac{t}{T_2}}e^{i\omega_R t} & \frac{1}{2}(1+(2|\beta|^2-1)e^{-\frac{t}{T_1}}) \end{pmatrix}$$

and relaxes to the equilibrium state:

$$\rho_{t\to\infty} = \begin{pmatrix} 1/2 & 0 \\ 0 & 1/2 \end{pmatrix}.$$

A fidelity between this two density matrix can defined as [94]

$$F(\rho_{theo}\rho_{exp}) = Tr(\rho_{theo}\rho_{exp}),$$

and is equal in this case to

$$F = \frac{1}{2}(1-e^{-\frac{t}{T_1}}) + 2|\alpha|^2|\beta|^2 e^{-\frac{t}{T_2}} + (|\alpha|^4+|\beta|^4)e^{-\frac{t}{T_1}}.$$

In the particular case where the initial state is $|0\rangle = (|\widetilde{0}\rangle + |\widetilde{1}\rangle)/\sqrt{2}$, one can calculate the fidelity as a function of the pulse duration:

$$F = \frac{1}{2}(1 + \exp -t/\widetilde{T_2}) \approx 1 - \frac{t}{\widetilde{T_2}}.$$

Note that $\widetilde{T_1}$ is not involved since the state $|0\rangle$ is purely transverse in the eigenbasis $\{|\widetilde{0}\rangle, |\widetilde{1}\rangle\}$. As an example, with a constant time $\widetilde{T_2} \approx 500$ns (see Sect. 4.4), a typical π pulse at a Rabi frequency of 200MHz takes ≈ 2.5ns and is thus characterized by a fidelity of ≈ 0.99, equivalent to a 1% error.

Apart from considering the fidelity of the rotation for a particular initial state, one can also define on average a fidelity for the rotation, by averaging over every initial state for a fixed pulse duration:

$$\overline{F}\,[U(\theta = \omega_R t)] = \frac{1}{2} + \frac{1}{4}e^{-\frac{t}{\widetilde{T_1}}} + \frac{1}{4}e^{-\frac{t}{\widetilde{T_2}}} \approx 1 - \frac{1}{4}(\frac{1}{\widetilde{T_1}} + \frac{1}{\widetilde{T_2}})t, \tag{4.60}$$

for short pulses.

4.3 Experimental characterization of decoherence during free evolution

In order to characterize decoherence in our quantronium sample and to compare with the theoretical predictions, we have measured the characteristic decay times of the diagonal (T_1) and nondiagonal (T_2, T_E) parts of the density matrix of the qubit during its free evolution. The switching probability p was measured over $25000 - 60000$ events, chosen to get a small statistical noise: $< 1\%$, with a repetition rate in the $10 - 60$kHz range slow enough to permit recombination of quasiparticles after switching of the readout junction. The measurement of one switching probability thus require about 1s, and the determination of any characteristic quantity like T_1 or T_2 needs several minutes. These measurements are thus sensitive to low frequency noise. In addition, as described in chapter 2, the readout is imperfect, and the shape of the switching curve of the readout junctions as a function of the bias current $p(I_M)$ after a π pulse (see Fig. 2.19) shows that the fidelity loss increases with p, which leads to a slight asymmetry of p oscillations in most of the experiments presented here (see, for instance, the lack of signal at the top of the oscillations on Figs. 4.9 and 4.18 below). This asymmetry limits the accuracy of our decoherence rate measurements. In order to minimize its effect, we have chosen to use the bottom of the envelopes of the p oscillations to quantify decoherence.

The decoherence measurements were done at different working points P located along the lines $\delta = 0$ and $N_g = 1/2$, as mentioned above. We describe now the different experimental protocols that were used, the results, and their interpretation.

4.3.1 Longitudinal relaxation: time T_1.

Relaxation of the longitudinal polarization is inferred from the decay of the switching probability p after a π pulse which has prepared the qubit in state $|1\rangle$. More precisely, a sequence that consists of a π pulse, a variable delay t, and a readout pulse is repeated to determine $p(t)$. An example of the relaxation curve, measured at the working point P_0, is shown in the inset of Fig. 4.7.

As predicted, the relaxation is exponential, with an absolute discrepancy between $p(t)$ and the fit being always smaller than 2%. The relaxation time T_1, varies with the working point as shown in Fig. 4.7: T_1 is about 0.5 μs in the vicinity of P_0 (which is three times shorter than in a previous experiment [95]) and shows rapid variations away from P_0 in the phase direction. Now, it is interesting to note that in the parameter range explored, the matrix element $D_{Ng,\perp}$ of Eq. (4.18) is approximately constant and that the matrix element $D_{\delta/2\pi,\perp}$ of Eq. (4.17) varies smoothly by a factor of only 2 with δ. Consequently, the measured variation of T_1 reflects quite directly the variation with frequency of the

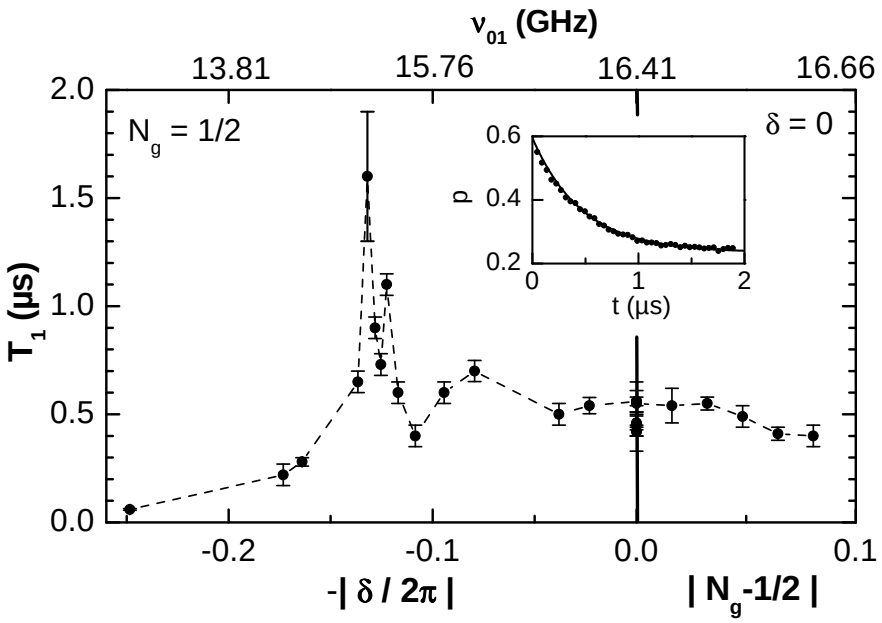

Figure 4.7: Experimental T_1 values measured at $N_g = 1/2$ as a function of δ (left panel), and at $\delta = 0$ as a function of N_g (right panel). The vertical line separating the two panels corresponds to the optimal point $P_0 = (N_g = 1/2, \delta = 0)$. The dashed line joining the points is a guide for the eye. The correspondence between δ, N_g, and ν_{01} is given by the upper horizontal axis. Inset: Example of T_1 measurement. The switching probability p (dots) is measured as a a function of the delay t between a π pulse and the readout pulse. The fit by an exponential (full line) leads to T_1 (0.5 μs at P_0 in this example)

density of environmental modes available for absorbing one photon $\hbar\omega_{01}$ from the qubit through the δ and N_g channels. Noting from Eq. (4.19) that the noise on E_J cannot induce relaxation of the qubit along the line $N_g = 1/2$, a natural question arises: can the measured relaxation rates be fully accounted for by the circuit alone, i.e. by Z_g and Y_R (see Fig. 4.1)? The values of T_1 at P_0 due to the noise spectra generated by (4.2),(4.3) are about $1-2$ and $3-6$ μs respectively. The combined effect of the two subcircuits gives thus $T_1 \sim 0.8 - 1.6\ \mu s$, which is close to the measured value. We conclude that a significant part of the relaxation is due to the gate circuit. Note however, that estimating the impedances as seen from the qubit above 14 GHz with an accuracy better than a factor of 2 is difficult, so that we can't exclude also a large contribution of microscopic degrees of freedom.

4.3.2 Transverse relaxation: coherence time T_2.

T_2 measurement from Ramsey fringes

Characterizing decoherence during the free evolution of a qubit can be done directly by measuring the temporal decay of the average transverse polarization of its effective spin. With a projective readout, this information can only be obtained by repeating a sequence which consists in preparing first a particular state with a nonzero transverse polarization, letting the spin evolve freely during a time Δt, and then reading one of its transverse components. Starting from state $|0\rangle$, the simplest experiment would consist in applying a $\pi/2$ pulse to align the spin along the X axis of the Bloch sphere, and for measurement projecting it onto X after the desired free evolution. Such an experiment is not possible with the quantronium, which is projected onto the Z axis at readout. The phase φ accumulated during the free precession has thus to be converted into a polarization along Z, which can be done by applying a second $\pi/2$ pulse. The two $\pi/2$ pulses form the so-called Ramsey sequence [95] which gives an oscillation of the Z polarization with Δt at the detuning frequency $\Delta\omega/2\pi$. Although choosing $\Delta\omega = 0$ gives a simple non oscillatory signal that decays in principle as $\{1 + e^{-\Gamma_1 \Delta t/2} \mathrm{Re}\,[f_{z,R}(\Delta t)]\}/2$ (see Sect. 4.2), this choice is inconvenient since any residual detuning would induce a very slow oscillation that could be taken the wrong way as an intrinsic decay. For that reason, we use here a detuning $\Delta\omega$ of several tens of MHz, chosen to be much larger than the decoherence rate. The rotation axis of the spin during the $\pi/2$ pulses makes an angle $\alpha = \arctan(\Delta\omega/\omega_{R0})$ with the equatorial plane of the Bloch sphere. The rotation angle of the so-called $\pi/2$ pulses is more exactly $\pi/2(1+\epsilon)$, where ϵ is a small positive or negative correction due to two effects. First, the pulse duration is optimized at zero detuning, by maximizing the switching probability of the readout junction immediately after two adjacent $\pi/2$ pulses. This duration is then kept constant for a Ramsey experiment at finite detuning, so that ideally, $0 \leq \epsilon = \sqrt{1+\tan(\alpha)^2} - 1 \lesssim 10^{-2}$. Second, the optimization procedure is done with a finite accuracy and ϵ can be different from this ideal value. The Ramsey oscillation p_R is given by

$$p_R = \frac{1-a}{2}[1 + a\ e^{-\Delta t/T_1} + (1+a)\ e^{-\Delta t/2T_1}\,|f_{z,R}(\Delta t)| \cos\left(\Delta\omega\Delta t + \zeta\right)], \tag{4.61}$$

where $a = \sin^2\alpha - \sin\epsilon(1-\sin^2\alpha)$ and $\zeta = \arctan\left[\sin\alpha\,(1+\sin\varepsilon)\,/\cos\epsilon\right]$ are geometrical corrections. Note that, at large Δt, the envelope of the oscillations has an amplitude and a saturation value that depends on $\Delta\omega$.

Figure 4.8 shows two typical Ramsey signals measured at the optimal working point P_0 with $\omega_{R0}/2\pi =$ 106 MHz and $\Delta\nu = 50$ MHz. These two signals differ significantly although they were recorded the same day with the same experimental protocol: N_g is first tuned so that the central frequency of the spectroscopic line is minimum and equal 2MHz. The Ramsey fringes are then recorded at a speed of 1 point per second, the longest record (middle frame of Fig. 4.8) taking thus 15 minutes. The relative nonreproducibility between the two records is typical of what has been observed during several months of experimentation. It is attributed to the frequency drift induced by the $1/f$ charge noise. This drift is partly continuous and partly due to sudden jumps attributed to a few strongly coupled charged TLFs, as

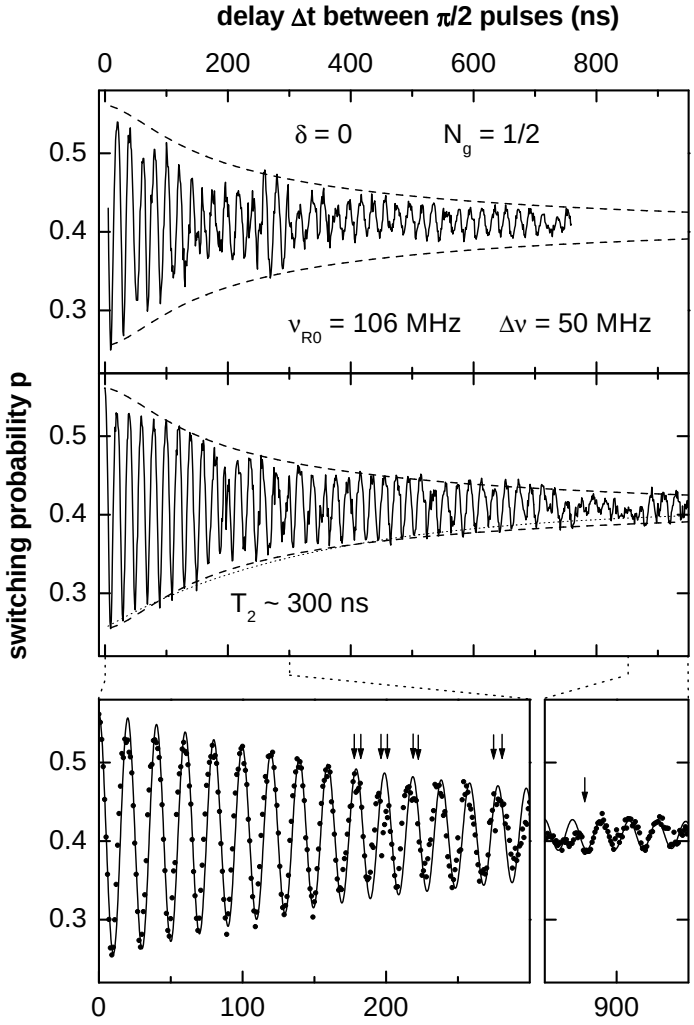

Figure 4.8: Ramsey signals at the optimal point P_0 for $\omega_{R0}/2\pi = 106$ MHz and $\Delta\nu \approx 50$ MHz, as a function of the delay Δt between the two $\pi/2$ pulses. Top and middle panels: solid lines are two successive records showing the partial irreproducibility of the experiment. Dashed lines are a fit of the envelope of the oscillations in the middle panel (see text) leading to $T_2 = 300$ ns. The dotted line shows for comparison an exponential decay with the same T_2. Bottom panels: zoom windows of the middle panel. The dots represent now the experimental points whereas the solid line is a fit of the whole oscillation with $\Delta\omega/2\pi = 50.8$ MHz. Arrows point out a few sudden jumps of the phase and amplitude of the oscillation, attributed to strongly coupled charged TLFs.

mentioned in Sects. 4.1.2 and 4.2. These sudden jumps are reversible and induce correlated phase and amplitude jumps of the Ramsey fringes, as shown by the arrows in the bottom panels of Fig. 4.8, but do not affect the global contrast of the Ramsey signal. On the contrary, the resonance linewidth whose total acquisition time is about 1 min is affected by these very slow fluctuators. The figure also shows a fit of the external envelope of the fringes to Eqs. (4.61) and (4.39), valid for a quadratic coupling to a static charge noise (this choice will be explained in Sect. 4.3.4). The values of T_1 and of the sensitivity to noise Eq. (4.14) being known, the fitting parameters are the amplitude and saturation value of the fringes, and the variance σ_λ^2 of the noise. The corresponding effective T_2 time is 300 ± 50 ns for this record, but it is found to vary in the range $200 - 300$ ns (see, for instance, top panel of Fig. 4.11 below) depending on the ability to set the working point precisely at P_0 and on the probability that the system stays at that point during a full record. Note that taking into account the coupling coefficients to phase and charge noise, the half width of the resonance line: 1MHz gives a rough estimate of the tuning accuracy at the optimal point: 0.7% in N_g and 0.4% in δ.

A series of Ramsey oscillations measured at different working points P is shown in Fig. 4.9. The observed decay law will be discussed in section 4.3.4. Since ω_{01} and therefore ω_{R0} (at constant microwave amplitude) vary with P, the microwave frequency was varied in order to keep $\Delta\omega$ between 40 and 100 MHz and the pulse duration was varied to maintain the rotation angle close to $\pi/2$. Note that the mean level and the amplitude of the oscillations vary due to these $\Delta\omega$ changes. A direct comparison between the Ramsey patterns shows that T_2 decreases dramatically when P is moved away from P_0. More precisely, each curve gives a value $T_2(P)$ with an uncertainty of about 30%, which is plotted on Fig. 4.17 below.

T_2 measurement with the "detuning pulse" method

Probing decoherence at different working points P with the Ramsey method presented above requires recalibrating for each P the frequency and duration of the two $\pi/2$ pulses. Now, the $\pi/2$ pulses and the free evolution period probing decoherence do not have to be performed at the same working point. It is thus experimentally more efficient to perform the $\pi/2$ rotations always at the optimal point P_0 with fixed optimized microwave pulses, and to move adiabatically to any point P where decoherence is to be measured, between these pulses. This scheme, which leads also to the coherence time $T_2(P)$, is referred in the following as the "detuning pulse" method. It has been demonstrated by moving back and forth the working point from P_0 to P with a trapezoidal N_g or δ pulse of duration Δt_2 inserted in the middle of a Ramsey sequence. The experimental setup is similar to the one used for the rotations around the z axis in Sect. 3.3. For pulsing the δ parameter, a trapezoidal pulse of duration Δt_2 generated by an arbitrary waveform generator Agilent 33250 is added to the current bias line with a combiner. The minimum rise time of this pulse is limited by the bandwidth of the current biasing line to $t_r = 60$ns. For pulsing the charge parameter N_g, the microwave excitation line is used and due to the broader bandwidth: DC-20GHz, the rise time of the detuning pulse is here limited only by the rise time of our pulse generator to a minimum value of $t_r = 10$ns. In this two case, the adiabaticity criterion mentioned in Sect. 3.3 is satisfied.

Since the qubit frequency is not the same at P than at P_0, the switching probability oscillates with Δt_2 at a new detuning frequency $\Delta\omega_2(P)$ different from $\Delta\omega$. These oscillations decay with the characteristic time $T_2(P)$. This method, which is of course limited to working points P where $T_2(P) \gtrsim t_r$, has been used in the ranges $|\delta| < 0.1$ and $|N_g - 1/2| < 0.05$. Examples of experimental curves are shown on Figs. 4.10 and 4.11.

Each curve leads to a $T_2(P)$ value with a 50% total uncertainty; these are also shown on Fig. 4.17.

T_2 measurement from resonance line shape

When the decoherence rate becomes comparable to the Rabi frequency, time domain experiments using resonant pulses can no longer be performed and one has to operate in the frequency domain. The

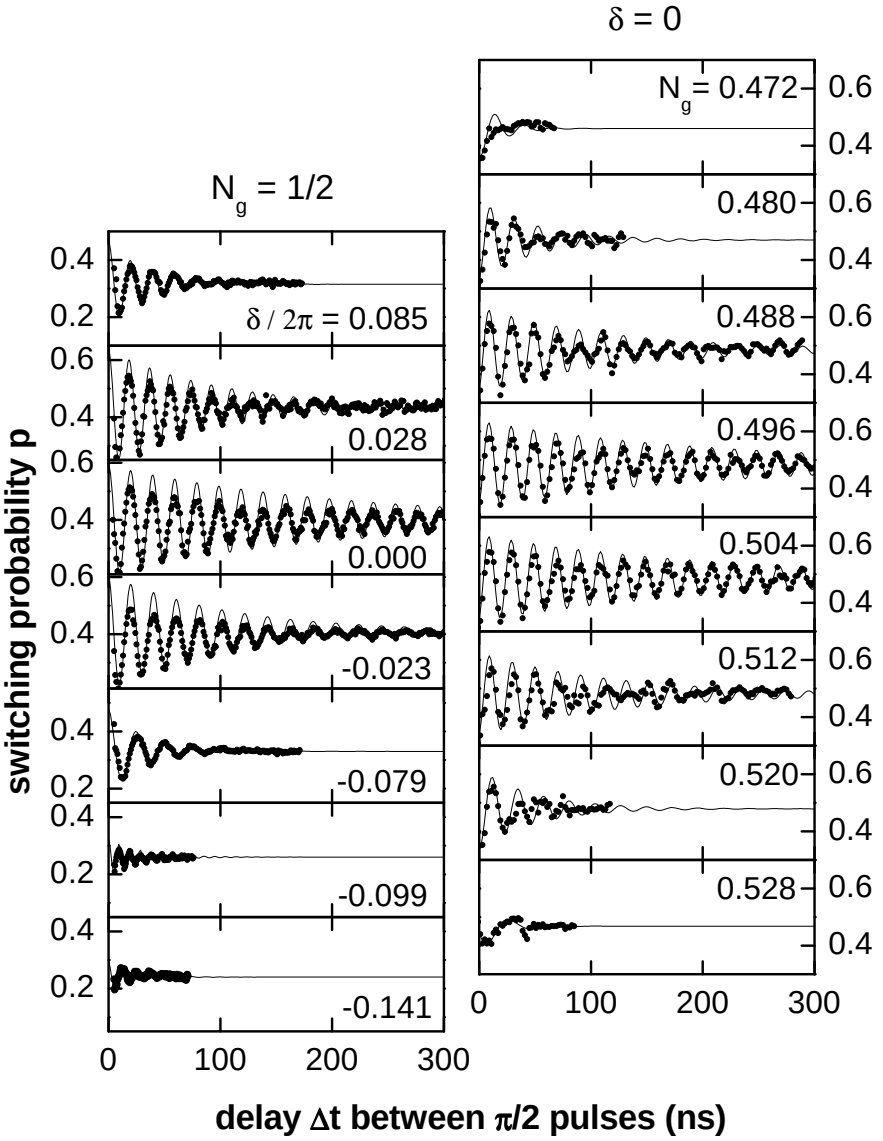

Figure 4.9: Ramsey oscillations as a function of the delay Δt between the two $\pi/2$ pulses, for different working points located on the lines $N_g = 1/2$ (left column) and $\delta = 0$ (right column). The Rabi frequency is $\omega_{R0}/2\pi = 162$ MHz for all curves. The nominal detunings $\Delta\nu$ are 50, 53, 50, 50, 40, 100, and 80 MHz (left, top to bottom) and $35 - 39$ MHz (right). Dots are experimental points whereas full lines are exponentially damped sinusoids fitting the experimental results and leading to the T_2 values reported on Fig. 4.17.

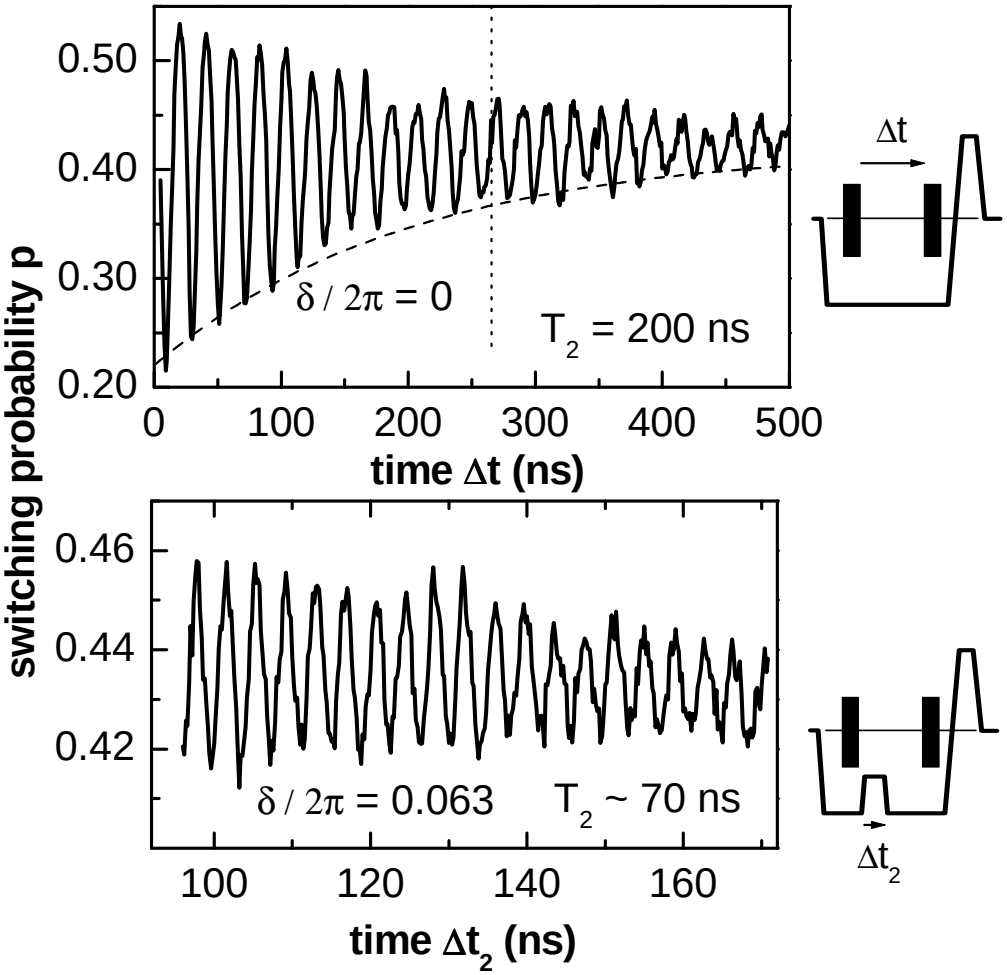

Figure 4.10: Phase detuning pulse technique for measuring T_2. Top: Ramsey signal at the optimal point P_0, with $\Delta\nu \simeq 50$ MHz, when no detuning dc pulse is applied. The dashed line corresponds to an exponential decay with $T_2(P_0) = 200$ ns. Bottom: signal obtained with a delay $\Delta t = 275$ ns between the two $\pi/2$ pulses (corresponding to the dashed vertical line of the upper panel) and with an adiabatic current pulse maintaining $\delta/2\pi = 0.063$ during a time Δt_2. The oscillation of the signal with Δt_2 decays with a characteristic time of about 70 ns (note the different horizontal scales on the two graphs). The pictograms on the right illustrate the two $\pi/2$ microwave pulses and the $I_b(t)$ signal.

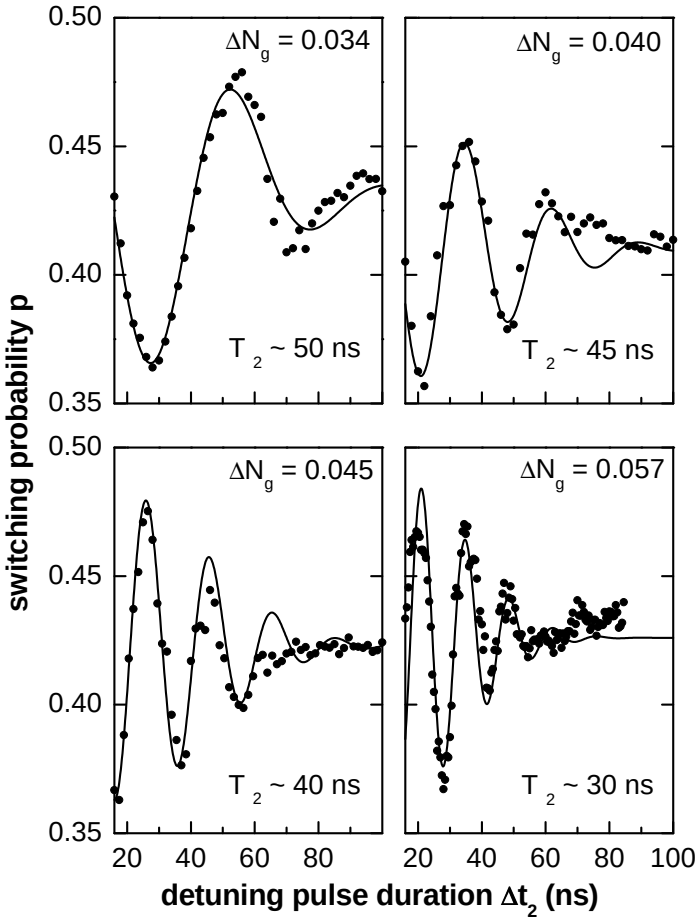

Figure 4.11: Charge detuning pulse technique used for measuring T_2 at four points $P = (0, 1/2 + \Delta N_g)$. Dots are experimental points whereas full lines are fits using Gaussian damped sinusoids at frequencies $\Delta\omega(\Delta N_g)$. The extracted T_2 are indicated on each panel.

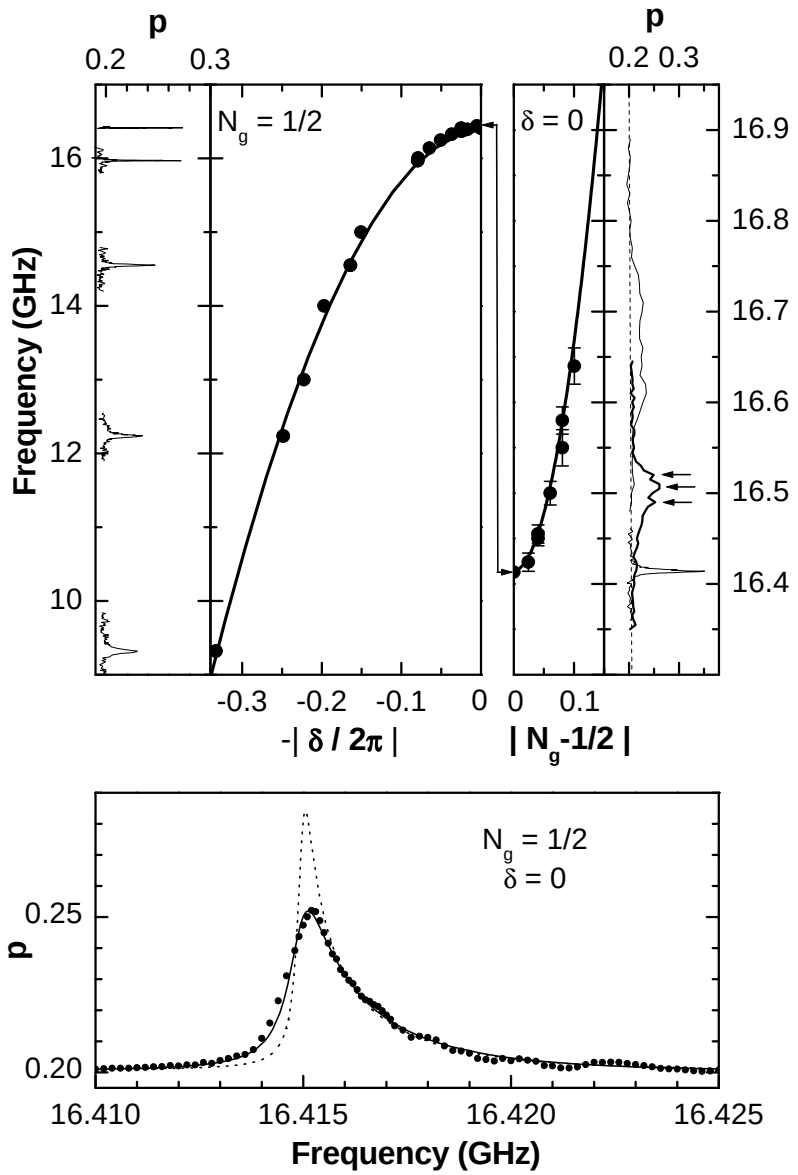

Figure 4.12: Top panels: line shape (thin lines) and central position (dots) of the resonance lines as a function of δ at $N_g = 1/2$ (left) and as a function of N_g at $\delta = 0$ (right). The optimal point P_0 corresponds to the double arrow in the center of the graph. Note the two different vertical scales and the occasional substructure of resonance lines pointed out by small arrows. Bold lines are fits of the peak positions leading to $E_J = 0.87 k_B$ K, $E_C = 0.66 k_B$ K, and $d < 13\%$. Bottom panel: asymmetric lineshape recorded (dots) at P_0 with a microwave power small enough to desaturate the line. The dashed line is the theory, with a T_φ that corresponds to that of Fig. 4.8. The solid line is the convolution of this theoretical line and of a Lorentzian corresponding to a decay time of 600 ns (see text).

resonance line of the qubit is recorded by applying long microwave pulses ($\approx 2\mu$s) and measuring the switching probability of the readout junction after such pulses.

In the linear response regime, i.e. at low microwave power, the shape of the resonance line is ideally the Fourier transform of the envelope of the free evolution decay (i.e. the Ramsey signal). Practically, this is not striclty true due to the different acquisition times of the two methods: Ramsey experiment and resonance line measurement.

Ideally, one has $T_2 = k/(\pi W)$ with W the resonance full width at half maximum and k a numerical coefficient that depends on the line shape: $k = 1$ for a Lorentzian, $k = 1.6$ for a Gaussian, etc. In order to reach the linear regime, the line shape is recorded at different decreasing microwave powers until the width saturates at the lower value. At that stage, the signal to noise ratio is usually small and the line shape has to be averaged over a few minutes. A series of resonance lines is shown on Fig. 4.12, together with their positions as a function of the working point (which leads to E_J and E_C as previously mentioned). The rapid broadening of the line when departing from P_0 is clearly visible. Line shapes at $N_g \neq 1/2$ are structured with several sub-peaks that are stable only on time scales of a few minutes. We again attribute this phenomenon to the presence of large individual charged TLF's. At $\delta \neq 0$, the lines are smoother but the low signal to noise ratio in the linear regime does not allow a discrimination between a Lorentzian or a Gaussian shape. We thus calculated a $T_2(P)$ using an intermediate value $k = 1.3$ and with an extra 30% uncertainty. These T_2's with typical uncertainty 50% are also shown on Fig. 4.17. Finally, the line shape at P_0 is averaged over 10 min and is shown on Fig. 4.12. Its exact shape is discussed in Sect. 4.3.4.

4.3.3 Echo time $\mathbf{T}_E$

In NMR [62] the spin-echo technique is a standard way to cancel an inhomogeneous broadening of the spins resonance lines due for instance to the spatial inhomogeneity of the magnetic field [78]. In our case, there is a single spin (i.e., the quantronium) measured repetitively and the echo technique can compensate for a drift of the transition frequency during the time needed (about 1 s) for the repeated measurement to obtain a probability p. The method thus cancels a low-frequency *temporal* inhomogeneity and leads to a more intrinsic coherence time $T_E > T_2$ independent of the measurement time of p. In practice, the spin-echo sequence is a modified Ramsey sequence with an extra π pulse placed just in the middle of the two $\pi/2$ pulses. This π rotation around the same axis as that of the $\pi/2$ pulses makes the spin trajectory along the equator longer or shorter depending on whether ν_{01} increases or decreases (see figure 4.13). Consequently, the random phases accumulated before and after the π pulse compensate exactly if the frequency does not change on the time scale of a sequence. The interaction with low frequency modes the environment can be averaged out coherently via this dynamical decoupling.

In Fig. 4.14, we show a series of echo signals recorded at P_0 by sweeping the delay Δt between the two $\pi/2$ pulses while keeping constant the delay Δt_3 between the π and second $\pi/2$ pulses. This protocol results in an oscillation $p(\Delta t)$ whose amplitude first decays as the usual Ramsey signal, and has then a second maximum at $\Delta t = 2\Delta t_3$. Note that at this precise echo time, the value of p is an oscillation minimum. By taking advantage of the time stability of our pulse sequencer, it was possible to map directly this minimum of p_E by sweeping Δt while keeping the π pulse precisely in the middle of the sequence (Hahn echo experiment), as shown in Fig. 4.15.

Ideally, at zero detuning, this mapping of p_E is expected to increase as $[1 - e^{-\Gamma_1 \Delta t/2} f_{z,E}(\Delta t)]/2$ (see Sect. 4.2). In practice, one has once again to take into account geometric corrections due to the finite detuning, to the finite duration of the $\pi/2$ and π pulses, and to the inaccuracy of their rotation angles. Using the generalized Bloch-Redfield approach, we find

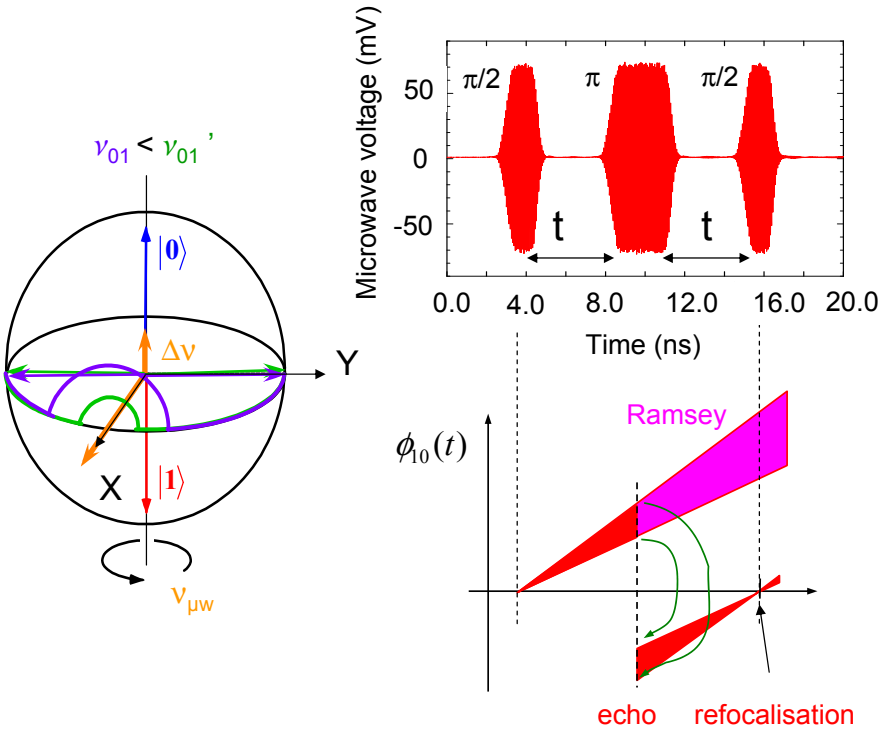

Figure 4.13: Schematics of the echo protocol. After the first $\pi/2$ pulse, the pseudo spin precesses in the equatorial plane and state $|1\rangle$ accumulates a phase $\phi_{10}(t)$ with respect to state $|0\rangle$. Due to low frequency fluctuations of the transition frequency, this phase $\phi_{10}(t)$ for a fixed t diffuses from one sequence to the other around an average value $\langle\omega_{01}\rangle t$. To compensate for this temporal inhomogeneity, an intermediate π pulse, acts like a time reversal, and refocuses the state vectors, obtained after each sequence, at the same position on the Bloch sphere. This echo sequence gives access to a more intrinsic coherence time T_E which is independent of the data acquisition protocol requiring long time averaging.

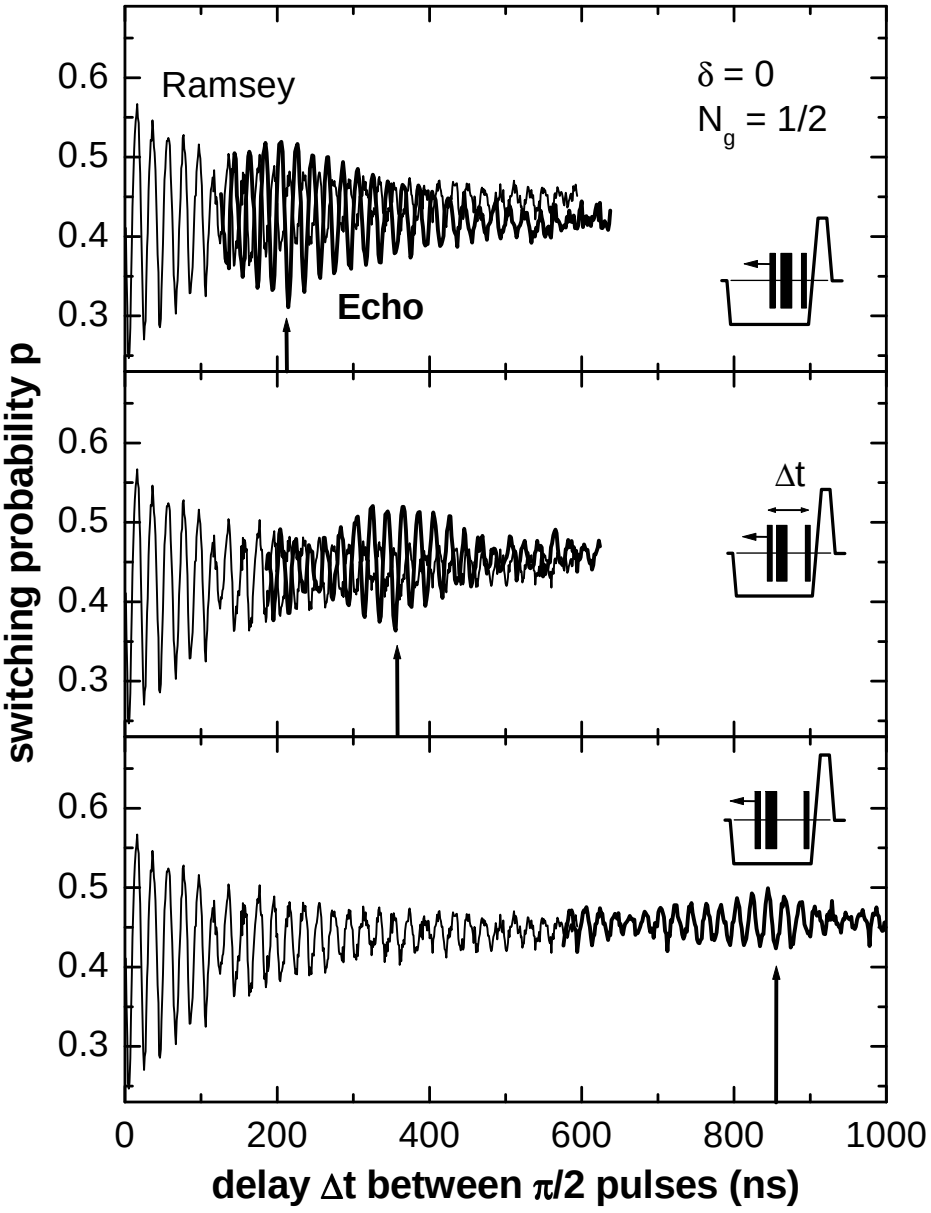

Figure 4.14: Spin echoes (bold lines) obtained at the optimal point P_0 with a detuning $\Delta\nu \simeq 50$ MHz. Pictograms illustrate the experimental protocol: the delay Δt_3 between the π pulse and the last $\pi/2$ pulse is kept constant while altering the timing of the first $\pi/2$ pulse. Each panel corresponds to a different Δt_3. Vertical arrows indicate the sequence duration $\Delta t = 2\Delta t_3$ for which the echo amplitude is expected to be maximal and where $p = p_E$ is minimum. For the sake of comparison, the corresponding Ramsey signal (thin lines) is shown in all panels.

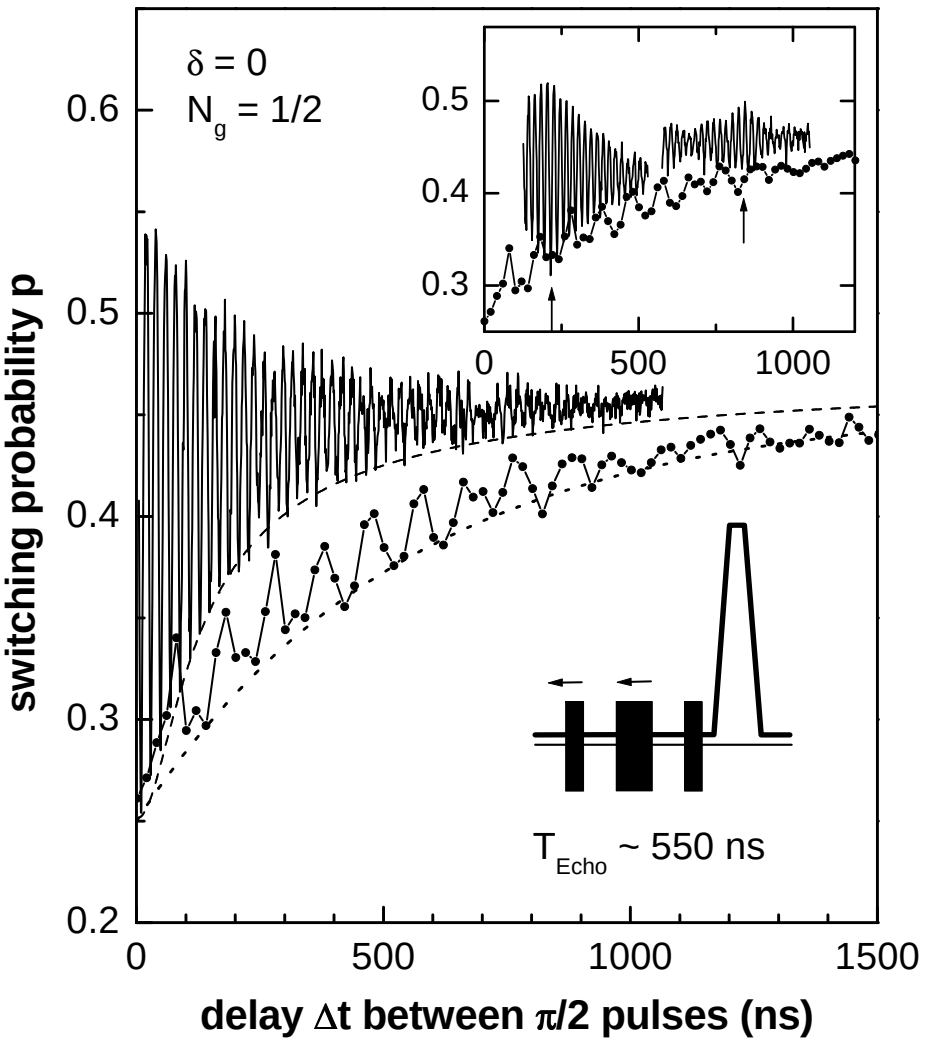

Figure 4.15: Echo signal p_E (linked dots) measured at the optimal point P_0 by keeping a π pulse precisely in the middle of the sequence while sweeping the sequence duration Δt (pictogram). The Rabi frequency is $\omega_{R0}/2\pi = 130$ MHz and the detuning $\Delta\nu = 20$ MHz. For comparison, the Ramsey signal (oscillating line) and its envelope (dashed line leading to $T_\varphi = 450$ ns) are also shown. The dotted line is a fit of p_E that leads to the characteristic decay time of $f_{z,E}$, $T_{\varphi,E}$ =1.3 μs, and that shows that the $\pi/2$ pulses were actually 15% too short whereas the π pulse was correct. The resulting echo time is $T_E \sim 600$ ns. Inset: comparison between p_E (linked dots) and the echo signal recorded with a fixed π pulse (solid line), as presented in Fig. 4.14.

$$2p_E = [1 - (a_1 + a_2 e^{-\Gamma_1 \Delta t/2} + a_3 e^{-\Gamma_1 \Delta t})] \\ - e^{-\Gamma_1 \Delta t/2}\{(1 - a_4)\, f_{z,E}(\Delta t) + a_5 \mathrm{Re}\left[e^{-i(\Delta\omega \Delta t + \xi_1)/2} f_{z,R}(\Delta t)\right] \\ + \left(a_6 e^{-\Gamma_1 \Delta t/4} + a_7 e^{-\Gamma_1 \Delta t/4}\right) \mathrm{Re}\left[e^{-i(\Delta\omega \Delta t + \xi_2)/2} f_{z,R}(\frac{\Delta t}{2})\right]\} \ , \quad (4.62)$$

where the a_i's are small geometrical coefficients that depend only on the angle η coming from the detuning and on the errors in the microwave pulse durations. The latter terms of Eq. (4.62) show that on top of the expected increase of p_E mentioned above, pulse imperfections induce small oscillations of p_E at the frequency $\Delta\omega/4\pi$, which is half the Ramsey frequency, and whose damping is given by the Ramsey function $f_{z,R}$ rather than by the echo function $f_{z,E}$.

Experimental curves $p_E(\Delta t)$ recorded at P_0, and at different working points, are shown on Figs. 4.15 and 4.16, respectively. A fit using Eq. (4.62) is shown on Fig. 4.15 and leads to $T_E(P_0) \simeq 550$ ns $> T_2$, which shows that part of the noise occurs at low frequency and is efficiently removed by the echo technique. Note that a naive exponential fit of the bottom envelope of $p_E(\Delta t)$ would have given about the same T_E. Then, $T_E(P)$ values with a 30% uncertainty are extracted from each curve of Fig. 4.16 and reported on Fig. 4.17. A quantitative analysis of $T_E(P)$ is given below.

4.3.4 Discussion of coherence times

A summary of all the coherence times (T_2, T_E) measured during free evolution using the various methods described above is given on Fig. 4.17. These results are in good agreement with one another and are comparable with those obtained from in previous work [44]. As expected, T_2 is maximum at P_0 and decays by two orders of magnitude for N_g or δ variations of 0.1 Cooper pair or 0.3 phase turn, respectively. This result clearly validates the concept of the optimal working point. Moreover, while T_2 decreases rapidly when departing from P_0, the estimated sensitivity to E_J noise given by Eq. (4.16) either decreases or stays constant. We thus conclude that E_J noise has a negligible contribution to decoherence in this device at all working points except possibly at P_0. Figure 4.17 also shows that the improvement T_E/T_2 provided by the echo technique decreases from a factor of about 2 to about 1 when moving away from P_0 in the phase direction, and increases from about 2 to about 50 when moving in the charge direction. We try below to provide a quantitative understanding of the variations of $T_2(P)$ and $T_E(P)$, using a simple model for the noise spectra $S_\lambda(\omega)$, for $\lambda = \delta/2\pi$ and N_g. Then, we discuss the decay of Ramsey fringes, $p_R(\Delta t)$, and of echo signals, $p_E(\Delta t)$, away from P_0. Finally, we discuss what limits coherence at P_0.

Noise spectral densities and $T_{2,E}(P)$ dependences

The fit to theory of the experimental $T_2(P)$ and $T_E(P)$ curves of Fig. 4.17 is performed in the following way. The dephasing factors f_z are computed numerically according to the theoretical expressions of Sect. 4.2 and multiplied by the relaxation term $\exp[-\Delta t/2T_1(P)]$, which is known from the independent measurements of Fig. 4.3.1; the coherence times correspond to a decay of these products by a factor $\exp(-1)$. As a starting point, the first order contribution of λ noises (considered here as Gaussian) is computed by numerical integration of Eqs. (4.25) and (4.27), using Eqs. (4.11) and (4.13) for the $D_{\lambda,z}$'s. Microscopic charge and phase noises being characterized by $1/f$ spectra at low frequency and noises due to the driving and readout subcircuits being characterized by white spectra below 10 MHz (see Sect. 4.1.3), the fit is done using for $Sc_{Ng}(\omega)$ and $Sc_{\delta/2\pi}(\omega)$ linear combinations of $1/f$ and white spectral densities. Due to the divergence of the $1/f$ contributions as $\omega \to 0$, an infrared cutoff is introduced in the integration, $\omega_{ir} = 1/t_{meas}$, where $t_{meas} = 1$ s is the measurement time of a single data point in a Ramsey or echo signal. Note that although this cutoff could be defined more rigorously by taking into

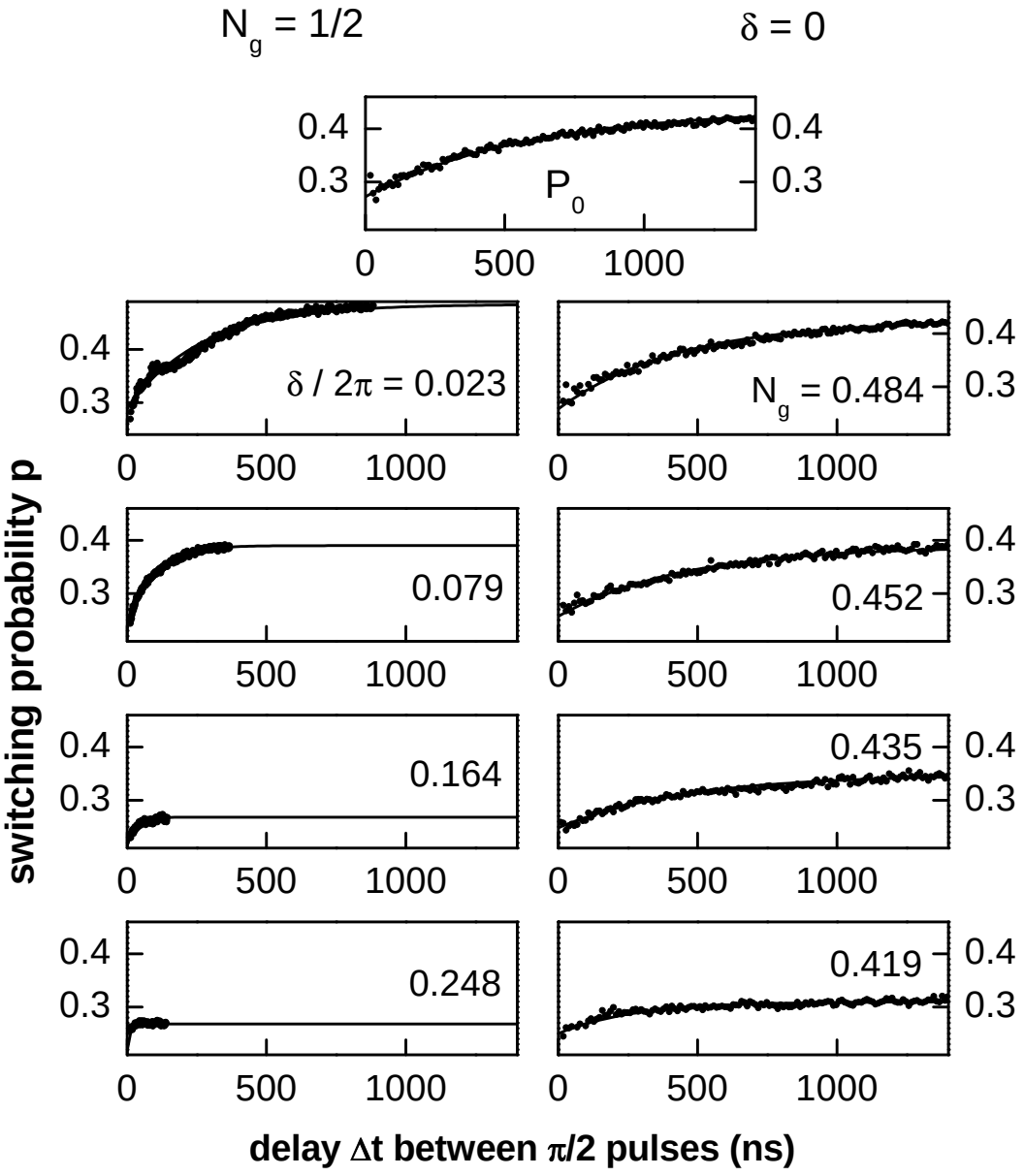

Figure 4.16: Echo signals $p_E(\Delta t)$ measured (dots) at different working points indicated in each panel, with a Rabi frequency $\omega_{R0}/2\pi = 140$ MHz and $\Delta\nu \approx 50$ MHz. Full lines are exponential fits leading to T_E values reported on Fig. 4.17. Note that the amplitude of the signal depends on the working point.

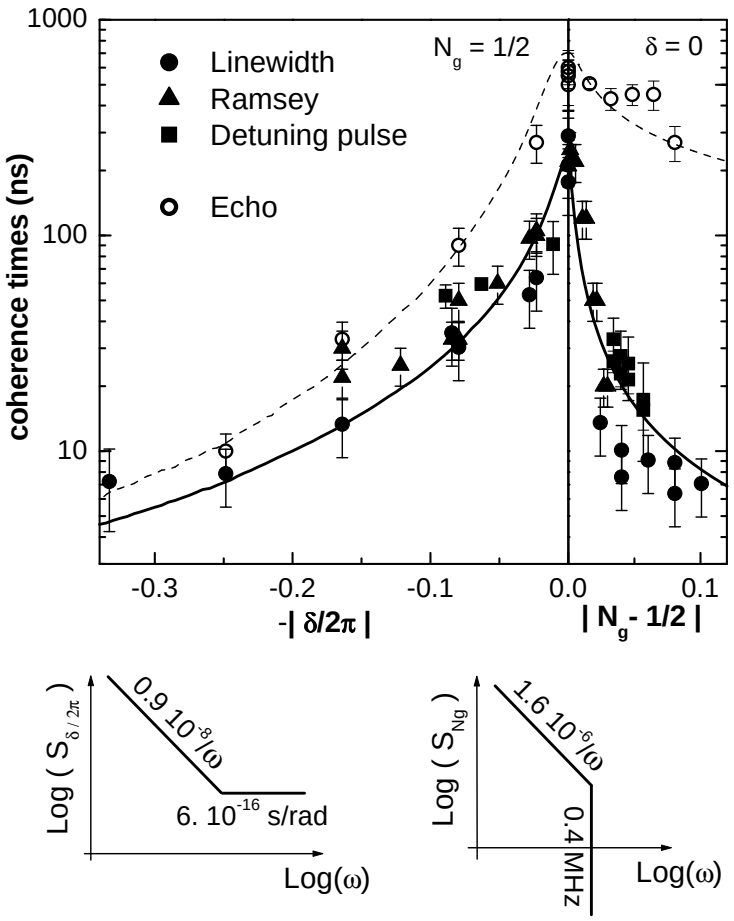

Figure 4.17: Echo times T_E (open circles) and coherence times T_2 measured from the resonance linewidth (solid dots), from the decay of Ramsey signals (triangles), and from the detuning pulse method (squares), at $N_g = 1/2$ as a function of δ (left panel) and at $\delta = 0$ as a function of N_g (right panel). The full and dashed lines are best fits (see text) of T_E and T_2 times, respectively, leading to the phase and charge noise spectral densities depicted at the bottom. The spectra are even functions of ω.

account the exact measuring protocols [44] this complication is of no benefit here because the computed coherence times depend only logarithmically on ω_{ir}. At this stage, the fit (not shown) captures the $T_2(P)$ dependencies but does not capture the large gain $g = T_E/T_2$ observed far from $N_g = 1/2$. This fact was expected since the echo technique is inefficient in the presence of high-frequency noise and because the gain deduced from Eqs. (4.31) and (4.32) in the case of a $1/f$ noise is $g \simeq \sqrt{\ln(t_{meas}/T_\varphi)/\ln(2)} \lessapprox 5$ over the explored range of T_2. Consequently, $S_{Ng}(\omega)$ has to decrease *faster than* $1/f$ above a certain frequency. A high-frequency sharp cutoff ω_c is thus introduced in the spectrum $Sc_{Ng}(\omega)$ as a new fitting parameter. The new fit (not shown) is then in fair agreement with the data except in the vicinity of P_0 where computed coherence times diverge due to the cancellation of the $D_{\lambda,z}$'s. Therefore, second order contributions have now to be included at this point using the $\partial^2\omega_{01}/\partial\lambda^2$'s given by Eqs. (4.12) and (4.14). For the sake of simplicity, λ^2 noises are first treated as Gaussian noises characterized only by their spectral densities S_{λ^2} estimated from the autoconvolution of S_λ (see Sect.4.2.3 and equation 4.37). This approximation leads to dephasing times at P_0 correct within a factor better than 2. By this way, the contribution of δ^2 is shown to be completely negligible with respect to that of N_g^2. The calculation is then performed using Eqs (4.39) and (4.44). Finally, the dephasing factors associated with N_g, δ, and N_g^2 are multiplied together. This procedure neglects the effect of correlations between λ and λ^2, which are relevant only when both contributions are of same order, namely, in a very narrow range in the vicinity of P_0. Moreover, our results are not affected by correlations between N_g and δ, which would exist if both noises were to be due to the same underlying mechanism(see Sect 4.1.3), since the coupling coefficient $\partial^2\omega_{01}/\partial N_g\partial\delta$ for the cross noise $Sc_{Ng-\delta}(\omega)$ is zero along $(\delta, N_g = 1/2)$ and $(\delta = 0, N_g)$ lines for symmetry reasons. The final fit shown on Fig. 4.17 leads to

$$Sc_{Ng}(\omega) = 1.6\ 10^{-6}/|\omega|,$$

for $|\omega| < \omega_c = 2\pi\times$ 0.4 MHz and to

$$Sc_{\delta/2\pi}(\omega) = 0.9 \times 10^{-8}/|\omega| + 6 \times 10^{-16}/(\text{rad/s}).$$

First we discuss the charge noise. The amplitude coefficient for the $1/f$ charge noise is in the range expected for a background charge noise Sc_{Ng}^{BCN} of microscopic origin (see Sect. 4.1.3). The high-frequency cutoff ω_c, necessary to provide even a qualitative fit, is an important result that had not been anticipated and that calls for a direct measurement of charge noise in the megahertz range, perhaps using a rf single-electron-transistor electrometer [96]. The white noise contribution to charge noise due to the gate impedance Z_g, deduced from Eqs. (4.2) and (4.29), provides a very large $T_\varphi > 1$ ms; this is compatible with our assumption of a high-frequency cutoff. Note that this cutoff is only related to the *classical part* of the charge noise and does not preclude the possibility that charge TLFs might absorb energy at high frequencies, and thus relax the qubit [52, 50, 49].

We now turn to the phase noise. The presence of $1/f$ phase noise is similar to the unexplained flux noise found in SQUIDS (see Sect. 4.1.3), although its amplitude corresponds here to a standard deviation $\sigma_{\Phi/\Phi 0}$ about ten times larger (spectral density 100 times larger) than that usually reported [69]. The value of the white phase noise of $\sim 6 \times 10^{-16}/(\text{rad/s})$ is about twice the estimated out-of-equilibrium noise expected from the AWG, whereas the impedance Y_R is expected to contribute by less than one percent to this white spectrum. This white phase noise contribution is responsible for the low efficiency of echoes at $\delta \neq 0$, $N_g = 1/2$.

Temporal decays of Ramsey and echo signals

The phase and charge noise spectra mentioned above imply precise shapes for the temporal variations of Ramsey and echo signals. For $\delta \neq 0$, the dominant contribution to decoherence arises from the first order contribution of the phase noise $Sc_{\delta/2\pi}$. The numerical integration of Eqs. (4.25) and (4.27) predicts that the Ramsey function $f_{z,R}(\Delta t)$ involved in p_R should be close to a Gaussian at small $|\delta|$ where the $1/f$ part

of the δ spectrum dominates the dephasing and should evolve towards an exponential at larger $|\delta|$ where the dephasing time is shorter and the influence of the high frequencies of the white part of the spectrum dominates. For the echo decay, $f_{z,E}(\Delta t)$ is expected to be almost exponential at all points, because of the white noise part of the δ noise. However, the contribution of the relaxation and of the second order noise at small δ on the first hand, and the contribution of the geometrical corrections included in Eqs. (4.61) and (4.62) on the second hand, favor exponential variations at short times $\Delta t < T_{2,E}$. Consequently, we find that the Ramsey signals are expected to decay more or less exponentially, as we observe on the left panels of Fig. 4.9, where the data were phenomenologically fitted by exponentially damped sinusoids. The echo variations shown on the left panels of Fig. 4.16 are exponential as expected, and are fitted accordingly.

For $N_g \neq 1/2$, the dominant contribution to decoherence has been found to be a first order $1/f$ charge noise truncated at 0.4 MHz, which is actually quasistatic according to Sect. 4.1.3, since $\omega_c T_{2,E} \ll 1$. Consequently, if this noise is really Gaussian, $f_{z,R}$ should be given by Eq. (4.33), i.e., purely Gaussian. The decay should fit to Eq. (4.61), which includes the relaxation contribution and geometrical errors. Now, it was found that this equation does not fit the data well, even with unreasonably large geometrical errors, since the decay is slower than a gaussian one at large time $\Delta t > T_2$. Consequently, Fig. 4.9 shows an empirical fit with exponentials. This mismatch between the simple theory and the experiment might be attributed to the non Gaussian character of the $1/f$ charge noise (see Sect. 4.2.4), which is known to contain large discrete TLF's as already mentioned and as observed in the line shapes. Depending on the distribution of these large fluctuators, Eq. (4.51) might be applicable. Our experimental p_R's could be compatible with a model which includes a dominant TLF inducing an initial Gaussian-like decay at short times $\Delta t < T_2$, and a large collection of further TLF's responsible for the exponential-like tail of the decay. In the same way, $f_{z,E}$ is expected to decay as $\exp[-(\Delta t/T_E)^n]$ with $n \geq 3$ if the quasistatic $1/f$ noise is Gaussian. The rather exponential character of the measured p_E's (see the right hand panels of Fig.4.16) also suggests that the non-Gaussian character of the noise lowers the exponent n, as predicted by Eq. (4.52). On the other hand, the higher sensitivity of p_E to geometrical errors (compared to p_R) also favors an exponential decay.

To summarize, the decay times $T_{2,E}$ are well explained, but the temporal dependence of the functions $f_{z,E}(t)$ is not fully accounted for, possibly due to the non-Gaussian character of the charge noise.

Decoherence at the optimal point P_0

Knowing from the fitting procedure that the phase noise gives a negligible contribution to decoherence at P_0, the following question arises: Can the quasistatic $1/f$ charge noise explain quantitatively the Ramsey decay shape at P_0? To answer this question, we plot on Fig. 4.8 the theoretical decay $\exp\left[-\Delta t/2T_1\right] \left\{1 + \left[7.3\left(\Delta t/T_\varphi\right)\right]^2\right\}^{-1/4}$ where the second term is a simple rewriting of Eq. (4.39), with $T_\varphi = 620$ ns calculated from the fitted noise spectrum $Sc_{Ng}(\omega)$. This curve is seen to be in good agreement with the envelope of the best experimental $p_R(\Delta t)$ records. Whereas it is close to an exponential at $\Delta t \lesssim T_2$, it predicts a significantly larger signal at long times, as observed. These results suggest that coherence at the optimal working point P_0 is limited by second order microscopic static charge noise. Do the data in the frequency domain also support this conclusion? First, we observe on Fig. 4.12 that the resonance line at P_0 is asymmetric, which is a key feature of decoherence due to a second order noise at an optimal point. The line has indeed a tail on its higher-frequency side because N_g noise can only increase ν_{01}, which is minimum at P_0. More precisely, the intrinsic theoretical line shape, i.e., the Fourier transform of Eq. (4.39), is nonzero only at $\Delta\nu = \nu - \nu_{01} \geq 0$, is proportional to $\Delta\nu^{-1/2}\exp(-2\pi\Delta\nu T_\varphi/7.3)$ and is to be convolved with the Lorentzian line shape due to relaxation. A subtle point already mentioned for $1/f$ noise is that decoherence data are actually dependent on the exact experimental protocol used to average them. In particular, T_φ depends on the averaging time through the infrared cutoff introduced in the calculation of σ_{Ng} [see Eq. (4.39)]. The 1 Hz cutoff used for interpreting p_R is no longer relevant for interpreting the line shape, which was averaged over several records of 10 min each, with a precise

tuning of N_g before each record. The corresponding cutoff is of order of $1/(600\text{ s})$ and the new T_φ value analogous to the 620 ns used in the time domain is now 415 ns. Figure 4.12 shows the corresponding theoretical line shape, which takes into account this T_φ and T_1. This line is significantly narrower than the experimental one. This mismatch cannot be reduced by changing T_φ (i.e., the infrared cutoff or the noise amplitude) since the line would be broadened only on its right side. Once more, this discrepancy might be attributed to the non Gaussian character of charge noise. To quantify the mismatch, we empirically fit the experimental line to the theoretical one convoluted with an additional Lorentzian. The width of this Lorentzian leading to the best fit corresponds to a characteristic decay time of 600 ns. This characteristic time can be used to place an upper bound for the E_J noise, which is possibly the second source of decoherence at the optimal working point. Indeed, attributing part of the additional contribution to this noise, assuming $Sc_{\delta E_J/E_J} = A/|\omega|$, and applying Eq. (4.25) with the same infrared cutoff as above, leads to $A < (3\times10^{-6})^2$, a value to be compared to the $(0.5\times10^{-6})^2$ mentioned in Sect. 4.1.3. In conclusion, decoherence at P_0 is well explained by microscopic charge noise at second order, the E_J noise contributing at most for 40% and probably much less. Finally, we point out that pure dephasing is efficiently suppressed at P_0 with the echo technique, due to the ultraviolet cutoff of $Sc_{Ng}(\omega)$. Indeed, the measured $T_E = 550$ ns corresponds to a dephasing time $T_{\varphi,E} = 1.3$ μs, partially hidden here by the short T_1 of the sample. A summary of these results is provided in Table I.

4.4 Decoherence during driven evolution

In the presence of a microwave driving voltage, the quantronium dynamics is best described in the rotating frame, as already mentioned in Sect. 4.2.5. Due to decoherence, the precession of the effective spin is progressively dephased after a characteristic coherence time $\tilde{T}_2$ and, after some time $\tilde{T}_1$, the spin is almost depolarized because $\hbar\omega_R \ll kT$ ($T = 20$mK corresponds to about 500MHz) in our experiment. In this section, we will describe the measurements of $\tilde{T}_2$ and $\tilde{T}_1$ at the optimal point P_0. We will compare them to the results of Sect. 4.2.5 and see if they can be understood from the noise spectra introduced in the preceding section.

4.4.1 Coherence time $\tilde{T}_2$ determined from Rabi oscillations

The coherence time during driven evolution is directly obtained from the decay of Rabi oscillations since the ground state $|0\rangle = (\left|\widetilde{0}\right\rangle + \left|\widetilde{1}\right\rangle)/\sqrt{2}$ is a coherent superposition of the eigenstates under driven evolution. A series of Rabi experiments performed at the optimal point P_0 on resonance ($\Delta\omega = 0$) is shown in Fig. 4.18. These decays can be fitted with exponentially damped sinusoids oscillating at ω_{R0}, whose corresponding decay times $\tilde{T}_2$ are reported in Fig. 4.19 as a function of the Rabi frequency $\omega_{R0}/2\pi$, in the range $1-100$ MHz.

The decay time $\tilde{T}_2$ is found to be almost constant at 480 ns under these conditions and gives access to $T_\nu = \Gamma_\nu^{-1} = 1.5\pm0.5$ μs using the equation $\tilde{\Gamma}_2 = 3\Gamma_1/4+\Gamma_\nu/2$. Then, one deduces from $\Gamma_\nu \equiv \pi Sc_{\delta\omega_z}(\omega_{R0})$ that $Sc_{\delta\omega_z}(\omega)$ is, at P_0, constant at about $(1.5-3)\times10^5$ rad/s for every ω in the $1-100$ MHz range. Being obtained at the optimal point, the latter value should be explained either by the first order noise of E_J or by second order noises N_g^2 and δ^2. The E_J noise, being of the $1/f$ type, cannot explain the constant $Sc_{\delta\omega_z}(\omega)$. Then, assuming that the classical noise on Ng is negligible at all frequencies above the low-frequency cutoff of 0.4 MHz found in the previous section, the autoconvolution of $Sc_{Ng}(\omega)$ has a negligible weight in the frequency range considered here and $Sc_{\delta\omega_z}(\omega)$ can only be due the δ^2 noise, whose spectral density is essentially given by the autoconvolution of the white δ noise introduced previously. Using a high-frequency cutoff much higher than 100 MHz indeed leads to a constant $Sc_{\delta\omega_z}(\omega)$ as observed. Nevertheless, we have not found a plausible phase noise spectrum $Sc_{(\delta/2\pi)}(\omega)$ that could account for the measured value of $Sc_{\delta\omega_z}(\omega)$ using Eq. (4.12).

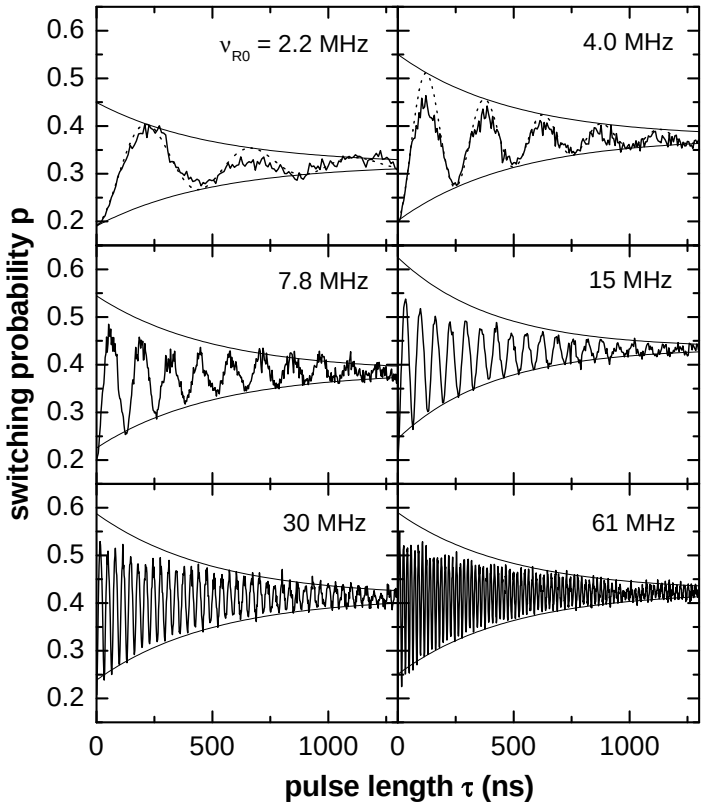

Figure 4.18: Decay of the Rabi signals at the optimal point P_0 for different Rabi frequencies $\nu_{R0} = \omega_{R0}/2\pi$. The experimental data (oscillating solid lines) are fitted by exponentially damped sinusoids (doted lines in the top panels), while their lower envelopes are fitted by exponentials (monotonous solid lines) leading to the $\widetilde{T}_2$ values reported in Fig. 4.19.

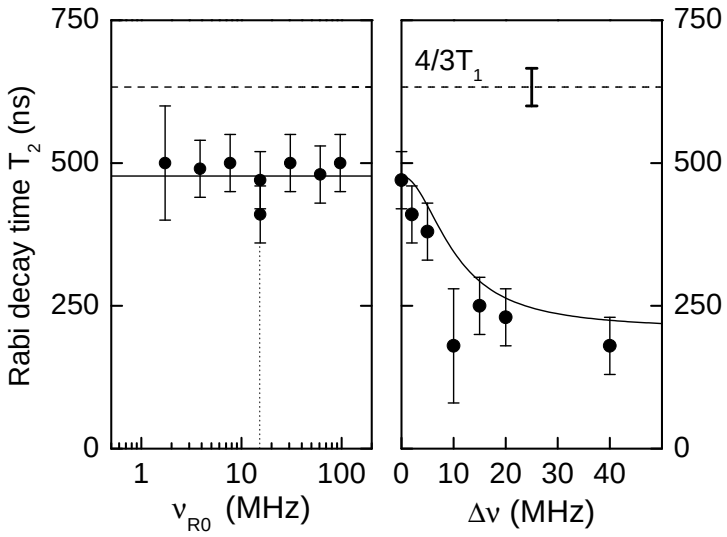

Figure 4.19: Characteristic decay times $\widetilde{T}_2$ of the Rabi oscillations at the optimal point P_0, as a function of the Rabi frequency ν_{R0} (left panel) at zero detuning $\Delta\nu$, and as a function of $\Delta\nu$ (right panel) at $\nu_{R0} = 15.4$ MHz (dotted vertical line). $\widetilde{T}_2(\nu_{R0}, \Delta\nu = 0)$ turns out to be a constant of order 0.48μs (left solid line). The difference with $(4/3)T_1$ leads to an estimate for $T_\nu = 1/\Gamma_\nu$. The right solid line corresponds to Eq. 4.58 plotted using the experimentally determined values of T_φ, T_1, and T_ν.

In order to test the $\tilde{\Gamma}_2(\eta)$ dependence with the frequency detuning, predicted by Eq. (4.58), a series of Rabi precession experiments was also performed at P_0 as a function of the detuning $\Delta\omega$, using a fixed microwave power corresponding to a Rabi frequency of $\omega_{R0}/2\pi = 15.4$ MHz on resonance. The experimental data are presented in Fig. 4.19 together with the expression of $\tilde{\Gamma}_2$ given by Eq. (4.58), plotted using the T_1, T_φ, and T_ν values determined previously. As the frequency detuning $\Delta\omega$ increases, $\widetilde{T_2}$ decreases from 480ns to the value $T_2 \approx 250$ns as predicted, the out of resonance microwave field is less and less efficient and one recovers progressively the free evolution case on a frequency scale which is the Rabi frequency ω_{R0}.

4.4.2 Relaxation time $\tilde{T}_1$ determined from spin-locking experiments

The relaxation time $\tilde{T}_1$ can be obtained using the spin-locking technique developed in NMR. After having prepared the fictitious spin along an axis in the equatorial plane of the Bloch sphere, the effective field is then oriented parallel or antiparallel to the spin. Experimentally, the spin is prepared along the Y axis using a resonant ($\Delta\omega = 0$) $\pi/2$ pulse around the X axis. A microwave gate voltage with a phase shifted by $\pm\pi/2$ is then applied so that the driving field is parallel (or antiparallel) to the prepared spin state, which becomes either $\left|\widetilde{0}\right\rangle$ or $\left|\widetilde{1}\right\rangle$, respectively. The polarization along the prepared direction then decays exponentially with a decay time $\tilde{T}_1$ called in NMR the relaxation time in the rotating frame [62]. A second $\pi/2$ or a $3\pi/2$ pulse is then applied around the X axis after a variable delay in order to measure the remaining polarization in the rotating frame. This decay measured with a locking microwave field of $\omega_{R0}/2\pi = 24$ MHz is shown in Fig. 4.20, together with the envelope of a Ramsey signal measured at $\Delta\omega/2\pi = 8$ MHz and a relaxation signal recorded during free evolution.

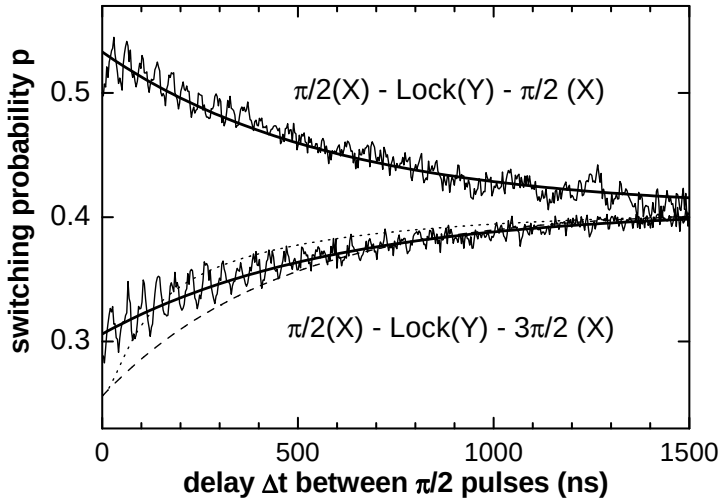

Figure 4.20: Spin locking signals (oscillatory lines) obtained at the optimal point P_0, using a detuning $\Delta\nu = 8$ MHz, a locking microwave power corresponding to 24 MHz, and a final microwave pulse of $\pi/2$ (top) or $3\pi/2$ (bottom). The bold solid lines are exponential fits corresponding to $\widetilde{T}_1 \backsim 580$ ns. For comparison, the Ramsey envelope (dotted line with $T_2 \backsim 250$ ns) and the longitudinal relaxation (dashed line with $T_1 \backsim 450$ ns) are shown.

The evolution of the spin-locking signals toward equilibrium follows an exponential law with $\tilde{T}_1 = 550 \pm 50$ ns, irrespective of whether the spin is parallel or antiparallel to the locking field. This is because the energy splitting $\hbar\omega_{R0}$ of the levels $\left|\widetilde{0}\right\rangle$ and $\left|\widetilde{1}\right\rangle$ in the rotating frame is small, $\hbar\omega_{R0} \ll k_B T$. Using Eq. (4.55) $\tilde{\Gamma}_1 = \Gamma_\nu + \frac{1}{2}\Gamma_1$, one obtains again $T_\nu = 1.5 \pm 0.5$ μs, in agreement with the analysis of Rabi oscillations.

4.5 Decoherence mechanisms in the quantronium: perspectives, and conclusions

4.5.1 Summary of decoherence mechanisms in the quantronium

We have characterized decoherence in the quantronium circuit, using techniques adapted from NMR. We have presented a general framework that describes these experiments. As expected, we have found that quantum coherence of the quantronium is maximum at the so-called optimal point P_0, where the decay laws of the transverse polarization can be significantly non-exponential, particularly in the presence of $1/f$ noise. Similar and complementary analyses of decoherence have now been performed in other Josephson qubits [52, 77, 97]. The noise spectra that characterize the sources was also derived leading to decoherence of the quantronium, at and away from P_0. We have shown that coherence is mainly limited by dephasing due to slow charge and phase noises of microscopic origin and that relaxation also contributes to decoherence.

An important feature of our analysis is the introduction of a *high-frequency cutoff* at about 0.5 MHz for the classical part of the *charge noise* spectrum. Finally, it was shown that in our qubit with $E_J \sim E_C$, second order charge noise is dominant at P_0.

Although this semi-empirical approach obviously could not provide any definite clues about the exact nature of the microscopic defects responsible for the noise spectra invoked to explain decoherence, the subject is very important and deserves further studies. To improve our understanding, more refined models could be built including a finite set of strongly coupled slow TLFs, with a close-to-continuous background of weakly coupled ones, including the non-Gaussian nature of their noise (see Refs. [88, 91]).

Finally, one should point out that some of the NMR methods that we have used to characterize decoherence in our circuit provide tools for improving coherence in a qubit. The interest of maintaining quantum coherence with these methods is now discussed, and how far the qubit is from meeting the requirements for quantum computing.

4.5.2 Does driving the qubit enhance coherence?

The observation that $\tilde{T}_2 > T_2$ suggests that the coherence is improved by driving the qubit. But what are the reason and the meaning of this observation? The improvement is actually due to the low frequency character of the dominant dephasing noise sources. Indeed, the low frequency fluctuations $\Delta\omega$ are not effective when the Rabi frequency is large enough, because the eigenstates $\left|\widetilde{0}\right\rangle$ and $\left|\widetilde{1}\right\rangle$ follow adiabatically the fluctuations of the effective driving field.

When a coherent superposition of these eigenstates is prepared, and a locking field applied afterward, the initial state is frozen with coherence time $\widetilde{T}_2 > T_2$ and mixing time $\tilde{T}_1 > T_1$. Consider now that a coherent superposition of the two eigenstates in the rotating frame, $\alpha\left|\widetilde{0}\right\rangle + \beta\left|\widetilde{1}\right\rangle$, has been prepared and that a Rabi field is applied. The superposition then evolves at the Rabi frequency, and the initial state is retrieved periodically (every Rabi period) with a coherence time $\widetilde{T}_2 > T_2$. By encoding the qubit in the basis $\left(\left|\widetilde{0}\right\rangle, \left|\widetilde{1}\right\rangle\right)$, quantum coherence is thus maintained during a longer time than for free evolution.

Although these results demonstrate that a qubit state can be stored during a longer time by driving it, it is clear that the qubit cannot be used at will during this driven evolution.

The echo technique can also be regarded as a "soft" driving of the qubit aiming at reducing decoherence. As shown in Sect. 4.3.3, it indeed removes the effect of the low-frequency fluctuations of $\Delta\omega$. It can be figured as a time-reversal operation that compensates frequency changes that are almost static over the duration of the pulse sequence. This error cancellation method is in fact more general, and the repeated application of π pulses can compensate for frequency fluctuations over longer durations. This so-called bang-bang technique in NMR [98] could be used for qubits provided that the coherence loss due to the pulses is small enough [86]. However, like in the case of the continuous driving, the qubit cannot be used for computation during this sequence.

4.5.3 Coherence and quantum computing

How far we are from meeting the requirements for quantum computing? Although the simple methods mentioned above could help in reducing decoherence, quantum error correction is mandatory for quantum computing. As discussed in the introduction, quantum error correction requires error rates smaller than about 10^{-4} for each logic gate. Presently, the gate error rate in superconducting qubits is about a few percent for single qubit gates in the quantronium, and would be significantly more for the two qubit gate protocols envisioned nowadays [37, 38, 99]. An improvement of quantum coherence by about three orders of magnitude would thus be required before quantum error correction is possible in quantronium circuits. We think that the mere extrapolation of the present work on superconducting qubits is insufficient to reach this goal, and that new concepts for preserving quantum coherence are needed. Qubit implementation in decoherence free subspaces might provide a solution to this formidable challenge [100].

Decoherence in a superconducting quantum bit circuit

G. Ithier,[1] E. Collin,[1] P. Joyez,[1] P. J. Meeson,[1,2] D. Vion,[1] D. Esteve,[1] F. Chiarello,[3] A. Shnirman,[4] Y. Makhlin,[4,5] J. Schriefl,[4,6] and G. Schön[4]

[1]*Quantronics Group, Service de Physique de l'Etat Condensé, DSM/DRECAM, CEA Saclay, 91191 Gif-sur-Yvette, France*

[2]*Department of Physics, Royal Holloway, University of London, Egham Hill, Egham, Surrey TW20 0EX, United Kingdom*

[3]*Istituto di Fotonica e Nanotecnologia, CNR, Via Cineto Romano, 42 00156 Roma, Italy*

[4]*Institut für Theoretische Festkörperphysik, Universität Karlsruhe, D-76128 Karlsruhe, Germany*

[5]*Landau Institute for Theoretical Physics, Kosygin street 2, 119334 Moscow, Russia*

[6]*Ecole Normale Supérieure de Lyon, 46 Allée d'Italie, 69364 Lyon cedex 07, France*

(Received 12 May 2005; revised manuscript received 22 July 2005; published 24 October 2005)

Decoherence in quantum bit circuits is presently a major limitation to their use for quantum computing purposes. We present experiments, inspired from NMR, that characterize decoherence in a particular superconducting quantum bit circuit, the quantronium. We introduce a general framework for the analysis of decoherence, based on the spectral densities of the noise sources coupled to the qubit. Analysis of our measurements within this framework indicates a simple model for the noise sources acting on the qubit. We discuss various methods to fight decoherence.

DOI: 10.1103/PhysRevB.72.134519 PACS number(s): 74.78.−w, 85.25.Cp, 85.25.Am, 03.65.Yz

I. INTRODUCTION

It has been demonstrated that several types of superconducting circuits based on Josephson junctions are sufficiently quantum that simple manipulations of their quantum state[1–7] can be performed. These circuits are candidates for implementing quantum bits (qubits), which are the basic building blocks of a quantum processor. The coherence time of the quantum state is an important figure of merit, being related to the number of qubit operations that can be performed without error. Despite significant advances in coherence times during recent years, with coherence times of order 0.5 μs reached, decoherence due to the coupling between the quantum circuit and the degrees of freedom of the environment still severely hinders using these circuits for the development of a quantum processor,[8] even with a small number of qubits. Thus the quantitative characterization and understanding of decoherence processes is presently a central issue for the development of qubit circuits. In this work, we present experiments that characterize the sources of decoherence in a particular qubit circuit, the quantronium. We also develop a general framework for the theoretical analysis of such data, a framework that can be adapted to other circuits. We address the problem of decoherence both during the free evolution of the qubit and during its driven evolution when coupled to a small ac excitation. For these two situations, we also consider particular control sequences that aim at maintaining quantum coherence. The analysis of our data leads to a simple model for the spectral densities of the noise sources coupled to the qubit.

The paper is organized as follows. In Sec. II, the quantronium device is introduced and manipulation and readout of its quantum state are described; the experimental setup is presented, and the principal noise sources responsible for decoherence are discussed. In Sec. III, a general framework is introduced for the description of decoherence processes in the two situations of free and driven evolutions, for both linear and quadratic coupling of the qubit to variations in the control parameters. In Secs. IV and V, we report experimental results on the measurement of decoherence in all these situations, and analyze them within the theoretical framework of Sec. III. We introduce methods inspired from nuclear magnetic resonance (NMR), such as spin echoes and spin locking, which probe the spectral density of the noise sources responsible for decoherence. From this we invoke constraints on the spectral density of the noise sources and develop a simple model of environmental noise. We also discuss how to improve the quantum coherence time of a qubit. Then, Sec. VI summarizes what has been learnt with the quantronium on decoherence processes in Josephson qubits, and how to fight decoherence.

II. THE QUANTRONIUM CIRCUIT

A. Principles

The quantronium circuit,[9] described in Fig. 1, combines a split Cooper pair box[10–12] (CPB) that plays the role of a qubit, and a hysteretic current-biased Josephson junction for readout. It consists of a superconducting loop interrupted by two adjacent tunnel junctions with Josephson energies $E_J/2(1\pm d)$, where d is an asymmetry coefficient made as small as possible, and by the readout junction with a Josephson energy $\mathcal{E}_J \gg E_J$. The two small junctions define the superconducting island of the box, whose total capacitance to ground is C_Σ and Cooper pair Coulomb energy $E_C = (2e)^2/2C_\Sigma$. The island is coupled to a voltage source U through a gate capacitance C_g, and an external magnetic flux Φ can be applied to the loop. The biasing parameters are thus the reduced gate charge $N_g = C_g U/2e$, and the reduced flux $\phi = 2\pi\Phi/\Phi_0$ ($\Phi_0 = 2\pi\varphi_0 = h/2e$). The latter determines, together with the bias current I_b, the phase difference δ across the small junctions. Quantum mechanically, the number $\hat{N}$ of excess Cooper pairs on the island and the superconducting phase difference $\hat{\gamma}$ across the readout junction form a set of

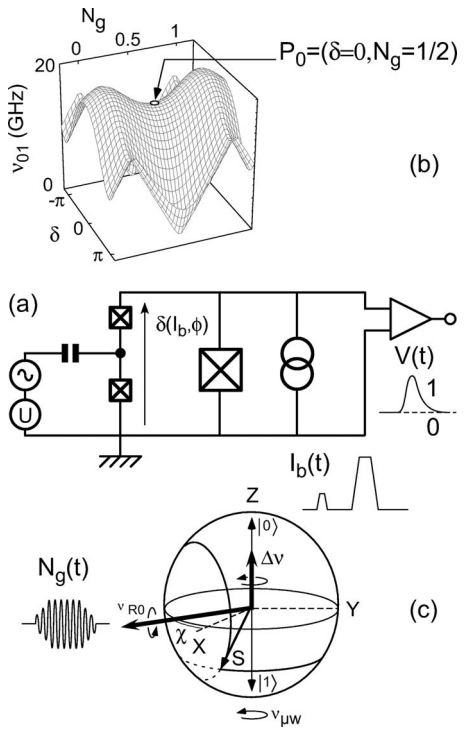

FIG. 1. (a) Circuit diagram of the quantronium. The Hamiltonian of this circuit is controlled by the gate charge $N_g \propto U$ on the island between the two small Josephson junctions and by the phase δ across their series combination. This phase is determined by the flux ϕ imposed through the loop by an external coil, and by the bias current I_b. The two lowest-energy eigenstates form a quantum bit whose state is read out by inducing the switching of the larger readout junction to a finite voltage V with a bias-current pulse $I_b(t)$ approaching its critical current. (b) Qubit transition frequency ν_{01} as a function of δ and N_g. The saddle point P_0 indicated by the arrow is optimal for a coherent manipulation of the qubit. (c) Bloch sphere representation in the rotating frame. The quantum state is manipulated by applying resonant microwave gate pulses $N_g(t)$ with frequency $\nu_{\mu w}$ and phase χ, and/or adiabatic trapezoidal N_g or $I_b(t)$ pulses. Microwave pulses induce a rotation of the effective spin S representing the qubit around an axis in the equatorial plane making an angle χ with X, whereas adiabatic pulses induce rotations around Z.

degrees of freedom that fully characterize the system. Using also their respective conjugate variables $\hat{\theta}$ and $\hat{q}$, together with the phase relation $\hat{\delta}=\hat{\gamma}+\phi$, the Hamiltonian $\hat{H}$ of the CPB and readout parts reads

$$\hat{H} = \hat{H}_{CPB} + \hat{H}_r, \tag{1}$$

$$\hat{H}_{CPB} = E_C(\hat{N} - N_g)^2 - E_J \cos(\hat{\delta}/2)\cos\,\hat{\theta} + dE_J \sin(\hat{\delta}/2)\sin\,\hat{\theta}, \tag{2}$$

$$\hat{H}_r = \mathcal{E}_C \hat{q}^2 - \mathcal{E}_J \cos\,\hat{\gamma} - \varphi_0 I_b \hat{\gamma}. \tag{3}$$

Here $\mathcal{E}_C=(2e)^2/2\mathcal{C}_J$ and $\mathcal{C}_J$ are the Cooper pair Coulomb energy and the capacitance of the readout junction, respectively. The coupling between both subsystems results from the phase constraint given above. Except at readout, when the bias current I_b is extremely close to the critical current $\mathcal{I}_0=\mathcal{E}_J/\varphi_0$ of the readout junction, a full quantum calculation using $\hat{H}$ shows that the quantum nature of $\hat{\gamma}$ can be ignored and that the approximation $\hat{\gamma} \simeq \gamma \simeq \arcsin(I_b/\mathcal{I}_0)$ that neglects the contribution of the current $\langle\hat{i}\rangle$ in the quantronium loop to the current in the readout junction is excellent. The CPB eigenstates are then determined only by N_g and $\hat{\delta} \simeq \delta = \gamma + \phi$. For a large range of N_g and δ, the energy spectrum of $\hat{H}_{CPB}$ is anharmonic and its two lowest-energy eigenstates $|0\rangle$ and $|1\rangle$ define a qubit with energy splitting $\hbar\omega_{01}(\delta,N_g)$. The Hamiltonian $\hat{H}_{qb}$ of this qubit, i.e., the restriction of $\hat{H}_{CPB}$ to the manifold $\{|0\rangle,|1\rangle\}$, is that of a fictitious spin-1/2 particle $\vec{\hat{\sigma}}=\hat{\sigma}_x\vec{x}+\hat{\sigma}_y\vec{y}+\hat{\sigma}_z\vec{z}$ in an effective magnetic field $\vec{H}_0=\hbar\omega_{01}\vec{z}$:

$$\hat{H}_{qb} = -\frac{1}{2}\vec{H}_0\vec{\hat{\sigma}} \tag{4}$$

in an eigenbasis that depends on the working point (δ,N_g). At the point $P_0=(\delta=0,N_g=1/2)$, ω_{01} is stationary with respect to small variations of all the control parameters (see Fig. 1), which makes the quantronium almost immune to decoherence, as previously demonstrated.[2,3] P_0 is therefore an optimal point for manipulating the quantronium state in a coherent way.

1. Manipulation of the quantum state

The manipulation of the quantronium state is achieved by varying the control parameters N_g and/or I_b, either in a resonant way at a microwave angular frequency $\omega_{\mu w}$ close to the transition frequency ω_{01}, or adiabatically. In the resonant scheme, a microwave pulse is applied to the gate and induces the variation $\Delta N_g \cos(\omega_{\mu w}t+\chi)$, where χ is the phase of the microwave with respect to a reference carrier. The qubit dynamics is conveniently described using the Bloch sphere in a frame rotating at $\omega_{\mu w}$ (see Fig. 1), where the effective magnetic field becomes $\vec{H}_0=\hbar\Delta\omega\vec{z}+\hbar\omega_{R0}[\vec{x}\cos\chi+\vec{y}\sin\chi]$, with $\Delta\omega=\omega_{01}-\omega_{\mu w}$ being the detuning and $\omega_{R0}=2E_C\Delta N_g|\langle 1|\hat{N}|0\rangle|/\hbar$ the Rabi frequency. At $\Delta\omega=0$, pure Rabi precession takes place around an axis lying in the equatorial plane and making an angle χ with respect to the X axis. Then, any single-qubit operation can be performed by combining three rotations around the X and Y axes.[8,13] The sequences used to characterize decoherence in this work involve principally two types of pulses, namely, $\pi/2$ and π rotations around the X or Y axes. Between microwave pulses, the free evolution of the spin corresponds to a rotation around the Z axis at frequency $-\Delta\omega$. Such Z rotations can also be induced with the adiabatic method,[13] that is, by adiabatically varying the transition frequency. This can be achieved by applying a pulse that satisfies the adiabaticity criterion[14] $|d\lambda/dt\langle 1|\partial\hat{H}_{qb}/\partial\lambda|0\rangle|/(\hbar\omega_{01}) \ll \omega_{01}$ to one of the reduced parameters $\lambda=N_g$ or $\lambda=\delta/2\pi$.

2. Readout

For readout, the quantronium state is projected onto the $|0\rangle$ and $|1\rangle$ states, which are then discriminated through the

difference in their supercurrents $\langle\hat{i}\rangle$ in the loop.[2] The readout junction is actually used to transfer adiabatically the information about the quantum state of the qubit onto the phase γ, in analogy with the Stern and Gerlach experiment, in which the spin state of a silver atom is entangled with its transverse position. For this transfer, a trapezoidal bias current pulse $I_b(t)$ with a maximum value I_M slightly below $\mathcal{I}_0$ is applied to the circuit. Starting from $\delta=0$, the phases γ and δ grow during the current pulse and the state-dependent supercurrent $\langle\hat{i}\rangle$ develops in the loop. This current adds algebraically to I_b in the large junction and thus modifies its switching rate Γ. By precisely adjusting I_M and the duration of the pulse, the large junction switches during the pulse to a finite voltage state with a large probability p_1 for state $|1\rangle$ and with a small probability p_0 for state $|0\rangle$.[9] A switching or non-switching event is detected by measuring the voltage across the readout junction with a room temperature amplifier, and the switching probability p is determined by repeating the experiment. Note that at the temperature used in this work, and for the readout junction parameters, switching occurs by macroscopic quantum tunneling of the phase γ.[15,16] The theoretical error rate in discriminating the two qubit states is expected to be lower than 5% at temperature $T\leqslant 40$ mK for the parameters of our experiment.[9] Note than the present readout scheme does not implement a quantum non-demolition (QND) measurement since the quantronium quantum states are fully destroyed when the readout junction switches. An alternative quantronium readout designed to be QND has been developed[17] after the present work.

B. Experimental implementation

The quantronium sample used for this work was fabricated using standard *e*-beam lithography and double-angle-shadow evaporation of aluminum. Scanning electron micrographs of its whole loop (with area $\sim 6\ \mu m^2$) and of the island region are shown in Fig. 2 with the schematic experimental setup. The quantronium loop was deposited on top of four gold pads designed to trap spurious quasiparticles in the superconductor, including those generated by the switching of the readout junction. This junction was also connected in parallel to an on-chip interdigitated gold capacitor $\mathcal{C}_J \simeq 0.6$ pF, designed to lower its bare plasma frequency to approximately 7 or 8 GHz. Separate gates with capacitances 40 and 80 aF were used for the dc and microwave N_g signals, respectively. The sample was mounted in a copper shielding box thermally anchored to the mixing chamber of a dilution refrigerator with base temperature 15 mK. The impedance of the microwave gate line as seen from the qubit was defined by 50 Ω attenuators placed at 20 and 600 mK. That of the dc gate line was defined below 100 MHz by a 1 kΩ resistor at 4 K, and its real part was measured to be close to 80 Ω in the 6–17 GHz range explored by the qubit frequency. The bias resistor of the readout junction, $R_b=4.1$ kΩ, was placed at the lowest temperature. Both the current biasing line and the voltage measurement lines were shunted above a few 100 MHz by two surface-mounted 150 Ω–47 pF *RC* shunts located a few millimeters away from the chip. These shunts define the quality factor Q of the readout junction. The external magnetic flux Φ was produced by a superconducting coil with a self-inductance $L=0.12$ H, placed 3 mm from the chip, and whose mutual inductance with the quantronium loop was $M=0.14$ pH. To filter current noise in this coil, a 50 Ω shunt resistor was placed at 1 K. The sample holder and its coil were magnetically shielded by a 3-mm-thick superconducting aluminum cylinder open at one end and supported by a screw from the sample holder. The whole assembly is placed in a second copper box also attached to the mixing chamber.

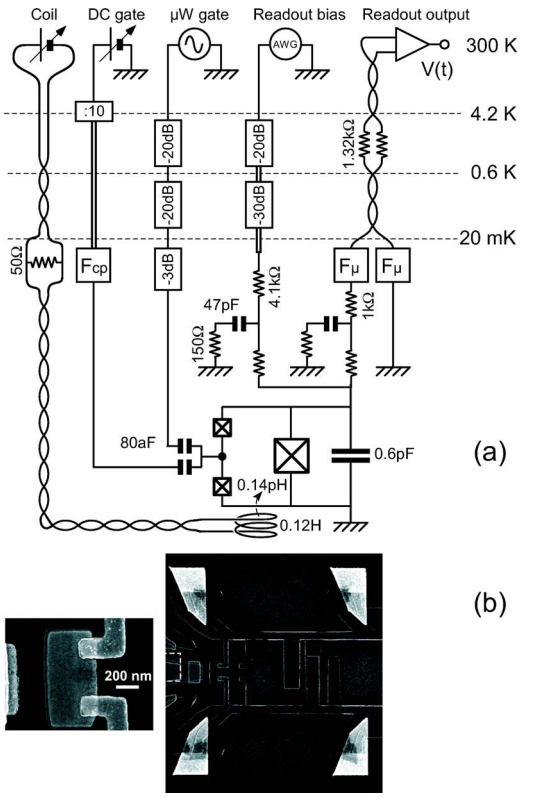

FIG. 2. (Color online) (a) Schematics of the experimental setup used in this work with temperatures indicated on the left. Rectangles labeled in dB are 50 Ω attenuators whereas rectangle labeled :10 is a high-impedance voltage divider by 10. Squares labeled Fcp and $F\mu$ are copper powder filters and microfabricated distributed *RC* filters, respectively. Single lines, double lines, and twisted pairs are 50 Ω coaxes, lossy coaxes made of a manganin wire in a stainless steel tube, and shielded lossy manganin twisted pairs, respectively. (b) Scanning electron microscope pictures of the sample. The whole aluminum loop (right) of about 5.6 μm^2 is defined by 200-nm-wide lines and includes a 890×410 nm^2 island (left) delimited by two 160×160 nm^2 junctions, and a 1.6 $\mu m\times 500$ nm readout junction. Note also the presence of gold quasiparticle traps (bright pads).

The microwave gate pulses used to manipulate the qubit were generated by mixing continuous microwaves with 1 ns rise time trapezoidal pulses with variable duration τ, defined here as the width at half maximum. With the 60 dB attenuation of the microwave gate line, the range of Rabi frequencies ω_{R0} that was explored extends up to 250 MHz. The switching probability p was averaged over 25 000–60 000 events, chosen to obtain good statistics, with a repetition rate

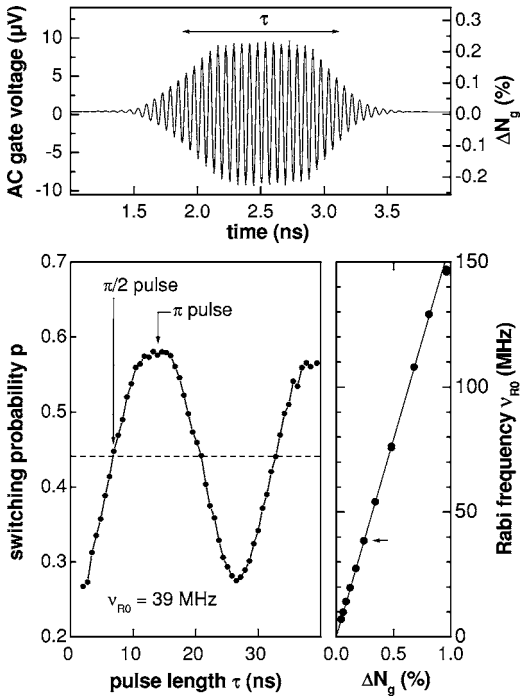

FIG. 3. Top: oscillogram of a typical microwave gate pulse, measured at the top of the cryostat. The arrow indicates the effective duration τ of the pulse. Bottom: the Rabi precession of the qubit state during a microwave pulse results in oscillations of the switching probability p with the pulse length τ, at a frequency $\nu_{R0}=\omega_{R0}/2\pi$ proportional to the reduced microwave amplitude ΔN_g (right). The two arrows in the left panel correspond to the so-called π and $\pi/2$ pulses used throughout this work. The arrow in the right panel indicates the point that corresponds to the data shown in the left panel.

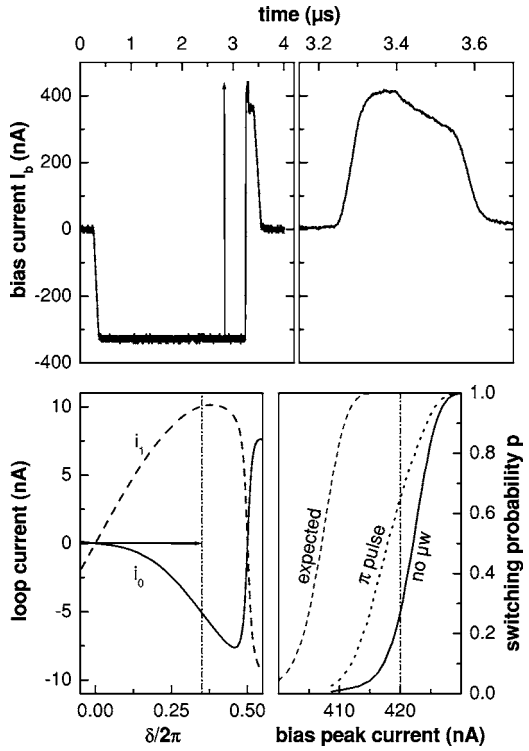

FIG. 4. Readout of the quantronium. Top left: full $I_b(t)$ variation measured at the top of the cryostat, when the qubit is operated at the optimal point (see text) and read out with maximum sensitivity. The current is first kept at zero to avoid heating in the bias resistor, then prebiased at a negative value that corresponds to $\delta=0$, then increased in about 50 ns to a value close to the critical current of the readout junction, and maintained at this value during about 100 ns, a time period over which the switching of the junction may occur. I_b is then slightly lowered and maintained at this lower value to let the voltage develop along the measuring line if the junction has switched. Finally it is set back to zero. Top right: detail of readout pulse (but without negative prebias), measured at room temperature at the bottom of the bias line, before cooling the cryostat. Bottom left: persistent currents in the loop for the $|0\rangle$ (solid line) and $|1\rangle$ (dashed line) states, computed at $N_g=1/2$ as a function of δ, using the measured sample parameters. The vertical dot-dashed line indicates the readout point δ_M where the experimental difference i_1-i_0 was found to be maximum. Bottom right: variation of the switching probability p with respect to the peak current I_M, measured without microwave (solid line), measured after a π microwave pulse (dotted line), and calculated from the sample parameters for state $|1\rangle$ (dashed line). The vertical dot-dashed line indicates a maximum fidelity of 0.4 (instead of the expected 0.95), obtained with the pulse shown in the top-left panel. The two arrows of the upper and lower left panels indicate the adiabatic displacement in δ between operation and readout of the qubit.

in the 10–60 kHz range, slow enough to allow quasiparticle retrapping. The electronic temperature during operation, $T_e\sim 40$ mK, and the relevant parameters $E_J=0.87k_B$ K, $E_C=0.66k_B$ K, $\omega_{01}(P_0)/2\pi=16.41$ GHz, $d\sim 3-4$ %, $\mathcal{I}_0=427$ nA, and $Q\sim 3$ were measured as reported in a previous work[16] by fitting spectroscopic data, such as those shown in Fig. 11 below. Figure 3 shows a typical gate pulse, Rabi oscillations of the switching probability p, and a check of the proportionality between the Rabi frequency ω_{R0} and ΔN_g. The loop currents i_0 and i_1 of the two qubit states, calculated using the values of E_J, E_C, and d mentioned above, are shown in Fig. 4.

The readout was performed with 100 ns wide pulses (Fig. 4) giving a switching probability in the 10–90 % range at $\gamma_M\sim 72°$. At the top of the readout pulse, the phase δ was close to $\delta_M\simeq 0.37\times 2\pi\simeq 130°$, where the difference between the loop currents for the two qubit states is the largest, and where the sensitivity was experimentally maximal. To reach this δ_M value starting from any value δ_{op} where the qubit was operated, we had to set I_b and Φ at the values I_{op} and Φ_{op} such that $\delta_{op}=\Phi_{op}+\gamma_{op}$ and $\delta_M=\Phi_{op}+\gamma_M$. The corresponding bias current I_b pulse when the quantronium is operated at the optimal point P_0 is shown in the top panels of Fig. 4: A negative "prebias" current I_{op} is used to compensate a positive flux. The fidelity η of the measurement, i.e., the largest value of p_1-p_0, was $\eta\approx 0.3-0.4$ in the present series of experiments, as shown in the bottom right panel of Fig. 4. Although η is larger than in our previous work,[2] this fidelity is nevertheless much smaller than the 0.95 expected. This loss, also observed in other Josephson qubits, e.g., Ref. 5, is attributed to spurious relaxation during the adiabatic ramp used to switch the readout on. Indeed, the signal loss after three adjacent short microwave π pulses is approximately

the same as after one. Moreover, it was found in some Josephson qubit experiments[5,18] that the fidelity is improved when increasing the readout speed. The shape of the $p(I_M)$ curve after a π pulse (see Fig. 4) also shows that the fidelity loss increases with p, which leads to a slight asymmetry of p oscillations in most of the experiments presented here (see, for instance, the lack of signal at the top of the oscillations on Figs. 8 and 16 below). This asymmetry limits the accuracy of our decoherence rate measurements. In order to minimize its effect, we have chosen to use the bottom of the envelopes of the p oscillations to quantify decoherence.

C. Decoherence sources

Like any other quantum object, the quantronium qubit is subject to decoherence due to its interaction with uncontrolled degrees of freedom in its environment, including those in the device itself. These degrees of freedom appear as noise induced in the parameters entering the qubit Hamiltonian (2), i.e., the Josephson energy E_J, the gate charge N_g, or the superconducting phase difference δ. Using dimensionless parameters $\lambda = E_J/E_{J0}$ (E_{J0} being the nominal E_J), $\lambda = N_g$, or $\lambda = \delta/(2\pi)$, each noise source is conveniently described by its quantum spectral density $S_\lambda(\omega) \equiv 1/(2\pi)\int dt \langle \delta\hat{\lambda}(0)\delta\hat{\lambda}(t)\rangle e^{-i\omega t}$, where $\delta\hat{\lambda}$ is regarded here as an operator acting on environmental variables. This function quantifies the ability of the source to absorb and to emit an energy quantum $\hbar|\omega|$, at positive and negative ω, respectively. The symmetrized spectral density $Ss_\lambda(\omega) = 1/2[S_\lambda(-\omega) + S_\lambda(\omega)]$ and its classical limit $Sc_\lambda(\omega)$ at $k_B T \gg \hbar\omega$ will also be used. Decoherence of the qubit will be described here in terms of energy exchange with a noise source on one hand, and in terms of random dephasing between states $|0\rangle$ and $|1\rangle$ due to adiabatic variations of the transition frequency on the other hand. Taking into account that $k_B T \ll \hbar\omega_{01}$ in our experiment, we distinguish relaxation processes involving $S_\lambda(+\omega_{01})$ and dephasing processes involving $Sc_\lambda(|\omega| \ll \omega_{01})$. The main noise sources acting in the quantronium are schematically depicted in Fig. 5, and their spectral densities are discussed below. Since "pure" dephasing (see Sec. III) dominates decoherence, special attention is paid to the low-frequency part $Sc_\lambda(\omega \approx 0)$.

1. Noise in E_J: Two-level fluctuators in the tunnel barriers

A first source of decoherence arises from the fluctuations of the Josephson energy E_J of the two small junctions. The associated critical current noise, which has not been measured in our sample, has been characterized, at frequencies f up to 10 kHz and at temperatures T between 100 mK and 4 K, in various Josephson devices[19,20] made of different materials and with different technologies, including those used in this work. The Josephson energy noise is empirically described, for a single junction with critical current $\mathcal{I}_0$, by a $1/f$ spectral density that scales with $\mathcal{I}_0^2$, T^2, and the inverse of the junction area. Extrapolating the results reported in Refs. 19 and 21 to the maximum electronic temperature T_e of the quantronium during its operation, i.e., 40 mK, leads to an estimate for the spectral density of relative E_J fluctuations:

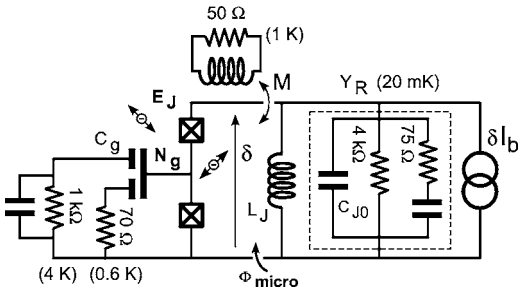

FIG. 5. Equivalent schematic drawing of the noise sources responsible for decoherence in the quantronium. These sources are coupled to E_J, N_g, or δ. In part they are of microscopic nature like the two-level fluctuators inside the junction that induce E_j variations, like a charged TLF (represented as a minus sign in a small double arrow) coupled to N_g, or like moving vortices (Φ_{micro}) in the vicinity of the loop. The macroscopic part of the decoherence sources is the circuitry, which is represented here as an equivalent circuit as seen from the qubit. The relevant resistances and temperatures of the dissipative elements are indicated. Capacitance with no label represent a shunt at the qubit frequency and an open circuit at frequencies below 200 MHz.

$Sc_{\delta E_J/E_J}(|\omega| < 2\pi \times 10\ \text{kHz}) \sim (0.5 \times 10^{-6})^2/|\omega|$. The critical current noise is presently attributed to atomic defects located in the oxide of the tunnel junctions. A simple model assumes that these defects are two-level fluctuators (TLFs) switching between two states that correspond to an open and a closed tunneling channel through the junction. The distribution in the energy splitting of these TLFs is thought to be very broad and to extend above the transition energies of Josephson qubits. This picture is supported by the observation of a coherent coupling between a phase qubit and uncontrolled TLFs randomly distributed in frequency.[22] With the quantronium sample used in this work, the authors have also observed in one of the experimental runs an avoided level crossing in the spectroscopic data, which demonstrated a strong coupling between the qubit and an unknown TLF that was later eliminated by annealing the sample at room temperature. These observations suggest that TLFs located in the tunnel barriers not only generate low-frequency E_J noise, but can also play an important role in the relaxation of Josephson qubits.

2. Noise in N_g: Background charged two-level fluctuators and gate line impedance

A second source of decoherence is the noise on the gate charge N_g. Like any Coulomb blockade device, the quantronium is subject to background charge noise due to microscopic charged TLFs acting as uncontrolled additional N_g sources. Although the whole collection of TLFs produces a noise whose spectral density approximately follows a $1/f$ law,[23–25] telegraph noise due to some well-coupled TLFs can be observed as well.[10] These well-coupled TLFs are, for instance, responsible for the substructure of the quantronium resonance line recorded at $N_g \neq 1/2$ (see Fig. 11). Complementary works[26] have shown that the charged TLFs are partly located in the substrate, partly in the oxide layer covering all the electrodes, and partly in the oxide barriers of the tunnel junctions themselves. It has been suggested that some

TLFs contribute both to the critical current noise and to the charge noise.[27] The typical amplitude A of the spectral density $Sc_{N_g}^{BCN}(|\omega|<2\pi\times 100\ \text{kHz})=A/|\omega|$ depends on temperature, on junction size, and on the screening of the island by the other electrodes. Its value is commonly found in the range $[10^{-6},10^{-7}]$ for the parameters of our experiment. The amount and the energy splitting distribution of charged TLFs in Josephson devices is still unknown at frequencies of the order of ω_{01}, and their role in the relaxation of a Josephson qubit has not been clearly established. Note that a recent work on a CPB qubit[28] suggests that they might contribute significantly to relaxation.

Another cause of charge noise is the finite impedance Z_g (see Fig. 5) of the gate line, which can be treated as a set of harmonic oscillators coupled to $\hat{N}$. As seen from the pure Josephson element of the CPB (junction capacitance not included), the gate circuit is equivalent[3] to an effective impedance Z_{eq} in series with a voltage source $\kappa_g V_g$, with $\kappa_g = C_g/C_\Sigma$. In the weak-coupling limit $\kappa_g \ll 1$ and for all relevant frequencies, one has $\mathrm{Re}(Z_{eq}) \simeq \kappa_g^2 \mathrm{Re}(Z_g)$. At thermal equilibrium, the contribution of the gate line to N_g fluctuations is characterized by the spectral density

$$S_{N_g}^{GL}(\omega) \simeq \kappa_g^2 \frac{\hbar^2\omega}{E_C^2} \frac{\mathrm{Re}[Z_g(\omega)]}{R_k}\left[1+\coth\left(\frac{\hbar\omega}{2k_BT}\right)\right], \quad (5)$$

where $R_k=h/e^2\simeq 26\ \text{k}\Omega$. Using the parameters previously mentioned, we find $Sc_{N_g}^{GL}(|\omega|<2\pi\times 10\ \text{MHz}) \simeq (20\times 10^{-9})^2/(\text{rad/s})$ at low frequency, and $S_{N_g}^{GL}(\omega) \simeq (1-4\times 10^{-9})^2/(\text{rad/s})$ in the 6–17 GHz frequency range. Finally, the out-of-equilibrium noise generated by the dc gate voltage source is fully filtered by the line and does not contribute to decoherence. The conclusion of this analysis is that the background charge noise dominates $S_{N_g}^{GL}(\omega)$ at low frequency.

3. Noise in δ: Magnetic flux noise and readout circuitry

The last source of decoherence encountered is the noise of the superconducting phase δ. One of its contributions is the noise in the macroscopic flux externally applied to the quantronium loop. It is however negligible because the external flux is shielded by a superconducting aluminum cylinder surrounding the sample holder, and because the coupling to the flux coil is weak $\kappa_L=M\,E_J/\varphi_0^2\ll 1$.

A second phase noise source arises from the magnetic vortices moving in the superconducting electrodes of the device. Taking the width ℓ of the aluminum lines used in this work, the depinning field of these vortices[27,29] $B_m\simeq\Phi_0/\ell^2$ is of order 50 mT, a value two orders of magnitude larger than the maximum field we apply, which suggests that vortices should be pinned. Nevertheless, many experiments on superconducting quantum interference devices (SQUIDs) have shown that an extra flux noise whose origin is unknown, and which does not depend on the temperature below a few 100 mK,[30] is always present with a spectral density $Sc_{\delta/2\pi}^{micro}(|\omega|<2\pi\times 1\ \text{kHz})\sim(10\times 10^{-6})^2/|\omega|$.

Finally, the readout circuitry also induces phase fluctuations, due to the admittance Y_R (see Fig. 5) in parallel with the pure Josephson element of the readout junction, and due to the out-of-equilibrium noise of the arbitrary waveform generator (AWG) used. More precisely, when a bias current $I_b<\mathcal{I}_0$ is applied to the quantronium, the effective inductance $\mathcal{L}_J\simeq(\varphi_0/\mathcal{I}_0)/\sqrt{1-(I_b/\mathcal{I}_0)^2}$ of the readout junction converts the current noise produced by Y_R into phase fluctuations characterized by the spectral density

$$S_{\delta/2\pi}^{YR}(\omega)=\frac{1}{64\pi^4}\kappa_J^2\frac{\hbar^2\omega}{E_J^2}\,\mathrm{Re}[Y_\delta(\omega)]R_k\left[1+\coth\left(\frac{\hbar\omega}{2k_BT}\right)\right], \quad (6)$$

where $Y_\delta(\omega)=Y_R(\omega)/|1+j\mathcal{L}_J\omega Y_R(\omega)|^2$ and $\kappa_J=E_J/\mathcal{E}_J$. Using the parameters mentioned in the previous section, we find $Sc_{\delta/2\pi}^{YR}(|\omega|<2\pi\times 10\ \text{MHz})\simeq(2\times 10^{-9})^2/(\text{rad/s})$ and $S_{\delta/2\pi}^{YR}(\omega)\simeq[(20-80)\times 10^{-9}]^2/(\text{rad/s})$ in the 6–17 GHz frequency range. Then, the noise spectrum of our AWG is flat up to 200 MHz, and corresponds to a spectral density $Sc_{\delta/2\pi}^{AWG}(|\omega|)\simeq(15\times 10^{-9}/\cos\gamma)^2/(\text{rad/s})$ that depends on the average phase γ across the readout junction. The conclusion of this analysis is that the phase noise is dominated at low frequency by local sources close to the junction loop, and at the qubit frequency by the contribution of the biasing circuitry.

III. THEORETICAL DESCRIPTION OF DECOHERENCE

We now consider the dynamics of a qubit from a general point of view in two situations: free evolution and evolution driven by a sinusoidal excitation.

In the first case, after initial preparation in a coherent superposition of the two qubit states, the effective spin precesses freely under the influence of the static field $\vec{H}_0$, set by the control parameters λ_0, and of its classical and quantum fluctuations, set by the fluctuations $\delta\lambda$. One distinguishes two time scales, the depolarization time T_1 (dominated at low temperatures by the relaxation to the ground state) for the decay of the diagonal Z component of the spin density matrix, and the decay time T_2 of the off-diagonal part, which is the qubit coherence time. As described in the experimental Section IV, the time T_2 is inferred from the decay of Ramsey oscillations in a two-$\pi/2$-pulse experiment. These Ramsey oscillations are the equivalent of the free induction decay in NMR.[31] Note that this decay can be nonexponential, the time T_2 being then defined by a decay by the factor $\exp(-1)$. In a modified version of the Ramsey experiment, an extra π pulse is applied in the middle of the sequence in order to perform a Hahn echo experiment.[31] The decay time T_E of this echo is longer than T_2, and the enhancement factor provides important information on the spectral density of the noise mechanisms.

In the second case of driven evolution, the decay of the spin density matrix is investigated in the rotating frame. Experimentally, this decay is obtained from spin-locking signals[31] and from Rabi oscillations. It is shown that time scales $\tilde{T}_1$ and $\tilde{T}_2$, similar to T_1 and T_2, describe the dynamics in the rotating frame.[31]

We first start by expanding the Hamiltonian $\hat{H}_{qb}$ of Eq. (4) to second order in the perturbation $\delta\lambda$:

$$\hat{H}_{qb} = -\frac{1}{2}\left(\vec{H}_0(\lambda_0) + \frac{\partial \vec{H}_0}{\partial \lambda}\delta\lambda + \frac{\partial^2 \vec{H}_0}{\partial \lambda^2}\frac{\delta\lambda^2}{2} + \cdots\right)\vec{\hat{\sigma}}. \quad (7)$$

Introducing the notations $\vec{D}_\lambda \equiv (1/\hbar)\partial \vec{H}_0/\partial\lambda$ and $\vec{D}_{\lambda 2} \equiv (1/\hbar)\partial^2 \vec{H}_0/\partial\lambda^2$, one finds in the eigenbasis of $\vec{H}_0(\lambda_0)\vec{\hat{\sigma}}$

$$\hat{H}_{qb} = -\frac{1}{2}\hbar(\omega_{01}\hat{\sigma}_z + \delta\omega_z\hat{\sigma}_z + \delta\omega_\perp\hat{\sigma}_\perp) \quad (8)$$

where $\hbar\omega_{01} \equiv |\vec{H}_0(\lambda_0)|$, $\delta\omega_z \equiv D_{\lambda,z}\delta\lambda + D_{\lambda 2,z}\delta\lambda^2/2 + \cdots$, and $\delta\omega_\perp \equiv D_{\lambda,\perp}\delta\lambda + \cdots$. Here $\sigma_\perp$ denotes the transverse spin components [i.e., the last term in Eq. (8) may include both σ_x and σ_y]. We write explicitly only the terms in the expansion that dominate decoherence (as will become clear below). These coefficients D are related to the derivatives of $\omega_{01}(\lambda)$:

$$\frac{\partial\omega_{01}}{\partial\lambda} = D_{\lambda,z} \quad (9)$$

and

$$D_{\lambda 2,z} = \frac{\partial^2\omega_{01}}{\partial\lambda^2} - \frac{D_{\lambda,\perp}^2}{\omega_{01}}. \quad (10)$$

As discussed below, $\partial\omega_{01}/\partial\lambda$ and $\partial^2\omega_{01}/\partial\lambda^2$ are sufficient to treat the low-frequency noise whereas the calculation of the depolarization rates involves $D_{\lambda,\perp}$.

The Bloch-Redfield theory[32,33] describes the dynamics of two-level systems (spins) in terms of two rates (times): the longitudinal relaxation (depolarization) rate $\Gamma_1 = T_1^{-1}$ and the transverse relaxation (dephasing) rate $\Gamma_2 = T_2^{-1}$. The dephasing process is a combination of effects of the depolarization (Γ_1) and of the so-called pure dephasing. The pure dephasing is usually associated with the inhomogeneous broadening in ensembles of spins, but occurs also for a single spin due to the longitudinal low-frequency noise. It is characterized by the rate Γ_φ. These two processes combine to a rate

$$\Gamma_2 = \frac{1}{2}\Gamma_1 + \Gamma_\varphi. \quad (11)$$

The Bloch-Redfield approach applies only if the noise is short correlated (e.g., white noise) and weak.[31] In more general situations the decay is nonexponential. In particular, when the pure dephasing is dominated by a noise singular near $\omega \approx 0$, the decay law $\exp(-\Gamma_\varphi t)$ is replaced by other decay functions which we denote as $f_{z,\ldots}(t)$ (additional indices … describe the particular experiment). It can be shown[34] that the decays due to the depolarization and the pure dephasing processes factorize, provided the high-frequency noise responsible for the depolarization is regular. That is instead of the exponential decay $e^{-\Gamma_2 t}$ with Γ_2 from Eq. (11), one obtains the decay law $f_{z,\ldots}(t)\exp(-\Gamma_1 t/2)$.

A. Depolarization (T_1)

The depolarization rate $\Gamma_1 = T_1^{-1}$ is given by the sum

$$\Gamma_1 = \Gamma_{rel} + \Gamma_{ex} \quad (12)$$

of the relaxation rate Γ_{rel} and the excitation rate Γ_{ex}. The golden rule gives

$$\Gamma_{rel} = \frac{\pi}{2}S_{\delta\omega_\perp}(\omega_{01}) = \frac{\pi}{2}D_{\lambda,\perp}^2 S_\lambda(\omega_{01}), \quad (13)$$

$$\Gamma_{ex} = \frac{\pi}{2}S_{\delta\omega_\perp}(-\omega_{01}) = \frac{\pi}{2}D_{\lambda,\perp}^2 S_\lambda(-\omega_{01}). \quad (14)$$

Thus

$$\Gamma_1 = \pi S s_{\delta\omega_\perp}(\omega_{01}) = \pi D_{\lambda,\perp}^2 S s_\lambda(\omega_{01}). \quad (15)$$

This result holds irrespective of the statistics of the fluctuations; in lowest order of the perturbation theory in $D_{\lambda,\perp}$ the rates are expressed through the correlator S_λ. This approximation is sufficient when the noise is weak enough with a smooth spectrum at the transition frequency ω_{01} on the scale of the relaxation rate Γ_1. At low temperatures $k_B T \ll \hbar\omega_{01}$ the excitation rate Γ_E is exponentially suppressed and $\Gamma_1 \approx \Gamma_R$.

B. Pure dephasing

1. Linear coupling

First, we analyze a noise source coupled linearly (and longitudinally) to the qubit, i.e., $\partial\omega_{01}/\partial\lambda = D_{\lambda,z} \neq 0$. The Bloch-Redfield theory gives for the pure dephasing rate

$$\Gamma_\varphi = \pi S_{\delta\omega_z}(\omega = 0) = \pi D_{\lambda,z}^2 S_\lambda(\omega = 0) = \pi D_{\lambda,z}^2 S c_\lambda(\omega = 0). \quad (16)$$

This result is of the golden rule type [similar to Eq. (15)] and is meaningful if the noise power Sc_λ is regular near $\omega \approx 0$ up to frequencies of order Γ_φ.

A more elaborate analysis is needed when the noise spectral density is singular at low frequencies. In this subsection we consider Gaussian noise. The random phase accumulated at time t,

$$\Delta\phi = D_{\lambda,z}\int_0^t dt'\,\delta\lambda(t'),$$

is then Gaussian distributed, and one can calculate the decay law of the free induction (Ramsey signal) as $f_{z,R}(t) = \langle\exp(i\Delta\phi)\rangle = \exp(-(1/2)\langle\Delta\phi^2\rangle)$. This gives

$$f_{z,R}(t) = \exp\left(-\frac{t^2}{2}D_{\lambda,z}^2\int_{-\infty}^{+\infty} d\omega\, S_\lambda(\omega)\mathrm{sinc}^2\frac{\omega t}{2}\right), \quad (17)$$

where $\mathrm{sinc}\, x \equiv \sin x/x$.

In an echo experiment, the phase acquired is the difference between the two free evolution periods,

$$\Delta\phi_E = -\Delta\phi_1 + \Delta\phi_2 = -D_{\lambda,z}\int_0^{t/2} dt'\,\delta\lambda(t') + D_{\lambda,z}\int_{t/2}^{t} dt'\,\delta\lambda(t'), \quad (18)$$

so that

$$f_{z,E}(t) = \exp\left(-\frac{t^2}{2}D_{\lambda,z}^2\int_{-\infty}^{+\infty} d\omega\, S_\lambda(\omega)\sin^2\frac{\omega t}{4}\mathrm{sinc}^2\frac{\omega t}{4}\right). \quad (19)$$

$1/f$ *spectrum*. Here and below in the analysis of noise with a $1/f$ spectrum we assume that the $1/f$ law extends in a wide range of frequencies limited by an infrared cutoff ω_{ir} and an ultraviolet cutoff ω_c:

$$S_\lambda(\omega) = A/|\omega|, \quad \omega_{ir} < |\omega| < \omega_c. \tag{20}$$

The infrared cutoff ω_{ir} is usually determined by the measurement protocol, as discussed further below. The decay rates typically depend only logarithmically on ω_{ir}, and the details of the behavior of the noise power below ω_{ir} are irrelevant to logarithmic accuracy. For most of our analysis, the same remark applies to the ultraviolet cutoff ω_c. However, for some specific questions considered below, frequency integrals may be dominated by $\omega \gtrsim \omega_c$, and thus the detailed behavior near and above ω_c ("shape" of the cutoff) is relevant. We will refer to an abrupt suppression above ω_c $[S(\omega) \propto \theta(\omega_c - |\omega|)]$ as a "sharp cutoff," and to a crossover at $\omega \sim \omega_c$ to a faster decay $1/\omega \to 1/\omega^2$ (motivated by modeling of the noise via a set of bistable fluctuators; see below) as a "soft cutoff."

For $1/f$ noise, at times $t \ll 1/\omega_{ir}$, the free induction (Ramsey) decay is dominated by the frequencies $\omega < 1/t$, i.e., by the quasistatic contribution,[3] and Eq. (17) reduces to:

$$f_{z,R}(t) = \exp\left[- t^2 D_{\lambda,z}^2 A \left(\ln \frac{1}{\omega_{ir} t} + O(1) \right) \right]. \tag{21}$$

The infrared cutoff ω_{ir} ensures the convergence of the integral.

For the echo decay we obtain

$$f_{z,E}(t) = \exp(- t^2 D_{\lambda,z}^2 A \ln 2). \tag{22}$$

The echo method thus only increases the decay time by a logarithmic factor. This limited echo efficiency is due to the high-frequency tail of the $1/f$ noise.

Static case. In many cases, the contribution of low frequencies $\omega \ll 1/t$ dominates the pure dephasing. This happens when the noise spectrum is strongly peaked at low frequencies [cf. Eq. (21)], in particular when it has a sufficiently low ultraviolet cutoff frequency ω_c. This simple regime pertains to the quantronium.

To fix the terminology we use here: under certain conditions we use the "static approximation" characterized by an effective distribution $P(\delta\lambda)$, for which the noisy control parameter λ is considered as constant during each pulse sequence. This approach allows for a direct evaluation of the Ramsey decay function $f_{z,R}(t)$. In the relevant cases of linear or quadratic coupling to the fluctuations, the decay function $f_{z,R}(t)$ is the Fourier- or Fresnel-type transform of the distribution $P(\delta\lambda)$, respectively. Since the static approximation would yield no decay for the echoes, the calculation of the echo decay function $f_{z,E}(t)$ requires a "quasistatic approximation" that takes into account variations within each pulse sequence. A noise with an ultraviolet cutoff frequency ω_c can be considered as quasistatic on time scales shorter than ω_c^{-1}. The relevant results obtained in Refs. 35–37 are given below.

In the static approximation, the contribution of low frequencies $\omega \ll 1/t$ to the integral in Eq. (17) is evaluated using the asymptotic value $\mathrm{sinc}(\omega t/2) \approx 1$:

$$f_{z,R}^{\mathrm{stat}}(t) = \exp\left(- \frac{t^2}{2} D_{\lambda,z}^2 \sigma_\lambda^2 \right), \tag{23}$$

where $\sigma_\lambda^2 = \int_{-\infty}^{+\infty} d\omega\, S_\lambda(\omega)$ is the dispersion of $\delta\lambda$.

For $1/f$ noise, $S_\lambda = (A/|\omega|)\theta(\omega_c - |\omega|)$, we obtain $\sigma_\lambda^2 = 2A \ln(\omega_c/\omega_{ir})$. The result is only logarithmically sensitive to the value of the ultraviolet cutoff ω_c and to the specific functional form of the suppression of noise at high $\omega \gtrsim \omega_c$. The static approximation is sufficient for the evaluation of the dephasing rate if, e.g., the latter indeed exceeds the ultraviolet cutoff ω_c, i.e., $D_{\lambda,z}^2 A \ln(\omega_c/\omega_{ir}) \gg \omega_c^2$.

In the opposite limit, for wideband $1/f$ noise at $t > 1/\omega_c$, the contribution of frequencies $\omega \ll 1/t$ is also given by Eq. (23) [cf. Eqs. (17) and (21)]. In this case, however, σ_λ^2 in Eq. (23) depends logarithmically on time: $\sigma_\lambda^2 = A \ln(1/\omega_{ir} t)$. This contribution dominates the decay of $f_{z,R}(t)$.

In general, for (quasi)static noise with distribution function $P(\delta\lambda)$ the static approximation yields the Ramsey decay,

$$f_{z,R}^{\mathrm{stat}}(t) = \int d(\delta\lambda) P(\delta\lambda) e^{i D_{\lambda,z} \delta\lambda t}, \tag{24}$$

which is the Fourier transform of $P(\delta\lambda)$.

Let us now analyze the echo decay. For $1/f$ noise with a low ω_c the integral in Eq. (19) over the interval $\omega \lesssim \omega_c$ is dominated by the upper limit. This indicates that the specific behavior at $\omega \gtrsim \omega_c$ is crucial. For instance, in the case of a sharp cutoff $[S = (A/|\omega|)\theta(\omega_c - \omega)]$ we obtain

$$f_{z,E}(t) = \exp\left(- \frac{1}{32} D_{\lambda,z}^2 A \omega_c^2 t^4 \right). \tag{25}$$

However, if the $1/f$ behavior for $\omega < \omega_c$ crosses over to a faster decay $\propto 1/\omega^2$ at $\omega > \omega_c$ (as one would expect when the noise is produced by a collection of bistable fluctuators with Lorentzian spectra; cf. Refs. 38, 39, and 41) then the integral in Eq. (19) is dominated by frequencies $\omega_c < \omega < 1/t$, and we find $\ln f_{z,E}(t) \propto D_{\lambda,z}^2 A \omega_c t^3$. In either case, one finds that the decay is slower than for $1/f$ noise with a high cutoff $\omega_c > D_{\lambda,z} A^{1/2}$: the exponent involved in the decay function is indeed reduced by a factor $\sim(\omega_c t)^2$ or $\omega_c t$, respectively.

2. Quadratic coupling

At the optimal working point, the first-order longitudinal coupling $D_{\lambda,z}$ vanishes. Thus, to first order, the decay of the coherent oscillations is determined by the relaxation processes and one expects $\Gamma_2 = \Gamma_1/2$ from Eq. (11). However, it turns out that due to a singularity at low frequencies the second-order contribution of the longitudinal noise can be comparable, or even dominate over $\Gamma_1/2$. To evaluate this contribution, one has to calculate

$$f_z(t) = \left\langle \exp\left(i \frac{1}{2} \frac{\partial^2 \omega_{01}}{\partial \lambda^2} \int_0^t \chi(\tau) \delta\lambda^2(\tau) d\tau \right) \right\rangle. \tag{26}$$

Equation (26) can be used for the analysis of the free induction decay (Ramsey signal) if one sets $\chi(\tau) = 1$, and for the investigation of the echo-signal decay using $\chi(\tau < t/2) = -1$ and $\chi(\tau > t/2) = 1$.

$1/f$ *noise*. The free induction decay for the $1/f$ noise with

a high cutoff ω_c (the highest energy scale in the problem) has been analyzed in Ref. 35. The decay law can be approximated[40] by the product of the low-frequency ($\omega < 1/t$, quasistatic) and the high-frequency ($\omega > 1/t$) contributions: $f_{z,R}(t) = f^{lf}_{z,R}(t) f^{hf}_{z,R}(t)$. The contribution of low frequencies is given by (cf. Refs. 35–37)

$$f^{lf}_{z,R}(t) = \frac{1}{\sqrt{1 - i(\partial^2\omega_{01}/\partial\lambda^2)\sigma^2_\lambda t}}. \tag{27}$$

For $1/f$ noise with variance of the low-frequency fluctuations $\sigma^2_\lambda = 2A \ln(1/\omega_{ir}t)$, this contribution is

$$f^{lf}_{z,R}(t) = \frac{1}{\sqrt{1 - 2i(\partial^2\omega_{01}/\partial\lambda^2)tA \ln(1/\omega_{ir}t)}}. \tag{28}$$

It dominates at short times $t < [(\partial^2\omega_{01}/\partial\lambda^2)A/2]^{-1}$. At longer times, the high-frequency contribution

$$\ln f^{hf}_{z,R}(t) \approx -t \int_{\sim 1/t}^{\infty} \frac{d\omega}{2\pi} \ln\left(1 - 2\pi i \frac{\partial^2\omega_{01}}{\partial\lambda^2} S_\lambda(\omega)\right) \tag{29}$$

takes over: when $t \gg [(\partial^2\omega_{01}/\partial\lambda^2)A/2]^{-1}$ we obtain asymptotically $\ln f^{hf}_{z,R}(t) \approx -(\pi/2)(\partial^2\omega_{01}/\partial\lambda^2)At$ [provided $\omega_c \gg \pi(\partial^2\omega_{01}/\partial\lambda^2)A$]. Otherwise the quasistatic result (27) is valid at all relevant times. One can also evaluate the preexponential factor in the long-time decay. This preexponent decays very slowly (algebraically) but differs from 1 and thus shifts the level of $f_{z,R}(t)$.[42]

Note that the experimentally monitored quantity is a spin component, say $\langle\sigma_x\rangle$, in the rotating frame which evolves according to $\langle\sigma_x\rangle = \mathrm{Re}[f_{z,R}(t)e^{i\Delta\omega t}]$, where $\Delta\omega$ is the detuning frequency. In a typical situation of interest $f_{z,R}(t)$ changes more slowly than the period of oscillations, and thus the envelope of the decaying oscillations is given by $|f_{z,R}(t)|$, the phase of $f_{z,R}(t)$ shifting the phase of the oscillations. In the opposite limit $\Delta\omega = 0$, the measured decay curve reproduces the real part of $f_{z,R}(t)$ (the imaginary part corresponds to σ_y and can also be measured).

Static case. In the quasistatic case, i.e., when the cutoff ω_c is lower than $1/t$ for all relevant times, the Ramsey decay is simply given by the static contribution (27). At all relevant times the decay is algebraic and the crossover to the exponential law is not observed. More generally, in the static approximation with a distribution $P(\delta\lambda)$, the dephasing law is given by the Fresnel-type integral transform

$$f^{st}_{z,R}(t) = \int d(\delta\lambda) P(\delta\lambda) e^{i(\partial^2\omega_{01}/2\partial\lambda^2)\delta\lambda^2 t}, \tag{30}$$

which reduces to Eq. (27) for a Gaussian $P(\delta\lambda) \propto \exp(-\delta\lambda^2/2\sigma^2_\lambda)$. In general, any distribution $P(\delta\lambda)$, finite at $\delta\lambda = 0$, yields a $t^{-1/2}$ decay for $f^{st}_{z,R}$ at long times.

For the echo decay and Gaussian quasistatic noise in λ we obtain

$$f_{z,E}(t) = \frac{1}{\sqrt{1 + (\partial^2\omega_{01}/\partial\lambda^2)^2\sigma^2_\lambda \int_{-\infty}^{+\infty} d\omega(\omega t/4)^2 S_\lambda(\omega) t^2}}, \tag{31}$$

where we assumed that the frequency integral converges at $|\omega| \ll 1/t$. This is the case, e.g., if $S_\lambda(\omega)$ has a sharp cutoff at $\omega_c \ll 1/t$. For $1/f$ noise, $S_\lambda = (A/|\omega|)\theta(\omega_c - |\omega|)$ with $\omega_c \ll 1/t$, Eq. (31) yields

$$f_{z,E}(t) = \frac{1}{\sqrt{1 + (1/16)(\partial^2\omega_{01}/\partial\lambda^2)^2\sigma^2_\lambda A\omega_c^2 t^4}}. \tag{32}$$

Note that this result is sensitive to the precise form of the cutoff.

C. $1/f$ noise, one fluctuator versus many

The background charge fluctuations are induced by random redistributions of charge near, e.g., trapping and release of electrons or by random rearrangements of charged impurities. Many groups have observed this noise with a smooth $1/f$ spectrum in the frequency range from 1 Hz to 1 MHz. Occasionally, single fluctuators have been observed, with a significant fraction of the total charge noise.[10] If individual fluctuators play an important part the noise statistics is non-Gaussian.[39,43] We summarize here some of the obtained results relevant to our work.

The noise $\delta\lambda(t)$ contains contributions from all TLFs:

$$\delta\lambda(t) = \sum_n v_n \sigma_{n,z}(t). \tag{33}$$

Every fluctuator switches randomly between two positions, denoted by $\sigma_{n,z} = \pm 1$ with rate γ_n (for simplicity, we assume equal rates in both directions for relevant TLFs) and thus contributes to the noise power $S_\lambda = \Sigma_n S_n$:

$$S_n = \frac{1}{\pi} \frac{\gamma_n v_n^2}{\omega^2 + \gamma_n^2}. \tag{34}$$

For a single fluctuator (longitudinally coupled to the qubit) the free induction (Ramsey) and the echo decays are given by

$$f_{z,R,n}(t) = e^{-\gamma_n t}\left(\cos\mu_n t + \frac{\gamma_n}{\mu_n}\sin\mu_n t\right), \tag{35}$$

and

$$f_{z,E,n}(t) = e^{-\gamma_n t}\left(1 + \frac{\gamma_n}{\mu_n}\sin\mu_n t + \frac{\gamma_n^2}{\mu_n^2}(1 - \cos\mu_n t)\right), \tag{36}$$

where $\mu_n \equiv \sqrt{(D_{\lambda,z}v_n)^2 - \gamma_n^2}$. Finally, the decay produced by all the fluctuators is just the product of the individual contributions, i.e., $f_{z,R}(t) = \Pi_n f_{z,R,n}(t)$ and $f_{z,E}(t) = \Pi_n f_{z,E,n}(t)$. If the noise is produced or dominated by a few fluctuators, the distribution of $\delta\lambda(t)$ may be strongly non-Gaussian, and the simple relation between decoherence and noise power does

not hold. In this case the conditions of the central limit theorem are not satisfied. In Ref. 43, a continuous distribution of v_n's and γ_n's was considered, with a long tail of the distribution of the coupling strengths v_n such that rare configurations with very large v_n dominate the ensemble properties. The distribution $P(v,\gamma)$ considered in Ref. 43 is defined in the domain $[v_{min},\infty]\times[\gamma_{min},\gamma_{max}]$:

$$P(v,\gamma)=\frac{\xi}{\gamma v^2}. \tag{37}$$

Let us introduce the parameter $v_{max}^{typ}\equiv Nv_{min}$, which gives the typical value of the strongest (closest) fluctuator. Normalization to N fluctuators requires that $\xi=v_{max}^{typ}/\ln(\gamma_{max}/\gamma_{min})$. For this distribution any quantity whose average value (that is integrals over v's and γ's) is dominated by TLFs with[43] $v\gtrsim v_{max}^{typ}$ is not self-averaging, i.e., has considerable sample-to-sample fluctuations. The ensemble-averaged free induction decay described by[43]

$$\ln|f_{z,R}(t)|\propto -D_{\lambda,z}\xi t\ln(\gamma_{max}/\gamma_{min})=-D_{\lambda,z}v_{max}^{typ}t \tag{38}$$

is dominated by the fluctuators with strength of order $v\sim v_{max}^{typ}$ and is thus not self-averaging. Consequently, it does not apply quantitatively to a specific sample.

Similarly, the ensemble-averaged echo signal is given by[43]

$$\ln|f_{z,E}(t)|\propto\begin{cases}-D_{\lambda,z}\xi\gamma_{max}t^2 & \text{for } t<\gamma_{max}^{-1},\\ -D_{\lambda,z}\xi t[\ln(\gamma_{max}t)+O(1)] & \text{for } t>\gamma_{max}^{-1}.\end{cases} \tag{39}$$

The situation depends on whether $D_{\lambda,z}\xi>\gamma_{max}$ or $D_{\lambda,z}\xi<\gamma_{max}$. In the former the dephasing is static (i.e., it happens on a time scale shorter than the flip time of the fastest fluctuators, $1/\gamma_{max}$) and the first line of Eq. (39) applies. The decay is self-averaging because it is dominated by many fluctuators with strength $v\approx\sqrt{\xi\gamma_{max}/D_{\lambda,z}}<\xi<v_{max}^{typ}$. In the opposite regime $D_{\lambda,z}\xi<\gamma_{max}$ the dephasing is due to multiple flips of the fluctuators and the second line of Eq. (39) applies. In this case, the decay is dominated by a small number of fluctuators with strength $v\approx\xi$, which is smaller than v_{max}^{typ} only by a logarithmic factor, and sample-to-sample fluctuations are strong.

D. Decoherence during driven evolution

In the presence of a harmonic drive $2\omega_{R0}\cos(\omega t)\hat{\sigma}_x$, the Hamiltonian reads

$$\hat{H}=-\frac{1}{2}\hbar[\omega_{01}\hat{\sigma}_z+\delta\omega_z\hat{\sigma}_z+\delta\omega_\perp\hat{\sigma}_\perp+2\omega_{R0}\cos(\omega t)\hat{\sigma}_x]. \tag{40}$$

The qubit dynamics is conveniently described in the frame rotating with the driving frequency ω, and a new eigenbasis $\{|\tilde{0}\rangle,|\tilde{1}\rangle\}$ is defined by the total static fictitious field composed of the vertical component given by the detuning $\Delta\omega=\omega_{01}-\omega$ and the horizontal (x) component ω_{R0}. That is, the static part of the Hamiltonian in the rotating frame reads

$$H_{st}=-\frac{1}{2}\hbar(\Delta\omega\hat{\sigma}_z+\omega_{R0}\hat{\sigma}_x). \tag{41}$$

The length of the total field is $\omega_R=\sqrt{\omega_{R0}^2+\Delta\omega^2}$ and it makes an angle η with the z axis: $\Delta\omega=\omega_R\cos\eta$, $\omega_{R0}=\omega_R\sin\eta$. The evolution of the spin is a rotation around the field at the Rabi precession frequency ω_R. As in the case of free evolution, decoherence during driven evolution involves the phenomena of relaxation and dephasing: one defines a relaxation time $\tilde{T}_1$ and a coherence time $\tilde{T}_2$ analogous to T_1 and T_2, which correspond to the decay of the longitudinal and of the transverse part of the density matrix[31] in the new eigenbasis, respectively. First, as a reference point, we present the golden-rule-type results which are valid if all the noises are smooth at frequencies near $\omega=0$, ω_R, and ω_{01}. Analyzing which parts of the fluctuating fields $\delta\omega_z$ and $\delta\omega_\perp$ are longitudinal and transverse with respect to the total field ω_R in the rotating frame, and taking into account the frequency shifts due to the transformation to the rotating frame we obtain

$$\tilde{\Gamma}_1=\sin^2\eta\,\Gamma_\nu+\frac{1+\cos^2\eta}{2}\Gamma_1, \tag{42}$$

where $\Gamma_\nu\equiv\pi S_{\delta\omega_z}(\omega_R)$ is the spectral density at the Rabi frequency. We have disregarded the difference in the noise power $S_{\delta\omega_\perp}$ at frequencies ω_{01} and $\omega_{01}\pm\omega_R$, which allows us to use the depolarization rate Γ_1 from Eq. (15). We do, however, distinguish between Γ_ν and $\Gamma_\varphi=\pi S_{\delta\omega_z}(\omega=0)$ in order to later analyze a noise spectrum singular at $\omega\approx 0$.

For the dephasing rate we again have the relation

$$\tilde{\Gamma}_2=\frac{1}{2}\tilde{\Gamma}_1+\tilde{\Gamma}_\varphi, \tag{43}$$

where

$$\tilde{\Gamma}_\varphi=\Gamma_\varphi\cos^2\eta+\frac{1}{2}\Gamma_1\sin^2\eta. \tag{44}$$

As a result we obtain

$$\tilde{\Gamma}_2=\frac{3-\cos^2\eta}{4}\Gamma_1+\Gamma_\phi\cos^2\eta+\frac{1}{2}\Gamma_\nu\sin^2\eta. \tag{45}$$

The derivation of these expressions is simplified if one notes that due to the fast rotation the high-frequency transverse noise $S_{\delta\omega_\perp}(\omega\approx\omega_{01})$ is effectively mixed to low frequencies $\lesssim\omega_R$. In the rotating frame it effectively reduces to "independent" white noises in both the x and y directions with amplitudes $\delta\omega_\perp/\sqrt{2}$ and corresponding noise powers $S_{\delta\omega_\perp}(\omega\approx\omega_{01})/2$. Only the noise along the x axis (its longitudinal component with factor $\sin^2\eta$) contributes to $\tilde{\Gamma}_\varphi$ (the noise along the y axis is purely transverse).

Note the limiting behavior of the rates: at zero detuning, one has $\cos\eta=0$ and $\tilde{\Gamma}_2=\frac{3}{4}\Gamma_1+\frac{1}{2}\Gamma_\nu$, whereas at large detuning compared to the Rabi frequency, $\cos\eta=1$, and $\tilde{\Gamma}_2=\frac{1}{2}\Gamma_1+\Gamma_\phi$: one recovers thus the decoherence rate Γ_2 of the free evolution.

For a noise spectrum which is singular at $\omega=0$ ($1/f$ noise) we no longer find the exponential decay. The simplest case is

when the Rabi frequency is high enough so that one still can use the rate Γ_ν and the associated exponential decay. We consider here only this regime. Then one should combine the exponential decay associated with the rates Γ_1 and Γ_ν with the nonexponential one substituting the rate Γ_φ. For the decay of the Rabi oscillations we obtain

$$f_{Rabi}(t) = f_{z,\cos\,\eta}(t)\exp\left(-\frac{3-\cos^2\eta}{4}\Gamma_1 t - \frac{\sin^2\eta}{2}\Gamma_\nu t\right), \tag{46}$$

where $f_{z,\cos\,\eta}(t)$ is given by one of the decay laws derived in the preceding sections (depending on whether the coupling is linear or quadratic, and whether the statistics is Gaussian or not) with the noise $\delta\omega_z$ substituted by $\cos\,\eta\delta\omega_z$. That is, in the linear case, we have to substitute $D_{\lambda,z}\to\cos\,\eta D_{\lambda,z}$, while in the quadratic case $(\partial^2\omega_{01}/\partial\lambda^2)\to\cos\,\eta(\partial^2\omega_{01}/\partial\lambda^2)$.

E. Application to the quantronium sample used in this work

As already mentioned in Sec. II B, the parameters of the qubit $E_J=0.87k_B$ K, $E_C=0.66k_B$ K were measured by fitting the spectroscopic data $\omega_{01}(N_g,\delta)$ (see Fig. 11) with a numerical diagonalization of the Hamiltonian $\hat{H}_{CPB}$. This fit gives an upper limit for the asymmetry of the qubit junctions, $d<13\%$. By using another property[16] this value was estimated as $d\sim 4\%$. From E_J, E_C, and d, the numerical values of the D_λ's introduced above were calculable exactly, as a function of the working point (δ,N_g). Nevertheless, since we have characterized decoherence only along the two segments $\delta/(2\pi)\in[-0.3,+0.3]$, $N_g=1/2$ and $\delta=0$, $N_g-1/2\in[-0.1,+0.1]$ in the (δ,N_g) plane, we only give below simple expressions that approximate ω_{01}, D_λ, and $\partial^2\omega_{01}/\partial\lambda^2$ with a $\pm 3\%$ accuracy in the range of parameters explored experimentally. We have thus for the transition frequency

$$\omega_{01}(\delta,N_g=1/2)\simeq[103-425(\delta/2\pi)^2]\times 10^9\ \text{rad/s}, \tag{47}$$

$$\omega_{01}(\delta=0,N_g)\simeq[103+145(N_g-1/2)^2]\times 10^9\ \text{rad/s}, \tag{48}$$

which lead for the longitudinal coefficients to

$$D_{\delta/2\pi,z}(\delta=0\ \text{or}\ N_g=1/2)=\frac{\pi}{e}(i_1-i_0)$$
$$\simeq -850\frac{\delta}{2\pi}\times 10^9\ \text{rad/s}, \tag{49}$$

$$\frac{\partial^2\omega_{01}}{\partial(\delta/2\pi)^2}\simeq -850\times 10^9\ \text{rad/s}, \tag{50}$$

$$D_{Ng,z}(\delta=0\ \text{or}\ N_g=1/2)=-\frac{2E_C}{\hbar}(\langle 1|\hat{N}|1\rangle-\langle 0|\hat{N}|0\rangle)$$
$$\simeq +290\left(N_g-\frac{1}{2}\right)\times 10^9\ \text{rad/s}, \tag{51}$$

$$\frac{\partial^2\omega_{01}}{\partial N_g^2}\simeq +290\times 10^9\ \text{rad/s}, \tag{52}$$

where i_0 and i_1 are the average currents $\langle\hat{i}\rangle$ in the two states. Note that $D_{Ng,z}$ vanishes at $N_g=1/2$ for all δ so that a gate microwave pulse corresponds to a purely transverse perturbation of the Hamiltonian. Consequently, the perturbed Hamiltonian of Eq. (40) does apply exactly to the quantronium at $N_g=1/2$, where the measurements were performed. At other values of N_g, Eq. (40) would nevertheless be a good approximation. For critical current noise, the coupling coefficient

$$D_{\delta E_J/E_J,z}(\delta=0)=\cot\left(\delta/2\right)(i_1-i_0)/e\simeq +85\times 10^9\ \text{rad/s}, \tag{53}$$

$$D_{\delta E_J/E_J,z}(N_g=1/2)\simeq\left[+85-240\left(\frac{\delta}{2\pi}\right)^2\right]\times 10^9\ \text{rad/s} \tag{54}$$

is maximal at the optimal working point P_0. Expressed in the same way, the transverse coefficients $D_{\lambda,\perp}$ are

$$D_{\delta/2\pi,\perp}(\delta=0\ \text{or}\ N_g=1/2)=\frac{2\pi}{e}|\langle 0|\hat{i}|1\rangle|$$
$$\simeq 380d\left[1+6.0\left(\frac{\delta}{2\pi}\right)^2\right]\times 10^9\ \text{rad/s}, \tag{55}$$

$$D_{Ng,\perp}(\delta=0\ \text{or}\ N_g=1/2)=\frac{4E_C}{\hbar}|\langle 0|\hat{N}|1\rangle|=193\times 10^9\ \text{rad/s}, \tag{56}$$

and

$$D_{\delta E_J/E_J,\perp}(\delta=0\ \text{or}\ N_g=1/2)$$
$$=\frac{2E_J\cos(\delta/2)}{\hbar}|\langle 0|\cos\,\hat{\theta}|1\rangle|=108\left|N_g-\frac{1}{2}\right|\times 10^9\ \text{rad/s}. \tag{57}$$

Finally, note that the cross derivative $\partial^2\omega_{01}/\partial\delta\partial N_g$ was found to be equal to zero along the two segments mentioned above.

IV. EXPERIMENTAL CHARACTERIZATION OF DECOHERENCE DURING FREE EVOLUTION

In order to characterize decoherence in our quantronium sample and to compare with the theoretical predictions, we have measured the characteristic decay times of the diagonal (T_1) and nondiagonal (T_2,T_E) parts of the density matrix of the qubit during its free evolution. These measurements were repeated at different working points P located along the lines $\delta=0$ and $N_g=1/2$, as mentioned above. We describe the different experimental protocols that were used, the results, and their interpretation.

A. Longitudinal relaxation time T_1

Relaxation of the longitudinal polarization is inferred from the decay of the switching probability p after a π pulse

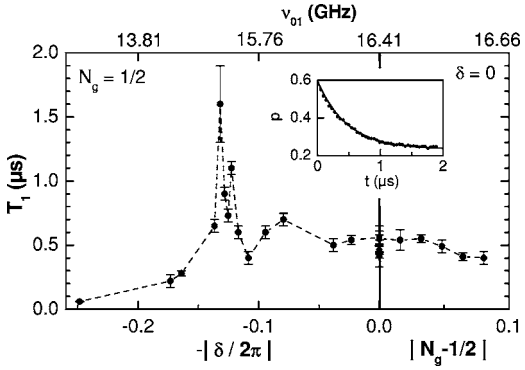

FIG. 6. Experimental T_1 values measured at $N_g=1/2$ as a function of δ (left panel), and at $\delta=0$ as a function of N_g (right panel). The vertical line separating the two panels corresponds to the optimal point $P_0=(N_g=1/2, \delta=0)$. The dashed line joining the points is a guide for the eye. The correspondence between δ, N_g, and ν_{01} is given by the upper horizontal axis. Inset: Example of T_1 measurement. The switching probability p (dots) is measured as a a function of the delay t between a π pulse and the readout pulse. The fit by an exponential (full line) leads to T_1 (0.5 μs at P_0 in this example).

has prepared the qubit in state $|1\rangle$. More precisely, a sequence that consists of a π pulse, a variable delay t, and a readout pulse is repeated to determine $p(t)$. An example of the relaxation curve, measured at the working point P_0, is shown in the inset of Fig. 6. As predicted, the relaxation is exponential, with an absolute discrepancy between $p(t)$ and the fit being always smaller than 2%. The relaxation time T_1, varies with the working point as shown in Fig. 6: T_1 is about 0.5 μs in the vicinity of P_0 (which is three times shorter than in a previous experiment[2]) and shows rapid variations away from P_0 in the phase direction. Now, it is interesting to note that in the parameter range explored, the matrix element $D_{Ng,\perp}$ of Eq. (56) is approximately constant and that the matrix element $D_{\delta/2\pi,\perp}$ of Eq. (55) varies smoothly by a factor of only 2 with δ. Consequently, the measured variation of T_1 reflects quite directly the variation with frequency of the density of environmental modes available for absorbing one photon $\hbar\omega_{01}$ from the qubit through the δ and N_g channels. Noting from Eq. (57) that the noise on E_J cannot induce relaxation of the qubit along the line $N_g=1/2$, a natural question arises: can the measured relaxation rates be fully accounted for by the circuit alone, i.e., by Z_g and Y_R (see Fig. 5)? We have calculated from Eq. (15) and from the noise spectra (5) and (6) of Z_g and Y_R, values of T_1 at P_0 of about $1-2$ μs and $5-10$ μs, respectively. The combined effect of the two subcircuits gives thus $T_1 \sim 0.8-1.6$ μs, which is close to the measured value. We conclude that a large part of the relaxation has to be attributed to the gate circuit. Note, however, that estimating the impedances as seen from the qubit above 14 GHz with an accuracy better than a factor of 2 is difficult, so that we cannot exclude also a large contribution of microscopic degrees of freedom.

B. Transversal relaxation time or coherence time T_2

1. T_2 measurement from Ramsey fringes

Characterizing decoherence during the free evolution of a qubit can be done directly by measuring the temporal decay of the average transverse polarization of its effective spin. With a projective readout, this information can only be obtained by repeating a sequence which consists in preparing first a particular state with a nonzero transverse polarization, letting the spin evolve freely during a time Δt, and then reading one of its transverse components. Starting from state $|0\rangle$, the simplest experiment would consist in applying a $\pi/2$ pulse to align the spin along the X axis of the Bloch sphere, and for measurement projecting it onto X after the desired free evolution. Such an experiment is not possible with the quantronium, which is projected onto the Z axis at readout. The phase φ accumulated during the free precession has thus to be converted into a polarization along Z, which can be done by applying a second $\pi/2$ pulse. The two $\pi/2$ pulses form the so-called Ramsey sequence,[2] which gives an oscillation of the Z polarization with Δt at the detuning frequency $\Delta\omega/2\pi$. Although choosing $\Delta\omega=0$ gives a simple non oscillatory signal that decays in principle as $\{1+e^{-\Gamma_1\Delta t/2}\mathrm{Re}[f_{z,R}(\Delta t)]\}/2$ (see Sec. III), this choice is inconvenient since any residual detuning would induce a very slow oscillation that could be misinterpreted as an intrinsic decay. For that reason, we use here a $\Delta\omega$ of several tens of MHz, which is chosen because it is much larger than the decoherence rate. The rotation axis of the spin during the $\pi/2$ pulses makes an angle $\alpha=\arctan(\Delta\omega/\omega_{R0})$ with the equatorial plane of the Bloch sphere. The rotation angle of the so-called $\pi/2$ pulses is more exactly $\pi/2(1+\epsilon)$, where ϵ is a small positive or negative correction due to two effects. First, the pulse duration is optimized at zero detuning, by maximizing the switching probability of the readout junction immediately after two adjacent $\pi/2$ pulses. This duration is then kept constant for a Ramsey experiment at finite detuning, so that ideally, $0 \leqslant \epsilon = \sqrt{1+\tan(\alpha)^2}-1 \lesssim 10^{-2}$. Second, the optimization procedure is done with a finite accuracy and ϵ can be different from this ideal value. The Ramsey oscillation p_R is given by

$$p_R = \frac{1-a}{2}\left[1 + ae^{-\Delta t/T_1} + (1+a)e^{-\Delta t/2T_1}\left|f_{z,R}(\Delta t)\right| \times \cos(\Delta\omega\Delta t + \zeta)\right], \tag{58}$$

where $a=\sin^2\alpha-\sin\epsilon(1-\sin^2\alpha)$ and $\zeta=\arctan[\sin\alpha(1+\sin\varepsilon)/\cos\epsilon]$ are geometrical corrections. Note that, at large Δt, the envelope of the oscillations has an amplitude and a saturation value that depends on $\Delta\omega$.

Figure 7 shows two typical Ramsey signals measured at the optimal working point P_0 with $\omega_{R0}/2\pi=106$ MHz and $\Delta\nu=50$ MHz. These two signals differ significantly although they were recorded the same day with the same experimental protocol: N_g is first tuned so that the central frequency of the spectroscopic line is minimum and the Ramsey fringes are then recorded at a speed of 1 point per second, the longest record (middle frame of Fig. 7) taking thus 17 minutes. The relative nonreproducibility between the two records is typical of what we have observed during several months of experimentation. It is attributed to the frequency drift induced by the $1/f$ charge noise. This drift is partly continuous and partly due to sudden jumps attributed to a few strongly coupled charged TLFs, as mentioned in Secs. II and III.

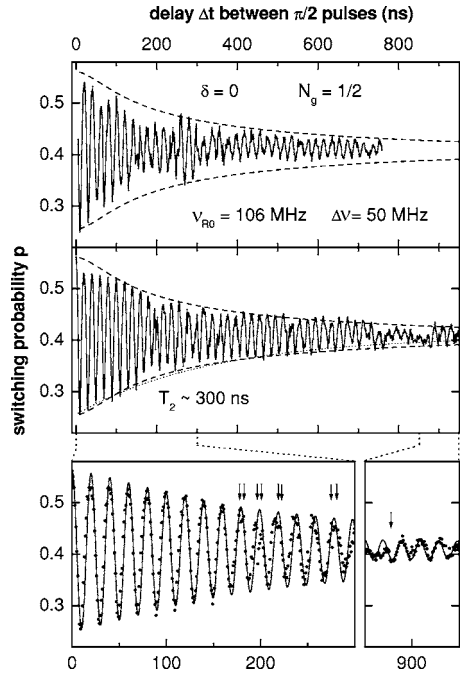

FIG. 7. Ramsey signals at the optimal point P_0 for $\omega_{R0}/2\pi = 106$ MHz and $\Delta\nu \approx 50$ MHz, as a function of the delay Δt between the two $\pi/2$ pulses. Top and middle panels: solid lines are two successive records showing the partial irreproducibility of the experiment. Dashed lines are a fit of the envelope of the oscillations in the middle panel (see text) leading to $T_2 = 300$ ns. The dotted line shows for comparison an exponential decay with the same T_2. Bottom panels: zoom windows of the middle panel. The dots represent now the experimental points whereas the solid line is a fit of the whole oscillation with $\Delta\omega/2\pi = 50.8$ MHz. Arrows point out a few sudden jumps of the phase and amplitude of the oscillation, attributed to strongly coupled charged TLFs.

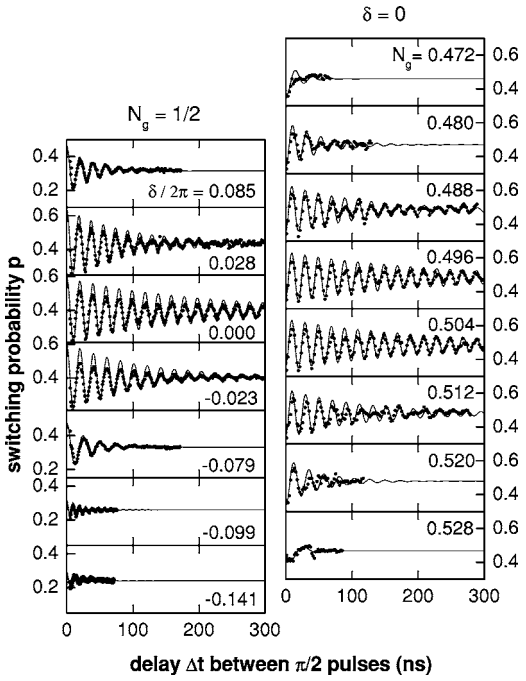

FIG. 8. Ramsey oscillations as a function of the delay Δt between the two $\pi/2$ pulses, for different working points located on the lines $N_g = 1/2$ (left column) and $\delta = 0$ (right column). The Rabi frequency is $\omega_{R0}/2\pi = 162$ MHz for all curves. The nominal detunings $\Delta\nu$ are 50, 53, 50, 50, 40, 100, and 80 MHz (left, top to bottom) and 35–39 MHz (right). Dots are experimental points whereas full lines are exponentially damped sinusoids fitting the experimental results and leading to the T_2 values reported on Fig. 15.

These sudden jumps are reversible and induce correlated phase and amplitude jumps of the Ramsey fringes, as shown by the arrows in the bottom panels of Fig. 7. The figure also shows a fit of the external envelope of the fringes to Eqs. (58) and (27), valid for a quadratic coupling to a static charge noise (this choice will be explained in Sec. IV D). The values of T_1 and of the sensitivity to noise Eq. (52) being known, the fitting parameters are the amplitude and saturation value of the fringes, and the variance σ_λ^2 of the noise. The corresponding effective T_2 time is 300 ± 50 ns for this record, but it is found to vary in the range 200–300 ns (see, for instance, top panel of Fig. 10) depending on our ability to set the working point precisely at P_0 and on the probability that the system stays at that point during a full record.

A series of Ramsey oscillations measured at different working points P is shown in Fig. 8. Since ω_{01} and therefore ω_{R0} (at constant microwave amplitude) vary with P, the microwave frequency was varied in order to keep $\Delta\omega$ between 40 and 100 MHz and the pulse duration was varied to maintain the rotation angle close to $\pi/2$. Note that the mean level and the amplitude of the oscillations vary due to these $\Delta\omega$ changes. A direct comparison between the Ramsey patterns shows that T_2 decreases dramatically when P is moved away from P_0. More precisely, each curve gives a value $T_2(P)$ with an uncertainty of about 30%, which is plotted on Fig. 15.

2. T_2 measurement with the "detuning pulse" method

Probing decoherence at different working points P with the Ramsey method presented above requires recalibrating for each P the frequency and duration of the two $\pi/2$ pulses. Now, the $\pi/2$ pulses and the free evolution period probing decoherence do not have to be performed at the same working point. It is thus experimentally more efficient to perform the $\pi/2$ rotations always at the optimal point P_0 with fixed optimized microwave pulses, and to move adiabatically to any point P where decoherence is to be measured, between these pulses. This scheme, which leads also to the coherence time $T_2(P)$, is referred in the following as the "detuning pulse" method. It has been demonstrated by moving back and forth the working point from P_0 to P with a trapezoidal N_g or δ pulse of duration Δt_2 inserted in the middle of a Ramsey sequence. Since the qubit frequency is not the same at P, the switching probability oscillates with Δt_2 at a new detuning frequency $\Delta\omega_2(P)$ different from $\Delta\omega$. These oscillations decay with the characteristic time $T_2(P)$. The adiabaticity criterion mentioned in Sec. II A 1 is easily satisfied even with a rate of change $\partial\lambda/\partial t$ as fast as 0.1/ns. In our experiment the shortest rise and fall times t_r were 10 and 60 ns for N_g and δ, respectively. This method, which is of course limited to working points P where $T_2(P) \gtrsim t_r$, has

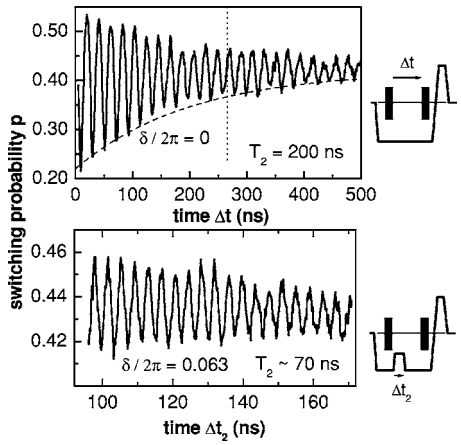

FIG. 9. Phase detuning pulse technique for measuring T_2. Top: Ramsey signal at the optimal point P_0, with $\Delta\nu \simeq 50$ MHz, when no detuning dc pulse is applied. The dashed line corresponds to an exponential decay with $T_2(P_0)=200$ ns. Bottom: signal obtained with a delay $\Delta t=275$ ns between the two $\pi/2$ pulses (corresponding to the dashed vertical line of the upper panel) and with an adiabatic current pulse maintaining $\delta/2\pi=0.063$ during a time Δt_2. The oscillation of the signal with Δt_2 decays with a characteristic time of about 70 ns (note the different horizontal scales on the two graphs). The pictograms on the right illustrate the two $\pi/2$ microwave pulses and the $I_b(t)$ signal.

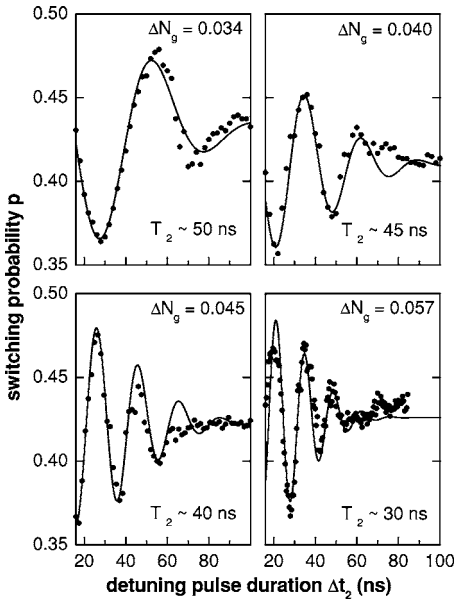

FIG. 10. Charge detuning pulse technique used for measuring T_2 at four points $P=(0,1/2+\Delta N_g)$. Dots are experimental points whereas full lines are fits using Gaussian damped sinusoids at frequencies $\Delta\omega(\Delta N_g)$. The extracted T_2 are indicated on each panel.

been used in the ranges $|\delta|<0.1$ and $|N_g-1/2|<0.05$. Examples of experimental curves are shown on Figs. 9 and 10. Each curve leads to a $T_2(P)$ value with a 50% total uncertainty; these are also shown on Fig. 15.

3. T_2 measurement from resonance line shape

When the decoherence rate becomes comparable to the Rabi frequency, time domain experiments using resonant pulses can no longer be performed and one has to operate in the frequency domain. In the linear response regime, i.e., at low microwave power, the shape of the resonance line recorded during continuous microwave excitation is simply the Fourier transform of the envelope of the free evolution decay (i.e. the Ramsey signal). One has $T_2=k/(\pi W)$ with W the resonance full width at half maximum and k a numerical coefficient that depends on the line shape: $k=1$ for a Lorentzian, $k=1.6$ for a Gaussian, etc. In order to reach the linear regime, the line shape is recorded at different decreasing microwave powers until its width saturates at the lower value. At that stage, the signal to noise ratio is usually small and the line shape has to be averaged over a few minutes. A series of resonance lines is shown on Fig. 11, together with their positions as a function of the working point (which leads to E_J and E_C as previously mentioned). The rapid broadening of the line when departing from P_0 is clearly visible. Line shapes at $N_g \neq 1/2$ are structured with several subpeaks that are stable only on time scales of a few minutes. We take this again to be due to the presence of large individual charged TLF's. At $\delta \neq 0$, the lines are smoother but the low signal to noise ratio in the linear regime does not really allow a discrimination between a Lorentzian or a Gaussian shape. We thus calculated a $T_2(P)$ using an intermediate value $k=1.3$ and with an extra 30% uncertainty. These T_2's with typical uncertainty 50% are also added to Fig. 15. Finally, the line shape at P_0 is averaged over 10 min and is shown on Fig. 11. Its exact shape is discussed in Sec. IV D.

C. Coherence time of spin echoes T_E

In NMR,[31] the spin-echo technique is a standard way to cancel the line shape broadening of an ensemble of spins due to the spatial inhomogeneity of the magnetic field. In our case, there is a single spin (i.e., the quantronium) measured repetitively and the echo technique can compensate for a drift of the transition frequency during the time needed (about 1 s) for the repeated measurement to obtain a probability p. The method thus cancels a low-frequency *temporal* inhomogeneity and leads to a more intrinsic coherence time $T_E > T_2$ independent of the measurement time of p. In practice, the spin-echo sequence is a modified Ramsey sequence with an extra π pulse placed symmetrically between the two $\pi/2$ pulses. This π rotation around the same axis as that of the $\pi/2$ pulses makes the spin trajectory along the equator longer or shorter depending on whether ν_{01} increases or decreases. Consequently, the random phases accumulated before and after the π pulse compensate exactly if the frequency does not change on the time scale of a sequence.

In Fig. 12, we show a series of echo signals recorded at P_0 by sweeping the delay Δt between the two $\pi/2$ pulses while keeping constant the delay Δt_3 between the π and second $\pi/2$ pulses. This protocol results in an oscillation $p(\Delta t)$ whose amplitude first decays as the usual Ramsey signal, and has then a second maximum at $\Delta t=2\Delta t_3$. Note that at this precise echo time, the value of p is an oscillation minimum. By taking advantage of the time stability of our pulse se-

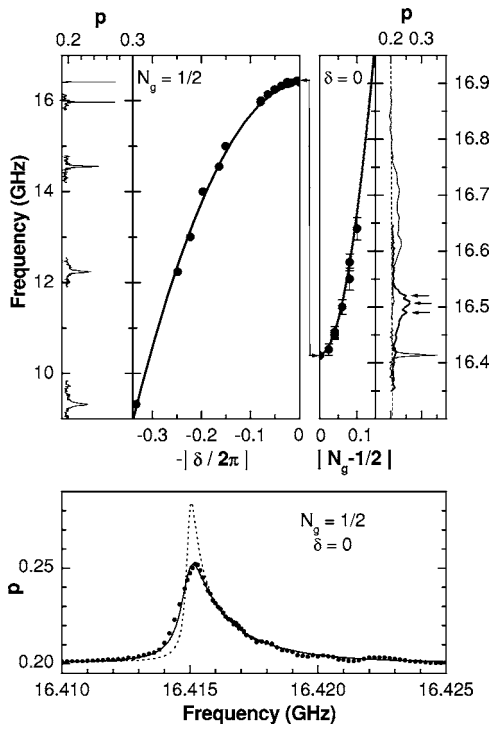

FIG. 11. Top panels: line shape (thin lines) and central position (dots) of the resonance lines as a function of δ at $N_g=1/2$ (left) and as a function of N_g at $\delta=0$ (right). The optimal point P_0 corresponds to the double arrow in the center of the graph. Note the two different vertical scales and the occasional substructure of resonance lines pointed out by small arrows. Bold lines are fits of the peak positions leading to $E_J=0.87k_B$ K, $E_C=0.66k_B$ K, and $d<13\%$. Bottom panel: asymmetric line shape recorded (dots) at P_0 with a microwave power small enough to desaturate the line. The dashed line is the theory, with a T_φ that corresponds to that of Fig. 7. The solid line is the convolution of this theoretical line and of a Lorentzian corresponding to a decay time of 600 ns (see text).

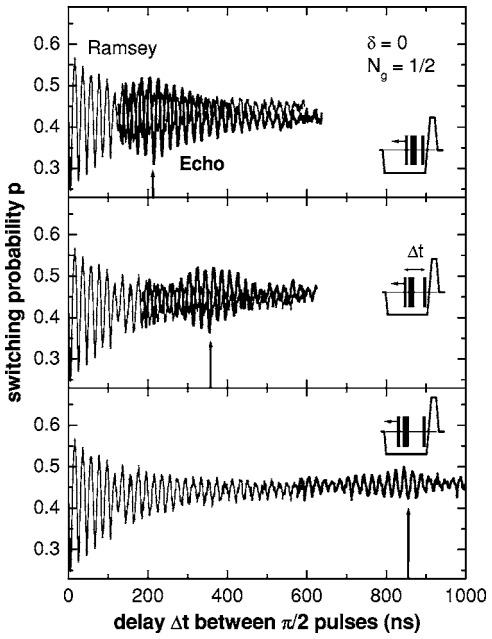

FIG. 12. Spin echoes (bold lines) obtained at the optimal point P_0 with a detuning $\Delta\nu\simeq 50$ MHz. Pictograms illustrate the experimental protocol: the delay Δt_3 between the π pulse and the last $\pi/2$ pulse is kept constant while altering the timing of the first $\pi/2$ pulse. Each panel corresponds to a different Δt_3. Vertical arrows indicate the sequence duration $\Delta t=2\Delta t_3$ for which the echo amplitude is expected to be maximal and where $p=p_E$ is minimum. For the sake of comparison, the corresponding Ramsey signal (thin lines) is shown in all panels.

quencer, it was possible to map directly this minimum p_E by sweeping Δt while keeping the π pulse precisely in the middle of the sequence, as shown in Fig. 13. Ideally, at zero detuning, this mapping of p_E is expected to increase as $[1-e^{-\Gamma_1\Delta t/2}f_{z,E}(\Delta t)]/2$ (see Sec. III). In practice, one has once again to take into account geometric corrections due to the finite detuning, to the finite duration of the $\pi/2$ and π pulses, and to the inaccuracy of their rotation angles. Using a generalized Bloch-Redfield approach, we find

$$2p_E = [1-(a_1+a_2e^{-\Gamma_1\Delta t/2}+a_3e^{-\Gamma_1\Delta t})] - e^{-\Gamma_1\Delta t/2}\Bigg\{(1-a_4)f_{z,E}(\Delta t) + a_5\,\mathrm{Re}[e^{-i(\Delta\omega\Delta t+\xi_1)/2}f_{z,R}(\Delta t)] + (a_6e^{-\Gamma_1\Delta t/4} + a_7e^{+\Gamma_1\Delta t/4})\mathrm{Re}\left[e^{-(\Delta\omega\Delta t+\xi_2)/2}f_{z,R}\left(\frac{\Delta t}{2}\right)\right]\Bigg\}, \quad (59)$$

where the a_i's are small geometrical coefficients that depend only on the angle α and on the errors in the microwave pulse durations. The latter terms of Eq. (59) show that on top of the expected increase of p_E mentioned above, pulse imperfections induce small oscillations of p_E whose damping is given by the Ramsey function $f_{z,R}$ rather than by the echo function $f_{z,E}$.

Experimental $p_E(\Delta t)$ curves recorded at P_0 and at different working points are shown on Figs. 13 and 14, respectively. A fit using Eq. (59) is shown on Fig. 13 and leads to $T_E(P_0)\simeq 550$ ns $> T_2$, which shows that part of the noise occurs at low frequency and is efficiently removed by the echo technique. Note that a naive exponential fit of the bottom envelope of $p_E(\Delta t)$ would have given about the same T_E. Then, $T_E(P)$ values with a 30% uncertainty are extracted from each curve of Fig. 14 and reported on Fig. 15. A quantitative analysis of $T_E(P)$ is given below.

D. Discussion of coherence times

A summary of all the coherence times (T_2, T_E) measured during free evolution using the various methods described above is given on Fig. 15. These results are in good agreement with each other and are comparable with those of our previous work.[3] As expected, T_2 is maximum at P_0 and decays by more than two orders of magnitude for N_g or δ variations of 0.1 Cooper pairs or 0.3 phase turns, respectively. This result clearly validates the concept of the optimal working point. Moreover, while T_2 decreases rapidly when departing from P_0, the estimated sensitivity to E_J noise given by Eq. (54) either decreases or stays constant. We thus conclude that E_J noise has a negligible contribution to decoher-

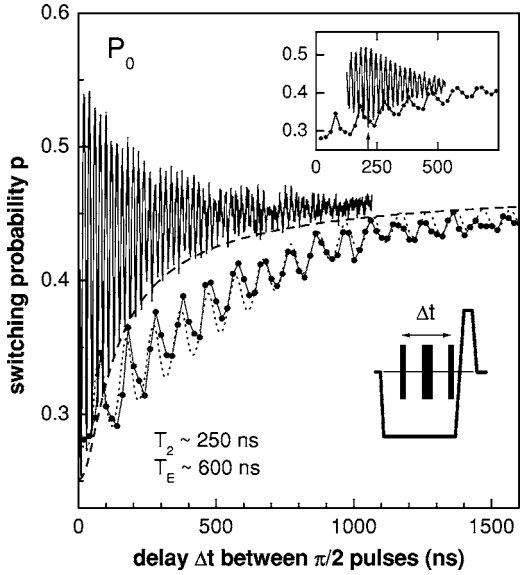

FIG. 13. Echo signal p_E (linked big dots) measured at the optimal point P_0 by keeping a π pulse precisely in the middle of the sequence while sweeping the sequence duration Δt (pictogram). The Rabi frequency is $\omega_{R0}/2\pi=130$ MHz and the detuning $\Delta\nu=20$ MHz. For comparison, the Ramsey signal (oscillating line) and its envelope (dashed line leading to $T_\varphi=450$ ns) are also shown. The dotted line is a fit of p_E that leads to the characteristic decay time of $f_{z,E}$, $T_{\varphi,E}=1.3$ μs, and that shows that the $\pi/2$ pulses were actually 15% too short whereas the π pulse was correct. The resulting echo time is $T_E\sim 600$ ns. Inset: comparison between p_E (linked dots) and the echo signal recorded with a fixed π pulse (solid line), as presented in Fig. 12.

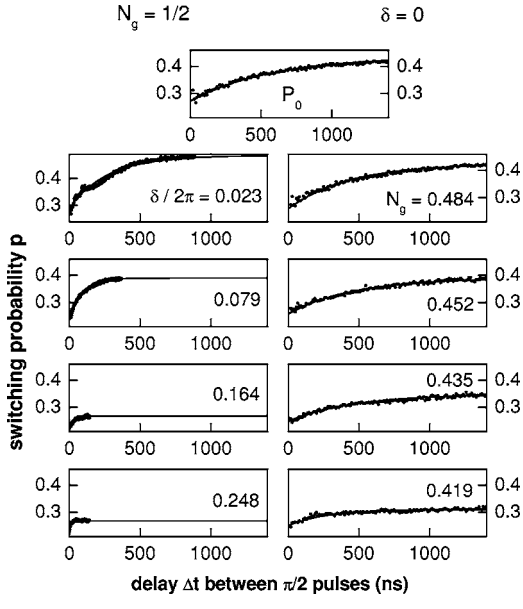

FIG. 14. Echo signals $p_E(\Delta t)$ measured (dots) at different working points indicated in each panel, with a Rabi frequency $\omega_{R0}/2\pi=140$ MHz and $\Delta\nu\approx 50$ MHz. Full lines are exponential fits leading to T_E values reported on Fig. 15. Note that the amplitude of the signal depends on the working point.

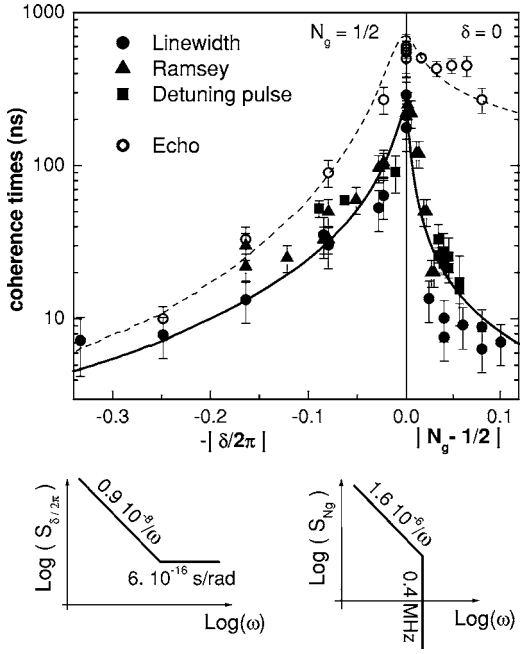

FIG. 15. Echo times T_E (open circles) and coherence times T_2 measured from the resonance linewidth (solid dots), from the decay of Ramsey signals (triangles), and from the detuning pulse method (squares), at $N_g=1/2$ as a function of δ (left panel) and at $\delta=0$ as a function of N_g (right panel). The full and dashed lines are best fits (see text) of T_E and T_2 times, respectively, leading to the phase and charge noise spectral densities depicted at the bottom. The spectra are even functions of ω.

ence in this device at all working points except possibly at P_0. Figure 15 also shows that the improvement T_E/T_2 provided by the echo technique decreases from a factor of about 2 to about 1 when moving away from P_0 in the phase direction, and increases from about 2 to about 50 when moving in the charge direction. We try below to provide a quantitative understanding of these $T_2(P)$ and $T_E(P)$ variations, using simple model $S_\lambda(\omega)$ noise spectra for $\lambda=\delta/2\pi, N_g$. Then, we discuss the decay of Ramsey fringes, $p_R(\Delta t)$, and of echo signals, $p_E(\Delta t)$, away from P_0. Finally, we discuss what limits its coherence at P_0.

1. Noise spectral densities and $T_{2,E}(P)$ dependences

The fit to theory of the experimental $T_2(P)$ and $T_E(P)$ curves of Fig. 15 is performed in the following way. The dephasing factors f_z are computed numerically according to the theoretical expressions of Sec. III and multiplied by the relaxation term $\exp[-\Delta t/2T_1(P)]$, which is known from the independent measurements of Fig. 6; the coherence times correspond to a decay of these products by a factor $\exp(-1)$. First, we compute only the first order contribution of λ noises (considered here as Gaussian) by numerical integration of Eqs. (17) and (19), using Eqs. (49) and (51) for the $D_{\lambda,z}$'s. Microscopic charge and phase noises being characterized by $1/f$ spectra at low frequency and noises due to the driving and readout subcircuits being characterized by white spectra below 10 MHz (see Sec. II C), we start the fit using for $Sc_{N_g}(\omega)$ and $Sc_{\delta/2\pi}(\omega)$ linear combinations of $1/f$ and

white spectral densities. Due to the divergence of the $1/f$ contributions as $\omega \to 0$, we introduce an infrared cutoff in the integration, $\omega_{ir}=1/t_{meas}$, where $t_{meas}=1$ s is the measurement time of a single data point in a Ramsey or echo signal. Note that although this cutoff could be defined more rigorously by taking into account the exact measuring protocols,[3] this complication is of no benefit here because the computed coherence times depend only logarithmically on ω_{ir}. At this stage, the fit (not shown) captures the $T_2(P)$ dependencies but does not capture the large gain $g=T_E/T_2$ observed far from $N_g=1/2$. This problem was expected since the echo technique is inefficient in the presence of high-frequency noise and because the gain deduced from Eqs. (21) and (22) in the case of a $1/f$ noise is $g \simeq \sqrt{\ln(t_{meas}/T_\varphi)/\ln(2)} \lessapprox 5$ over the explored range of T_2. Consequently, $S_{N_g}(\omega)$ has to decrease *faster than* $1/f$ above a certain frequency. We thus introduce a high-frequency sharp cutoff ω_c in the spectrum $Sc_{N_g}(\omega)$ as a new fitting parameter. The new fit (not shown) is then in fair agreement with the data except in the vicinity of P_0 where computed coherence times diverge due to the cancellation of the $D_{\lambda,z}$'s. Therefore, second order contributions have now to be included at this point using the $\partial^2\omega_{01}/\partial\lambda^2$'s given by Eqs. (50) and (52). For the sake of simplicity, λ^2 noises are first treated as Gaussian noises characterized only by their spectral densities S_{λ^2} estimated from the autoconvolution of S_λ. This rough approximation leads to dephasing times at P_0 correct within a factor better than 2. We show in this way that the contribution of δ^2 is completely negligible with respect to that of N_g^2. The calculation is then redone properly using Eqs. (27) and (31). Finally, the dephasing factors associated with N_g, δ, and N_g^2 are multiplied together. This procedure neglects the effect of correlations between λ and λ^2, which are relevant only when both contributions are of same order, namely, in a very narrow range in the vicinity of P_0. Moreover, our results are not affected by correlations between N_g and δ, which would exist if both noises were to be due to the same underlying mechanism, since the coupling coefficient $\partial^2\omega_{01}/\partial N_g\partial\delta$ for the cross noise $Sc_{N_g-\delta}(\omega)$ is zero along $(\delta, N_g=1/2)$ and $(\delta=0, N_g)$ lines. The final fit shown on Fig. 15 leads to $Sc_{N_g}(\omega)=1.6\ 10^{-6}/|\omega|$ for $|\omega|<\omega_c=2\pi\times 0.4$ MHz and to $Sc_{\delta/2\pi}(\omega)=0.9\times 10^{-8}/|\omega| + 6\times 10^{-16}/(\text{rad/s})$.

First we discuss the charge noise. The amplitude coefficient for the $1/f$ charge noise is in the range expected for a background charge noise $Sc_{N_g}^{BCN}$ of microscopic origin (see Sec. II C). The high-frequency cutoff ω_c, necessary to provide even a qualitative fit, is an important result that had not been anticipated and that calls for a direct measurement of charge noise in the megahertz range, perhaps using a rf single-electron-transistor electrometer.[44] The white noise contribution to charge noise due to the gate impedance Z_g, deduced from Eqs. (5) and (16), provides a very large $T_\varphi > 1$ ms; this is compatible with our assumption of a high-frequency cutoff. Note that this cutoff is only related to the *classical part* of the charge noise and does not preclude the possibility that charge TLFs might absorb energy at high frequencies, and thus relax the qubit.[28]

We now turn to the phase noise. The presence of $1/f$ phase noise is similar to the unexplained flux noise found in SQUIDS (see Sec. II C), although its amplitude corresponds here to a standard deviation σ_{Φ/Φ_0} about ten times larger (spectral density 100 times larger) than that usually reported.[30] The value of the white phase noise of $\sim 6\times 10^{-16}/(\text{rad/s})$ is about twice the estimated out-of-equilibrium noise expected from the AWG, whereas the impedance Y_R is expected to contribute by less than one percent more to this white spectrum. This white phase noise contribution is responsible for the low efficiency of echoes at $\delta \neq 0$, $N_g=1/2$.

2. Temporal decays of Ramsey and echo signals

The phase and charge noise spectra mentioned above imply precise shapes for the temporal variations of Ramsey and echo signals. For $\delta \neq 0$, the dominant contribution to decoherence arises from the first order contribution of the phase noise $Sc_{\delta/2\pi}$. The numerical integration of Eqs. (17) and (19) predicts that the Ramsey function $f_{z,R}(\Delta t)$ involved in p_R should be close to a Gaussian at small $|\delta|$ and should evolve towards an exponential at larger $|\delta|$, whereas the echo decay function $f_{z,E}(\Delta t)$ is expected to be almost exponential at all points. However, the contribution of the relaxation and of the second order noise at small δ on the first hand, and the contribution of the geometrical corrections included in Eqs. (58) and (59) on the second hand, favor exponential variations at short times $\Delta t < T_{2,E}$. Consequently, we find that the Ramsey signals are expected to decay more or less exponentially, as we observe on the left panels of Fig. 8, where the data were phenomenologically fitted by exponentially damped sinusoids. The echo variations shown on the left panels of Fig. 14 are exponential as expected, and are fitted accordingly. For $N_g \neq 1/2$, the dominant contribution to decoherence has been found to be a first order $1/f$ charge noise truncated at 0.4 MHz, which is actually quasistatic according to Sec. II C, since $\omega_c T_{2,E} \ll 1$. Consequently, if this noise is really Gaussian, $f_{z,R}$ should be given by Eq. (23), i.e., purely Gaussian. The decay should fit to Eq. (58), which includes the relaxation contribution and geometrical errors. Now, it was found that this equation does not fit the data well, even with unreasonably large geometrical errors, because oscillations survive much too strongly at large time $\Delta t > T_2$. Consequently, Fig. 8 shows an empirical fit with exponentials. This mismatch between the simple theory and the experiment might be attributed to the non Gaussian character of the $1/f$ charge noise, which is known to contain large discrete TLF's as already mentioned and as observed in the line shapes. Depending on the distribution of these large fluctuators, Eq. (38) might be applicable. But such a formula gives an exponential decay for the ensemble average over all possible distributions of TLFs and is not supposed to describe quantitatively the non-self-averaging decay of single Ramsey samples (like those we have measured), for which a few TLFs are expected to dominate. Our experimental p_R's could be compatible with a model which includes a dominant TLF inducing an initial Gaussian-like decay at small times $\Delta t < T_2$, and a large collection of further TLF's responsible for the exponential-like tail of the decay. In the same way, $f_{z,E}$ is expected to decay as $\exp[-(\Delta t/T_E)^n]$ with $n \geqslant 3$ if the quasistatic $1/f$ noise is Gaussian. The rather exponential character

of the measured p_E's (see the right hand panels of Fig. 14) also suggest that the non-Gaussian character of the noise lowers the exponent n, as predicted by Eq. (39). On the other hand, the higher sensitivity of p_E to geometrical errors (compared to p_R) also favors an exponential decay. To summarize, the decay times $T_{2,E}$ are well explained, but the temporal dependence of the functions $f_{z,E}(t)$ is not fully accounted for, possibly due to the non-Gaussian character of the charge noise.

3. Decoherence at the optimal point P_0

Figure 15 shows that the best fit away from P_0 automatically leads to correct $T_{2,E}$ values at P_0. Knowing from the fitting procedure that the phase noise gives a negligible contribution to decoherence at this point, the following question arises: Can the quasistatic $1/f$ charge noise explain quantitatively the Ramsey decay shape at P_0? To answer this question, we plot on Fig. 7 the theoretical decay $\exp[-\Delta t/2T_1]\{1+[7.3(\Delta t/T_\varphi)]^2\}^{-1/4}$ where the second term is a simple rewriting of Eq. (27), with $T_\varphi=620$ ns calculated from the fitted noise spectrum $Sc_{N_g}(\omega)$. This curve is seen to be in good agreement with the envelope of the best experimental $p_R(\Delta t)$ records. Whereas it is close to exponential at $\Delta t \lesssim T_2$, it predicts a significantly larger signal at long times, as we always observe. These results suggest that coherence at the optimal working point P_0 is limited by second order microscopic static charge noise. Do the data in the frequency domain also support this conclusion? First, we observe on Fig. 11 that the resonance line at P_0 is asymmetric, which is a key feature of decoherence due to a second order noise at an optimal point. The line has indeed a tail on its higher-frequency side because N_g noise can only increase ν_{01}, which is minimum at P_0. More precisely, the intrinsic theoretical line shape, i.e., the Fourier transform of Eq. (27), is nonzero only at $\Delta\nu=\nu-\nu_{01}\geqslant 0$, is proportional to $\Delta\nu^{-1/2}\exp(-2\pi\Delta\nu T_\varphi/7.3)$ and is to be convolved with the Lorentzian line shape due to relaxation. A subtle point already mentioned for $1/f$ noise is that decoherence data are actually dependent on the exact experimental protocol used to average them. In particular, T_φ depends on the averaging time through the infrared cutoff introduced in the calculation of σ_{N_g} [see Eq. (27)]. The 1 Hz cutoff used for interpreting p_R is no longer relevant for interpreting the line shape, which was averaged over several records of 10 min each, with a precise tuning of N_g before each record. The corresponding cutoff is of order of $1/(600\ \text{s})$ and the new T_φ value analogous to the 620 ns used in the time domain is now 415 ns. Figure 11 shows the corresponding theoretical line shape, which takes into account this T_φ and T_1. This line is significantly narrower than the experimental one. This mismatch cannot be reduced by changing T_φ (i.e., the infrared cutoff or the noise amplitude) since the line would be broadened only on its right side. Once more, this discrepancy might be attributed to the non Gaussian character of charge noise. To quantify the mismatch, we empirically fit the experimental line to the theoretical one convoluted with an additional Lorentzian. The width of this Lorentzian leading to the best fit corresponds to a characteristic decay time of 600 ns. This characteristic time can be used to place an upper bound for the E_J noise. Indeed, attributing part of the additional contribution to this noise, assuming $Sc_{\delta E_J/E_J}=A/|\omega|$, and applying Eq. (17) with the same infrared cutoff as above, leads to $A<(3\times10^{-6})^2$, a value to be compared to the $(0.5\times10^{-6})^2$ mentioned in Sec. II C. In conclusion, decoherence at P_0 is dominated by microscopic charge noise at second order, the E_J noise contributing at most for 40% and probably much less. Finally, we point out that pure dephasing is efficiently suppressed at P_0 with the echo technique, due to the ultraviolet cutoff of $Sc_{N_g}(\omega)$. Indeed, the measured $T_E=550$ ns corresponds to a dephasing time $T_{\varphi,E}=1.3\ \mu$s, partially hidden here by the short T_1 of the sample. A summary of these results is provided in Table I.

V. DECOHERENCE DURING DRIVEN EVOLUTION

In the presence of a microwave driving voltage, the quantronium dynamics is best described in the rotating frame, as already mentioned in Sec. III D. Due to decoherence, the precession of the effective spin is progressively dephased after a characteristic coherence time $\tilde{T}_2$ and, after some time $\tilde{T}_1$, the spin is almost depolarized because $\hbar\omega_R \ll kT$ in our experiment. In this section, we will describe the measurements of $\tilde{T}_2$ and $\tilde{T}_1$ at the optimal point P_0. We will compare them to the results of Sec. III D and see if they can be understood from the noise spectra introduced in the preceding section.

A. Coherence time $\tilde{T}_2$ determined from Rabi oscillations

The coherence time during driven evolution is directly obtained from the decay of Rabi oscillations since the ground state $|0\rangle=(|\tilde{0}\rangle+|\tilde{1}\rangle)/\sqrt{2}$ is a coherent superposition of the eigenstates under driven evolution. A series of Rabi experiments performed at the optimal point P_0 on resonance ($\Delta\omega=0$) is shown in Fig. 16. These decays can be fitted with exponentially damped sinusoids oscillating at ω_{R0}, whose corresponding decay times $\tilde{T}_2$ are reported in Fig. 17 as a function of the Rabi frequency $\omega_{R0}/2\pi$, in the range 1–100 MHz. The decay time $\tilde{T}_2$ is found to be almost constant at 480 ns under these conditions. This value being significantly shorter than $4T_1/3$, it gives access to $T_\nu=\Gamma_\nu^{-1}=1.5\pm0.5\ \mu$s using Eq. (45), $\tilde{\Gamma}_2=3\Gamma_1/4+\Gamma_\nu/2$. Then, one deduces from $\Gamma_\nu\equiv\pi Sc_{\delta\omega_z}(\omega_{R0})$ that $Sc_{\delta\omega_z}(\omega)$ is, at P_0, constant at about $(1.5-3)\times10^5$ rad/s in the whole 1–100 MHz range. Being obtained at the optimal point, the latter value should be explained either by the first order noise of E_J or by second order noises N_g^2 and δ^2. The E_J noise, being of the $1/f$ type, cannot explain the constant $Sc_{\delta\omega_z}(\omega)$. Then, assuming that the classical noise on N_g is negligible at all frequencies above the low-frequency cutoff of 0.4 MHz found in the previous section, the autoconvolution of $Sc_{N_g}(\omega)$ has a negligible weight in the frequency range considered here and $Sc_{\delta\omega_z}(\omega)$ can only be due to the δ^2 noise, whose spectral density is essentially given by the autoconvolution of the white δ noise introduced previously. Using a high-frequency

TABLE I. Summary of the relevant spectral densities, of the sensitivity coefficients to noise, and of the characteristic times characterizing decoherence at the optimal point P_0. Angular frequencies in the formula have to be expressed in rad/s. Note that these evaluations take into account experimental errors of 2×10^{-3} in $\delta/2\pi$ and of 3×10^{-3} in N_g, made when tuning the working point.

Noise	$\lambda=N_g$		$\lambda=\delta/2\pi$		$\lambda=\delta E_J/E_J$	Total	Measured	
	Gate	Micro.	Readout	Micro.	Micro.			
$S_\lambda(\omega_{01})$ (s/rad)	$(3-4\times10^{-9})^2$	?	$(20\times10^{-9})^2$	?	?			
$D_{\lambda,\perp}$ (10^{11} rad/s)	1.93		$3.8d\simeq0.12$		<0.003			
T_1	1–2 μs	?	5–10 μs	?	?	0.8–1.6 μs	0.5–1 μs	
$Sc_\lambda(\omega_{01})$ (s/rad)	$(2\times10^{-9})^2$	$(1.3\times10^{-3})^2/\omega$ $\lvert\omega/2\pi\rvert<0.4$ MHz	AWG: $\simeq(30\times10^{-9})^2$ Y_R: $\simeq(2\times10^{-9})^2$	$(10^{-4})^2/\omega$	$<(3\times10^{-6})^2/\omega$			
$D_{\lambda,z}$ $\partial^2\omega_{01}/\partial\lambda^2$ (10^{11} rad/s)	<0.01 2.9		<0.02 -8.5		0.85			
T_φ	1 ms-1 s	0.6 μs	0.1-1 ms	$\sim$50 μs	>0.7 μs	0.6 μs	0.6 μs	$T_2=0.3$ μs
$T_{\varphi,E}$	-	1.3 μs	0.1-1 ms	-	?	1.3 μs	1.3 μs	$T_E=0.55$ μs

cutoff much higher than 100 MHz indeed leads to a constant $Sc_{\delta\omega_z}(\omega)$ as observed. Nevertheless, we have not found a plausible phase noise spectrum $Sc_{(\delta/2\pi)}(\omega)$ that could account for the measured value of $Sc_{\delta\omega_z}(\omega)$ using Eq. (50).

In order to test the $\tilde{\Gamma}_2(\eta)$ dependence predicted by Eq. (45), a series of Rabi precession experiments was also performed at P_0 as a function of the detuning $\Delta\omega$, using a fixed microwave power corresponding to a Rabi frequency of $\omega_{R0}/2\pi=15.4$ MHz on resonance. The data are also presented on Fig. 17 together with the $\tilde{\Gamma}_2$ expression given by Eq. (45), plotted using the T_1, T_φ, and T_ν values determined previously.

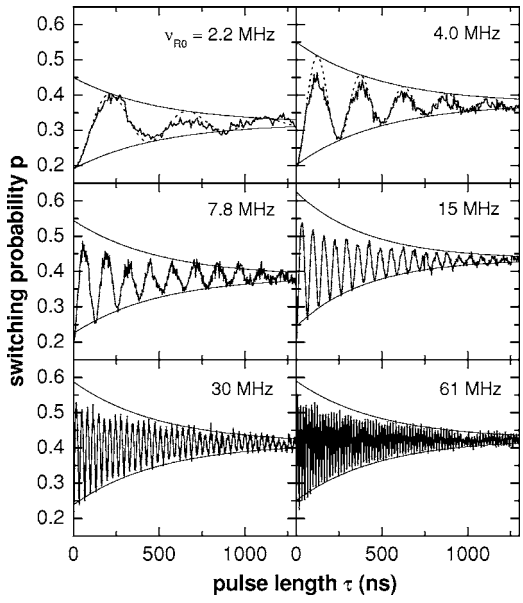

FIG. 16. Decay of the Rabi signals at the optimal point P_0 for different Rabi frequencies $\nu_{R0}=\omega_{R0}/2\pi$. The experimental data (oscillating solid lines) are fitted by exponentially damped sinusoids (dotted lines in the top panels), while their lower envelopes are fitted by exponentials (monotonous solid lines) leading to the $\tilde{T}_2$ values reported in Fig. 17.

B. Relaxation time $\tilde{T}_1$ determined from spin-locking experiments

The relaxation time $\tilde{T}_1$ can be obtained using the spin-locking technique developed in NMR. After having prepared

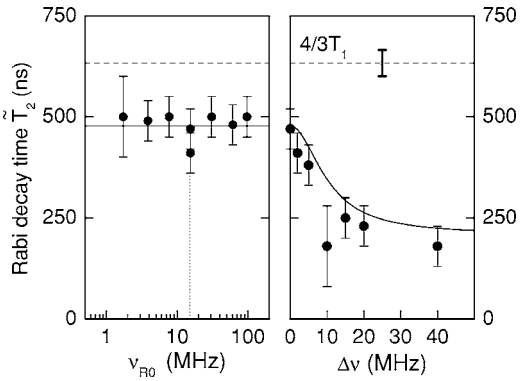

FIG. 17. Characteristic decay times $\tilde{T}_2$ of the Rabi oscillations at the optimal point P_0, as a function of the Rabi frequency ν_{R0} (left panel) at zero detuning $\Delta\nu$, and as a function of $\Delta\nu$ (right panel) at $\nu_{R0}=15.4$ MHz (dotted vertical line). $\tilde{T}_2(\nu_{R0},\Delta\nu=0)$ turns out to be a constant of order 0.48 μs (left solid line). The difference with $4/3T_1$ leads to an estimate for $T_\nu=1/\Gamma_\nu$. The right solid line corresponds to Eq. (45) plotted using the experimentally determined values of T_φ, T_1, and T_ν.

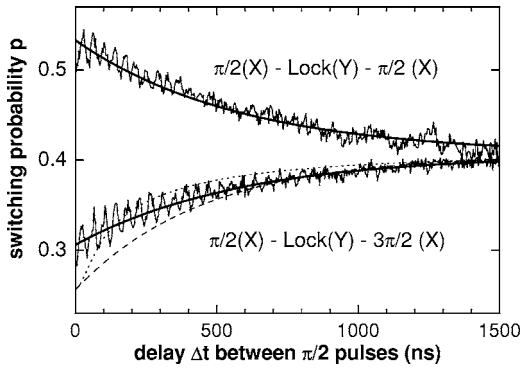

FIG. 18. Spin-locking signals (oscillatory lines) obtained at the optimal point P_0, using a detuning $\Delta\nu=8$ MHz, a locking microwave power corresponding to 24 MHz, and a final microwave pulse of $\pi/2$ (top) or $3\pi/2$ (bottom). The bold solid lines are exponential fits corresponding to $\tilde{T}_1\sim 580$ ns. For comparison, the Ramsey envelope (dotted line with $T_2\sim 250$ ns) and the longitudinal relaxation (dashed line with $T_1\sim 450$ ns) are shown.

the fictitious spin along an axis in the equatorial plane of the Bloch sphere, the effective field is immediately oriented parallel or antiparallel to the spin. Experimentally, the spin is prepared along the Y axis using a resonant $(\Delta\omega=0)$ $\pi/2$ pulse around the X axis. A microwave gate voltage with a phase shifted by $\pm\pi/2$ is then applied so that the driving field is parallel (or antiparallel) to the prepared spin state, which becomes either $|\tilde{0}\rangle$ or $|\tilde{1}\rangle$, respectively. The polarization along the prepared direction then decays exponentially with a decay time $\tilde{T}_1$ called in NMR the relaxation time in the rotating frame.[31] A second $\pi/2$ or a $3\pi/2$ pulse is then applied around the X axis after a variable delay in order to measure the remaining polarization in the rotating frame. This decay measured with a locking microwave field of $\omega_{R0}/2\pi=24$ MHz is shown in Fig. 18, together with the envelope of a Ramsey signal measured at $\Delta\omega/2\pi=8$ MHz and a relaxation signal recorded during free evolution. The evolution of the spin-locking signals toward equilibrium follows an exponential law with $\tilde{T}_1=550\pm 50$ ns, irrespective of whether the spin is parallel or antiparallel to the locking field. This is because the energy splitting $\hbar\omega_{R0}$ of the levels $|\tilde{0}\rangle$ and $|\tilde{1}\rangle$ in the rotating frame is small, $\hbar\omega_{R0}\ll k_BT$. Using Eq. (42) $\tilde{\Gamma}_1=\Gamma_\nu+\frac{1}{2}\Gamma_1$, one obtains again $T_\nu=1.5\pm 0.5$ μs, in agreement with the analysis of Rabi oscillations.

VI. DECOHERENCE MECHANISMS IN THE QUANTRONIUM, PERSPECTIVES, AND CONCLUSIONS

A. Summary of decoherence mechanisms in the quantronium

We have characterized decoherence in a superconducting qubit circuit, the quantronium, using techniques adapted from NMR. We have presented a general framework that describes these experiments. As expected, we have found that quantum coherence of the quantronium is maximum at the so-called optimal point P_0, where the decay laws of the transverse polarization can be significantly non-exponential, particularly in the presence of $1/f$ noise. Similar and complementary analyses of decoherence have now been performed in other Josephson qubits.[28,45–47] We have also derived the noise spectra that characterize the sources leading to decoherence of the quantronium, at and away from P_0. We have shown that coherence is mainly limited by dephasing due to charge and phase noises of microscopic origin, and that relaxation also contributes. An important feature of our analysis is the introduction of a *high-frequency cutoff* at about 0.5 MHz for the classical part of the *charge noise* spectrum. Finally, it was shown that in our qubit with $E_J\sim E_C$, second order charge noise is dominant at P_0.

Although our semiempirical approach obviously did not aim at providing any definite clues about the exact nature of the microscopic defects responsible for the noise spectra invoked to explain decoherence, the subject is very important and deserves further studies. To improve our understanding, more refined models could be built including a finite set of strongly coupled slow TLFs, with a close-to-continuous background of weakly coupled ones, including the non-Gaussian nature of their noise (see Refs. 39 and 43).

Finally, we point out that some of the NMR methods that we have used to characterize decoherence in our circuit provide tools for improving coherence in a qubit. We now discuss the interest of maintaining quantum coherence with these methods, and how far we are from meeting the requirements for elementary quantum computing.

B. Does driving the qubit enhance its coherence?

The observation that $\tilde{T}_2>T_2$ suggests that the coherence is improved by driving the qubit. But what are the reason and the meaning of this observation? The gain is actually due to the divergence of the noise spectral density $Sc_{\delta\omega}(\omega)$ at low frequency. Indeed, when the Rabi frequency is large enough, the low-frequency fluctuations $\delta\omega$ are not effective because the eigenstates $|\tilde{0}\rangle$ and $|\tilde{1}\rangle$ follow adiabatically the fluctuations of the effective driving field, as predicted by Eq. (42). Consider now that a coherent superposition of the two eigenstates in the rotating frame, $\alpha|\tilde{0}\rangle+\beta|\tilde{1}\rangle$, has been prepared and that a Rabi field is applied. The superposition then evolves at the Rabi frequency, and the initial state is retrieved periodically with a coherence time $\tilde{T}_2>T_2$. By encoding the qubit in the basis $(|\tilde{0}\rangle,|\tilde{1}\rangle)$, quantum coherence is thus maintained during a longer time than for free evolution. Rabi precession provides a direct test of this result because the ground state is an equal weight superposition $|0\rangle=|\tilde{0}\rangle+|\tilde{1}\rangle$. When a coherent superposition of these eigenstates is prepared, and a locking field applied afterward, the initial state is frozen with coherence time $\tilde{T}_2>T_2$ and mixing time $\tilde{T}_1>T_1$. Although these two examples show that a qubit state can indeed be stored during a longer time by driving it, it is clear that the qubit cannot be used at will during its driven evolution.

The echo technique can also be regarded as a soft driving of the qubit aiming at reducing decoherence. As shown in Sec. IV C, it indeed removes the effect of the low-frequency

fluctuations of $\delta\omega$. It can be figured as a time-reversal operation that compensates frequency changes that are almost static over the duration of the pulse sequence. This method is in fact more general, and the repeated application of π pulses can compensate for frequency fluctuations over longer durations. This so-called bang-bang technique in NMR could be used for qubits provided that the coherence loss due to the pulses is small enough.[37]

C. Coherence and quantum computing

Although the simple methods mentioned above could help in reducing qubit decoherence, real quantum error correcting codes are mandatory for quantum computing. These codes are known to require error rates smaller than about 10^{-4} depending on the nature of the errors for each logic gate. Presently, the gate error rate can be estimated at a few percent for single qubit gates (e.g., the quantronium), and significantly more for two qubit gates such as coupled Cooper pair boxes.[48] The coherence time is about a few hundred times longer than the duration of a single qubit gate operation in the quantronium, and would be at best a few ten times the duration of a two qubit gate. Since decoherence is equivalent to making errors, the quantronium requires an improvement of coherence time by two or three orders of magnitude. The operation of a quantum processor based on this qubit circuit, or on any other one presently developed, thus appears to be a significant challenge.

This is, however, not a reason to give up because conceptual and technical breakthroughs are to be expected in the rather new field of quantum circuits. Progress in junction fabrication might in particular lead to a significant increase of coherence times in Josephson qubit circuits. Furthermore, it is already close to possible to run simple algorithms such as Grover's search algorithm, and to address important questions in quantum mechanics. The extension of quantum entanglement from the microscopic to the macroscopic world, and the location and nature of the frontier between the quantum and classical worlds, are two essential issues. For instance, the accurate measurement of the correlations between two coupled qubits in order to test the violation of Bell's inequalities could indeed probe whether or not the collective variables of qubit circuits follow quantum mechanics. Such an experiment will become possible as soon as a high fidelity readout is available, which is clearly an important step to pass.

ACKNOWLEDGMENTS

We acknowledge numerous discussions in the Quantronics group, discussions with G. Falci, the technical help of P. F. Orfila, P. Sénat, and J. C. Tack, the support of the European project SQUBIT, of Yale University (Grant No. DAAD 19-02-1-0044), of the Landesstiftung BW, and of the Dynasty Foundation. P.J. Meeson acknowledges support from the Marie Curie foundation.

[1] Y. Nakamura, Yu. A. Pashkin, and J. S. Tsai, Nature (London) **398**, 786 (1999); Y. Nakamura Y. A. Pashkin, T. Yamamoto, and J. S. Tsai Phys. Rev. Lett. **88**, 047901 (2002).

[2] D. Vion, A. Aassime, A. Cottet, P. Joyez, H. Pothier, C. Urbina, D. Esteve, and M. H. Devoret, Science **296**, 886 (2002).

[3] A. Cottet, Ph.D. thesis, Université Paris VI, 2002 http://www-drecam.cea.fr/drecam/spec/Pres/Quantro/.

[4] J. M. Martinis, S. Nam, J. Aumentado, and C. Urbina, Phys. Rev. Lett. **89**, 117901 (2002).

[5] I. Chiorescu, Y. Nakamura, C. J. P. M. Harmans, and J. E. Mooij, Science **299**, 1869 (2003).

[6] J. Claudon, F. Balestro, F. W. J. Hekking, and O. Buisson, Phys. Rev. Lett. **93**, 187003 (2004).

[7] A. Wallraff, D. I. Schuster, A. Blais, L. Frunzio, R.-S. Huang, J. Majer, S. Kumar, S. M. Girvin, and R. J. Schoelkopf, Nature (London) **431**, 162 (2004).

[8] M. A. Nielsen and I. L. Chuang, *Quantum Computation and Quantum Information* (Cambridge University Press, Cambridge, U.K., 2000).

[9] A. Cottet, D. Vion, A. Aassime, P. Joyez, D. Esteve, and M. H. Devoret, Physica C **367**, 197 (2002).

[10] V. Bouchiat, Ph.D. thesis, Université Paris VI, 1997 http://www-drecam.cea.fr/drecam/spec/Pres/Quantro/

[11] V. Bouchiat, D. Vion, P. Joyez, D. Esteve, and M. H. Devoret, Phys. Scr., T **76**, 165 (1998).

[12] Y. Nakamura, C. D. Chen, and J. S. Tsai, Phys. Rev. Lett. **79**, 2328 (1997).

[13] E. Collin, G. Ithier, A. Aassime, P. Joyez, D. Vion, and D. Esteve, Phys. Rev. Lett. **93**, 157005 (2004).

[14] A. Messiah, *Quantum Mechanics* (North-Holland Publishing Company, Amsterdam, 1962), Vol. II, p. 379.

[15] M. H. Devoret, D. Esteve, C. Urbina, J. M. Martinis, A. N. Cleland, and J. Clarke, in *Quantum Tunneling in Condensed Media*, edited by Yu. Kagan, and A. J. Leggett (Elsevier Science, Amsterdam, 1992), pp. 313–345.

[16] G. Ithier, E. Collin, P. Joyez, D. Vion, D. Esteve, J. Ankerhold, and H. Grabert, Phys. Rev. Lett. **94**, 057004 (2005).

[17] I. Siddiqi, R. Vijay, F. Pierre, C. M. Wilson, M. Metcalfe, C. Rigetti, L. Frunzio, and M. H. Devoret, Phys. Rev. Lett. **93**, 207002 (2004).

[18] P. Bertet, I. Chiorescu, K. Semba, C. J. P. M. Harmans, and J. E. Mooij, Phys. Rev. B **70**, 100501(R) (2004).

[19] D. J. Van Harlingen, T. L. Robertson, B. L. T. Plourde, P. A. Reichardt, T. A. Crane and John Clarke, Phys. Rev. B **70**, 064517 (2004).

[20] J. M. Martinis, S. Nam, J. Aumentado, K. M. Lang, and C. Urbina, Phys. Rev. B **67**, 094510 (2003).

[21] I. Siddiqi and M. Devoret (private communication).

[22] R. W. Simmonds, K. M. Lang, D. A. Hite, S. Nam, D. P. Pappas and John M. Martinis, Phys. Rev. Lett. **93**, 077003 (2004).

[23] G. Zimmerli, T. M. Eiles, R. L. Kautz and John M. Martinis, Appl. Phys. Lett. **61**, 237, (1992).

[24] E. H. Visscher, S. M. Verbrugh, J. Lindeman, P. Hadley, and J. E. Mooij, Appl. Phys. Lett. **66**, 3, (1995).

[25] J. Pettersson, P. Wahlgren, P. Delsing, D. B. Haviland, T. Claeson, N. Rorsman, and H. Zirath, Phys. Rev. B **53**, R13272 (1996).
[26] A. B. Zorin, F.-J. Ahlers, J. Niemeyer, T. Weimann, H. Wolf, V. A. Krupenin, and S. V. Lotkhov, Phys. Rev. B **53**, 13682 (1996), and references therein.
[27] R. H. Koch, J. Clarke, W. M. Goubau, J. Martinis, C. W. Pegrum, and D. J. Van Harlingen, J. Low Temp. Phys. **51**, 207 (1983).
[28] O. Astafiev, Yu. A. Pashkin, Y. Nakamura, T. Yamamoto, and J. S. Tsai, Phys. Rev. Lett. **93**, 267007 (2004).
[29] G. Stan, S. B. Field, and J. M. Martinis, Phys. Rev. Lett. **92**, 097003 (2004).
[30] F. C. Wellstood, C. Urbina, and J. Clarke, Appl. Phys. Lett. **85**, 5296 (2004).
[31] C. P. Slichter, *Principles of Magnetic Resonance*, 3rd ed. (Springer-Verlag, Berlin, 1990).
[32] R. K. Wangsness and F. Bloch, Phys. Rev. **89**, 728 (1953); A. G. Redfield, IBM J. Res. Dev. **19**, 1 (1957); A. Abragam *The Principles of Nuclear Magnetism* (Oxford University, Oxford, 1961).
[33] E. Geva, R. Kosloff, and J. L. Skinner, J. Chem. Phys. **102**(21), 8541 (1995).
[34] Yu. Makhlin, and A. Shnirman, JETP Lett. **78**, 497 (2003).
[35] Yu. Makhlin and A. Shnirman, Phys. Rev. Lett. **92**, 178301 (2004).
[36] K. Rabenstein, V. A. Sverdlov, and D. V. Averin, JETP Lett. **79**, 646 (2004).
[37] G. Falci, A. D'Arrigo, A. Mastellone, and E. Paladino, Phys. Rev. A **70**, 040101(R) (2004).
[38] P. Dutta and P. M. Horn, Rev. Mod. Phys. **53**, 497 (1981).
[39] E. Paladino, L. Faoro, G. Falci and Rosario Fazio, Phys. Rev. Lett. **88**, 228304 (2002).
[40] This approximation allows one to find the decay law qualitatively; moreover, in the short—and long-time limits one of the terms dominates, and one finds accurate estimates.
[41] M. B. Weissman, Rev. Mod. Phys. **60**, 537 (1988).
[42] J. Schriefl, Ph.D. thesis, 2005 (unpublished).
[43] Y. M. Galperin, B. L. Altshuler, and D. V. Shantsev, in *Fundamental Problems of Mesoscopic Physics*, edited by I. V. Lerner *et al.* (Kluwer Academic Publishers, The Netherlands, 2004), pp. 141–165. Also in cond-mat/0312490
[44] A. Aassime, G. Johansson, G. Wendin, R. J. Schoelkopf, and P. Delsing, Phys. Rev. Lett. **86**, 3376 (2001).
[45] G. Burkard, D. P. DiVincenzo, P. Bertet, I. Chiorescu, and J. E. Mooij, Phys. Rev. B **71**, 134504 (2005).
[46] D. I. Schuster, A. Wallraff, A. Blais, L. Frunzio, R.-S. Huang, J. Majer, S. M. Girvin, and R. J. Schoelkopf, Phys. Rev. Lett. **94**, 123602 (2005).
[47] T. Duty, D. Gunnarsson, K. Bladh, and P. Delsing, Phys. Rev. B **69**, 140503(R) (2004).
[48] Yu. Pashkin, T. Yamamoto, O. Astafiev, Y. Nakamura, D. V. Averin, and J. S. Tsai, Nature (London) **421**, 823 (2003).

Chapter 5

Towards a Non Demolition measurement of the quantronium

After the successful operation of the quantronium, it appeared that implementing a Quantum Non Demolition (QND) measurement of the quantum state of the qubit would be an important goal. Such a QND measurement is an ideal projective measurement that leaves the qubit state after the readout on states $|0\rangle$ or $|1\rangle$ according to their probability amplitudes in the state before readout(see fig. 5.1).

A non destructive measurement should improve the fidelity by avoiding relaxation or excitation during readout. This would be useful for probing quantum correlations between coupled qubits and in particular, Bell inequalities for mesoscopic systems. On the other hand, the readout could be repeated, which would further improve the readout fidelity.

The qubit state can also be re-used after readout which could be interesting for certain types of quantum algorithms, although a QND measurement is not indispensable for Quantum computing [64].

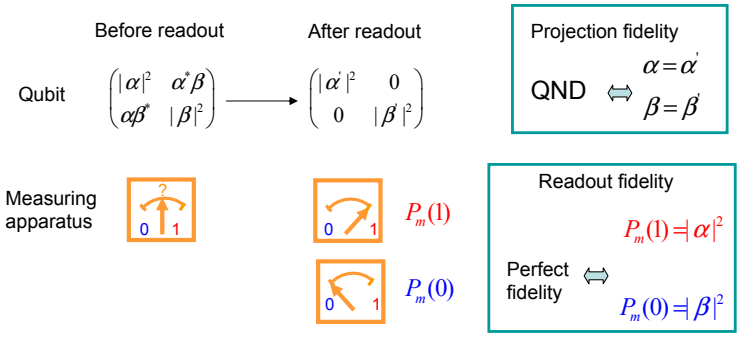

Figure 5.1: During a ideal QND measurement, the qubit state is projected on its eigenstates with probabilities given by $|\alpha|^2$ and $|\beta|^2$. In practice, relaxation or excitation during the readout can corrupt the result of the projection. Note that a QND measurement is not necessary single shot.

5.1 Readout strategies

5.1.1 Drawbacks of the switching readout

In chapters 3 and 4, the switching to the voltage state of an hysteretic Josephson junction was used for reading out the qubit state (see Sec. 2.3). This method has also been used by other groups [101, 40, 61] but suffers from several drawbacks as pointed out in Sect. 2.4.6. A first drawback is the absence of signal at the optimal working point. Indeed the signal corresponds to a first derivative $\partial\omega_{01}/\partial\lambda$ with λ an external parameter, and cancels at the optimal working point since it is a stationary point. This absence of signal is related to the decoupling with the noise on λ. As a consequence, one needs to go away from P_0 to get a detectable signal. During the adiabatic displacement of the working point, the transition frequency is divided roughly by a factor 2, and the qubit can cross spurious resonances of the environment, and thus loose polarization. A readout setup allowing to stay at the optimal working point or at least at its vicinity would thus be of great interest.

The second drawback is the switching of the readout junction itself. During this process the phase δ across the readout junction stays no longer around an average value which controls the Hamiltonian of the qubit but acquires a dynamical dissipative behavior. This modifies drastically the Hamiltonian which becomes time dependent. For this reason, the readout is not QND. In addition the quasiparticles generated limit the maximum repetition rate to a value of $\approx$ 50kHz leading to long acquisition times of about $\approx$ 1s per data point, and could spoil other nearby qubits.

5.1.2 New dispersive strategies

The manipulation of the quantronium and soon after of the flux-qubit at an optimal point, raised the problem of how to further improve this strategy. In particular, could it be possible to perform the readout without moving away from the optimal working point? A new readout strategy, now being developed by several groups ([102, 47, 103, 104]), permits to stay in the vicinity of the optimal working point. It is based on a purely dispersive measurement of the qubit. The idea for staying in the vicinity of the optimal working point during the readout is to measure the susceptibility of the qubit, i.e. the second derivative of the energy with respect to an external parameter. For instance, the Cooper pair box capacitance [104, 102]:

$$\frac{1}{C_k} = \frac{1}{(2e)^2}\frac{\partial^2 E_k}{\partial {N_g}^2} = \frac{1}{2e}\frac{\partial V_k}{\partial N_g},$$

where N_g is a gate voltage, and $V_k = \langle k|\widehat{V}|k\rangle$, $\widehat{V}$ being the voltage operator of the qubit island, can be measured. The inductance of a flux or of a charge-phase qubit

$$\frac{1}{L_k} = \frac{1}{\varphi_0^2}\frac{\partial^2 E_k}{\partial \delta^2} = \frac{1}{\varphi_0}\frac{\partial I_k}{\partial \delta},$$

where $I_k = \langle k|\widehat{I}|k\rangle$, $\widehat{I}$ being the current operator of the qubit, can also be mesured [47]. In these schemes, the qubit is coupled to a tank circuit (Nb coplanar cavity [105], discrete LC circuit [103], or shunted Josephson junction [47]) whose resonance is affected by the state dependent susceptibility of the qubit. The frequency resonance of the tank circuit is chosen far below the transition frequency of the qubit, in order to achieve a dispersive measurement of the qubit susceptibility. This measurement is performed with a small enough probing signal in order to avoid quasi-particles generation and on-chip dissipation. During the measurement, the transition frequency of the qubit explores a smaller frequency range than for the DC switching setup, but this frequency scan is performed several times rather than once. Whereas with the former switching readout method, a large level signal was measured using room temperature amplifiers, here low noise cryogenic amplifiers are required in order to measure the response of the tank circuit.

5.2 The Josephson bifurcation amplifier

For reading out the state of the quantronium, we use the setup invented at Yale University by Michel Devoret's group and called the Josephson bifurcation amplifier (JBA), which is based on the dynamics of a Josephson junction excited by a nearly resonant microwave signal [46, 47]. Its purpose is to use the readout junction of the quantronium as a tank circuit for measuring the effective state dependent L_{Q_k} inductance of the split Cooper pair box.

5.2.1 Principle of the qubit state discrimination

The dynamics of the resonator formed by the readout junction indeed depends on the qubit state because its dynamics is affected by the state dependent qubit inductance L_{Q_k} connected in parallel (see figure 5.2).

At low microwave power, the behavior of the Josephson junction shunted by its on-chip capacitor is the one of an LC oscillator, the inductance being the one of the junction: $L = \varphi_0/I_c$. Although a direct measurement of the state dependent resonance could be envisioned, the frequency change between state 0 and 1 is too small to achieve readout in a time smaller than the relaxation time. Indeed, the sensitivity of a cryogenic microwave amplifier does not allow a fast measurement ($\approx$ 100ns) of the very small (≈ -115dBm $\sim 1\mu$V on 50Ω) signal required for the linear regime of the oscillator.

The bifurcation phenomenon, explained below, permits to work with higher signal level compatible with our amplifiers and gives the sensitivity required.

Indeed, when increasing the driving microwave power, the non-linear regime of the Josephson junction resonance is explored, and, at large enough driving power, the readout junction undergoes a dynamical transition to an oscillation state with a larger amplitude and a different phase. This bifurcation phenomenon is identical to the transition of the well known Duffing anharmonic oscillator [48] in classical mechanics. The two oscillation states for the phase of the junction in the Josephson potential can coexist. The switching from one dynamical state to the other permits to discriminate between the qubit states because it is extremely sensitive to the different parameters and in particular to the effective inductance of the readout junction. It provides a sensitive amplifier suitable single shot readout.

Fig. 5.2 shows the setup of this Josephson bifurcation amplifier. The reflected signal is separated from the input signal by a directional coupler. Since no other dissipation sources are present, the reflected voltage U_r has the same amplitude as the incident voltage U_i. Due to the output impedance of the generator and to the input impedance of the amplifier, the incident microwave voltage is equal to half the voltage U of the generator. One has thus

$$V = U_i + U_r = \frac{U}{2} + U_r. \tag{5.1}$$

The information about the oscillator $\{L, C\}$ is carried by the phase of oscillation of U_r, related to the one of V. Depending on the two possible oscillation states of the JBA, two different phases for the reflected microwave pulses are possible.

We analyze in the next paragraph the zero temperature dynamics of the readout junction under an AC drive.

5.2.2 Dynamics of the JBA at zero temperature

The problem of an AC driven Josephson junction has been extensively studied theoretically by M. Dyckman [106, 107, 108], and both experimentally and theoretically by M. Devoret's group at Yale University [46, 47]. The next paragraphs, largely inspired from P. Ribero and F. Nguyen internship reports [109, 110], summarize the most important results relevant to this work.

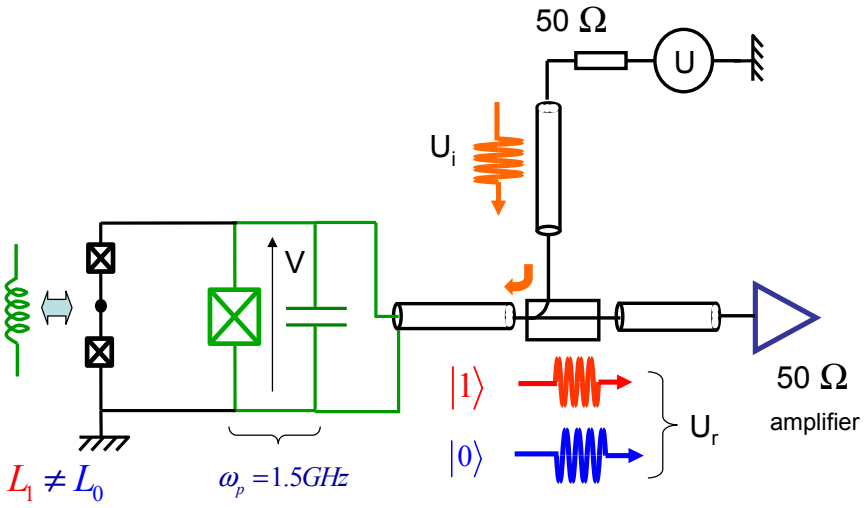

Figure 5.2: Principle of the AC readout of the quantronium with a JBA. The qubit has a state dependent inductive behavior that affects the plasma resonance of the anharmonic resonator formed by the readout junction in parallel with an on-chip capacitor. At large driving amplitude, this resonator undergoes a bifurcation between two oscillation states in the Josephson potential which is sensitive to the qubit state. The signature of this bifurcation and thus the qubit state is encoded in the phase of the reflected microwave U_r.

Equation of motion for the superconducting phase of a driven junction

Using the constitutive relations of the Josephson junction, of the capacitance and the Kirchoff's laws, one gets the equation of evolution of the phase δ across the readout junction:

$$Z_0 C\varphi_0 \partial_t^2 \delta + \varphi_0 \partial_t \delta + Z_0 I_0 \sin(\delta) = u_{dc} + \frac{U}{2}\cos(\omega_d t), \tag{5.2}$$

where $Z_0 = 50\Omega$ is the characteristic impedance of the microwave line, and ω_d is the frequency of the driving signal. Introducing the dimensionless variables

$$\alpha = \tfrac{\varphi_0 \omega_p}{Z_0 I_0}$$

$$\eta = \tfrac{U}{2Z_0 I_0} \qquad u = \tfrac{u_{dc}}{Z_0 I_0}$$

$$\omega = \tfrac{\omega_d}{\omega_p} \qquad \omega_p t = \tau,$$

where $\omega_p = \sqrt{I_0/\varphi_0 C}$ is the plasma frequency of the readout junction, one obtains the reduced equation of evolution

$$\partial_\tau^2 \delta + \alpha \partial_\tau \delta + \sin(\delta) = u + \eta\cos(\omega\tau). \tag{5.3}$$

This equation shows that the system is the analog of a unit mass particle in a tilted cosine potential well $V(\delta) = -u\delta - \cos(\delta)$ subject to a viscous friction force $-\alpha\partial_\tau\delta$, and to an ac driving force $\eta\cos(\omega\tau)$.

Monochromatic approximation

The monochromatic approximation consists in developing the solution $\delta(\tau)$ of Eq. 5.3 in Fourier series, keeping only the fundamental term oscillating at the driving frequency and neglecting all the contributions from other multiples or sub-multiples of the excitation frequency. One thus looks for a solution of Eq. 5.3 in the form

$$\delta(\tau) = \delta_0 + \Delta\cos(\omega\tau + \phi). \tag{5.4}$$

This approximation gives analytical relations between the amplitude of oscillation Δ of the superconducting phase δ, the phase ϕ of the oscillations and the driving amplitude η.

Using the following Bessel decomposition,

$$\sin\left[\Delta\cos(\omega\tau+\phi)\right] = J_0(\Delta) + 2\sum_{k=0}^{\infty}(-1)^k J_{2k}(\Delta)\cos\left[2k(\omega\tau+\phi)\right] \tag{5.5}$$

$$\cos\left[\Delta\cos(\omega\tau+\phi)\right] = 2\sum_{k=0}^{\infty}(-1)^k J_{2k+1}(\Delta)\cos\left[(2k+1)(\omega\tau+\phi)\right], \tag{5.6}$$

where J_k, with $k = 0, 1, ...$, are Bessel function of the first kind, and keeping only the oscillating terms at ω, Eq. 5.3 can be rewritten as [111]

$$\partial_\tau^2\delta + \alpha\partial_\tau\delta + \sin(\delta_0)J_0(\Delta) + \cos(\delta_0)\frac{2J_1(\Delta)}{\Delta}\delta = u + \eta\cos(\omega\tau). \tag{5.7}$$

This linearized equation is the starting point for the analysis of the dynamics.

Analytical determination of the stationary solutions

The stationnary solutions of Eq. 5.7 are given by the system

$$\sin(\delta_0) = \frac{u}{J_0(\Delta)} \tag{5.8}$$

$$-\Delta\omega^2 + \cos(\delta_0)2J_1(\Delta) = \cos(\phi)\,\eta \tag{5.9}$$

$$-\alpha\Delta\omega = \sin(\phi)\,\eta. \tag{5.10}$$

Combining these equations, a self-consistent equation system for the oscillation amplitude Δ and the phase ϕ is obtained:

$$\begin{cases} \Delta^2\left[\left(-\omega^2+\Omega^2\right)^2 + \alpha^2\omega^2\right] = \eta^2 \\ \phi = \arctan\left(\frac{\alpha\omega}{\Omega^2-\omega^2}\right) \end{cases} \tag{5.11}$$

with

$$\Omega^2 = \frac{2J_1(\Delta)}{\Delta}\cos(\delta_0). \tag{5.12}$$

Note that Ω is an effective resonance frequency of the junction in the absence of driving that depends on the amplitude of oscillation Δ.

A qualitative and noticeable effect of the non-linearity is that Eq. 5.11 can have more than one solution at large driving amplitude η, as shown on Fig. 5.3.

One notices that below a certain excitation frequency, there is one solution in the domain (A) and three solutions in the domain (B). As demonstrated in the next section, in domain (B), the solutions

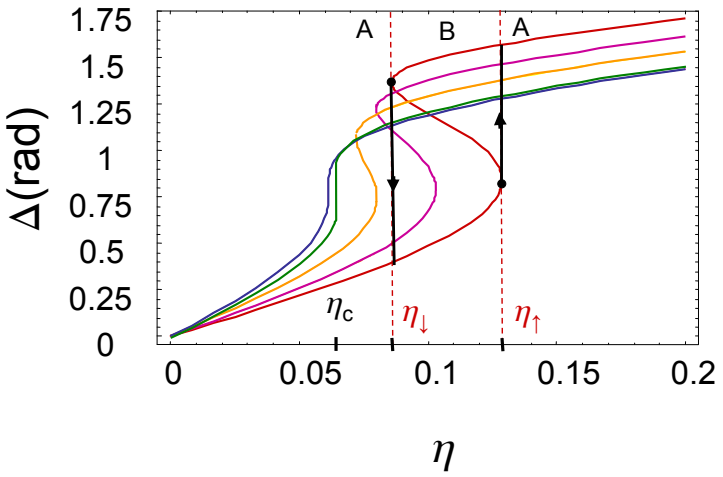

Figure 5.3: Amplitude of oscillation Δ of the stationary solutions as a function of the driving force η and for different reduced driving frequencies ($\omega = 0.94, 0.935, 0.92, 0.9$), given by Eq. 5.11 with $\alpha = 1/Q \approx 1/14$. Below a critical frequency ω_c, the Δ curve is multivalued and several solutions are possible. In region B, there exist two stable stationary solutions, which leads to an hysteretic character of the dynamics of the oscillator. Depending on its history, the oscillator can bifurcate at $\eta\uparrow$ from the lower branch to the upper one, or at $\eta_\downarrow$ from the upper branch to the lower one.

$\{\Delta_1, \phi_1\}$ of lower amplitude and $\{\Delta_2, \phi_2\}$ of higher amplitude are stable, whereas the third one $\{\Delta_3, \phi_3\}$ is unstable. By extension, the notation $\Delta_1 = \Delta_2 = \Delta_3 = \Delta$ and $\phi_1 = \phi_2 = \phi_3 = \phi$ in domain (A) is adopted.
For a given ω, the smaller and larger driving amplitudes leading to exactly two solutions are called the smaller and larger bifurcation driving amplitudes $\eta_\downarrow$ and $\eta_\uparrow$, respectively. Note that for both dynamical states, the phase δ stays confined in one well of the Josephson potential.

5.2.3 Solution stability and dynamics in the quadrature phase-space

The monochromatic solutions of Eq. 5.3 can also be represented in the frame rotating at ω, i.e. in the space of the in-phase and quadrature components of δ: $\{p, q\} = \{\Delta\sin(\phi), \Delta\cos(\phi)\}$. This phase space gives a better visualization of the dynamics than the space $\{\delta, d\delta/dt\}$ since $\{p, q\}$ are slow variables.

Within this frame, we have

$$\begin{aligned} \delta(\tau) &= \Delta\cos(\omega t + \phi) = \cos(\omega\tau)q - \sin(\omega\tau)p \\ \dot{\delta}(\tau) &\approx -\omega\left[q\sin(\omega\tau) + p\cos(\omega\tau)\right] \\ \ddot{\delta} &= -\omega^2\delta - 2\omega\left[\dot{q}\sin\omega\tau + \cos(\omega\tau)\dot{p}\right]. \end{aligned} \tag{5.13}$$

(5.14)

Developing the potential in Bessel functions and retaining only terms at the driving frequency, Eq. 5.3 writes:

$$\dot{q} = F_1(p,q) = \frac{\partial h}{\partial p} - \frac{\alpha}{2}q \tag{5.15}$$

$$\dot{p} = F_2(p,q) = -\frac{\partial h}{\partial q} - \frac{\alpha}{2}p \tag{5.16}$$

where:

$$h(p,q) = \frac{\omega}{4}(p^2+q^2) + \frac{1}{\omega}J_0(\sqrt{p(t)^2+q(t)^2}) + \frac{\eta}{2\omega}p. \tag{5.17}$$

The zeros of the effective velocity field: $\vec{v} = \{\dot{p}, \dot{q}\}$ give the stationary solutions (see Fig. 5.4). Note that the speed field is also zero at a third extremum which is the dynamical saddle point.

The stability of a stationary solutions $x_{stat} = \{p_{stat}, q_{stat}\}$ is characterized by studying the characteristics of transient solutions in the vicinity of a stationary solution. This is achieved by linearizing the system 5.15 in the vicinity of x_{stat} and studying the eigensystem of the Jacobian matrix J given by:

$$J(\{p_{stat}, q_{stat}\}) = \begin{bmatrix} \frac{\partial F_1}{\partial p} & \frac{\partial F_1}{\partial q} \\ \frac{\partial F_2}{\partial p} & \frac{\partial F_2}{\partial q} \end{bmatrix} \tag{5.18}$$

The stability is given by the real part of the eigenvalues λ of J. The stationary solution is unstable for $\mathrm{Re}\{\lambda\} > 0$; in this case there exist transient perturbations around this stationary solution that diverge exponentially. On the contrary, the stationary solution is stable (and called "attractor") for $\mathrm{Re}\{\lambda\} < 0$. In this case any transient regime coming from a small perturbation around the stationary solution is exponentially damped: if $\mathrm{Im}\{\lambda\} = 0$, the system converges exponentially to the attractor , and if $\mathrm{Im}\{\lambda\} \neq 0$, the system is spiraling to the attractor. In both cases, the characteristic damping time is given by $1/\omega_p\mathrm{Re}(\lambda)$.

Depending on the parameters (ω, α, η) these different situations can occur. Typically, for small driving amplitudes, a single attractor exists. As the driving amplitude increases, a pair of stable-unstable

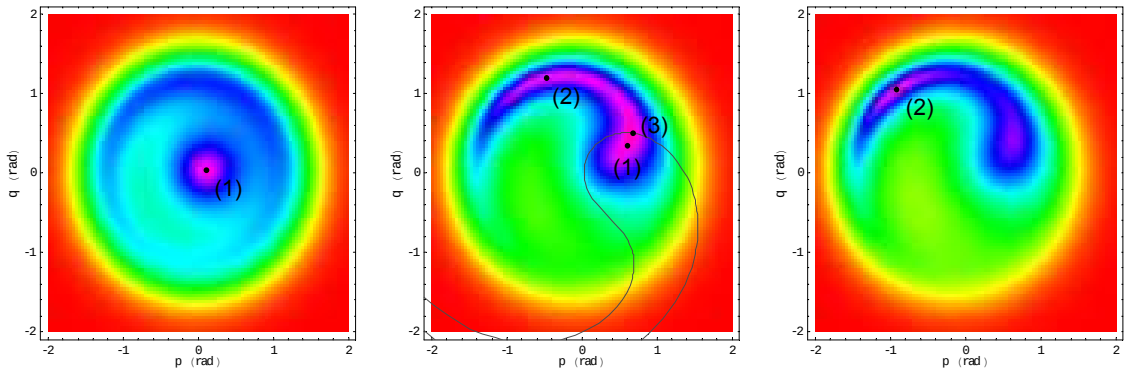

Figure 5.4: Amplitude of the speed field $\|\vec{v}\| = \sqrt{\dot{p}^2 + \dot{q}^2}$ (increasing from black to white) in the $\{p, q\}$ phase space for $\alpha = 0.07$, $\omega = 0.91$ and $\eta = 0.02$ (left panel), $\eta = 0.09$ (midle panel) and $\eta = 0.12$ (right panel). The stationary solutions are represented by black dots and the separatrix by a black line (middle graph). Courtesy of P.Ribero.

solutions is created. At the bifurcation points the unstable solution and one of the stable solutions are identical which means that one of the eigenvalues of J is zero. The amplitude Δ of oscillation at the bifurcation points are thus given by

$$det(J) \quad = \quad \omega^2\alpha^2 + \left(\omega^2 - \frac{2J_1(\Delta)}{\Delta}\right)^2 + J_2(\Delta)\left(\omega^2 - \frac{2J_1(\Delta)}{\Delta}\right) = 0 \tag{5.19}$$

The driving amplitude $\eta_\downarrow$ and $\eta_\uparrow$, for which the bifurcation occurs are computed from Δ using Eq. 5.11 and shown on Fig. 5.5 . A comparison with the result of the Dykman approach [108] which considers a quartic potential instead of a cosine one, is also shown.

In the $\{\eta, \omega\}$ space the bifurcation points $B_\downarrow = \{\eta_\downarrow, \omega\}$ and $B_\uparrow = \{\eta_\uparrow, \omega\}$ generate two lines (see Fig.5.5) ending at a critical point C $\{\eta_c, \omega_c\}$ that corresponds to a triply degenerated solution. This point is completely determined by the quality factor Q, and can be calculated in the Dykman framework (quartic approximation of the cosine potential) : the reduced frequency of the point C is $\omega_c = 1 - \sqrt{3}/2/Q$.

It is interesting to note that the damping time of the transient regime depends both on the quality factor (like for a harmonic oscillator) and on the detuning $\omega = \omega_d/\omega_p$. This is an effect of the non-linearity of the Josephson potential. When the working point comes closer to the critical point C, the damping time of the transient regime diverges.

On Fig. 5.5, the two bifurcation lines delimit two regions (A) and (B) where one or three dynamic solutions exist respectively.

In region (B) (2 stable and 1 unstable solutions) one can define in the $\{p, q\}$ phase space, the two regions corresponding to initial conditions $\{q(0), p(0)\}$ evolving towards one of the two stable solutions. The separatrix is then defined as the boundary between these two regions. Note that the unstable solution is located on the separatrix.

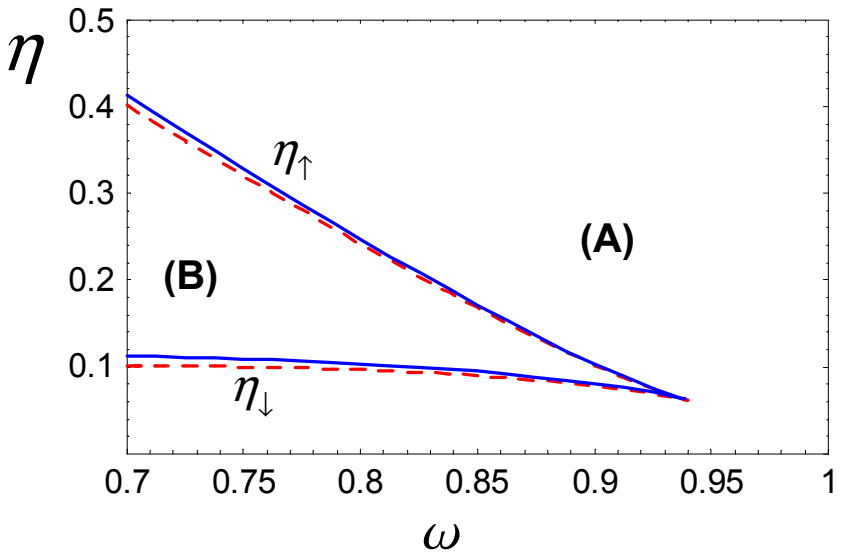

Figure 5.5: Bifurcation lines calculated from Eq. 5.19 (solid line) or from Dykman's formalism (dashed line) with a qulaity factor of 14. The error introduced on $\eta_\uparrow$ by the cubic approximation is 4% maximum in the range plotted here. The bifurcation lines $(\eta_\uparrow, \eta_\downarrow)$ divide the plane $\{\eta, \omega\}$ in two regions. In region A, the dynamics of the system has a single solution. In region B, it has three solutions: two stable and one unstable. The two bifurcation lines end at a spinode point C, which corresponds to a triply degenerate solution.

Effect of a parasitic inductance

The effect of a parasitic inductance between the 50Ω line and the JBA is now considered. As we'll see in section 5.3, such a parasitic inductance was always present in the experiment and affects the location of the bifurcation points. However, the stationary solutions and the bifurcation points can still be calculated analytically.

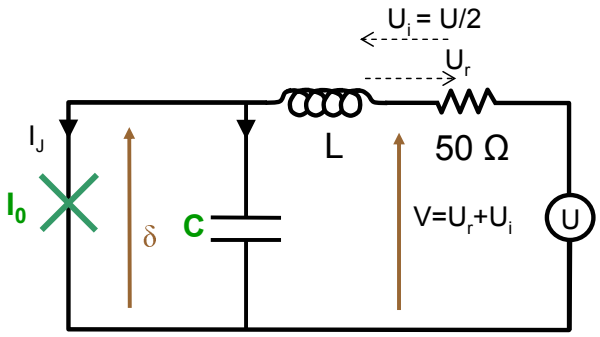

Figure 5.6: Readout circuit with a parasitic series inductance from the 50Ω transmission line to the JBA.

Within the monochromatic approximation, Eq. 5.3 is now replaced by

$$\alpha\beta\partial_\tau^3\delta + \partial_\tau^2\delta + \alpha\left[1+\beta(J_0(\Delta)+J_2(\Delta))\right]\partial_\tau\delta + \frac{2J_1(\Delta)}{\Delta}\delta = \eta\cos(\omega\tau) \tag{5.20}$$

where $\beta = L/L_J$, and the stationary solutions are the roots of the system

$$\begin{cases} \eta^2 &= \left(\frac{2J_1(\Delta)}{\Delta}-\omega^2\right)^2\Delta^2 + \alpha^2\Omega^2\left(1+\beta(J_0(\Delta)+J_2(\Delta))-\omega^2\beta\right)^2\Delta^2 \\ \phi &= \frac{\alpha\omega(1+\beta(J_0(\Delta)+J_2(\Delta))-\omega^2\beta)}{2J_1(\Delta)/\Delta-\omega^2} \end{cases} \tag{5.21}$$

This system differs from system 5.11 in the sense that the effective friction depends now on the oscillation amplitude Δ. Following the same method as in section 2.2, we derive from the Jacobian of the system an equation for the driving amplitude at the bifurcation points. On Fig. 5.7, the two cases, with and without parasitic inductance are compared. One can notice that for typical experimental β values ($\beta \approx 10$ for sample B), the effect of the parasitic inductance is quantitatively important: it shifts ω_c by several percent.

5.2.4 Theory at finite temperature

Up to now, we have only studied the deterministic dynamics of the JBA at zero temperature. However, the JBA is connected to a 50Ω environment thermalized at the base temperature of the cryostat.

This 50 Ω environment produces a thermal voltage noise that induces fluctuations of the phase δ. When δ oscillates in mode (1) in domain (B) at a point $P_0 = \{\eta, \Omega\}$ close to the bifurcation line $B_\downarrow$,

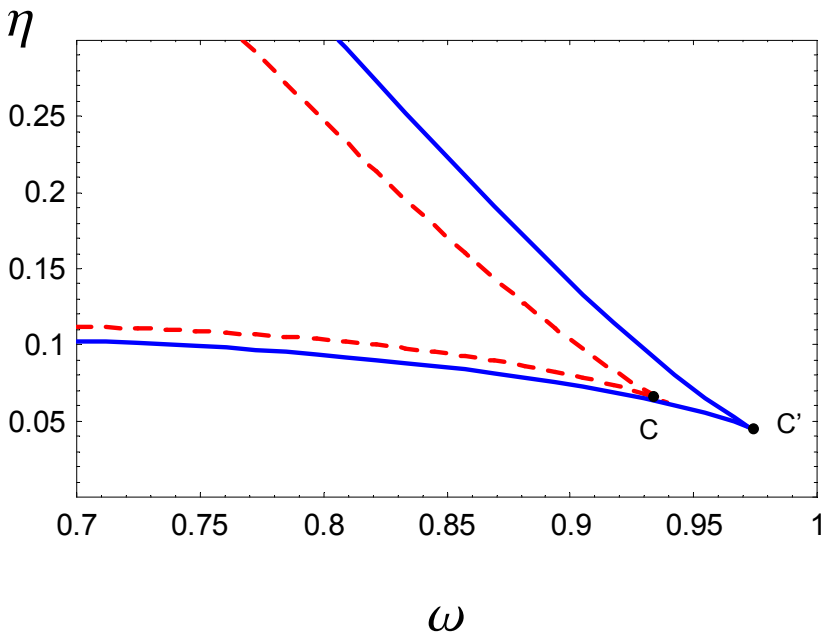

Figure 5.7: Bifurcation lines with parasitic inductance (full line, $\beta = 10$) and without (dashed line). The spinode point C is moved to higher frequencies by the presence of the parasitic inductance.

these thermal fluctuations can activate the dynamical switching from the oscillation mode (1) to the oscillation mode (2). This switching phenomenon is a stochastic process characterized by a transition rate Γ that depends on temperature and on the distance between P_0 and $B_\downarrow$. The aim of this paragraph is to calculate Γ. We first write the stochastic differential equations of motion of the phase δ and derive then the corresponding Fokker-Planck equation that describes the time evolution of the probability distribution of $\{\Delta, \phi\}$, both approach being suitable for numerical calculations. Then, we introduce the Dykman's approximation which give analytical results for the rate Γ.

Langevin equation for the superconducting phase

The thermal noise is taken into account by adding a Johnson current noise source $i_R(t)$ in parallel with the 50 Ω impedance of the environment of the JBA. This source obeys the fluctuation-dissipation theorem

$$< i_R(t) > = 0 \tag{5.22}$$

$$< i_R(t) i_R(t') > = \frac{2k_B T}{R}\delta(t-t'). \tag{5.23}$$

and equation 5.2 is transformed into the Langevin equation

$$Z_0 C\phi_0 \partial_t^2 \delta + \phi_0 \partial_t \delta + Z_0 I_0 \sin(\delta) = U\cos(\omega t) + Z_0 i_R(t), \tag{5.24}$$

or in reduced units into

$$\partial_\tau^2 \delta + \alpha \partial_\tau \delta + \sin(\delta) = \eta\cos(\Omega\tau) + \xi(\tau), \tag{5.25}$$

where $< \xi(\tau)\xi(\tau') >= 2\theta\delta(\tau-\tau')$ and $\theta = k_B T\omega_p/(RI_0^2)$ is the reduce temperature. As previously, we describe the motion using the quadratures $\{p, q\}$. The passage to the slow varying variables p and q can be seen as an average of the dynamics within a period of the driving force:

$$\xi_P(\tau) = \frac{1}{\omega}\int_{\tau-\frac{\pi}{\omega}}^{\tau+\frac{\pi}{\omega}} \cos(\omega\tau')\xi(\tau')\frac{d\tau'}{\frac{2\pi}{\omega}} \tag{5.26}$$

$$\xi_Q(\tau) = -\frac{1}{\omega}\int_{\tau-\frac{\pi}{\omega}}^{\tau+\frac{\pi}{\omega}} \sin(\omega\tau')\xi(\tau')\frac{d\tau'}{\frac{2\pi}{\omega}}. \tag{5.27}$$

By performing this averaging within the monochromatic approximation (as in Eq. 5.15), the quadrature components $\xi_P(\tau), \xi_Q(\tau)$ appear in the Langevin Equation

$$\dot{q}(\tau) = \frac{\partial h}{\partial p}(\tau) - \frac{\alpha}{2}q(\tau) + \xi_Q(\tau) \tag{5.28}$$

$$\dot{p}(\tau) = -\frac{\partial h}{\partial q}(\tau) - \frac{\alpha}{2}p(\tau) + \xi_P(\tau). \tag{5.29}$$

For large times compared with the period $\frac{2\pi}{\omega}$, the random forces $\{\xi_Q, \xi_P\}$ can be treated as two independent white noise distributions:

$$\langle \xi_P(\tau)\rangle = \langle \xi_Q(\tau)\rangle = \langle \xi_P(\tau)\xi_Q(\tau')\rangle = 0 \tag{5.30}$$

$$\langle \xi_P(\tau)\xi_P(\tau')\rangle = \langle \xi_Q(\tau)\xi_Q(\tau')\rangle = \frac{\theta}{\omega^2}\delta(\tau-\tau'). \tag{5.31}$$

Probability distribution of the solutions: the Fokker-Planck equation

The Langevin approach gives an intuitive picture of the effect of the fluctuations but it can be useful to formulate the problem in the Fokker-Planck framework. The Fokker-Planck equation is a deterministic differential equation for the evolution of the density of probability $\rho(p,q,\tau)$ for the system to be at the point (p,q) at time τ given an initial distribution $\rho(p,q,0)$. This probability is obtained by considering different particular realizations of the same physical system, i.e. different realizations of the noise. The Fokker-Planck equation has a one to one correspondence with the Langevin equation and can be deduced from it by multiple methods (see for instance [112]). The potential term gives a deterministic contribution and the stochastic noise gives rise to a diffusion term whose coefficient is related to the correlation function of the noise.

The dynamics is then a competition between the deterministic term, which favor the localization of the probability around the stable solutions, and the diffusion that spreads the probability:

$$\frac{\partial\rho(p,q,\tau)}{\partial\tau} = -\vec{\nabla}.\left(\vec{v}(p,q)\rho(p,q,\tau)\right) + \frac{\theta}{2\omega^2}\nabla^2\rho(p,q,\tau) \tag{5.32}$$

where $\vec{v} = (\dot{p},\dot{q})$.

Transition Rates between stable solutions

We assume the system to be in region (B) where two stable stationary solutions exist. At zero temperature, any non-stationnary solution converges to one of the attractors depending on which side of the separatrix the initial conditions are. For small but finite T, one expects trajectories to fluctuate around the attractors which gives the possibility of passing from the basin of attraction (1) to the bassin of attraction (2).

The transition rate from one attractor to the other can be calculated within the Langevin formalism by numerically integrating Eq. (5.28) several times with different initial conditions $\{p(0),q(0)\}$ and different realizations of the noise [110].

An equivalent result can be obtain by solving numerically the Fokker-Planck equation 5.32 [109].

However, as we would like analytical formulas for the transition rate, we now look at the results obtained in Dykman's framework, which consists in considering only the most probable path from one attractor to the other in the phase space.

5.2.5 Dykman's approach of the bifurcation

Dykman's results [108], reported here, are valid for the case of the non-linear Duffing oscillator (i.e. with a quartic potential). The analytical calculation of Dykman consists in expanding the Jacobian(5.18) at first order in $\eta-\eta_\uparrow$, and in recasting the problem in a one-dimensional Fokker-Planck equation along the direction of the most probable path of escape. This framework leads thus to a saddle approximation in the metapotential defined by the velocity field.

Expression of the bifurcation rate

Using Kramer's method for solving this one-dimentionnal equation, Dykman obtains the transition rate between the two attractors.

$$\Gamma = \frac{\omega_A}{2\pi}\exp-\frac{\Delta U}{k_B T},$$

where ΔU is the barrier height along the most probable path and ω_A is the oscillation frequency around the attractor and along the escape path. These two quantities are given by

$$\frac{\Delta U}{E_j} = \frac{64}{9\sqrt{3}}\omega^3(1-\omega)\left[1-\left(\frac{\eta}{\eta_\uparrow}\right)^2\right]^{3/2} \tag{5.33}$$

$$\frac{\omega_A}{\omega_p} = \frac{4}{3\sqrt{3}}Q(1-\omega)\left[1-\left(\frac{\eta}{\eta_\uparrow}\right)^2\right]^{1/2} \tag{5.34}$$

where E_j is the Josephson energy of the junction.

One notice that for a fixed driving frequency, the expression of the rate is formally identical to the switching rate of a DC current biased junction. The critical current in the DC case is replaced here by the bifurcation current $I_b = \eta_\uparrow I_c$, and the plasma oscillation frequency in the well of the tilted potential is replaced by the frequency of the small oscillations ω_A in the metapotential.

The bifurcation probability during a microwave driving pulse of duration τ is given by

$$P_b = 1 - e^{-\Gamma\tau},$$

and is plotted on figure 5.8 as a function of ω for parameters close to those used in our experiment. We define $\omega_{50\%}(\eta)$ by the equation $P_b(\omega_{50\%}, \eta) = 0.5$.

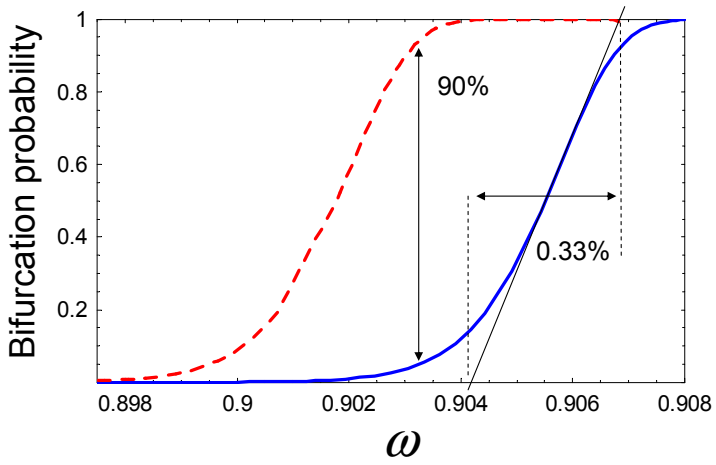

Figure 5.8: Sensitivity of the JBA in Dykman's framework. The parameters are set to $\eta = 0.12$, $k_BT/E_j = 0.0025$ (which corresponds to $T = 50mK$ for a 1μA critical current junction) and $E_j = 0.87$, $E_c = 0.655$ (sample A). The reduced driving frequency here is $\omega = \omega_d/\omega_p^0$ where ω_p^0 stands for the plasma frequency of the JBA when the qubit is in state 0. Full line: theoretical bifurcation probability for the ground state of the qubit and as a function of ω. The inverse of the maximum slope give the frequency sensitivity which corresponds to 0.33% of the plasma frequency. Dashed line: expected bifurcation probability curve for state $|1\rangle$.

Sensitivity of the JBA to a parallel inductance

For evaluating the sensitivity to the qubit inductance, one notice that ΔU is only a function of the reduced frequency of driving ω and of the reduced microwave driving amplitude η. Thus, at $\eta = cst$ and $\omega_d = cst$, the only effect of the qubit to the bifurcation rate appears by the change of ω_p and thus ω.

The inverse of the slope of the $P_b(\omega)$ curve at $\omega_{50\%}$ defines the frequency sensitivity of the bifurcation and can be calculated for different points $(\eta, \omega_{50\%}(\eta))$. It is found to be weakly dependant on η or equivalently on $\omega_{50\%}(\eta)$. There is thus no optimal driving frequency for operating the JBA as far as the sensitivity of the device itself to the qubit state is concerned. However, we'll see in the experimental section that experimental constrains impose the choice of the driving frequency.

For the parameters considered: $k_BT/E_j = 0.0025$ (which corresponds to $T = 50$mK with a 1μA critical current junction), and $\eta = 0.12$, the frequency sensitivity is equal to

$$\frac{\Delta\omega_p}{\omega_p} \approx 0.33\%,$$

Noting that

$$\frac{\Delta\omega_p}{\omega_p} = \frac{\Delta L_{JBA}}{2L_{JBA}} = \frac{L_{JBA}}{2}\frac{1}{L_\parallel},$$

where $L_\parallel$ is the parallel inductance added to the JBA, and $L_{JBA} = \varphi_0/I_c$, the frequency sensitivity can be recasted into a parallel inductance sensitivity

$$\Delta(\frac{1}{L_\parallel}) = \frac{\Delta\omega_p}{\omega_p}\frac{2}{L_{JBA}} \approx 16(\mu H)^{-1},$$

with $L_{JBA} = 0.39$nH, corresponding to a junction with a 1μA critical current.

We now consider the case of a quantronium connected in parallel with the JBA. For the sample A of this thesis ($E_j = 0.87K \pm 1\%$ and $E_c = 0.655K \pm 1\%$) we have $L_Q^1 = -990$nH ± 10nH and $L_Q^0 = 50$nH ± 0.5nH, which leads to a relative change of $1/L_\parallel \approx 21(\mu H)^{-1}$, which is above the sensitivity of the JBA. The expected bifurcation curve for both states 0 and 1 are plotted on Fig. 5.8. The maximum contrast between the two bifurcation curves is $\approx 90\%$ for the set of parameters considered.

For a given sample, the sensitivity of the JBA to a plasma frequency change is only given by the temperature, and gets better as T decreases like for any thermally activated phenomenon.

An interesting questions then arises: what happens at sufficiently low temperatures compared to the plasma frequency of the JBA (1.5GHz for the sample B, equivalent to 60mK), what are the caracteritics of the quantum regime of the bifurcation.

5.3 Experimental characterization of the JBA

First, I would like to thank M.Devoret, I.Siddiqi and F.Pierre for advices and informations which were extremelly useful for building up this experiment, and for providing me with the sample whose results are reported here (sample B).

Experimental Setup

For characterizing the JBA and measuring the quantronium state we have used the experimental setup described on Fig. 5.9. This setup is similar to the one used at Yale by M. Devoret's group and in Ref. [113] and has the additional possibility to perform both AC switching and DC switching experiments on the same sample using a bias tee.

The plasma frequency of the sample was lowered in the $1 - 2$GHz bandwidth by adding an on chip capacitor $\approx$ 30pF in parallel to the junction. In this bandwidth, low noise cryogenic amplifiers are available, with the appropriate circulators. It is also easier to control the macroscopic electromagnetic environment in this frequency range than at higher frequencies, and in addition, thermal population of the resonator is still negligible ($\hbar\omega_p/k_BT \approx 3$).

For generating and demodulating the microwave pulses, the output of a microwave generator (Anritsu MG3692) is split in two channels. One of the channels is used for the homodyne detection of the reflected signal on the JBA. The other one is mixed into Minicircuit ZEM-4300MH mixers (similar mixing setup than in section 3.3) with trapezoidal pulses coming from an arbitrary waveform generator (Agilent 33250). The obtained microwave pulses are then sent to the microwave excitation line which is strongly attenuated in order to use the full dynamic range of the microwave generator, and thus increase the signal to noise ratio at the level of the sample. At 20mK, this line is coupled to the main line connected to the sample with a directionnal coupler (-16dB coupling).

This main line is strongly filtered to get a working bandwidth of $1.2 - 1.8$GHz, and thus avoid any spurious noise that could excite the qubit. A bias tee provides a DC coupling to the sample suitable for achieving DC switching experiments (see chapter 2). A microwave excitation pulse incident on the sample is completely reflected on the JBA due to the absence of dissipation. The reflected pulse goes first through two circulators at 20mK. The circulators are non-symmetrical components: they permit the signal to go from the sample to the amplifier but any noise going through the reverse path is absorbed in a 50Ω load. These circulators are equivalent to Faraday rotators in optics. The thermalized noise generated by this 50Ω resistor is emitted to the sample, and constitute the noise source of the Langevin equation in Eq. 5.24. As they use magnetic material, a proper magnetic shielding is required in order to limit much as possible parasitic magnetic fields on the quantronium circuit.

The reflected signal on the sample is then amplified in a cryogenic amplifier (Quinstar L-1.5-30H) having a very low noise temperature: $T_N = 2.4$K at 1.5GHz. A third circulator complete the total isolation of the line to 60dB which strongly attenuate the room temperature noise in the bandwidth $1 - 2$GHz.

A second stage of amplification is required and provided by an amplifier (Miteq AFS4-01200160-15-15P-6) placed at room temperature. A 6dB attenuator placed between the two amplifiers suppresses the effect of any spurious standing wave due to possible impedance mismatch. The amplified signal goes through a bandpass filter K&L (5BT-1000/2000) centered at a tunable frequency and having a bandwidth of about 100MHz in order to suppress the main part of the noise generated by the amplifier and which could saturate the demodulation card. This demodulation card (Analog Device AD8346) provides the in-phase and quadrature components of the reflected microwave with respect to the carrier reference.

Characterization of the JBA under continuous microwave excitation

The sample considered in the following was fabricated at Yale University by F.Pierre and has the following parameters: $L_0 \simeq 0.39$nH, $C = 32$pF and $Q \simeq 14$. The first experiment performed was to characterize the bifurcation of the JBA under a continuous microwave excitation with the qubit in its ground state (see Fig. 5.10).

For this purpose, a CW signal is applied to the sample, and the phase of the reflected signal is measured as a function of the frequency, either with the demodulation card or with a network analyser (Anritsu 37247B).

At low driving amplitude we can observe the plasma resonance of the readout circuit and the associated phase shift (see figure 5.10). When increasing the microwave power, the phase shift of the plasma resonance gets steeper and steeper, as the superconducting phase starts to explore the nonlinear region of the Josephson potential. The bifurcation occurs above a certain microwave amplitude where the phase of the reflected signal jumps suddenly at a frequency which depends on the driving amplitude.

The theory does not fit the data. First the total phase shift when crossing the plasma resonance is not 360° as expected for an LC oscillator, because of parasitic reflections due to impedance mismatches on the measuring microwave line. Second, it appeared that the critical point C was higher in frequency than the theory predicts: $\omega_c \approx 0.965$ instead of ≈ 0.94. We attribute this discrepancy to a parasitic inductance between the 50Ω line and the JBA.

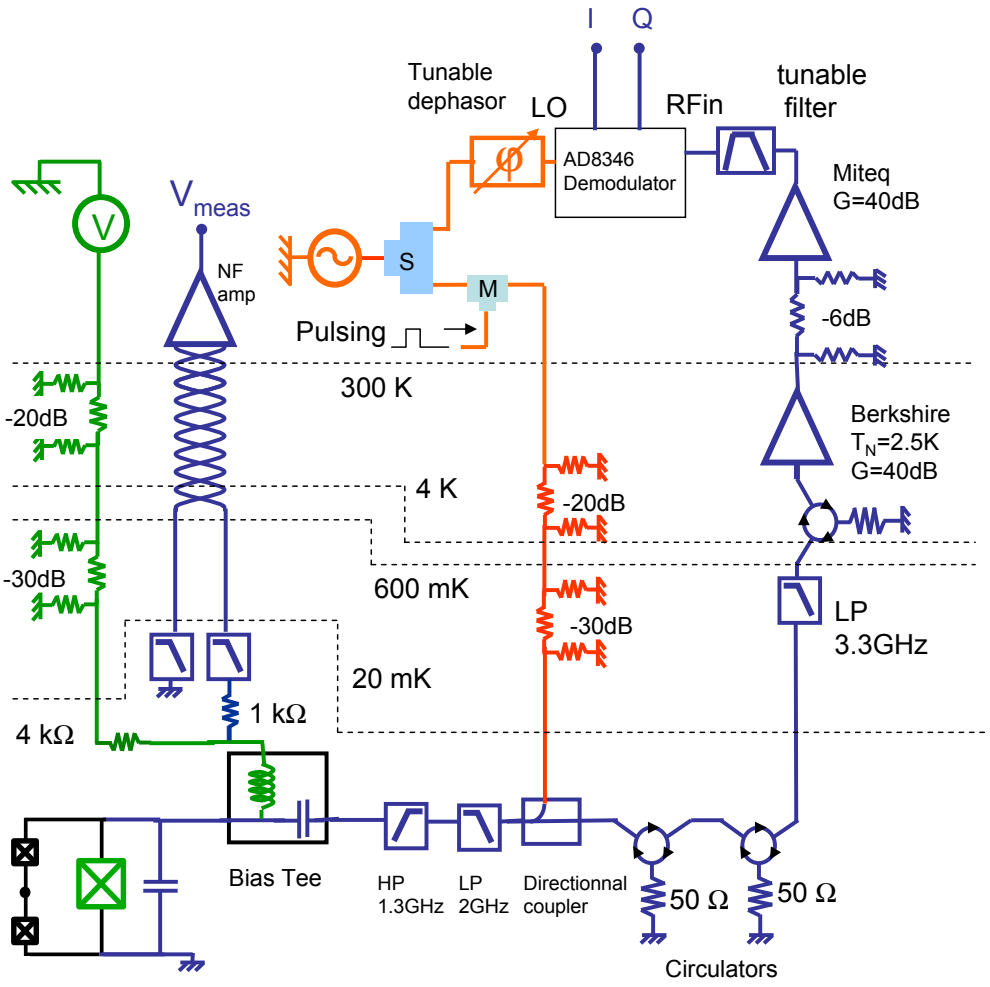

Figure 5.9: Experimental setup. The quantronium circuit (bottom left) is coupled through a bias tee to a DC switching measuring setup (left) and to an AC measuring setup (right). The AC measuring setup has a strongly attenuated microwave excitation line (middle), which is coupled to the return line with a directional coupler. The probing pulses come from a continuous microwave source mixed with trapezoidal pulses. The return line has several circulators which prevents the room temperature noise and the input amplifier noise to go down the line. A tunable filter suppress the noise outside the bandwidth of interest before an homodyne detection gives the $I-Q$ components of the reflected microwave pulses.

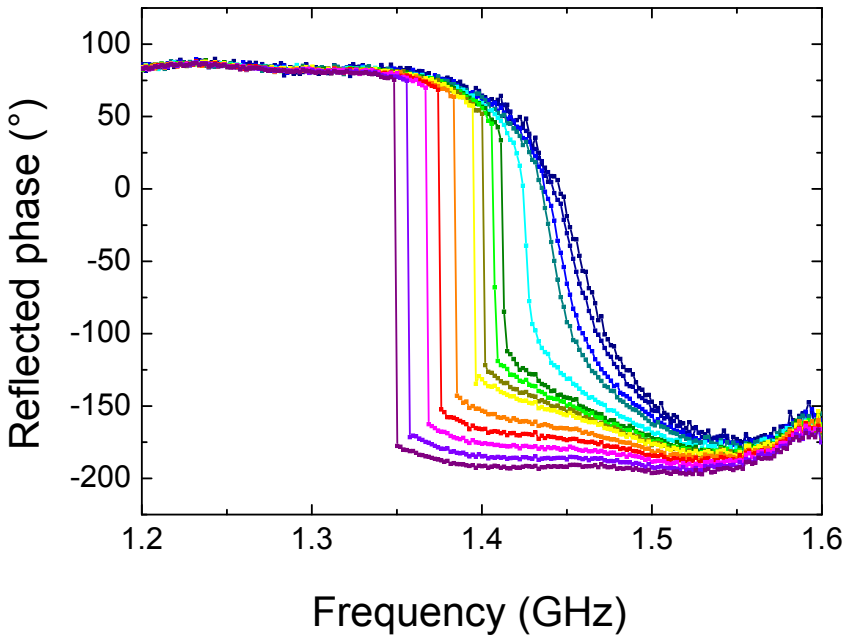

Figure 5.10: Reflected microwave phase as a function of the driving frequency and for different microwave powers (from -35dBm to -15dBm at the output of the generator, which corresponds to ≈ -105dBm to ≈ -85dBm at the sample level, taking into account the attenuation along the line). At low microwave power, one can observe the phase shift associated with the plasma resonance (right most curve). When the microwave power is increased (from right to left), the phase shift gets steeper and steeper, and at a certain microwave amplitude related to the critical excitation amplitude $\eta_\uparrow$ introduced in section 5.10, one observe discrete phase jumps. The parameters of this sample (sample B) are $L_0 \simeq 0.39$nH, $C = 32$pF and $Q \simeq 14$, measured by fitting the reflected phase curve at low microwave driving amplitude.

Parasitic inductance

In the experimental implementation of the JBA, it is difficult to avoid a series inductance L between the 50 Ω line and the readout circuit (see Fig. 5.6). Indeed, in our setup, the chip was connected to the measuring line through a few millimeter-long metallic wires with an inductance of order 1nH/mm. Using the theoretical formula of section 5.2.3, it is possible to explain the experimental data at least in the vicinity of the critical point. Fig. 5.11 shows the best fit which leads to $L \simeq 4$nH, or equivalently $\beta \simeq 10$. This fit is not quantitative at large driving amplitude possibly due to another spurious inductance in series with the capacitance C.

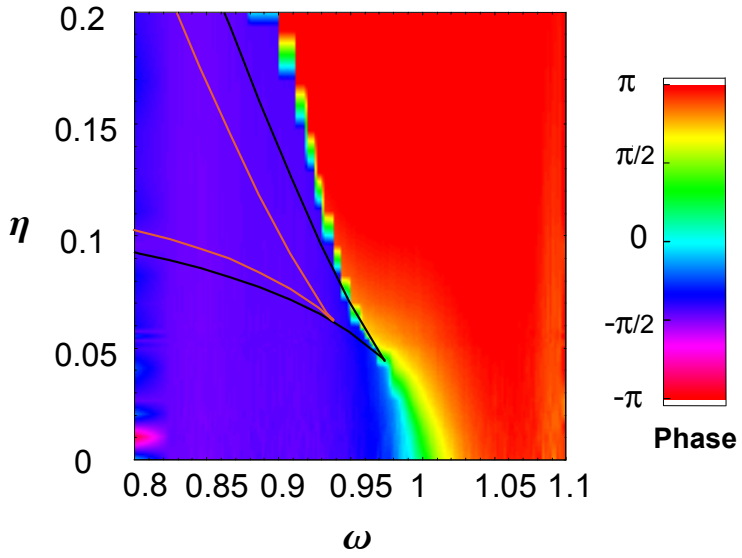

Figure 5.11: Measured reflected phase and comparison with theory: without parasitic inductance (white line or red) and with parasitic inductance (black).

These first measurements raise the problem of implementing better controlled environment for Josephson elements, in the frequency range of several GHz. It raises also the problem of achieving proper reflectometry measurements in the microwave range. All our preliminary work on the JBA is limited to a qualitative agreement with the theory, most probably because of parasitic microwave elements in the circuit. In the next experiments, dedicated microwave circuit boards and connectors will be used, in order to improve this reflectometry measurement.

Pulsed measurements

After having characterized the JBA in a CW excitation mode, we discuss now the pulsed mode.

As we want to use this anharmonic oscillator under stationary conditions the readout time needs to be longer than the characteristic transient decay time of the readout junction oscillator. In the linear regime, this time is given by the quality factor of the oscillations $T_{trans} = Q/\omega_p \approx 10$ns. The quality factor has thus to be low enough for a fast readout. On the other hand, the final goal being to readout a quantum bit, the readout time has to be much smaller than the relaxation time of the qubit T_1 which is

expected to be in the μs range. As a consequence, we will study the bifurcation probability of the JBA during microwave excitation pulses of duration around $\approx$ 100ns.

These readout pulses, shown on Fig. 5.13 are constituted of two parts. The first part aims at inducing or not the bifurcation from attractor (1) to attractor (2) whereas the second part is a sustain using the hysteresis for maintaining the dynamics on the same state during the averaging of the demodulator output ("latching" mode).

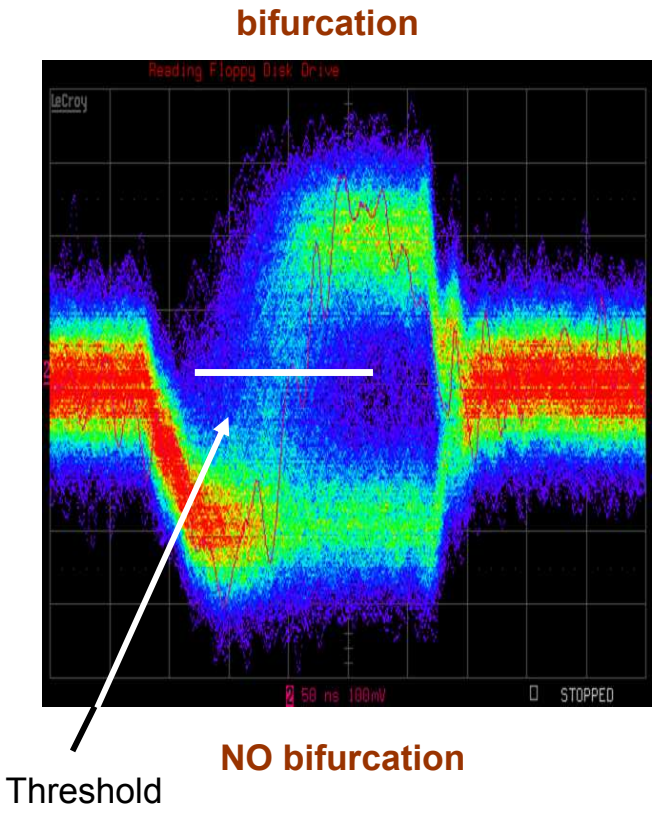

Figure 5.12: Oscillogram of one quadrature in persistent mode with a time base of 50ns per division. The microwave pulse used is shown on Fig. 5.13. It extends from the 2nd to the 7th division. The bifurcation occurs or not between the 3rd and the 5th division. The threshold of a counter is tuned in order to detect the jump of the quadrature.

We have first measured the bifurcation probability of the JBA, as a function of the microwave amplitude and for fixed frequency and temperature (see Fig. 5.13). The histograms of the reflected microwave phase are also plotted on Fig. 5.13.

The temperature study of the bifurcation phenomenon is similar to the one of the DC switching of a Josephson junction and is described on Fig. 5.14. However, it was not possible to get a quantitative agreement with the Dykman framework. We attribute this discrepancy to the parasitic microwave elements already mentioned.

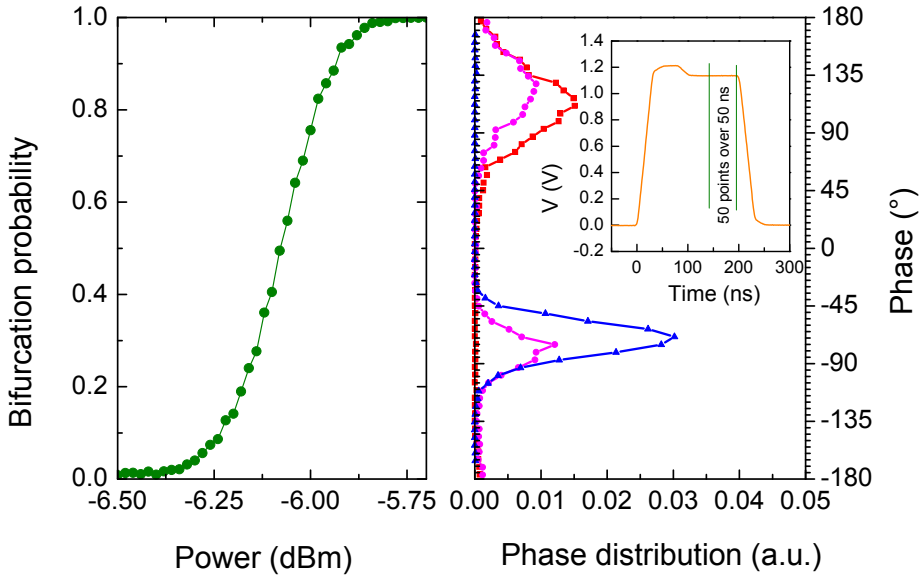

Figure 5.13: Left: bifurcation probability of the JBA as a function of the microwave power for a fixed frequency. Right: histograms of the reflected phase for 0% bifurcation rate (triangles), 50% bifurcation rate (circles) and 100% bifurcation rate (squares). Each data point corresponds to an average of both quadratures over the last 50ns of the probing pulse. The width of these histograms is determined both by the noise characteristics of the amplification setup and by the averaging process. The frequency is 1.42GHz and the temperature is $\approx$ 25mK. Inset: envelope of the microwave probing pulse.

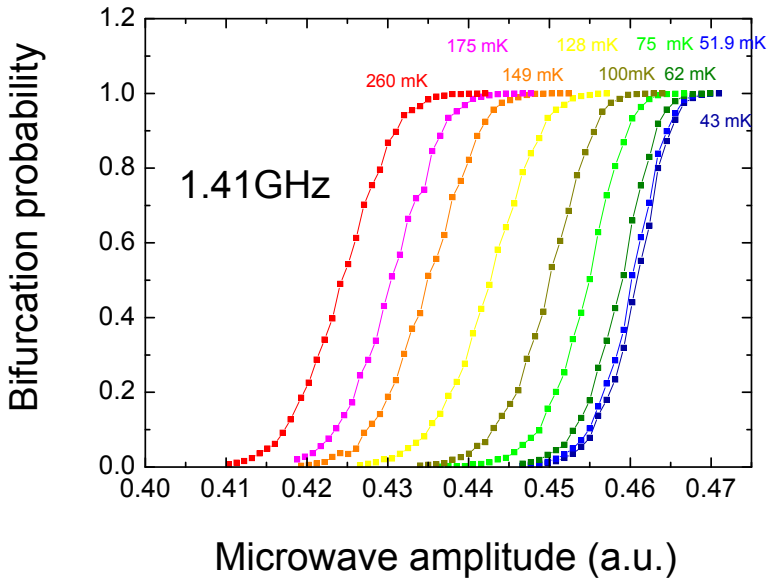

Figure 5.14: Temperature study of the bifurcation phenomenon. As the temperature decreases (from left to right), the mean microwave amplitude required for 50% bifurcation probability increases, and the slope of the bifurcation curve increases, as expected. However, there is no quantitative agreement with Dykman's theory.

5.4 Measurement of the qubit with a JBA

Despite it was not possible to explain quantitatively the behavior of the JBA, we can use this detector for measuring the quantum state of the quantronium. The first advantage compared to the DC switching method is that the repetition rate is higher $\approx$ 1MHz leading to faster data acquisition rates.

By applying long microwave excitation pulses on the qubit gate, the resonance line was found at 8.205GHz for the sample B. The dependance of the transition frequency with N_g and δ allows one to determine the parameters $E_j = 0.397\text{K} \pm 1\%$ and $E_c = 1.12\text{K} \pm 1\%$ for sample B, and to obtain the expected effective inductances of the qubit for state 0 and 1:

$$\frac{1}{L_Q^i} = \frac{1}{\varphi_0^2}\frac{\partial^2 E_i}{\partial \delta^2},$$

$L_Q^1 \approx -200\text{nH}$ and $L_Q^0 \approx +150\text{nH}$ at $N_g = 1/2$.

Fidelity of the bifurcation readout

The bifurcation probability curves were measured for the two qubit states 0 and 1, as a function of the microwave amplitude. The experimental results are plotted on Fig. 5.15. The maximum contrast between

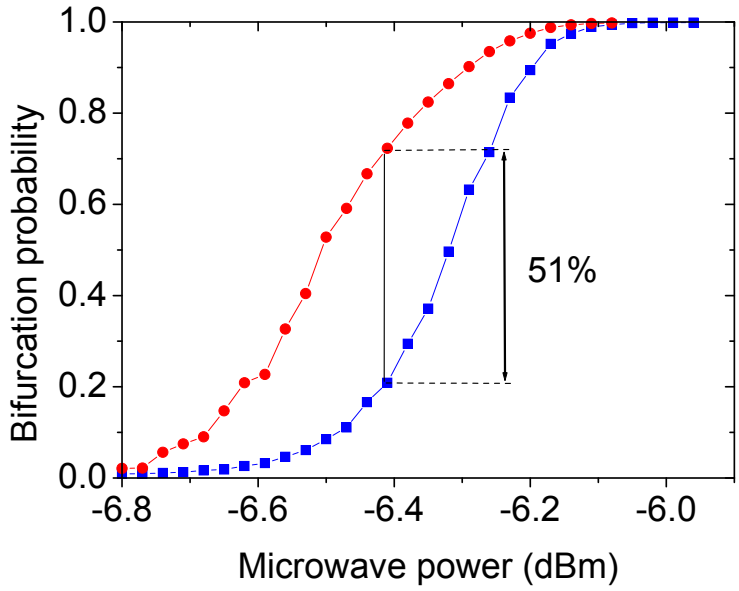

Figure 5.15: Bifurcation probability curves of the JBA for the ground state (squares) of the quantronium and after a π pulse (circles), for a microwave readout frequency of 1.43GHz. The maximum contrast is $\approx 50\%$.

state 1 and 0 is $\approx 50\%$.

The linewidth of the resonance line is sufficiently small ($\approx$ 2.5MHz) to permit time resolved experiments.

Rabi oscillations

The results of a Rabi experiment (see section 3.1.2) are plotted on Fig. 5.16.

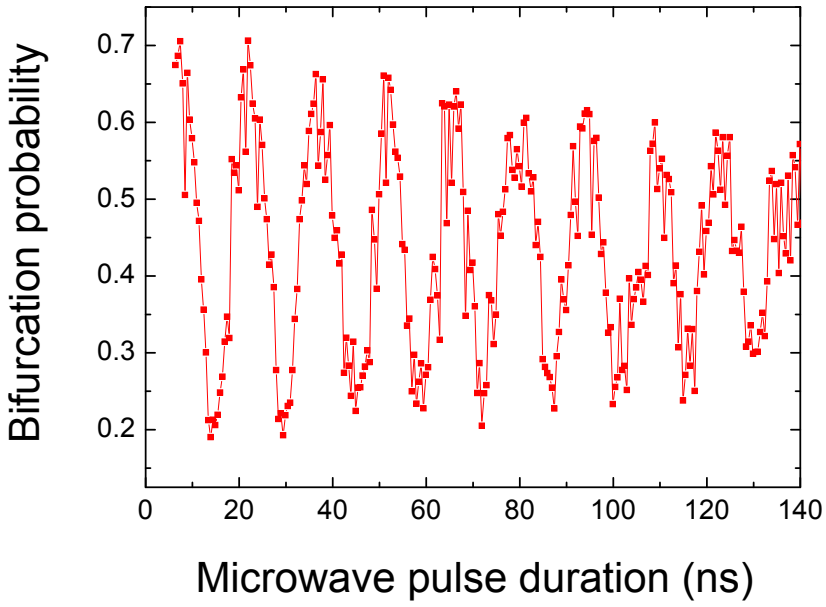

Figure 5.16: Rabi oscillations of the quantum state of the quantronium, measured with the JBA. The maximum contrast is $\approx 50\%$.

One can notice the decrease of the contrast of the Rabi oscillations as the duration of the microwave pulse increases. This phenomenon is related to the decoherence during driven evolution as discussed in section 4.2.5.

Coherence time measurements

The Ramsey and Echo times (see section 4.3) were measured on the sample B (see Fig. 5.17). The fitted decays give the values of $T_2 \approx 140$ns and $T_{echo} \approx 300$ns. These characteristic times are of the same order of magnitude than for previous samples.

Back-action of the readout on the qubit

During the readout, the phase δ across the qubit oscillates at ω_d on a range of about 2 rad before the bifurcation and ≈ 3 rad after the bifurcation. As a consequence, the transition frequency of the qubit is modulated at ω_d between $\nu_{01} = 8.3$GHz and ≈ 7GHz. The qubit frequency does not explore a frequency range as large as in the case of the DC switching, but the modulation lasts during ≈ 100ns. The possibility of level crossings with spurious resonance is then also possible, which could induce relaxation of the qubit state, and explain partially the limited visibility of the readout.

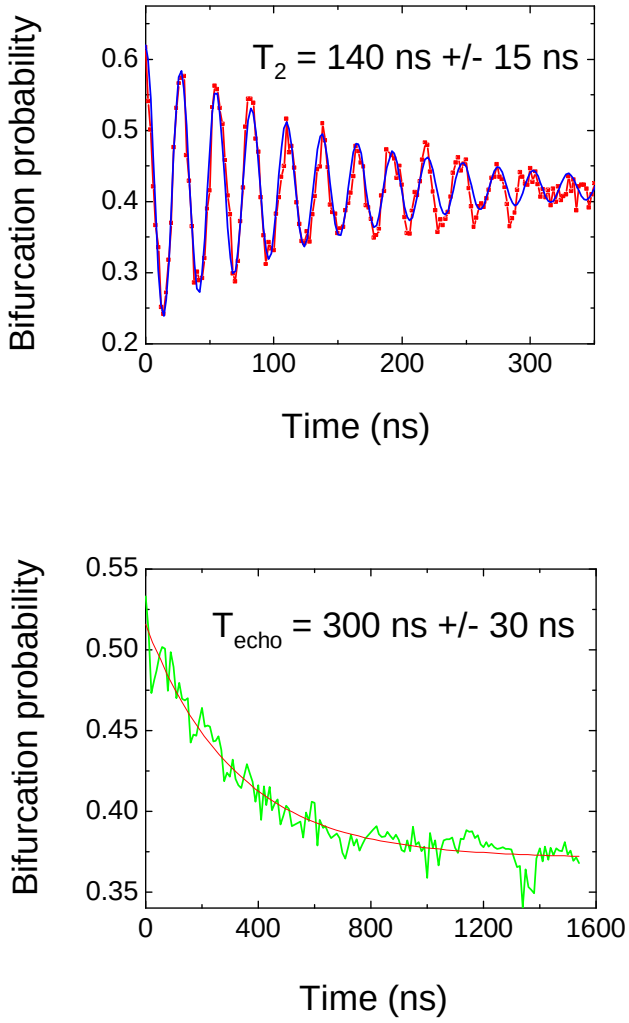

Figure 5.17: Left: Ramsey experiment. Right: echo experiment. The coherence times T_2 and T_{echo} are measured by fitting the decay of the Ramsey fringes and of the echo signal respectively (see section 4.3).

5.4.1 Characterization of the QND behavior of the readout

Excitation and relaxation induced by the readout not only corrupt the measurement response but also introduce projection errors on the final qubit state after the measurement is completed. In order to evaluate the error made during the projection, we define the QND fraction q_1 (resp. q_0) for state $|1\rangle$ (resp. $|0\rangle$) as the probability for the qubit to stay in state $|1\rangle$ (resp. $|0\rangle$) after the measurement knowing that it was in the same state before. For determining these QND fractions, we have achieved a two readout pulse experiment. The qubit is prepared in state $|1\rangle$ (resp. $|0\rangle$), by applying a π pulse (resp. no π pulse), and the bifurcation probability of the JBA is measured during two adjacent probing pulses A and B (see Fig. 5.18).

The difficulty for evaluating the QND fraction comes from the finite sensitivity of the readout which induces errors on the measurement results. In order to extract the QND fraction of the measurement, we have used a simple model which involves the 8 probabilities

$$P^A(|i\rangle, r, |f\rangle)$$

for getting the result r ($r = 0$ or 1) during pulse A, starting from state $|i\rangle$ before pulse A and letting the qubit in state $|f\rangle$ after pulse A. These probabilities are related to the measured bifurcation probabilities $P^A(|i\rangle, 1)$ during the readout pulse (A), the qubit being prepared in state $|i\rangle$ before pulse (A), and to $P^B(|i\rangle, 1)$ the probability of bifurcation during pulse B knowing that the qubit was prepared in state $|i\rangle$ *before pulse A*:

$$\begin{aligned} P^A(|i\rangle, 1) &= P^A(|i\rangle, 1, |0\rangle) + P^A(|i\rangle, 1, |1\rangle) && (5.35)\\ &= 17.5 \pm 1\%(\mathrm{i} = 0) && (5.36)\\ &= 61 \pm 1\%(\mathrm{i}{=}1), && (5.37)\\ & && (5.38) \end{aligned}$$

$$\begin{aligned} P^B(|i\rangle, 1) &= (P^A(|i\rangle, 1, |1\rangle) + P^A(|i\rangle, 0, |1\rangle))p^B(|1\rangle, 1) && (5.39)\\ &\quad +(P^A(|i\rangle, 1, |0\rangle) + P^A(|i\rangle, 0, |0\rangle))p^B(|0\rangle, 1) && (5.40)\\ &= 13 \pm 1\%(i = 0) && (5.41)\\ &= 28 \pm 1\%(i = 1), && (5.42)\\ & && (5.43) \end{aligned}$$

where $p^B(|i\rangle, 1)$ is the probability of bifurcation during the readout pulse B when the qubit is prepared in state $|i\rangle$ *before pulse B* .

Ideally, $p^B(|0\rangle, 1)$ and $p^B(|1\rangle, 1)$ should be equal to $P^A(|0\rangle, 1)$ and $P^A(|1\rangle, 1)$ respectively, if the two pulses had the same microwave amplitude. In practice the amplitude of the second pulse is slightly lower because of a parasitic interaction between very close pulses in the mixing setup.

We observe indeed experimentally that $P^B(|0\rangle, 1) < P^A(|0\rangle, 1)$. We assume that this discrepancy is only due to the reduction of the microwave amplitude and that no excitation occurs during readout pulse A. One thus obtains

$$p^B(|0\rangle, 1) = P^B(|0\rangle, 1) = 13 \pm 1\%.$$

We calculate then the value of $p^B(|1\rangle, 1)$ from the probability shift $\Delta p = p^B(|0\rangle, 1) - P^A(|0\rangle, 1) = -4.1\%$, which gives

$$p^B(|1\rangle, 1) = P^A(|1\rangle, 1) + \Delta p = 57 \pm 1\%.$$

One can notice that this probability shift corresponds to a microwave power reduction of ≈ 0.02dB (0.2% in amplitude - see Fig. 5.15).

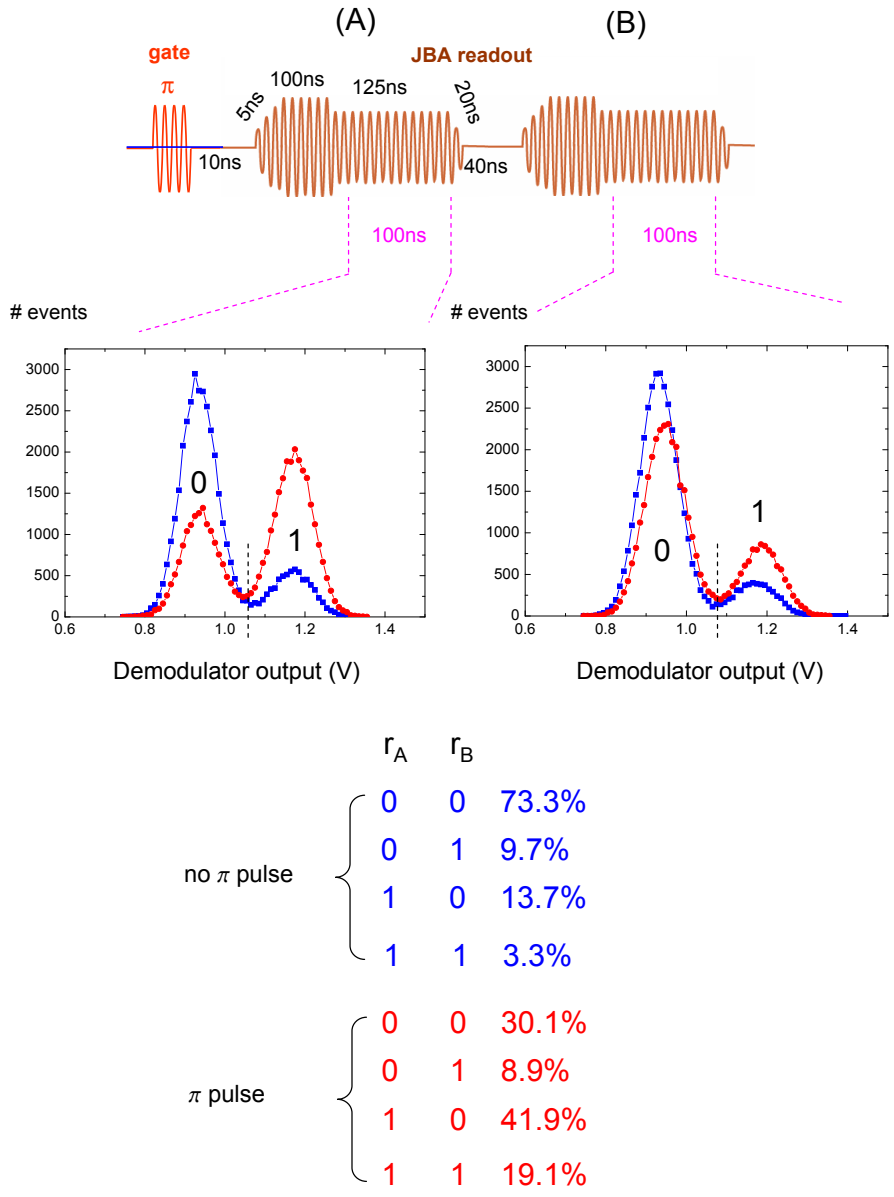

Figure 5.18: Measurement of the QND fraction of the quantronium read out with the JBA. Top panel: the qubit is prepared in state 1 (resp. 0) by applying a π pulse (resp. no π pulse) on the qubit gate. Then two adjacent probing pulses A and B are applied. The two successive demodulator voltages are averaged during the last 100ns of the sustain part of the pulses. Middle panels: corresponding histograms for each readout pulse: squares when the qubit is prepared in state $|0>$ and circles when the qubit is prepared in state $|1>$ before the first readout. A properly tuned threshold (dashed vertical line) leads to the boolean responses of the readout. Bottom panel: corresponding 8 probabilities of getting two successive responses (r_A, r_B).

Then, one obtains two more equations by considering the probabilities of the system to bifurcate during both pulses A and B, $P^{A,B}(|i\rangle, 1, 1)$, which are related to the $P(|i\rangle, r, |f\rangle)$ probabilities by

$$\begin{aligned} P^{A,B}(|i\rangle, 1, 1) &= P(|i\rangle, 1, |0\rangle)\ p^B(|0\rangle, 1) + P(|i\rangle, 1, |1\rangle)\ p^B(|1\rangle, 1) && (5.44)\\ &= 3.5 \pm 1\%\ (i = 0) && (5.45)\\ &= 19 \pm 1\%\ (i = 1). && (5.46)\\ & && (5.47) \end{aligned}$$

The last two equations come from the normalization of the $P(|i\rangle, r, |f\rangle)$. By inverting the linear system obtained, one gets the QND fraction of each state:

$$\begin{aligned} q_1 &= P^A(|1\rangle, 0, |1\rangle) + P^A(|1\rangle, 1, |1\rangle) = 34 \pm 2\% && (5.48)\\ q_0 &= P^A(|0\rangle, 0, |0\rangle) + P^A(|0\rangle, 1, |0\rangle) = 100 + 0 - 2\% && (5.49)\\ & && (5.50) \end{aligned}$$

Note that the q_0 result is consistent with the assumption made about the absence of excitation by a readout pulse. Fig. 5.19 summarizes a single measurement.

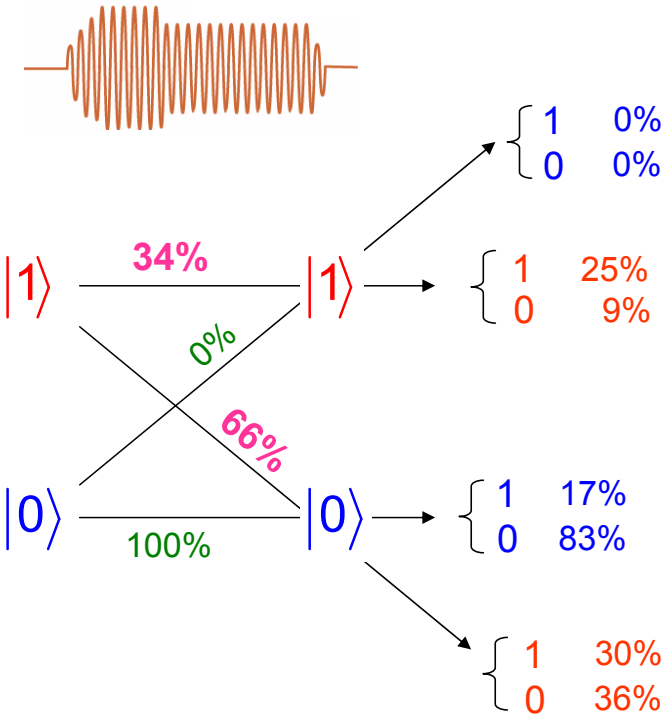

Figure 5.19: Calculated QND fraction of the readout and probabilities $P(|i\rangle, r, |f\rangle)$ by assuming that the readout does not induce excitation of the qubit state.

Finally, one can also calculate a QND fraction corrected from the relaxation that would occur during the time of the first pulse if it was not applied. As the relaxation time is 1.3μs and the duration of the probing microwave pulse is 300ns, the expected loss is $1 - \exp(-t/T_1) = 0.20$. The QND fraction for state 1 corrected from this relaxation is thus $43 \pm 1\%$. This value has therefore to be taken with caution since there is no proof that relaxation during free evolution adds independently to the relaxation induced by the readout alone.

5.5 Conclusion

A new dispersive measurement of the quantronium has been implemented. This setup uses the readout junction of the quantronium as a tank circuit whose dynamics is affected by the effective inductance of the qubit. At large driving amplitude, the bifurcation phenomenon provides a sensitive detection scheme of the qubit state which is sufficient to perform simple manipulation of the quantum state of the qubit. This readout scheme has several advantages compared to the DC switching one used in chapter 2,3, and 4. First, the absence of on-chip dissipation permits higher repetition rates. Second, this method keeps the qubit in the vicinity of the optimal working point, preserving it from possible sources of relaxation. Finally, this setup is partially QND: we have measured a QND fraction $q_1 = 32 \pm 2\%$ for state $|1\rangle$ assuming $q_0 = 100$ for state $|0\rangle$. The perspectives are now to improve the microwave environment of the sample, in order to perform properly microwave reflectometry measurements. The use of microwave dedicated substrates and connectors will suppress the parasitic inductance previously discussed. A better controlled microwave environment of the sample should then lead to a quantitative understanding of the JBA. An increase of the filtering and attenuation of the microwave excitation line should permit to observe and characterize the crossover from the classical to the quantum regime of this non-linear oscillator.

Chapter 6

Conclusions and perspectives

During this thesis, the quantum state of a superconducting bit has been coherently manipulated, demonstrating that any rotation on the Bloch sphere can be achieved. In addition the use of composite pulse techniques, developed from procedures in NMR, has permitted a decrease in the sensitivity of an operation to systematic errors and to slow errors and has thus increased the rotation accuracy.

The phenomenon of decoherence was fully characterized during both driven and free evolution of the qubit. During the free evolution the concept of the optimal working point was validated. It was demonstrated that the low frequency charge noise, probably of microscopic origin, was the dominant source of dephasing for this mixed charge phase qubit and the possibly non-gaussian behavior of this charge noise was put into light. In order to improve the phase coherence one could increase the ratio E_j/E_c by increasing the size of the Josephson junctions or by adding in parallel to the junctions a capacitor. Further research on the material properties will also give information about the source of this charge noise and its location (substrate, aluminum oxide, ...).

The study of relaxation did not provide a definite conclusion as to whether it is the microscopic or macroscopic nature of the electromagnetic environment that is responsible for it. However, observation of non-reproducible level crossings, indicates that the microscopic environment could contribute significantly to relaxation for particular working points. A special care must then be taken during the fabrication process in order to minimize the probability of defects that are probably involved in these level crossings, and which are similar to the ones observed at Martinis' group [50, 49]. On the other hand, a better control of the macroscopic electromagnetic environment could be relatively easily achieved by the use of superconducting cavities, which decouples the qubit from the measuring and biasing lines outside the resonances frequencies [105, 102]. It has also become clear that the impact of the parasitic junction due to the shadow evaporation process needs to be better understood [114].

The study of decoherence during the driven evolution of the qubit demonstrated that this phenomenon was responsible for random errors which diminish the accuracy of any operation. The accuracy of the manipulation has been estimated for a π pulse to be $\approx 1\%$, which, compared to the most optimistic value needed for operating quantum error correcting codes ($\approx 10^{-4}$), is far from being sufficient. The coherence time needs to be increased at least by two orders of magnitude.

The evaluation of the precision of a rotation is presently limited by the readout fidelity. Indeed, the first readout setup which used the macroscopic quantum tunneling of a Josephson junction suffered from several drawbacks: first, an extra relaxation appeared during the readout process and, second a new phenomenon consisting of Landau-Zener crossing during the tunneling of the superconducting phase, modifies drastically the tunneling rate of the readout junction for a particular range of parameters. It appears that the adiabatic hypothesis which decouples the dynamics of the qubit and the readout junction and which underlies all predictions of discrimination power is not valid. One has to consider the full dynamics of the coupled system qubit and readout junction. In this formalism it is no longer clear

what the observable which is measured during readout actually is, and only switching curves for the two states of the qubit can be predicted. Further investigation is required to understand more deeply this phenomenon.

In order to improve the readout fidelity a new readout based on microwave reflectometry was developed during this thesis. Following an idea of M. Devoret it uses a bifurcation phenomenon and allows for non dissipative readout of the qubit state. However, the results obtained were disappointing regarding the fidelity and indicated again that a better control of the microwave environment is required in order to avoid spurious relaxation of the qubit during readout. However, results obtained at Delft with a similar setup are promising [115]. The non-demolition behavior of this new readout has been measured and indicates that the relaxation of state one is induced by the measurement with a probability of 33% whereas state zero is not modified by the measurement. This relaxation process might be avoided by applying a gate modulation during the readout in order to keep the transition frequency of the qubit at a constant value.

The medium-term project now is to operate a two-qubit gate and demonstrate the violation of Bell inequalities [116, 117, 118, 119]. Apart from the interest to implement 2 qubit algorithms, such an experiment would be the first direct proof of entanglement in a solid state system. The main issue to be solved is to operate two qubits, both simultaneously on resonance and tuned to their optimal working points. This is at first sight not possible because of the lack of control of fabrication parameters. However, even if the two qubits are off resonance, it is possible to bring them on resonance in the rotating frame [120], which allows for an efficient and flexible coupling of the two qubits. This technique, inspired here also from NMR is very promising. Another technique, which has also the advantage to be a switchable coupling, employs a parametric modulation of the coupling [121] and could also be used.

Finally, the property of $2e$ periodicity of the quantronium could be used to construct a current to frequency converter and thus provide a metrological current standard. By using Bloch oscillations of the superconducting phase of the island this technique could allow for frequencies of several hundreds of MHz, which is much higher than present day current electron pumps. The resulting currents are higher and the usefulness of such devices would be much improved. Preliminary experiments [122] have demonstrated the viability of this approach for frequencies of a few MHz. A high impedance current source needs still to be implemented.

Bibliography

[1] D. Deutsch. Quantum theory, the Church−Turing principle and the universal quantum computer. *Proc.R.Soc.Lond.A*, **400**:97–117, (1985).

[2] P. Shor. Polynomial-time algorithm for prime factorization and discrete logarithms on a quantum computer. *SIAM J.Comp.*, **26(5)**:1484–1509, (1997).

[3] D. Dieks. Communication by EPR devices. *Phys.Rev.A*, **92(6)**:271–272, (1982).

[4] L. K. Grover. Quantum mechanic helps for searching for a needle in a haystack. *Phys.Rev.Lett.*, **79(2)**:325, (1997).

[5] C. H. Bennett and S. J. Wiesner. Communication via one- and two-particle operators on Einstein-Podolsky-Rosen states. *Phys.Rev.Lett.*, **69**:2881–2884, (1992).

[6] C. H. Bennett, G. Brassard, C. Crépeau, R. Jozsa, A. Peres, and W. K. Wootters. Teleporting an unknown quantum state via dual classical and Einstein-Podolsky-Rosen channels. *Phys.Rev.Lett.*, **70**:1895–1899, (1993).

[7] Y. S. Weinstein, M. A. Pravia, E. M. Fortunato, S. Lloyd, and D. G. Cory. Implementation of the quantum Fourier transform. *Phys.Rev.Lett.*, **86**:1889–1891, (2001).

[8] R. Feynman. Simulating physics with computers. *International Journal of Theoretical Physics*, **21**:467–488, (1982).

[9] C. H. Tseng, S. Somaroo, Y. Sharf, E. Knill, R. Laflamme, T. F. Havel, and D. G. Cory. Quantum simulation of a three-body-interaction Hamiltonian on an NMR quantum computer. *Phys.Rev.A*, **61**(012302), (2000).

[10] P. Shor. Scheme for reducing decoherence in quantum memory. *Phys.Rev.A*, **52**:2493, (1995).

[11] A. M. Steane. Error correcting codes in quantum theory. *Phys.Rev.Lett.*, **77**:793, (1996).

[12] D. Gottesman. Theory of fault-tolerant quantum computation. *Phys.Rev.A*, **57**(1):127–137, (1998).

[13] D. P. DiVincenzo. The physical implementation of quantum computation. *Fortschritte der Physik*, **48(9-11)**:771–783, (2000). Special issue: experimental proposals for quantum computation.

[14] W. S. Warren, N. Gershenfeld, and I. Chuang;. The usefulness of NMR quantum computing. *Science*, **277**:1688–1690, (1997).

[15] D. G. Cory, A. F. Fahmy, and T. F. Havel. Ensemble quantum computing by NMR spectroscopy. *Proc.Nat.Acad.Sci.USA*, **94**:1634–1639, (1997).

[16] I. L. Chuang, L. M. K. Vandersypen, X. Zhou, D. W. Leung, and S. Lloyd. Experimental realization of a quantum algorithm. *Nature*, **393**:143–146, (1998).

[17] L. M. K. Vandersypen, M. Steffen, G. Breyta, C. S. Yannoni, M. H. Sherwood, and I. L. Chuang. Experimental realization of Shor's quantum factoring algorithm using nuclear magnetic resonance. *Nature*, **414**:883–887, (2001).

[18] I. Cirac and P. Zoller. Quantum computation with cold, trapped ions. *Phys.Rev.Lett.*, **74(20)**:4091–4094, (2005).

[19] Ch. Roo, Th. Zeiger, H. Rohde, H. C. Nägerl, J. Eschner, D. Leibfried, F. Schmidt-Kaler, and R. Blatt. Quantum state engineering on an optical transition and decoherence in a Paul trap. *Phys.Rev.Lett.*, **83**:4713–4716, (1999).

[20] C. Monroe, D. M. Meekhof, B. E. King, W. M. Itano, and D. J. Wineland. Demonstration of a fundamental quantum logic gate. *Phys.Rev.Lett.*, **75**:4714, (1995).

[21] F. Schmidt-Kaler, H. Häffner, M. Riebe, S. Gulde, G. P. T. Lancaster, T. Deuschle, C. Becher, C. F. Roos, J. Eschner, and R. Blatt. Realization of the CiracZoller controlled−NOT quantum gate. *Nature*, **422**:408–411, (2003).

[22] C. A. Sackett, D. Kielpinski, B. E. King, C. Langer, V. Meyer, C. J. Myatt, M. Rowe, Q. A. Turchette, W. M. Itano, D. J. Wineland, and C. Monroe. Experimental entanglement of four particles. *Nature*, **404**:256–259, (2000).

[23] J. Chiaverini, D. Leibfried, T. Schaetz, M. D. Barrett, R. B. Blakestad, J. Britton, W. M. Itano, J. D. Jost, E. Knill, C. Langer, R. Ozeri, and D. J. Wineland. Realization of quantum error correction. *Nature*, **432**:602, (2004).

[24] D.Kielpinski, C.Monroe, and D.Wineland. Architecture for a large-scale ion-trap quantum computer. *Nature*, **417**:709, (2002).

[25] M. Brune, F. Schmidt-Kaler, A. Maali, J. Dreyer, E. Hagley, J. M. Raimond, and S. Haroche. Quantum Rabi oscillation: A direct test of field quantization in a cavity. *Phys.Rev.Lett.*, **76**:1800–1803, (1996).

[26] M. Brune, E. Hagley, J. Dreyer, X. Maître, A. Maali, C. Wunderlich, J. M. Raimond, and S. Haroche. Observing the progressive decoherence of the meter in a quantum measurement. *Phys.Rev.Lett.*, **77**:4887–4890, (1996).

[27] A. Rauschenbeutel, G. Nogues, S. Osnaghi, P. Bertet, M. Brune, J. M. Raimond, and S. Haroche. Step-by-step engineered multiparticle entanglement. *Science*, **288**:2024–2028, (2000).

[28] W. Hänsel, P. Hommelhoff, T. W. Hänsch, and J. Reichel. Bose−Einstein condensation on a microelectronic chip. *Nature*, **413**:498–501, (2001).

[29] D. Loss and D. P. DiVincenzo. Quantum computation with quantum dots. *Phys.Rev.A*, **57**:120–126, (1998).

[30] J. M. Elzerman, R. Hanson, L. H. Willems van Beveren, B. Witkamp, L. M. K. Vandersypen, and L. P. Kouwenhoven. Single-shot read-out of an individual electron spin in a quantum dot. *Nature*, **430**:431–435, (2004).

[31] A. C. Johnson, J. R. Petta, J. M. Taylor, A. Yacoby, M. D. Lukin, C. M. Marcus, M. P. Hanson, and A. C. Gossard. Triplet Singlet spin relaxation via nuclei in a double quantum dot. *Nature*, **435**:925–928, (2005).

[32] A. Bertoni, P. Bordone, R. Brunetti, C. Jacoboni, and S. Reggiani. Quantum logic gates based on coherent electron transport in quantum wires. *Phys.Rev.Lett.*, **84**:5912–5915, (2000).

[33] R. Ionicioiu, G. Amaratunga, and F. Udrea. Quantum computation with ballistic electrons. *Int.J.Mod.Phys.*, **B15**:125, (2001).

[34] T. Hayashi, T. Fujisawa, H. D. Cheong, Y. H. Jeong, and Y. Hirayama. Coherent manipulation of electronic states in a double quantum dot. *Phys.Rev.Lett.*, **91**(226804), (2003).

[35] P. Samuelsson, E. V. Sukhorukov, and M. Büttiker. Two-particle Aharonov-Bohm effect and entanglement in the electronic Hanbury Brown & Twiss setup. *Phys.Rev.Lett.*, **92**(026805), (2004).

[36] Y. Nakamura, Yu. A. Pashkin, and J. S. Tsai. Coherent control of macroscopic quantum states in a single Cooper pair box. *Nature*, **398**:786–788, (1999).

[37] Yu. A. Pashkin, T. Yamamoto, O. Astafiev, Y. Nakamura, D. V. Averin, and J. S. Tsai. Quantum oscillations in two coupled charge qubits. *Nature*, **421**:823–826, (2003).

[38] T. Yamamoto, Yu. A. Pashkin, O. Astafiev, Y. Nakamura, and J. S. Tsai. Demonstration of conditional gate operation using superconducting charge qubits. *Nature*, **425**:941–944, (2003).

[39] I. Chiorescu, P. Bertet, K. Semba, Y. Nakamura, C. J. P. M. Harmans, and J. E. Mooij. Coherent dynamics of a flux qubit coupled to a harmonic oscillator. *Nature*, **431**:159–162, (2004).

[40] J. M. Martinis, S. Nam, J. Aumentado, and C. Urbina. Rabi oscillations in a large Josephson junction qubit. *Phys.Rev.Lett.*, **89**:117901, (2002.

[41] V. Bouchiat. *Quantum fluctuations of the charge in single electron and single Cooper pair devices.* PhD thesis, Université Paris VI, http://www-drecam.cea.fr/drecam/spec/Pres/Quantro/, (1997).

[42] Caspar H. van der Wal, A. C. J. ter Haar, F. K. Wilhelm, R. N. Schouten, C. J. P. M. Harmans, T. P. Orlando, Seth Lloyd, and J. E. Mooij. Quantum superposition of macroscopic persistent-current states. *Science*, **290** :773–777, (2000).

[43] G. Ithier, E. Collin, P. Joyez, P. Meeson, D. Vion, D. Esteve, F. Chiarello, A. Shnirman, Y. Makhlin, and G. Schön. Decoherence measurement during the free evolution of a Josephson quantum bit: the quantronium. *In Quantum Computation: solid state systems.*, (2004). P. Delsing, C. Granata, Y. Pashkin, B. Ruggiero and P. Silvestrini (Eds). (Kluwer Academic Plenum).

[44] A. Cottet. *Implementation of a quantum bit in a superconducting circuit.* PhD thesis, Quantronics Group, CEA-Saclay, (2002). http://www-drecam.cea.fr/drecam/spec/Pres/Quantro/.

[45] L. M. K. Vandersypen and I. L. Chuang. NMR techniques for quantum control and computation. *Rev.Mod.Phys.*, **76**:1037–1069, (2004).

[46] I. Siddiqi, R. Vijay, F. Pierre, C. M. Wilson, M. Metcalfe, C. Rigetti, L. Frunzio, and M. H. Devoret. RF-driven Josephson bifurcation amplifier for quantum measurement. *Phys.Rev.Lett.*, **93**:207002, (2004).

[47] I. Siddiqi, R. Vijay, F. Pierre, C. M. Wilson, L. Frunzio, M. Metcalfe, C. Rigetti, R. J. Schoelkopf, M. H. Devoret, D. Vion, and D. Esteve. Direct observation of dynamical bifurcation between two driven oscillation states of a Josephson junction. *Phys.Rev.Lett.*, **94**:027005, (2005).

[48] L. D. Landau and E. M. Lifshitz. *Mechanics.* Mir, (1960).

[49] K. B. Cooper, M. Steffen, R. McDermott, R. W. Simmonds, S. Oh, D. A. Hite, D. P. Pappas, and J. M. Martinis. Observation of quantum oscillations between a Josephson phase qubit and a microscopic resonator using fast readout. *Phys.Rev.Lett.*, **93**:180401, (2004).

[50] R. W. Simmonds, K. M. Lang, D. A. Hite, S. Nam, D. P. Pappas, and J. M. Martinis. Decoherence in Josephson phase qubits from junction resonators. *Phys.Rev.Lett.*, **93**:077003, (2004).

[51] V. Bouchiat, D. Vion, P. Joyez, D. Esteve, and M. H. Devoret. Quantum coherence with a single cooper pair. *Phys. Scr.*, **T 76**:165, (1998).

[52] O. Astafiev, Yu. A. Pashkin, Y. Nakamura, T. Yamamoto, and J. S. Tsai. Quantum noise in the Josephson charge qubit. *Phys.Rev.Lett.*, **93**:267007, (2004).

[53] R. F. Voss and R. A. Webb. Macroscopic quantum tunneling in 1μm Nb Josephson junctions. *Phys.Rev.Lett.*, **47**:265–268, (1981).

[54] J. M. Martinis, M. H. Devoret, and J. Clarke. Experimental tests for the quantum behavior of a macroscopic degree of freedom: The phase difference across a Josephson junction. *Phys.Rev.B*, **35**:4682–4698, (1987).

[55] U. Weiss. *Quantum dissipative systems.* World Scientific, (1999).

[56] J. Ankerhold and H. Grabert. Enhancement of macroscopic quantum tunneling by Landau-Zener transitions. *Phys.Rev.Lett.*, **91**:016803, (2003).

[57] G. Ithier, E. Collin, P. Joyez, D. Vion, D. Esteve, J. Ankerhold, and H. Grabert. Zener enhancement of quantum tunneling in a two-level superconducting circuit. *Phys.Rev.Lett.*, **94**:057004, (2005).

[58] W. H. Zurek. Pointer basis of quantum apparatus: Into what mixture does the wave packet collapse? *Phys.Rev.D*, **24**:1516–1525, (1981).

[59] W. H. Zurek. Environment-induced superselection rules. *Phys.Rev.D*, **26**:1862–1880, (1982).

[60] T. Duty, D. Gunnarsson, K. Bladh, and P. Delsing. Coherent dynamics of a Josephson charge qubit. *Phys.Rev.B*, **69**:140503, (2004).

[61] I. Chiorescu, Y. Nakamura, C. J. P. M. Harmans, and J. E. Mooij. Coherent quantum dynamics of a superconducting flux qubit. *Science*, **299**:1869–1871, (2003).

[62] C. P. Slichter. *Principles of Magnetic Resonance.* Series in Solid-State Sciences. Springer, (1990).

[63] R. K. Wangsness and F. Bloch. *Phys.Rev.*, **89**:728.

[64] M. A. Nielsen and I. L. Chuang. *Quantum Computation and Quantum Information.* Cambridge University Press, (2000).

[65] H. K. Cummings, G. Llewellyn, and J. A. Jones. Tackling systematic errors in quantum logic gates with composite rotations. *Phys.Rev.A*, **67**(042308), (2003).

[66] G. Ithier, E. Collin, P. Joyez, P. J. Meeson, D. Vion, D. Esteve, F. Chiarello, A. Shnirman, Y. Makhlin, J. Schriefl, and G. Schön. Decoherence in a superconducting quantum bit circuit. *Phys.Rev.B*, **72**:134519, (2005).

[67] D. J. Van Harlingen, T. L. Robertson, B. L. T. Plourde, P. A. Reichardt, T. A. Crane, and John Clarke. Decoherence in Josephson-junction qubits due to critical-current fluctuations. *Phys.Rev.B*, 70:064517, (2004).

[68] J. M. Martinis, S. Nam, J. Aumentado, K. M. Lang, and C. Urbina. Decoherence of a superconducting qubit due to bias noise. *Phys.Rev.B*, **67**:094510, (2003).

[69] F. C. Wellstood, C. Urbina, and J. Clarke. Flicker (1/f) noise in the critical current of Josephson junctions at $0.09 - 4.2$ K. *Appl. Phys. Lett.*, **85**:5296, (2004).

[70] G. Zimmerli, T. M. Eiles, R. L. Kautz, and J. M. Martinis. Noise in the Coulomb blockade electrometer. *Appl. Phys. Lett.*, **61**:237, (1992).

[71] E. H. Visscher, S. M. Verbrugh, P. Hadley J. Lindeman, and J. E. Mooij. Fabrication of multilayer single-electron tunneling devices. *Appl. Phys. Lett.*, **66**:3, (1995).

[72] P. Delsing D. B. Haviland T. Claeson N. Rorsman J. Pettersson, P. Wahlgren and H. Zirath. Extending the high-frequency limit of a single-electron transistor by on-chip impedance transformation. *Phys.Rev.B*, **53**:R13272, (1996).

[73] A. B. Zorin, F.-J. Ahlers, J. Niemeyer, T. Weimann, H. Wolf, V. A. Krupenin, and S. V. Lotkhov. *Phys. Rev. B*, **53**:13682, (1996).

[74] R. H. Koch, J. Clarke, W. M. Goubau, J. Martinis, C. W. Pegrum, and D. J. Van Harlingen. *J. Low Temp. Phys.*, **51**:207, (1983).

[75] G. Stan, S. B. Field, and J. M. Martinis. Critical field for complete vortex expulsion from narrow superconducting strips. *Phys.Rev.Lett.*, **92**:097003, (2004).

[76] F. C. Wellstood. *Excess noise in the dc SQUID;* $4.2K$ *to* $20mK$. PhD thesis, Lawrence Berkeley Laboratory, University of California, (1988).

[77] G. Burkard, D.P. DiVincenzo, P. Bertet, I. Chiorescu, and J. E. Mooij. Asymmetry and decoherence in double-layer persistent-current qubit.

[78] E. L. Hahn. Spin echoes. *Phys.Rev.*, **80**:580–594, (1950).

[79] E. Geva, R. Kosloff, and J. L. Skinner. On the relaxation of a two-level system driven by a strong electromagnetic field. *J. Chem. Phys.*, **102**:(21), 8541, (1995).

[80] F. Bloch. Generalized theory of relaxation. *Phys.Rev.*, **105**(4):1206, 1957.

[81] Yu. Makhlin and A. Shnirman. Dephasing of qubits by transverse low-frequency noise. *JETP Lett.*, **78**:497, (2003).

[82] Y. Nakamura, Y. A. Pashkin, T. Yamamoto, and J. S. Tsai. Charge echo in a Cooper pair box. *Phys.Rev.Lett.*, **88**:047901, (2002).

[83] E. Knill L. Viola and S. Lloyd. Dynamical decoupling of open quantum systems. *Phys.Rev.Lett.*, **82**:2417–2421, (1999).

[84] Yu. Makhlin and A. Shnirman. Dephasing of solid-state qubits at optimal working points. *Phys.Rev.Lett.*, **92**:178301, (2004).

[85] K. Rabenstein, V. A. Sverdlov, and D. V. Averin. Qubit decoherence by gaussian low frequency noise. *JETP Lett.*, **79**(646), (2004).

[86] G. Falci, A. D'Arrigo, A. Mastellone, and E. Paladino. Dynamical suppression of telegraph and 1/f noise due to quantum bistable fluctuators. *Phys.Rev.A*, **70**(040101(R)), (2004).

[87] P. Dutta and P. M. Horn. Low-frequency fluctuations in solids: 1/f noise. *Rev.Mod.Phys.*, **53**:497, (1981).

[88] E. Paladino, L. Faoro, G. Falci, and R. Fazio. Decoherence and 1/f noise in Josephson qubits. *Phys.Rev.Lett.*, **88**:228304, (2002).

[89] M. B. Weissman. 1/f noise and other slow, nonexponential kinetics in condensed matter. *Rev.Mod.Phys.*, **60**:537, (1988).

[90] J. Schriefl. PhD thesis, ENS-Lyon, (2005).

[91] Y. M. Galperin, B. L. Altshuler, and D. V. Shantsev. Low-frequency noise as a source of dephasing of a qubit. *Fundamental Problems of Mesoscopic Physics*, pages 141–165, (2003). edited by I.V. Lerner *et al.* (Kluwer Academic Publishers, The Netherlands,2004) also on cond-mat/0312490.

[92] R. Klauder and P.W. Spectral diffusion decay in spin resonance experiments. *Phys.Rev.*, **125**:912, (1962).

[93] J. L. Black and B. I. Halperin. Spectral diffusion, phonon echoes, and saturation recovery in glasses at low temperatures. *Phys.Rev.B*, **16**:2879, (1977).

[94] E. M. Fortunato, M. A. Pravia, N. Boulant, G. Teklemariam, T. F. Havel, and D. G. Cory. Design of strongly modulating pulses to implement precise effective Hamiltonians for quantum information processing. *Journal of Chemical Physics*, **116**(17):7599–7606, (2002).

[95] D. Vion, A. Aassime, A. Cottet, P. Joyez, H. Pothier, C. Urbina, D. Esteve, and M. H. Devoret. Manipulating the quantum state of an electrical circuit. *Science*, **296**:886–889, (2002).

[96] A. Aassime, G. Johansson, G. Wendin, R. J. Schoelkopf, and P. Delsing. Radio-frequency single-electron transistor as readout device for qubits: Charge sensitivity and back-action. *Phys.Rev.Lett.*, **86**(3376), (2001).

[97] D. I. Schuster, A. Wallraff, A. Blais, L. Frunzio, R.-S. Huang, J. Majer, S. M. Girvin, and R. J. Schoelkopf. AC stark shift and dephasing of a superconducting qubit strongly coupled to a cavity field. *Phys.Rev.Lett.*, **94**:123602, (2005).

[98] L. Viola and S. Lloyd. Dynamical suppression of decoherence in two-state quantum systems. *Phys.Rev.A*, 58:2733–2744, (1998).

[99] R. McDermott, R. W. Simmonds, M. Steffen, K. B. Cooper, K. Cicak, K. D. Osborn, S. Oh, D. P. Pappas, and J. M. Martinis. Simultaneous state measurement of coupled Josephson phase qubits. *Science*, **307**:1299–1302, (2005).

[100] D. Kielpinski, V. Meyer, M. A. Rowe, C. A. Sackett, W. M. Itano, C. Monroe, and D. J. Wineland. A decoherence-free quantum memory using trapped ions. *Science*, **291**, (2001).

[101] J. P. Pekola O. Buisson, F. Balestro and F. W. J. Hekking. One-shot quantum measurement using a hysteretic dc squid. *Phys.Rev.Lett.*, **90**:238304, (2003).

[102] A. Wallraff, D. I. Schuster, A. Blais, L. Frunzio, R.-S. Huang, J. Majer, S. Kumar, S. M. Girvin, and R. J. Schoelkopf. Strong coupling of a single photon to a superconducting qubit using circuit quantum electrodynamics. *Nature*, **431**:162, (2004).

[103] E. Il'Ichev, N. Oukhanski, A. Izmalkov, Th. Wagner, M. Grajcar, H.-G. Meyer, A. Yu. Smirnov, A. Maassen van den Brink, M. H. S. Amin, and A. M. Zagoskin. Continuous monitoring of Rabi oscillations in a Josephson flux qubit. *Phys.Rev.Lett.*, **91**:097906, (2003).

[104] M. A. Sillanpää, T. Lehtinen, A. Paila, Yu. Makhlin, L. Roschier, and P. J. Hakonen. Direct observation of a Josephson capacitance. *Phys.Rev.Lett.*, **95**:206806, (2005).

[105] L. Frunzio, A. Wallraff, D. Schuster, J. Majer, and R. Schoelkopf. Fabrication and characterization of superconducting circuit QED devices for quantum computation. *IEEE Trans. on Appl. Superc.*, **15**:860–863, (2005).

[106] M. I. Dykman and M. A. Krivoglaz. Time correlation functions and spectral distributions of the Duffing oscillator in a random force field. *Physica*, **104A**:495–508, (1980).

[107] M. I. Dykman and M. A. Krivoglaz. Theory of fluctuational transitions between stable states of a nonlinear oscillator. *Sov.Phys.JETP*, **50(1)**, (1979).

[108] M. I. Dykman and M. A. Krivoglaz. Fluctuations in nonlinear systems near bifurcations corresponding to the appearance of new stable states. *Physica*, **104A**:480–494, (1980).

[109] P. Ribeiro. A new readout method for the quantronium qubit circuit. (2005). Internship Report CEA/Saclay.

[110] Francois Nguyen. Readout of a superconducting quantum bit by microwave reflectometry: the quantronium and the Josephson bifurcation amplifier. (2005). Internship Report CEA/Saclay.

[111] N. Grönbech-Jensen, M. G. Castellano, F. Chiarello, M. Cirillo, C. Cosmelli, V. Merlo, R. Russo, and G. Torrioli. Anomalous thermal escape in Josephson systems perturbed by microwaves. (2004). cond-mat/0412692.

[112] VanKampen. *Stochastic Processes in Physics and Chemistry*. Elsevier, (1992).

[113] P. K. Day, H. G. LeDuc, B. A. Mazin, A. Vayonakis, and J. Zmuidzinas. A broadband superconducting detector suitable for use in large arrays. *Nature*, **425**:817–821, (2003).

[114] Guido Burkard, David P. DiVincenzo, P. Bertet, I. Chiorescu, and J. E. Mooij. Asymmetry and decoherence in a double-layer persistent-current qubit. *Physical Review B (Condensed Matter and Materials Physics)*, 71(13):134504, 2005.

[115] L. Roschier C. J. P. M. Harmans A. Lupascu, E. F. C. Driessen and J. E. Mooij. High-contrast dispersive readout of a superconducting flux qubit using a nonlinear resonator. *Phys.Rev.Lett.*, **96**(127003), 2006.

[116] John F. Clauser, Michael A. Horne, Abner Shimony, and Richard A. Holt. Proposed experiment to test local hidden variable theories. *Phys. Rev. Lett.*, 24(10):549, Mar 1970.

[117] John F. Clauser and Michael A. Horne. Experimental consequences of objective local theories. *Phys. Rev. D*, 10(2):526–535, Jul 1974.

[118] Alain Aspect, Philippe Grangier, and Gérard Roger. Experimental realization of einstein-podolsky-rosen-bohm gedankenexperiment: A new violation of bell's inequalities. *Phys. Rev. Lett.*, 49(2):91–94, Jul 1982.

[119] Alain Aspect, Jean Dalibard, and Gérard Roger. Experimental test of bell's inequalities using time-varying analyzers. *Phys. Rev. Lett.*, 49(25):1804–1807, Dec 1982.

[120] C. Rigetti, A. Blais, , and M. Devoret. Protocol for universal gates in optimally biased superconducting qubits. *Phys.Rev.Lett.*, **94**(240502), 2005.

[121] P. Bertet, C. J. P. M. Harmans, and J. E. Mooij. Parametric coupling for superconducting qubits. *Physical Review B (Condensed Matter and Materials Physics)*, 73(6):064512, 2006.

[122] N. Boulant, G. Ithier, F. Nguyen, P. Bertet, H. Pothier, D. Vion, C. Urbina, and D. Esteve. Bloch oscillations in a josephson circuit. *cond-mat/0605061*, 2006.